Newcastle University

Doctoral Thesis

Investigating the *in vivo* dynamics of FtsZ and FtsZ-Interacting Proteins using Vertical Cell Imaging by Nanostructured Immobilisation (VerCINI).

Calum Steven Jukes

January 2021

Acknowledgements

I would like to start by thanking my supervisor Séamus Holden for not only giving me the opportunity to study for a PhD in his lab, but for the guidance and support he has provided me with over the years. I would also like to thank the rest of the lab for the friendly and collaborative atmosphere that has made this PhD such a joy to undertake.

There are many people who deserve to be acknowledged, but it goes without saying that I would not be where I am today without the support of my family. Lynda, Steven, Laura and Charlotte have always been there for me, from cheering me on throughout my PhD to putting up with my moods when feeling stressed. In particular, I'd like thank my parents Lynda and Steven, who it is really down to that I stand where I am today.

I would also like to thank Emily Abbot, Christophe Noel and Sharon Coulson for giving me my first lab job as a scared undergrad, and the constant support, advice and friendship they have offered me over the years, even when I no longer worked alongside them. I genuinely believe that without their help, I would never have gained the skills and experience to undertake a PhD and thus I shall be forever grateful.

For making my time in Newcastle such an excellent experience, I would like to thank Charles, Lauren and Kasia, friends I know I have made for life. This PhD thesis was written during the Covid-19 pandemic and as such I would like to thank Bernhard Kepplinger and Martyna Pastok for the support and friendship offered through this difficult time, for not only inviting me to into their "bubble", but for making me feel part of their family when I could see my own.

PhD candidate's authorship statement, Newcastle University

PhD candidate's name: Calum Steven Jukes

Principle Investigator: Dr Séamus Holden

Title of PhD thesis: Investigating *the in vivo* dynamics of FtsZ and FtsZ-Interacting Proteins using Vertical Cell Imaging by Nanostructured Immobilisation (VerCINI).

Chapter 1: Introduction

I fully wrote and outlined this chapter with revisions made by comments from Dr Séamus Holden.

Chapter 2: A novel vertical immobilization imaging technique shows that FtsZ filaments treadmill bi-directionally around the division site in B. subtilis division

The research question for this chapter was defined by Dr Séamus Holden and resulted in a multi-lab collaboration as published[1]. Silicon Micropillars were etched by Dr Fabai Wu at TU Delft and initial proof of concept measurements of the vertical cell immobilization method was performed by Dr Séamus Holden. I applied the vertical immobilization microscopy method to determine FtsZ and FtsA dynamics in vertically immobilised cells. I performed manual kymograph analysis and quantitative data analysis. Dr Séamus Holden wrote the image analysis code for kymograph generation. Single molecule TIRF experiments and simultaneous dual colour TIRF experiments were conducted by the Garner Lab at Harvard University. I created and validated the new strains used in this chapter as described in methods and materials except for the already established strains indicated. I wrote this chapter with revisions made based on comments by Dr Séamus Holden. I created all figures except for Figure 2.8 which was reproduced from[1].

Chapter 3: Amendment to previous statement

The research aims of this chapter were defined by Dr Séamus Holden, Professor Ethan Garner at Harvard university and myself. I conducted the imaging described in this chapter. I also conducted the Western Blots, PCRs, Growth Curves and cell morphology assays. Collaborators in the Garner Lab conducted the complementation assays and mixed expression strain controls. Whole genome sequencing was conducted by MicrobesNG and sequences reassembled by Dr Alex Bisson-Filho. I created the strains as described in the methods and materials. I wrote this chapter with changes made based on comments by Dr Séamus Holden and created all figures except Figures 3.3 and 3.4 which were created by the Dr Alex Bisson-Fhilo and reproduced from[2].

Chapter 4: Development of VerCINI

The research aims in this chapter were defined by Dr Séamus Holden, Dr Kevin Whitley and myself. I completely redesigned, optimised and quantified the VerCINI cell loading protocol. The new silicon micropillars were designed between Dr Séamus Holden, Dr Kevin Whitley and myself. New silicon micropillars were etched by Dr Kevin Whitey supervised by Professor Cees Dekker at TU Delft. I imaged cells expressing cytoplasmic GFP and these images where then used by Dr Séamus Holden in order to devise and implement the custom background subtraction algorithm. Dr Séamus Holden implemented the VerCINI image processing algorithms and installed the ring-HiLO illuminator. I measured and quantified the performance of the new sample illumination and image processing methods. I performed and optimised the imaging conducted in this chapter in addition to manual data analysis and created the strains as described in the methods and materials. I wrote this chapter with changes made based on comments by Dr Séamus Holden and created all figures except Figure 4.1 which was created by Dr Séamus Holden.

Chapter 5: FtsZ Treadmilling is essential for Z-ring condensation in B. subtilis cell division

The research aims presented in this chapter were defined by Dr Séamus Holden and myself. I conducted all the experiments presented in this chapter and all manual data analysis. I performed the automated quantitative data analysis with initial assistance from Dr Séamus Holden. Dr Kevin Whitley wrote the code for quantification of division protein septal location. I wrote this chapter with changes made based on comments by Dr Séamus Holden and created all figures except for figure 5.6, which was made by Dr Séamus Holden

Chapter 6: Imaging the in vivo dynamics of the FtsZ associated proteins

The research aims presented in this chapter were defined by Dr Séamus Holden and myself. I created all new strains defined in the materials and methods. I performed all experiments and conducted all data analysis. I wrote this chapter and created all figures, with changes made based on comments by Dr Séamus Holden.

__Chapter 7: General discussion and future outlook__

I wrote and outlined this chapter with changes made based on comments by Dr Séamus Holden.

Date:	07/01/2021
PhD candidate signature:	C. S. Jukes
Principal Investigator signature:	Séamus Holden

Abstract

Division is arguably one of the most difficult mechanistic tasks that cells face, requiring precise temporal and spatial regulation. Gram-positive bacteria also face an additional mechanistic problem - high turgor pressure. In order to successfully divide, Gram-positive organisms synthesise a peptidoglycan septum which cleaves the cell in two, yielding two daughter cells.

Prior to cell division, the almost universally essential cytoskeletal tubulin homologue FtsZ polymerizes into a highly dynamic, ring-like band of short filaments at mid-cell- the Z-ring. The Z-ring is tethered to the plasma membrane via anchor proteins, following which the Z-ring recruits septal PG synthases forming the mature divisome. These synthases build the septum which partitions the cell in two.

This work investigates the organisation and dynamics of the Z-ring in the Gram-positive model organism *B. subtilis*. In this thesis, I established a high-throughput approach of Vertical Cell Imaging by Nanostructured Immobilisation (VerCINI) in order to visualise the dynamics of the division machinery around the entirety of the division plane. Using this technique in combination with advanced fluorescence microscopy, I discovered that FtsZ filaments treadmill around the division plane in live bacteria, a phenomenon previously only described *in vitro*. Treadmilling is a type of motion whereby an asymmetric filament undergoes plus-end polymerization and minus-end depolymerisation. I investigated how the organisation and dynamics of filaments within the Z-ring develops over the cell cycle. My results indicate that FtsZ treadmilling is unstable in nascent Z-rings, but stabilizes during the transition to mature rings, before constriction has been initiated. This shows that both FtsZ filament assembly to midcell and FtsZ filament treadmilling dynamics are actively cell cycle regulated. I examined the dynamics of a number of key FtsZ interacting proteins (EzrA, SepF and DivIVA), observing a range of static and dynamic protein motions in ZIPs imaged, arguing against a single, monolithic divisome complex.

Research output

Published and submitted works (refer to Appendix III):

Alexandre Wilson Bisson Filho, Yen-Pang Hsu, Georgia Squyres, Erkin Kuru, Fabai Wu, Calum Jukes, Cees Dekker, Séamus Holden, Michael VanNieuwenhze, Yves Brun, Ethan Garner, Treadmilling by FtsZ filaments drives peptidoglycan synthesis and bacterial cell division. Science, 355, 739-743 (2017).

Kevin D. Whitley*, Calum Jukes*, Nick Tregidgo, Eleni Karinous, Pedro Almada, Yann Cesbron, Ricardo Henriques, Cees Dekker, and Séamus Holden, FtsZ treadmilling is essential for Z-ring condensation and septal constriction initiation in *Bacillus subtilis* cell division. *Nat Commun* **12,** 2448 (2021). https://doi.org/10.1038/s41467-021-22526- *Equal author contribution.

Oral Presentations:

2019: "Divided we stand: Using vertical immobilisation to reveal the effects of FtsZ associated proteins on the Z ring". The Great Wall Symposium 2019. Paris, France.

2017: "The great divide: How a motile cytoskeleton drives bacterial cell division". 5th Molecular Microbiology Meeting & 4th Midlands Molecular Microbiology Meeting (M4), Birmingham, UK.

Poster Presentations:

2019: "Divided we stand: Using vertical immobilisation to reveal the effects of FtsZ associated proteins on the Z ring". The Great Wall Symposium 2019. Paris, France.

2019: "Divided we stand: Vertical immobilisation reveals the divisome's dynamics". 6th Molecular Microbiology Meeting. Newcastle, UK.

2018: "Super-resolving the Bio-physical mechanisms of bacterial cell division". Gordon Research Conference, Plant and Microbial Cytosketelon, New Hampshire, USA

2017: "The great divide: How a motile cytoskeleton drives bacterial cell division". 5th

Molecular Microbiology Meeting & 4th Midlands Molecular Microbiology Meeting (M4), Birmingham, UK

List of figures and tables

General Abbreviations

(ADC)	analogue-to-digital converter
ATP	adenosine-5'-triphosphate
cAMP	cyclic adenosine monophosphate
cat	chloramphenicol
CCD	charge-coupled device
CDM	chemically defined medium
CMOS	complementary metal oxide semiconductor
DNA	deoxyribonucleic acid
e.g.	*exempli gratia* (for example)
erm	erythromycin
EDTA	ethylene diamine tetraacetic acid
EMCCD	Electron multiplying charge-coupled device
et al.	*et alii* (and others)
FOV	field of view
GFP	green fluorescent protein
GTP	guanosine triphosphate
PG	peptidoglycan
gDNA	genomic DNA
HiLO	highly inclined and laminated optical sheet microscopy
IFM	immunofluorescence microscopy
IQR	interquartile range
kan	kanamycin
Kb	kilo base pair

kDa	kilo Dalton
LB	Luria-Bertani medium
Linc	Lincomycin
OD_{600}	optical density measured at wavelength 600 nm
PSF	point spread function
MOS	metaloxide superconductor
NA	nutrient agar
PAGE	polyacrylamide gel electrophoresis
PALM	photoactivation localisation microscopy
PCR	polymerase chain reaction
sCMOS	scientific complementary metal oxide semiconductor
SIM	structured illumination microscopy
SDS	sodium dodecyl sulphate
SNR	signal to noise ratio
Spec	spectinomycin
STED	stimulated emission depletion microscopy
STORM	stochastic optical reconstruction microscopy
TIRF	total internal reflection microscopy
TLM	time lapse medium
VerCINI	Vertical Cell Imaging by Nanostructured Immobilisation
Wt	wild-type

Contents

Chapter 1 : Introduction

Cell division is arguably one of the most difficult mechanistic tasks that bacteria face, requiring precise temporal and spatial regulation. Bacterial cells must also overcome another physical obstacle - turgor pressure. This leads to one of the central issues of bacterial cell division, how do cells cleave themselves in two without bursting?

1.1 The physical problem of bacterial cell division

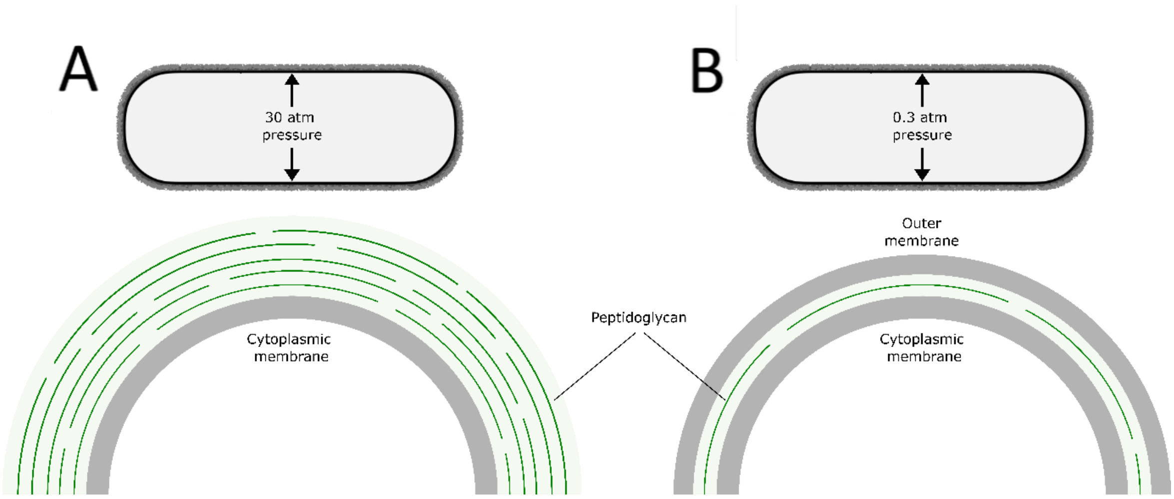

Figure 1.1: The architecture of the bacterial cell envelope. (A) The model Gram-positive *B. subtilis* possesses a cytoplasmic membrane surrounded by a thick, multi-layered cell wall. **(B)** Gram-negative bacteria like *E. coli* possesses both an inner and outer membrane. The outer membrane surrounds a thin, mainly single layered cell wall.

The majority of bacterial species are surrounded by a peptidoglycan (PG) sacculus which maintains cells shape and provides mechanical strength to resist osmotic challenges[3]. This mesh-like sacculus surrounds the cytoplasmic or inner membrane and is composed of glycan strands which are crosslinked by short peptides. Gram-positive bacteria possess a single plasma membrane encased by a thick, multi-layered cell wall, allowing cells to maintain an osmotic pressure of up to 30 atmospheres (Figure 1.1A)[4]. In order to divide, Gram-positive bacterium build a PG septum at the division site which is later degraded and remodelled to form the new cell poles (Figure 1.2A)[5]. In contrast to this, Gram-negative bacteria possess both an inner (cytoplasmic) and outer membrane which surrounds a thin, mainly single layered cell wall (Figure 1.1B)[6]. As such, Gram-negative bacteria maintain a lower osmotic pressure (about 0.3 atmospheres)[7]. Rather than building a septal crosswall, Gram-negative cells form a constricting invagination at the midcell. This is most likely the result of the synthesis of new PG at the midcell while the older outer layers are hydrolysed and the outer membrane is remodelled (Figure 1.2B)[8,9].

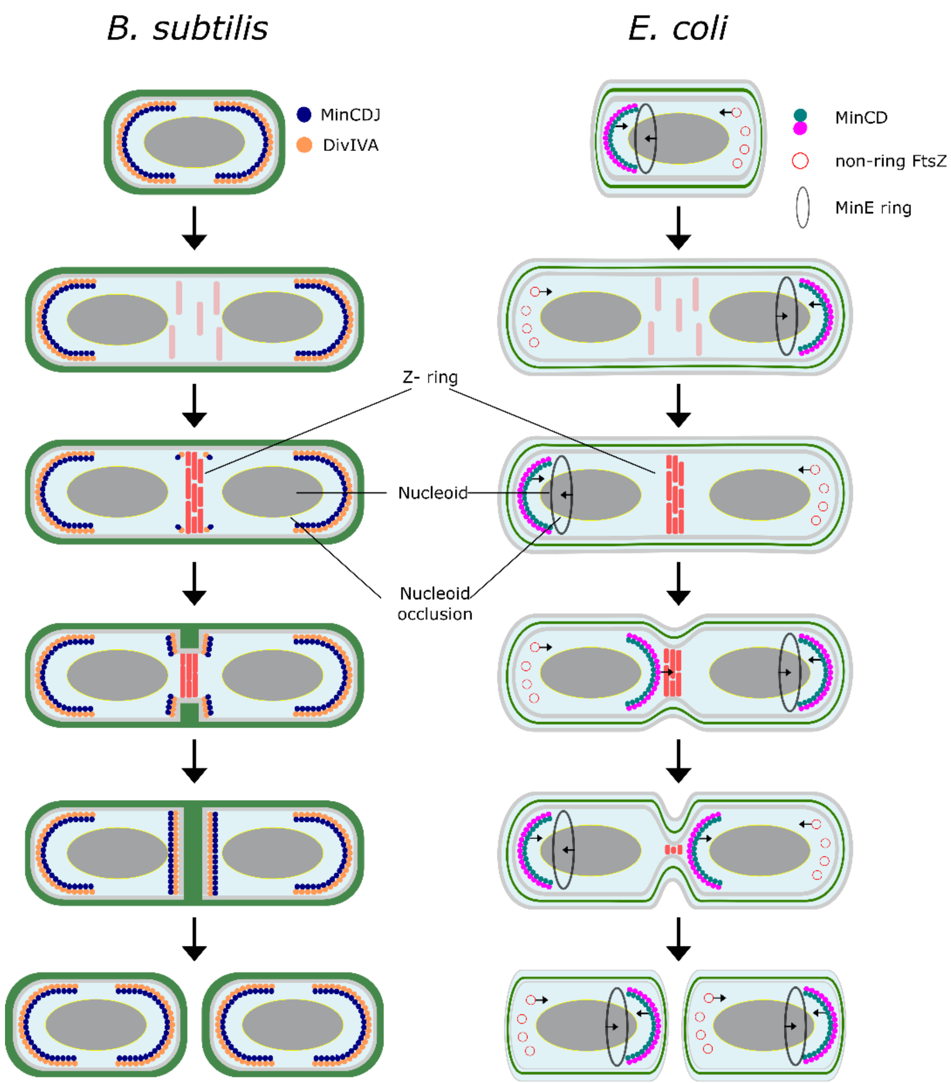

Figure 1.2: Mechanistic principles of Gram-positive *B. subtilis* and Gram-negative *E. coli* cell division . Following chromosome replication and segregation into nucleoids, FtsZ monomers polymerise to form the Z-ring which constricts as cell division progresses. **(A)** In *B. subtilis* a septal crosswall is synthesised which cleaves the cell in two before being degraded and remodelled to form the new cell poles. DivIVA localizes to the cell poles and the leading edge of constriction and recruits MinJ, which subsequently recruits the MinC–MinD complex. Nucleoid occlusion is mediated by Noc. **(B)** In *E. coli*, MinE migrates toward complexes of MinC–MinD at one pole, stimulating the ATPase activity of MinD. This causes causing MinC and MinD to cycle to the opposite pole creating oscillating dynamics. Non-ring FtsZ oscillates as well in response to MinC. When cell division is almost complete, MinC and MinD pause at the septum, likely to ensure equal distribution into daughter cells. Finally, cells divide and each daughter cell has an oscillating Min system. Nucleoid occlusion is mediated by SlmA.

In order to accomplish successful division bacterial cells assemble a macromolecular complex of proteins known as the divisome (Figure 1.3) [10]. At the heart of the divisome is the almost universally essential tubulin homologue FtsZ, which localises to the division site early in the cell division cycle. Here it polymerises into short filaments and forms a ring-like structure called the Z-ring [11]. As FtsZ has no direct affinity for the cytoplasmic membrane, in *Bacillus subtilis* the Z-ring is tethered to the membrane via its functionally redundant membrane anchors FtsA[12] and SepF[13]. The Z-ring then serves as a scaffold, recruiting subsequent division proteins in order to form the mature divisome. At the core of this synthesis complex is an essential glycosyltransferase, (FtsW[12]) which synthesizes glycan strands and an essential transpeptidase (PBP2B) which polymerises new glycan strands into existing cell wall[14]. As division progresses, the Z-ring constricts, its diameter decreasing as the septum is synthesised at the midcell.

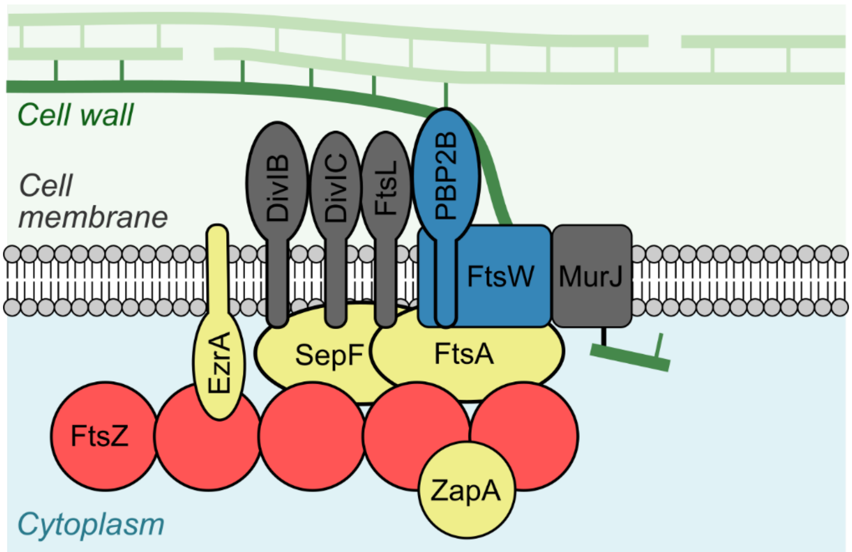

Figure 1.3: Simplified overview of the core proteins in the *B. subtilis* divisome. FtsZ lies at the heart of the divisome and is tethered to the membrane via the functionally redundant anchors FtsA and SepF. FtsZ also directly interacts with modulating proteins; the positive regulator ZapA, and the negative regulator EzrA. Also associated with the divisome are the synthases required to constrict the septum- the glycosyltransferase FtsW and the transpeptidase PBP2B.

Our understanding of the divisome has evolved dramatically since the discovery that FtsZ localises to the midcell nearly 30 years ago. Fluorescence microscopy has greatly expanded our knowledge of the division process, and recent advances in these techniques have made important contributions into answering how the divisome works mechanistically.

1.1.1 Initial Sightings of FtsZ

Cell division genes in *E. coli* were originally called *fts* genes due that the fact that thermosensitive mutants conferred a filamentous temperature-sensitive phenotype[15]. Although unable to divide, cells could still replicate and segregate their nucleoids suggesting that *fts* genes were specifically involved in cytokinesis. However, electron microscopy was unable to discern any type of structure visible by negative staining in normally dividing cells [16].

Bi and Lutkenhaus provided the first evidence that FtsZ, the product of the final *fts* gene in a highly conserved segment of cell wall and division genes in the division and cell wall (cdw) cluster, is a cytoskeletal protein that localises at the midcell in a ring-like structure [17]. Using immunogold labelling, antibody coated gold beads localised near the membrane at the leading site of invagination in cells that were just starting constriction. The authors defined the localisation pattern of FtsZ in different stages of the cell cycle in *E. coli* and hypothesised that FtsZ formed a ring-like structure at the site of division, the diameter of which would decrease as septation progressed. By imaging cross sections of cells that lacked DNA and had a narrow diameter (two characteristics that imply septal cross sections or polar regions), the authors screened for cells in which a ring like structure could be observed[17]. Following this pioneering work, a number of methods involving fluorescence microscopy were adapted for bacterial cell biology that permitted direct visualisation of FtsZ in intact cells.

1.2 The Fundamentals of light microscopy

Light microscopy has been used for centuries to broaden our understanding of how biological systems work, relying on the manipulation and control of light to form an image that has been magnified to reveal the finer details of the sample under observation. If we describe a microscope as an instrument that allows us to visualise objects or structures that are normally invisible to the naked eye, then we can trace its inception back to the late 16th century[18]. Historically, the first known mention of a compound microscope dates back to 1595 when letters by William Borel, the Dutch envoy to the court of France, mentions Hans

Jansen – a Dutch spectacle maker- and his son Zacharais as its inventors. This microscope had two lenses combined in a tube and was capable of varying magnification by altering the distances between the two lenses. However, there are no known publications of any observations made by the Jansens and thus the two names most commonly associated with the origin of the microscope are Robert Hooke and Antonie van Leeuwenhoek [18].

In 1665, Robert Hooke published the first scientific book on microscopy known as Micrographia, and this contained an illustration and description of his refined compound microscope that was a forerunner to modern microscopes. Hooke used this device to develop many scientific theories in addition to describing many biological specimens that were accompanied by exceptionally beautiful drawings. These included a louse, seed and plant cross sections and the compound eye of a fly, all of which he observed under his microscope [19].

Dutch draper Antonie van Leeuwenhoek had no formal scientific training but became fixated on the magnifying glasses used to count threads in cloth [18]. As such, he learned to grind and polish lenses and further developed these methods, creating microscopes capable of resolving details as small as 1 micrometre. Despite the fact that his microscopes only used a single lens, they were in fact superior to Hooke's as multiple lenses increased the problems of spherical and chromatic aberration. Using his simple microscope, van Leeuwenhoek was the first to describe sperm cells as well as observe bacteria and protozoa[20].

Over time, many advancements have been made in the field of optical microscopy which have improved the contrast, specificity and resolution[21].

1.2.1 Contrast in optical microscopy

In terms of imaging, contrast is potentially the most important aspect of image formation as it describes the difference in intensity between an object and the background. If there was no contrast, one would be unable to discern any visible detail. Due to the transparency of many biological specimens, methods that increase contrast must often be implemented.

Brightfield transmission microscopy is potentially the most commonly used microscopy technique and is a result of the of work Ernst Abbe and Carl Zeiss[22]. The compound microscope is widely regarded as the founding tool of modern microscopy and this instrument possessed multiple optical elements to correct aberrations and focus an incoherent light source onto the specimen. An object lens collected transmitted light and an image was formed in several conjugate image planes throughout the microscope before passing through the ocular lens[23]. In order to achieve optimum contrast, homogenous illumination is required. August Köhler developed a method for ensuring that a field of view is homogenously illuminated (Köhler illumination). This is now the standard method for illumination and requires the precise alignment of conjugate image and aperture planes, which occur along the image[24].

Despite its widespread use, brightfield microscopy has very low contrast and when used to study bacteria is only able to provide limited information on features such as the cell outline. As such, techniques which enhance contrast are an essential necessity in order to further probe subcellular features. While absorption-based chemical dyes, Darkfield, Phase Contrast and Differential Interference Microscopy are able of increasing contrast, this introduction will focus on the techniques most relevant to the PhD project.

1.2.2 Fluorescence Microscopy

One of the most commonly used methods to increase contrast is fluorescent labelling to identify subcellular structures. In a properly configured microscope, only the light emitted from a point of fluorescence should reach the detector, causing the resulting fluorescent structures to be superimposed on a dark background, offering very high contrast. A major advantage of fluorescence microscopy has been the development of different staining techniques that allow specific molecules and cells to be labelled. For example fluorescence in situ hybridization (FISH) detects DNA and RNA molecules with specific sequences, whereas immunofluorescent labels and fluorescent proteins allow the imaging of specific proteins in cells[16].

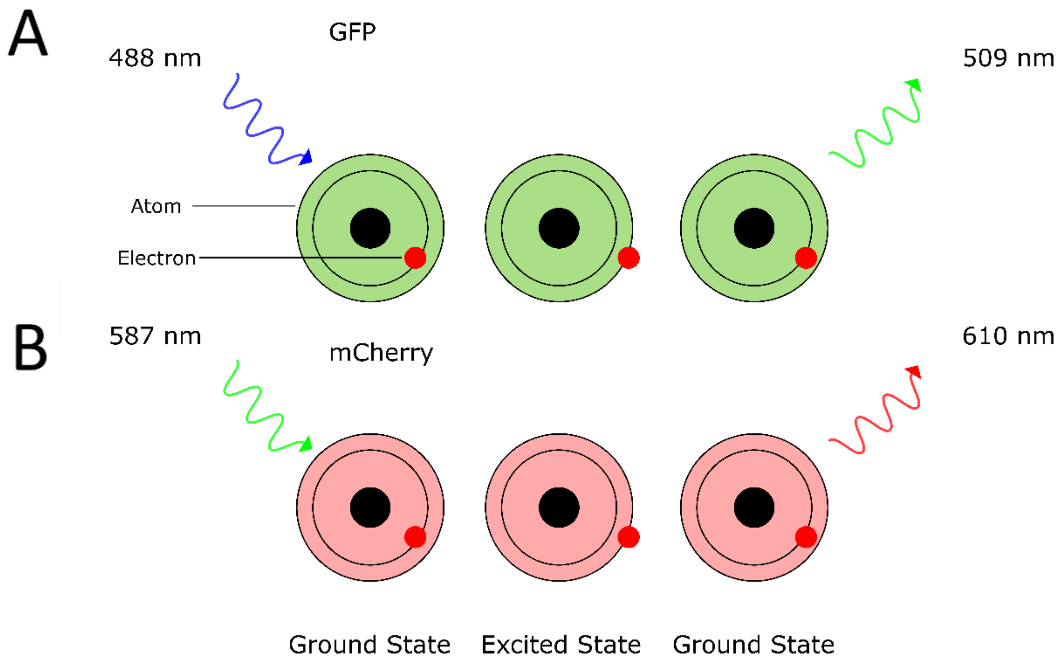

Figure 1.4: Excitation principle of fluorescent proteins. Excitation and emission of **(A)** GFP and **(B)** mCherry. Electrons in a specific residue of the fluorescent protein are excited by a specific wavelength of light. The electrons return to their ground state, emitting their surplus energy as light with a longer wavelength.

Fluorescence microscopy works on the principle that a fluorescent substrate absorbs light of a specific wavelength, and emits light of a longer wavelength (Figure 1.4). In order to understand how this occurs, it is important to understand the vibrational states of the outer electrons of a fluorophore. This is best described through the use of a Jablonski diagram which represents the different vibrational states that outer electrons can occupy, and their decay which induces the release of a photon that is detected as the emission signal in microscopy (Figure 1.5A). In principle, an incident photon excites the electron in the outer shell. This causes the electron to shift from their ground state (S_0) to their lower (S_1) or higher (S_2) signet sate. A photon is then emitted as the energy is converted and the electron returns to its ground state (S_0)[25,26]. This process is extremely rapid, occurring over several nanoseconds. The difference between a fluorophore's peak absorption and emission spectra is known as the Stokes shift (Figure 1.5B)[27,28].

A

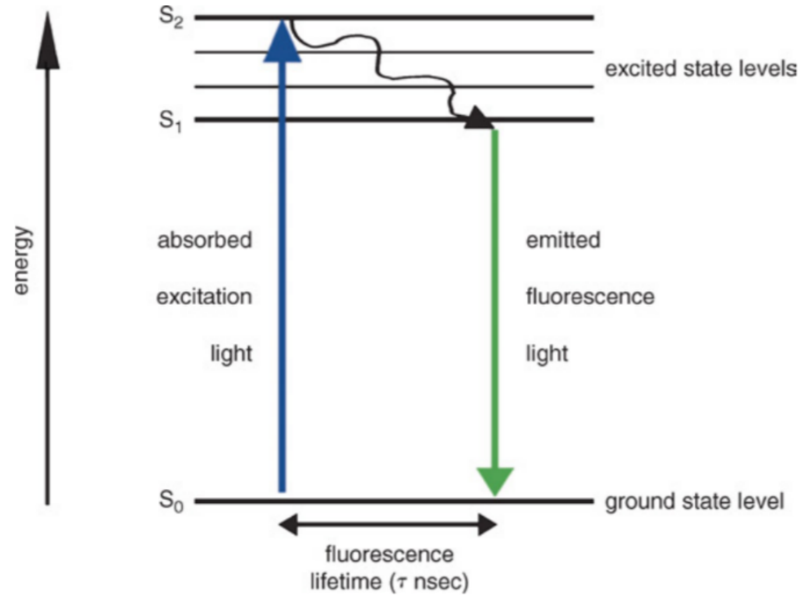

B

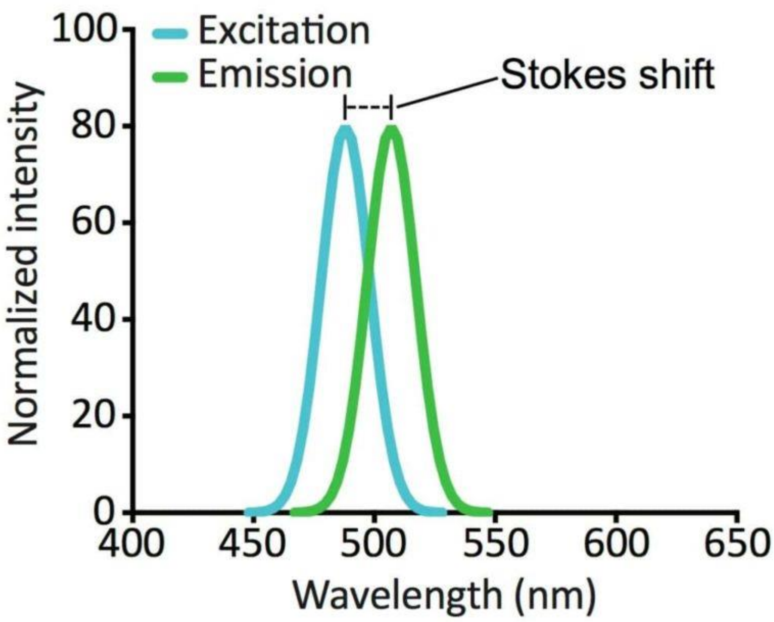

Figure 1.5: Fluorescence excitation and emission. (A) A Jablonski diagram showing how excitation of an electron results in its energy being transferred from its ground state (S_0) to a higher state (S_1 or S_2). Following return to its ground state a photon may be released. **(B)** Simplified Stokes shift diagram where the difference between peak excitation and peak emission gives Stokes shift. Adapted from [26].

The first documented use of fluorescence microscopy was by Oskar Heimstädt, who implemented this method to visualise autofluorescent specimens[29]. Heimstädt observed two main challenges, the first being able to concentrate enough UV light on a specimen to make it fluoresce, and the second was to capture only the emitted fluorescence. These problems were circumvented by the use of special cuvettes that eliminated all but the UV light generated by an arc lamp, and the use of darkfield illumination that ensured no excitation light would enter the objective lens. However, the reliance on autofluorescence and darkfield condensers greatly limited the initial applications of fluorescence microscopy, with Heimstädt himself being sceptical of its longevity[30].

The development of secondary fluorescence via non-autofluorescent compounds (fluorophores/ fluorochromes) that were capable of staining cellular structures propelled the field of fluorescence miscroscopy[31]. Max Haitinger is credited with the discovery of fluorophores, as he used plant extracts, and later chemicals, which enabled him to stain animal and human tissues[31].

The notion of molecular specificity was later refined by Coons and co-workers, in work that dramatically highlighted the power and versatility of fluorescent microscopy through the use of fluorescent antibodies[32]. The idea of using antibodies to visualise structures was first conceived to observe group A haemolytic streptococci in the Aschoff nodules that characterize rheumatic fever[33]. Coons *et al* fused a novel form of fluorescein to label an anti-Pneumococcus strain 3 serum. In addition to maintaining antibody specificity, fluorescence was also observed in infected mouse tissue[32].

1.2.3 Conventional fluorescence microscopy techniques

The development of fluorescent probes and proteins necessitated the development of microscopes capable of visualising fluorescently labelled structures. While the problem of relying on autofluorescence had been overcome, efficient methods of capturing only the emitted light from fluorescent probes remained a blocking issue[30]. In 1929, a prototype of the epifluorescent microscope came close to solving this problem. With this configuration, excitation and emission light passed through the objective allowing more efficient sample excitation[30]. Termed the “Itravital microscope”, excitation light passed through a series of filters, leaving only the right wavelength of light to hit the object lens and trigger emission. A yellow filter was then placed between the object and the ocular to prevent most reflected excitation light from interfering with the observation[30].

Decades later, Johan Sebastian Ploem became for responsible for developing the modern fluorescent microscope by the invention of dichromatic beam splitters [34]. While traditional filters absorb specific wavelengths of light, dichromatic filters are able to reflect a narrow width of wavelengths while the rest are transmitted. This allows the sample to be illuminated with a precise wavelength, while ensuring none of the excitation light is transmitted to the detector (Figure 1.7).

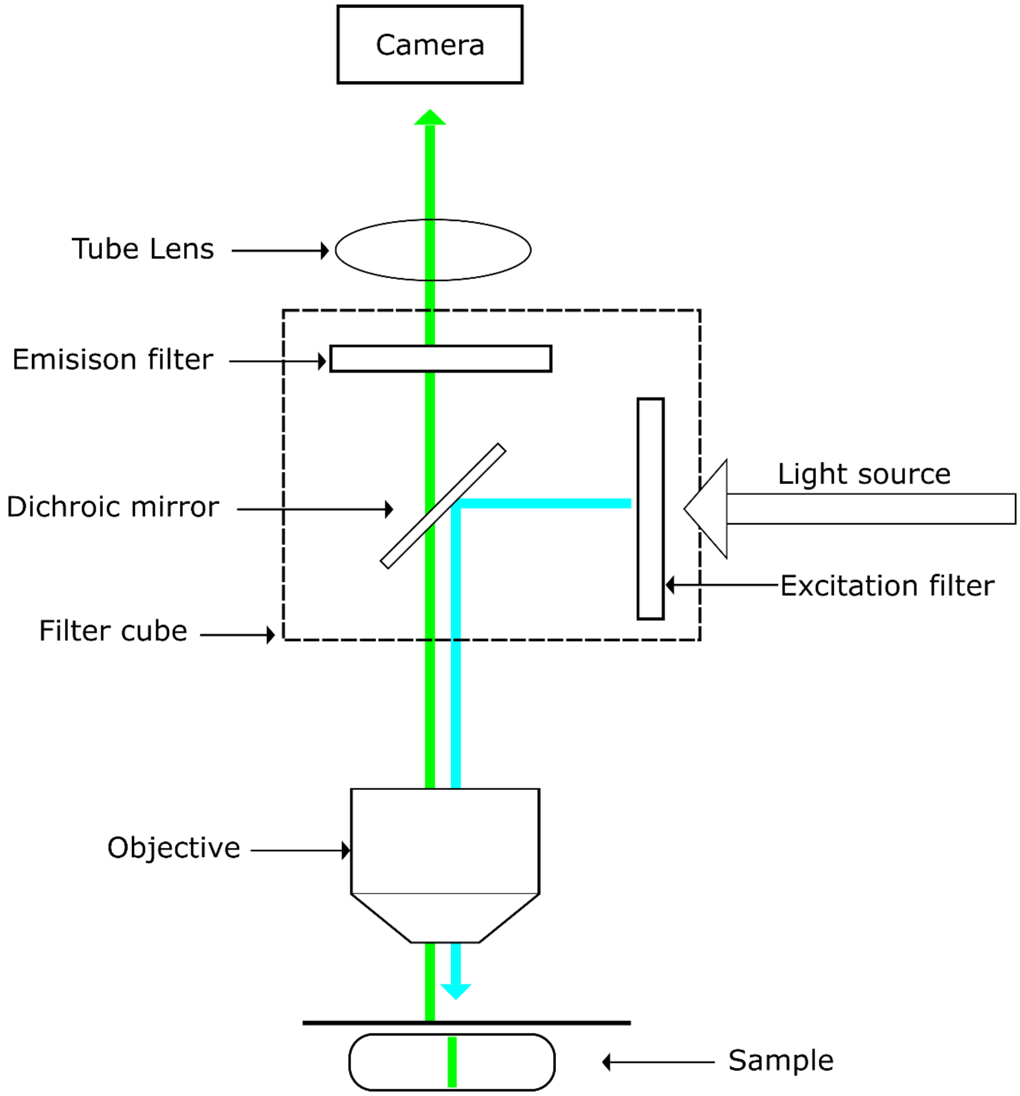

Figure 1.6: Schematic of a modern epifluorescent microscope. Incident light encounters a excitation filter which only transmits a specific wavelength of light. The excitation light then encounters a dichroic mirror which reflects the incident light through the objective which acts as a condenser, ensuring homogenous illumination of the sample. At the sample, the incident light excites the fluorophores resulting in emission of a longer wavelength of light. This is collected by the objective and transmitted through the dichroic mirror, emission filter and tube lens which directs it to a detector.

In modern epifluorescent microscopes, these mirrors are fixed at a 45^{o} angle to the incident light and are capable of reflecting up to 95% of the shorter wavelength light while transmitting the longer wavelength. In an upright microscope, the reflected beam of excitation light then enters the objective, which also acts as condenser to ensure the sample is evenly illuminated. The objective then collects the longer wavelength of light that is emitted by the sample, which passes back through the dichromatic mirror and an emission filter to the detector (Figure 1.6).

Despite the molecular specificity and increased contrast that fluorescence microscopy grants, this technique is not without its own drawbacks. For example, widefield fluorescence microscopy is prone to high background signal due to the fact that excitation is not limited to the focal plane. Thus, a background signal is collected from out of focus planes which results in the acquired imaged having a lower contrast. Excitation of fluorophores above and below the focal plane is also damaging in terms of photobleaching[35]. Photobleaching occurs as a result of excessive excitation causing degradation of the fluorochrome[36]. The rate of photobleaching increases with incident light intensity and over time, and as such limits the observations that can be made from a specimen, in particular, the dynamics of proteins over long time scales. Phototoxicity is another drawback to fluorescence microscopy as it requires the use of strong light to excite fluorophores and thus can have potentially invasive side effects[37]. Phototoxicity from fluorescent microscopy experiments can originate from multiple different sources[37]. For example, organic molecules such as the vitamin riboflavin and the amino acid tryptophan, which are naturally present in cells, absorb visible wavelengths of light and are then degraded when they react with oxygen[38–40]. This results in the production of reactive oxygen species (ROS) which can damage cells in various ways such as the oxidation of DNA (potentially causing mutations) or the oxidation of proteins rendering them non-functional [37]. An additional source of phototoxicity occurs due to photobleaching, as ROS are produced during this phenomenon[37]. Thus despite being separate processes, photobleaching and phototoxicity are intrinsically linked.

1.2.4 Total internal fluorescence microscopy

Total internal fluorescence microscopy is a method of increasing the signal to noise ratio (SNR). However, it does so with the caveat that it can only be used for observations at a biological interface, or structures close to the cell surface. In 1981, Daniel Axelrod built a microscope in which a laser beam hit a glass slide at a high angle[41], building on work from the late 1800s on the detection of scattered photons from total internal reflection excitation[42]. This exploits the principle that when the indecent angle is greater than the critical angle, the beam is completely reflected from the coverslip-slide interface. At the same time, if the refractive index of the sample is less than the refractive index of the coverslip, an evanescent wave is generated which penetrates into the sample and can stimulate excitation of any fluorophores present. As the evanescent wave decays exponentially, it penetrates the sample for only about 200nm. While this greatly restricts illumination to a thin slice at the interface, it also results in a dramatic increase in the SNR as planes outside the focal plane are not illuminated (Figure 1.7). As only a thin slice is illuminated, this also reduces phototoxicity and allows one to lower the light dose to image for longer time periods, thus increasing the time before fluorescent molecules will photobleach[43].

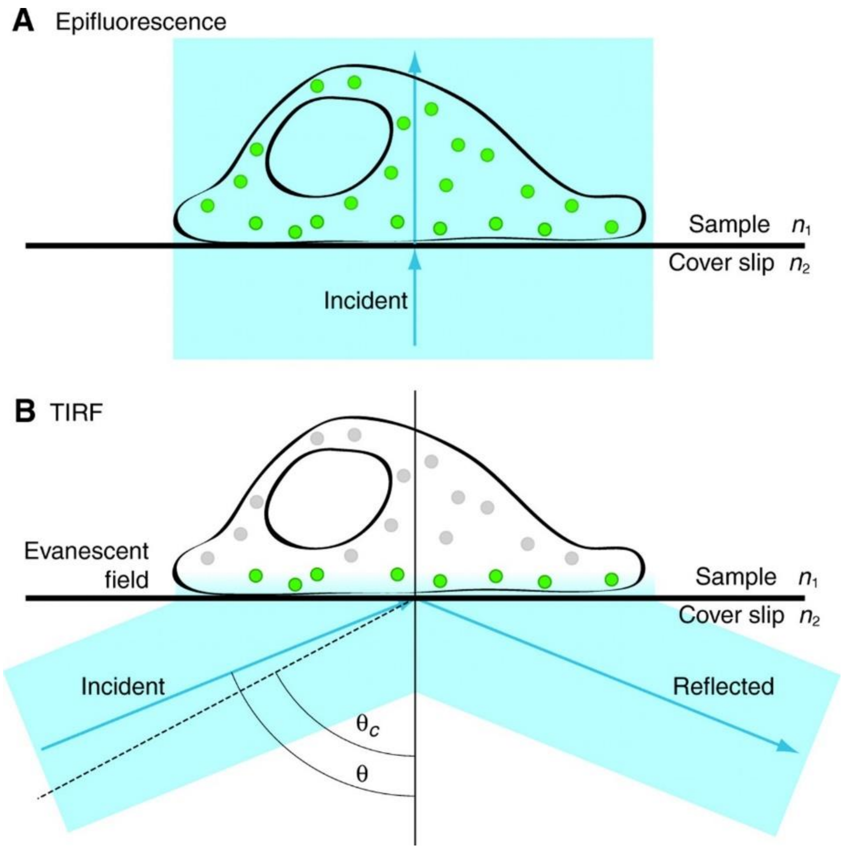

Figure 1.7: ***The physical basis of epifluorescence and TIRF illumination.*** **(A)** Epiflouresence**.** The incident light beam travels directly through the coverslip-sample interface. As such, all the fluorophores are excited. **(B)** TIRF. The incident light beam enters at an angle (θ) that is greater than the critical angle (θ_C). Thus the excitation light beam is reflected from the coverslip-sample interface and an evanescent wave is generated at the opposite side of the interface. The evanescent field decays exponentially and as such only penetrates ~200nm into the sample. Only fluorophores within the field are excited. The refractive index of the sample (n1) must be less than the index of refraction of the cover slip (n2) to achieve TIR. Reproduced from [41].

1.2.5 Microscope Cameras

The majority of microscopy applications require multi-megapixel cameras that are able of operating with an extremely high sensitivity and a high dynamic range [44]. The dynamic range of a CCD or CMOS sensor, the two most commonly used sensors in microscopy , is defined as the instruments maximum achievable signal divided by the camera noise [45]. Thus as the dynamic range increases, the ability of a camera to quantitatively measure the dimmest intensity improves. Sensors that are capable of imaging at rapid frame rates are also desired in order to capture dynamics with high temporal resolution[44]. Furthermore, it terms of microscopy there are three main sources of noise which are generated by the digital cameras used[46].

Photon noise (shot noise) is generated by the statistical fluctuations in the number of photons detected at a specified exposure time[46]. Unfortunately, photon noise is present in all optical systems due to the stochastic nature of photon emission[46]. Photon noise follows a Poisson distribution[46]

Dark noise occurs as a result of thermal agitation of electrons[46]. As the temperature of the camera increases, silicon atoms present in the cameras sensor substrate begin to vibrate. This causes the release of electrons even when no photons are detected[46]. As such, this adds stochastic noise to the background of an image, instead of it being null[46]. Dark noise also follows a Poisson distribution [46]

Readout noise is the result of imperfect nature of the output amplifier when electron charges are translated to voltages. When modeled, readout noise is defined as an additive component with a zero-net mean and Normal distribution[46].

A CCD photodetector is composed of a silicon wafer which has been divided into a regular array of thousands (or millions) of light sensitive regions [47]. Due to the fact that silicon is a semiconductor, a CCD chip is able to trap and store photon-induced charge carriers when a positive-electrical bias is applied[47]. Each element in the array corresponds to a pixel and the signal associated with each pixel is rapidly translated into an intensity value for the corresponding image location[47]. The intensity value is subsequently digitized and the image reconstituted on a monitor almost instantaneously[47].

Within a CCD, a metaloxide superconductor (MOS) is the light sensing unit, and individual structures are separated in one direction by electrodes on the surface, and are separated in the other direction by channel stops (insulating barriers)[47]. When a CCD is used, image generation can be broadly split into 4 different stages: 1) photon induced charge generation, 2) collection and storage of charge, 3) charge transfer and 4) charge measurement [47]. During the first stage, electrons are produced when incident light interacts with the MOS and these freed electrons localize into a well beneath a positively biased electron gate[47]. Generally, the stored charge is linearly proportional to the intensity of light sensed by a pixel, and can be stored up to the full-well capacity at which the pixel will saturate[47]. Following the exposure time for each frame, the stored charge at each pixel is quantified. This occurs one pixel at a time and is achieved by a series of parallel and serial transfers of the charge of each pixel into a single measuring node[47]. This measuring node contains an output amplifier which converts the charge into a proportional voltage which is subsequently converted to a digital value by an analog-to-digital converter (ADC). The image is then reconstituted on a computer monitor[47].

When CCDs are employed, a compromise must often be reached when trying to find the ideal imaging conditions. For example due to their serial read out nature, when generating images with low readout noise, frame rate must be sacrificed[44]. Conversely, when attempting to image at fast frame rates, resolution and FOV size are commonly reduced (resulting in fewer pixels per frame to read out), and read noise and dynamic range can suffer [44]. Conventional CCDs produce a readout noise of about 5-6 electrons rms[44]. While respectable, this value is often too high when attempting to image the dynamics of proteins in live cells [44].

EMCCD cameras combat this through the action of an on-chip activation mechanism called "Impact Ionization". Impact ionization works by multiplying photoelectrons generated in the silicon, meaning that the signal from a single photon is amplified above the read noise[44]. However, the way in which the amplification works also introduces "multiplicative noise" as the read noise is effectively increased by a factor of 1.41 [44]. This can effectively lower the SNR of an image.

sCMOS cameras combat the tradeoffs that must be made when using CCD based technology. This is because with sCMOS cameras, each individual pixel possess an amplifier and each column of pixels is connected to an ADC[48]. As such, sCMOS cameras have a higher frame rate than CCDs. This also results in sCMOS cameras having a lower read noise, due to the fact that more time is granted to reading the electrons, meaning it can be done more slowly and is thus less error prone then a CDD camera[49]

1.3 Fluorescence microscopy as a tool for studying bacterial cell division

The first fluorescence microscopy technique to be implemented for the study of bacterial cell division was immunofluorescence microscopy (IFM), which had previously been used for many years in eukaryotic cells. Although immunogold labelling offers higher resolution than IFM, the latter is comparatively easier with higher throughput. Additionally, while immunoelectron microscopy can suffer from low SNR, in fluorescence microscopy faint signal can often be enhanced by increasing exposure time. Colocalization using two or more probes with different absorbance and emission spectra is also fairly straightforward[50]. Harry et al first used IFM in *Bacillus subtilis* to observe the localisation of β-galactosidase, whose production was under the control of different RNA polymerase sigma factors [51]. Alongside cell fixation and incubation with a primary antibody followed by a fluorescent secondary antibody, the key step involved cell permeabilization by limited lysozyme treatment, allowing the antibodies to enter the bacterial cells. The method was subsequently adapted for *E.coli* and a number of other bacterial species. IFM was used to show that FtsZ localised between segregated nucleoids and was present in the vast majority of cells[52,53]. Re-examining temperature sensitive FtsZ mutants revealed that Z-rings were unable to form at 42°C, while FtsZ functioned normally at 30°C. It was observed that wildtype (wt) FtsZ could still form a Z-ring in the absence of other fts genes [54].

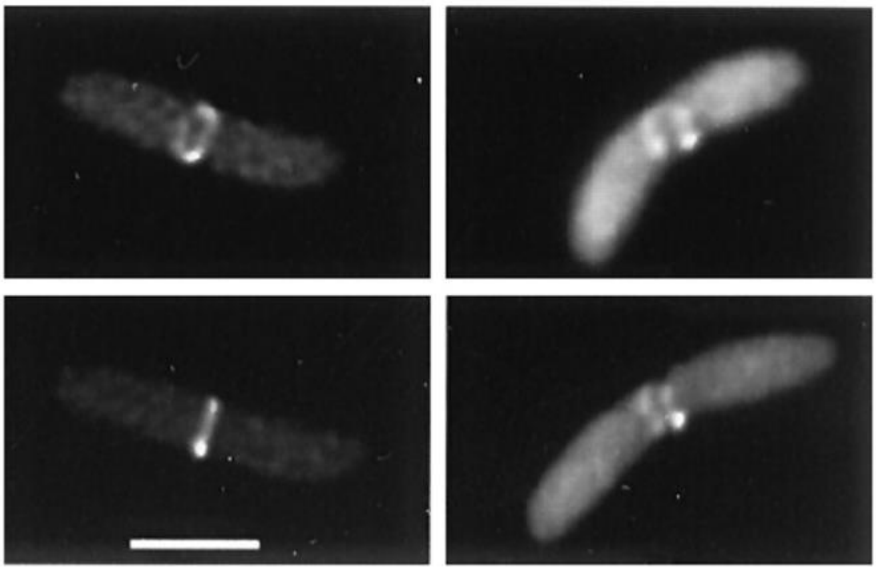

Figure 1.8: Deconvolution images of FtsZ-GFP expressed as a dilute label alongside native FtsZ show a ring like structure at the midcell. Reproduced from[47].

Around the same time that IFM was developed for use in prokaryotes, the potential of green fluorescent protein (GFP) as a genetically encoded tag was discovered[55]. GFP was first used in bacteria to visualise the localisation of specific sporulation proteins in *B. subtilis* [56]*.* Later, FtsZ-GFP and FtsA-GFP fusion proteins (FPs) were obtained allowing their direct observation in live cells for the first time. This confirmed that FtsZ localised to the midcell between segregated nucleoids and deconvolution showed that FtsZ formed a ring-like structure (Figure 1.8). In addition, they showed that FtsA colocalises with FtsZ and also forms a ring like structure [57].

The use of fluorescent FPs is advantageous as proteins in live cells can be observed, enabling their dynamics to be investigated and eliminating the need for specific antibodies. However, their use is not without drawbacks as FPs can perturb protein function[58] and cause aggregative effects[59]. For example, FtsZ-GFP is non- functional in *E.coli* and can only be used when expressed alongside native FtsZ at concentrations equal to or lower than its wt counterpart[57]. In *B. subtilis* Levin et al created a complete FtsZ-GFP replacement. However, the protein is temperature sensitive and the cells are unable to divide at 45°C[52]. Advances in fluorescent protein biochemistry has led to the discovery and creation of new fluorescent proteins. This has led to the production of a native replacement FtsZ-YFP fusion protein in *E. coli* [60] .

1.4 FtsZ is the master regulator of cell division

1.4.1 A low resolution understanding of the divisome

The use of fluorescence microscopy has granted us an understanding of the low-resolution structure of the divisome in a number of model organisms including *E. coli, B. subtilis* and *Caulobacter crescentus* [16]. It has also proved an invaluable tool in screening for FtsZ interacting proteins that are difficult to identify by genetic or biochemical tools alone, due to transient interactions or mild phenotypes when perturbed.

Fluorescence microscopy has been used alongside classic biochemical and genetic techniques to reveal that FtsZ is a master regulator of bacterial cell division, with the Z-ring acting as a scaffold for assembly of the divisome. This was shown by examining which division proteins could still properly localise in the absence of other divisome components. Though deletions of divisome proteins are usually lethal, filamentous cells of *E. coli* and *B. subtilis* remain viable for a few doubling times. This allows the use of sophisticated genetic tools such as thermosensitive mutants, regulatable promoters or suicide plasmids that can rapidly induce the depletion of a specific protein from the cell. While FtsZ has been shown to localise in the absence of other divisome components, products of other *fts* genes such as FtsA and FtsW were only shown to localise to the division site provided FtsZ was present [61–64]. Thus, without the Z-ring, the divisome is unable to assemble.

Fluorescence microscopy techniques have also defined the recruitment order of proteins to the divisome. In *B. subtilis*, assembly of the divisome occurs via a two-step mechanism. The first step is the establishment of the Z-ring and during this time the early assembling proteins (FtsZ, FtsA, SepF, ZapA and EzrA) are directly recruited to the Z-ring. After a substantial delay, the late assembling proteins (DivIB, DivIC, FtsL, PBP2B, and FtsW) are then recruited in an interdependent fashion[65]. If any of these proteins are mutated or deleted, all other proteins fail to correctly localise to the divisome[66]. In contrast to this, assembly of the *E. coli* divisome appears to be largely linear [66].

1.4.2 Defining protein-protein interactions

However, simply looking at the localisation and recruitment order of divisome proteins is insufficient to resolve how its components interact. As such, much work has been expended into defining binary protein-protein interactions. Bacterial two hybrid (BTH) assays are a commonly used technique in assessing such interactions and are based on two fragments of the *Bordetella pertussis* adenylate cyclase [67]. While these two fragments do not usually interact, if each is attached to a protein that interreacts with another *in vivo*, the two adenylate cyclase fragments are brought together and cAMP is synthesised. When expressed in a background that is incapable of expressing cAMP endogenously, the production of cAMP results in the induction of the *lac* operon. This can then be measured by colorimetric substrates such as X-gal or MacConkey dye[16]. BTH assays have been used to show interactions such as FtsA dimerization as well as FtsA-FtsZ in addition to many others [67–69]. However, BTH assays are prone to producing false positive results[16], and as such, they are mainly used as a genetic screen in which hypotheses are generated to be tested by more rigorous methods.

Förster Resonance Energy Transfer (FRET) is another technique that has used to define protein-protein interactions within the divisome. FRET works on the principle that a donor fluorophore is able to transfer energy to a receptor fluorophore when the formers emission wavelength overlaps the excitation wavelength of the latter. This transfer can only occur efficiently when the donor and acceptor fluorophore are in close proximity to each other (between 1 and 8 nm apart)[16].

FRET has been used to confirm interactions between multiple components of the divisome in *E. coli* [70]. Together, these techniques have shown the divisome is not simply a result of linear interactions, rather its overall architecture is a complex network of interactions[67–72]. For example, it has been extensively shown that FtsL and DivIC readily interact [73–75]. It has also been observed that FtsL and DivIC can form a subcomplex with DivIB in the absence of other divisome components [72,76]. It is thought that these proteins work to cooperatively stabilise each other [77–79]. These proteins appear to form a subcomplex which acts as a scaffold for the recruitment of other divisome proteins in addition to regulating the divisome [80,81].

1.5 The diffraction limit of light

Despite fluorescence microscopy being the most commonly used method of observing biological specimens, the technique is inherently hindered by limits of resolution. Resolution can be thought of as spatial resolution, e.g. lateral(in x,y) or axial (in z), or temporal resolution (the minimum time required to acquire two consecutive images).

Spatial resolution is defined as the minimum distance at which two point sources can still be distinguished as separate entities [82]. In optical systems, resolution is limited due to the wave-like nature of light imposing a fundamental constraint known as the diffraction limit of light. Ernst Abbe first demonstrated the resolution limit of light in 1893. Abbe showed that the diffraction of light caused by a point source, in addition to the optical elements of a microscope, induced a resolution limit. This lead to the observation that more sophisticated designs of microscopes were possible that would reduce optical aberrations[83]. Rayleigh's criterion, based upon Abbe's principles of image formation is commonly used to determine the resolution limits of conventional light microscopy (Figure 1.9).

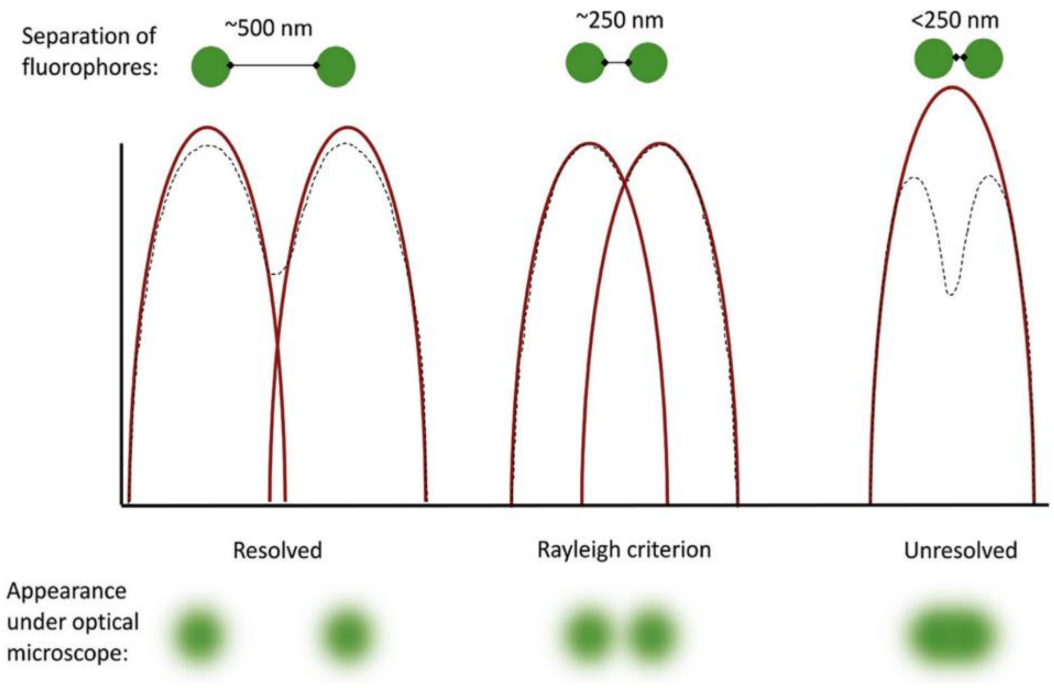

Figure 1.9: Defining resolution and the ability to distinguish between two point sources. Point-like objects cannot be revolved if they are closer together that ~ 250nm. Reproduced from [25].

However, one constraint that could not be overcome was the diffraction limit of light. This is due to the fact that when focussed by a microscope, light does not focus to an infinitely small "focal point" [84]. Rather, the diffraction pattern of a point source (i.e. a single molecule of GFP) results in the formation of an Airy disk pattern. An Airy disk has a central focal spot with concentric maxima and minima that decrease in intensity as they move away from the centre[85] (Figure 1.10). One can then use two Airy disks that are in close proximity in order to define lateral resolution. When the space between two Airy disk patterns narrows, one can note the resolution as the point where the primary maximum of the first Airy disk aligns with the primary minimum of the second. The intensity profile of an Airy disk can then be reconstructed into a three dimensional representation referred to as the Point Spread Function (PSF), which in turn is used to define the resolution of an optical system [27]. The PSF describes how blurry a single point-like emitter (e.g. a single molecule of GFP) is, and by taking the full width at half maximum (FWHM) value of the PSF, resolution can be easily defined [86]. The FWHM of the PSF is equivalent to the diameter from the centre of the focal spot to the first minima. Thus, the FWHM defines the resolution limit as set by the Rayleigh Criterion[87] .

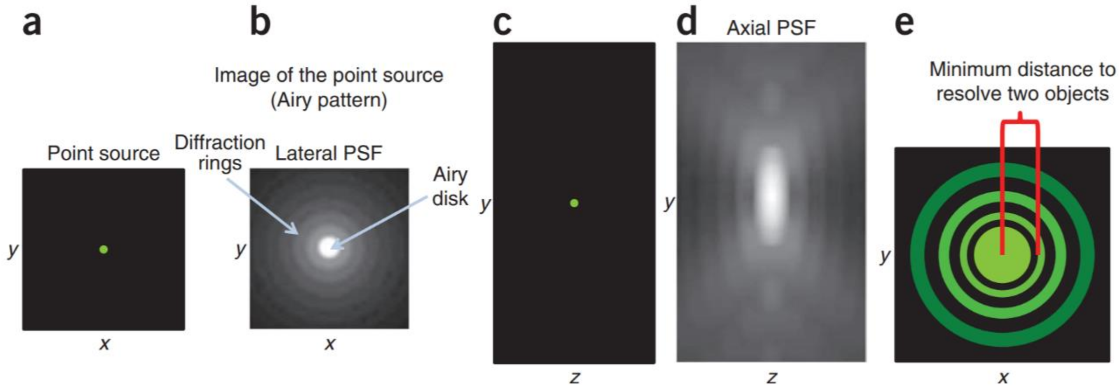

Figure 1.10: Schematic of PSF. Representation of a point source in the XY plane **(a-b)** and Z plane **(c-d).** **(e)** Diagrammatic representation of the diffraction pattern which shows the minimum distance apart that two objects can be in order to be resolved via the Rayleigh criterion. The red line shows the centre of the first Airy disk and the primary minimum of the second. Reproduced form [84].

In a practical setting, the resolution of a light microscope (d) is defined by the wave length of light (λ) and the numerical aperture (NA) of the objective lens[24]. The NA is defined as the light collecting ability of the objective lens and is the product of the refractive index of the sample medium (n) and the half-angle (θ) of the cone of light which is collected by the objective lens or that is transmitted through the condenser (Equation 1)[27].

$$NA = nsin\theta$$

Thus the lateral resolution of a light microscope is defined by Equation 2[27].

$$d_{x,y} = 0.61\frac{\lambda}{NA}$$

Calculating the axial diffraction limit works on a similar principle, that is two point objects will be resolved axially if they are separated by a greater distance than the space between the focal spot and the first order minimum. Though the axial PSF has concentric maxima and minima like the lateral PSF, the former is elongated due to the non-symmetrical wavefront that propagates from the objective lens [27]. Thus the axial resolution can be calculated by equation 3[27].

$$d_z = \frac{2\lambda}{NA^2}$$

As the practical upper limit for a NA is 1.5, the maximum achievable lateral resolution is ~200nm, while the maximum achievable axial resolution of ~500nm.

1. 6 Structure of the FtsZ monomer and protofilament

Due to the fact that light microscopy is unable to resolve the structures of individual proteins, this must done through methods such as X-ray crystallography. The crystal structure of FtsZ has revealed it is a cytoplasmic globular protein that is highly conserved amongst the majority of bacterial species (Figure 1.11A). For example, FtsZ of *Pseudomonas aeruginosa* is 67% identical to that of *E. coli* across the globular domains [88]. Despite significant differences in their amino acid sequence, FtsZ shares a remarkably similar tertiary structure with eukaryotic tubulin and like tubulin it is a self-activating GTPase [12,89]. FtsZ monomers polymerise into tubulin-like protofilaments via head-to-tail associations (Figure 1.11B).

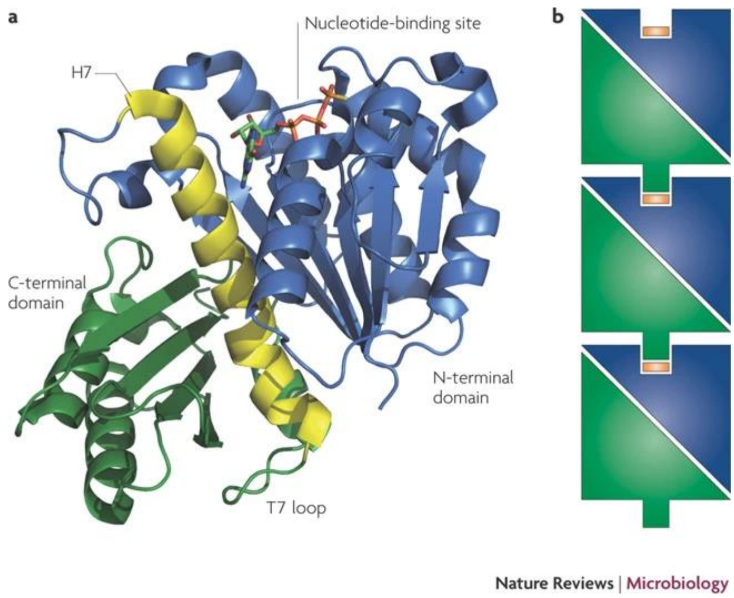

Figure 1.11: Polymerisation of FtsZ monomers (A) The crystal structure of a Bacillus subtilis FtsZ monomer bound to GTP-γS (Protein Data Bank entry 2RHO). **(B)** FtsZ polymerizes by the head-to-tail association of individual subunits. Reproduced from[80].

Although FtsZ and tubulin share a remarkably similar structure, their functions as a components of the cellular cytoskeleton differ greatly. In eukaryotes, α- and β-tubulin assemble into microtubules which play roles in structural support, intracellular transport and DNA segregation. In terms of cell division, microtubules form the spindle apparatus that are responsible for separating sister chromatids between daughter cells [89].

Structurally, an FtsZ monomer can be broadly separated into 5 domains: the unstructured and poorly conserved N-terminal domain, the highly conserved globular core, a flexible highly unstructured C-terminal linker (CTL), a short well conserved C-terminal tail (CTT) and a short highly variable set of residues (CTV) [90]. FtsZ's globular domain consists of two independently folding subdomains which can be independently expressed and are separated by a disordered central helix-H7. The N-terminal subdomain is composed of a six-stranded parallel-sheet surrounded by two and three helices on both sides- a classic Rossman Fold [91]. As would be expected from this structure, the N-terminal domain contains the amino acids required for GTP binding. The C-terminal domain is composed of mainly parallel four-stranded central-sheet supported by two helices on one side [12]. At the base of the C-terminal domain is a T7 synergy loop which is required to activate the proteins GTPase activity (Figure 1.11A)[92,93]. During polymerisation the synergy loop from one monomer inserts into the nucleotide binding pocket of another. This interaction allows two catalytic aspartate residues to be placed in close proximity to the gamma-phosphate. It is thought that these aspartate residues are able to activate FtsZ's GTPase activity by polarising an attacking water molecule[93]. Thus FtsZ's GTPase activity relies of filament polymerisation.

Following the core is the CTL. While in *B. subtilis* and *E.coli* the CTL is ~50aa in length, it is highly variable across species reaching over 300 residues in some species of bacteria[94]. The CTL is unable to be resolved by crystal structure and thus it is commonly modelled as an unstructured peptide[88]. It has been suggested that length, flexibility and/or disorder dependent roles of the CTL control FtsZ assembly and function *in vivo*[90,95]. In *C. crescentus* it has been suggested that the CTL plays a role in reducing FtsZ filament bundling [96].

The CTT of FtsZ is essential for interaction with several of its modulating proteins, a feature that is analogous to tubulin's C-terminal tail. In *B. subtilis,* the CTT is essential for interaction with FtsA and SepF and is thus essential for membrane anchoring[97]. EzrA, a negative regulator of the Z-ring, does not appear to interact with FtsZ in the absence of the CTT[98].

The CTV includes the residues between the CTT and the extreme C-terminus. In *B. subtilis* FtsZ, this region is 6 residues but spans up to 10 residues in *Staphylococcus aureus* and can be positive, negative, or neutral in charge[90]. It has been suggested that this region is important for promoting lateral interactions between FtsZ protofilaments [90].

1.6.1 Structure of the protofilament

Due to the fact that de Broglie wavelength of an electron is much shorter than visible light, electron microscopy possess a much higher resolution than optical microscopy[27] and thus has been used to study the structure of the FtsZ protofilaments.

As stated previously FtsZ protofilaments assemble via head to tail association of individual FtsZ monomers[97]. FtsZ displays cooperative assembly *in vitro*- that is FtsZ monomers display a greater affinity for the growing polymer rather than each other [99–103]. Protofilaments have also been shown to assemble into higher order structures *in vitro*, such as rings, bundles, tubules and sheets[104–107]. FtsZ polymerisation has been shown to require GTP binding but not hydrolysis [104]. *In vitro* FtsZ shows two transitions during assembly. The first occurs at a critical concertation of 0.1-0.5 µM and sees the individual monomers assemble into the FtsZ protofilaments [101]. The second transition occurs at about 3 µM which reflects the assembly of protofilaments into higher order structures. While it is not yet known if FtsZ filaments form bundles *in vivo* the cellular concentration of FtsZ is 3-10 µM [108], suggesting the potential for the formation of lateral contacts *in vivo.*

1.7 Breaking the diffraction barrier: The ultra-structure of the Z-ring

Due to the resolution limits of conventional fluorescence microscopy, the Z-ring appears as a uniform band at the midcell when imaged by this method, suggesting a continuous ring like structure. Furthermore, transmission electron microscopy had been unable to detect the Z-ring[109]. A major advancement in our understanding of the Z-ring ultra-structure came from examining the Z-ring in plunge frozen *C. crescentus* cells using cryo-electron tomography (cryo-ET)[110]. Interestingly, multiple short filaments of FtsZ were observed, rather than a continuous ring. Despite this, it was unclear if these findings reflected the true nature of the Z-ring due to the then low contrast of cryo-ET and missing wedge failing to detect all FtsZ filaments[110].

Thus the Z-ring is an attractive structure to study by super-resolution microscopy- multiple different methods of breaking the diffraction barrier, resulting in sub-diffraction resolution. This is advantageous as it allows high resolution *in vivo,* high protein specific contrast and single molecule sensitivity.

The first of these methods employed to study the Z-ring was Photoactivated Localization Microscopy (PALM). PALM is a type of localisation microscopy that relies on the action of fluorescent tags that are in an "off state" until they are turned into their "on state" by a specific excitation wavelength[16]. Sub diffraction resolution is achieved by the stochastic activation of individual fluorophores in the cell. Positions of these individual fluorophores are then defined by measuring the centre of their diffraction limited fluorescent spot that is spread amongst multiple pixels [16]. The fluorophore is then bleached, and another activated. This occurs over many hundreds to thousands of imaging rounds before the final image is reconstructed. As such this achieved a lateral resolution of 10-40nm and an axial resolution of 20-100nm[111,112]. This technique was used to measure the axial width of the Z-ring in *E. coli* which was found to be ~100nm wide(Figure 1.12A) [110]. This suggested the Z-ring is composed of multiple overlapping filaments that are loosely packed due to the difficulty in assembling such a thick structure from a single continuous FtsZ filament.

Following this work, 3D-Structured illumination microscopy (SIM) was used to investigate the overall architecture of the entire Z-ring [113]. 3D-SIM works by projecting a 3D striped light

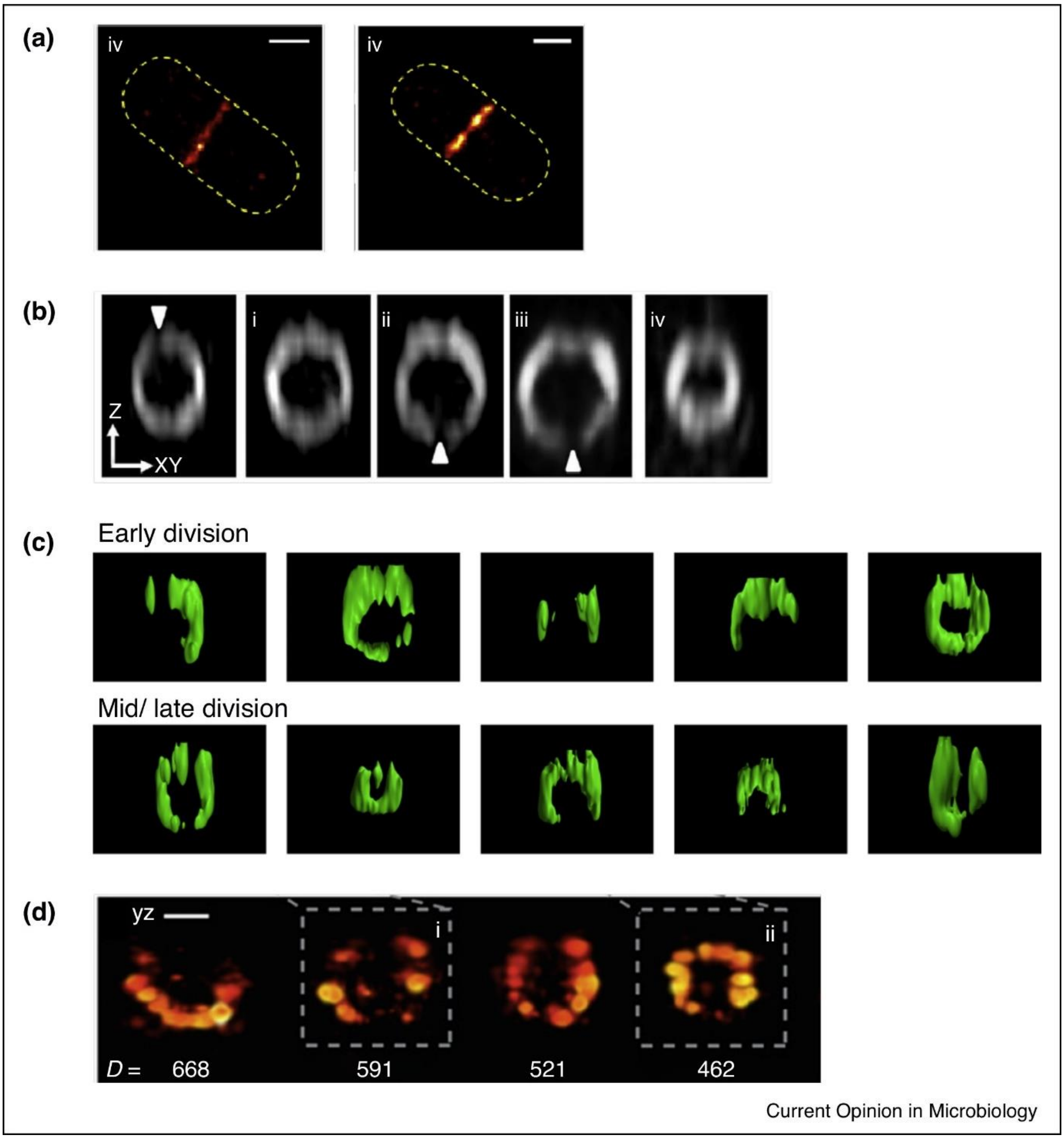

Figure 1.12: The Z-ring ultrastructure as obtained by super-resolution microscopy. (a) Axial thickness of Z-rings in *E.coli* obtained by 2D localization microscopy. Scale bar, 500 nm. **(b)** 3D-SIM of *B. subtilis* FtsZ **(c)** 3D-PALM of *C. crescentus* FtsZ. **(d)** 3D-PALM of *E. coli* FtsZ. Scale bar, 300 nm. Reproduced from [100].

pattern onto the sample. This pattern is then shifted through 5 phases and three angles.

Interaction of the projected light pattern with fluorescent structures creates Moiré fringes - an interference pattern that allows structural information that would be otherwise unresolvable to be encoded into the image. Reconstituting the different images obtained by imaging through the different phases and angles allows the sub-diffraction information to be extracted and computationally reconstructed to produce a 3D image. This permits a lateral resolution of 100-130 nm and an axial resolution of 280-350 nm[84]. Using this method, it was revealed that the Z-ring was a highly heterogenous structure, with occasional 100-200nm gaps(Figure 1.12B)[113].

The first 3D localisation microscopy study of the Z-ring was conducted by Biteen *et al* in *C. crescentus.* These preliminary results indicated that Z-rings are composed of loosely packed bands of FtsZ [114]. Later, a high throughput 3D-PALM method was developed and used to examine the organisation of *C. crescentus* Z-rings throughout the cell cycle (Figure 1.12C) [115]. Large gaps of several hundred nanometres were commonly observed and similar findings were also observed in *E. coli* (Figure 1.12D)[116,117]. When these results are taken together, it suggests that the Z-ring is a patchy, heterogenous toroidal structure that is 80-100nm thick radially [115,117]. However, the cryo-ET studies complicate this model. Not only is the data from cryo-ET conflicting as to whether the Z-ring is composed of long continuous filaments[110,118] or short overlapping filaments [119], these studies have only detected FtsZ in a thin layer about 15nm from the inner-membrane [118]. Though this spacing is consistent with FtsA membrane anchor spacing [118], it is possible that due to low contrast, cryoET studies could miss short FtsZ filaments that extend further away from the cytoplasmic membrane [109].

1.8 FtsZ dynamics

One of the major advantages of labelling proteins with a genetically encoded fluorescent tag is that it allows dynamics to be followed in live cells. Division is an inherently dynamic process and the Z-ring is known to be a highly dynamic structure itself. This was first demonstrated by showing that Z-ring constricts down to a diffraction limited spot (Figure 1.13)[120].

Fluorescence Recovery After Photobleaching (FRAP) has also been used to measure the time taken for a section of the Z-ring labelled with FtsZ-GFP to regain fluorescence after being photobleached. Due to the fact the photobleaching permanently removes the ability of a GFP molecule to fluoresce, the only way in which fluorescence of the bleached part of the ring could be regained would be replacement with FtsZ-GFP monomers from elsewhere in the cell. Following photobleaching the Z-ring has been shown to regain fluorescence, and in both *E. coli* and *B. subtilis* the Z-ring has been shown to entirely turnover in less than 10 s [121,122]. Thus this shows that the Z-ring is a highly dynamic structure that undergoes constant monomer turnover.

The dynamic nature of the Z-ring has been shown to be dependent upon the intrinsic GTPase activity of FtsZ, as the turnover time of the Z-ring in cells that express FtsZ with an impaired GTPase activity increases[103]. FtsA was also shown to exhibit similar dynamics [123].

Single molecule tracking has also been conducted on the Z-ring to investigate the dynamics of individual FtsZ monomers within the ring. This lead to the observation that individual subunits of FtsZ are immobile within the ring[124]. Strauss *et al* [113] used 3D-SIM to observe that the Z-ring undergoes dynamic structural rearrangement throughout constriction in both *B. subtilis* and *S. aureus*. This suggests that Z-rings not only undergo subunit turnover but largescale structural rearrangement.

Perhaps one of the most interesting findings regarding Z-ring dynamics was the observation that FtsZ filaments can treadmill *in vitro* when reconstituted on artificial lipid bilayers [125]. Treadmilling is a type of asymmetric motion whereby filaments move by plus-end polymerisation, minus-end depolymerisation while individual subunits remain static. Treadmilling of FtsZ filaments was found to be GTP-hydrolysis driven, and FtsA was also shown to co-localise and move in similar patterns [125]. If FtsZ treadmills *in vivo*, this would reconcile how individual subunits of FtsZ within the ring can be stationary, but the Z-ring undergo massive structural rearrangement during its lifetime [113,124].

Surprisingly, it has been observed that perturbation of the GTPase activity of FtsZ in *E. coli* does not affect constriction rate [116]. By combining localisation microscopy with brightfield imaging of the constriction site, it was discovered that FtsZ turnover does not affect cytokinesis in *E. coli*, instead, cell wall synthesis is likely rate limiting [116]

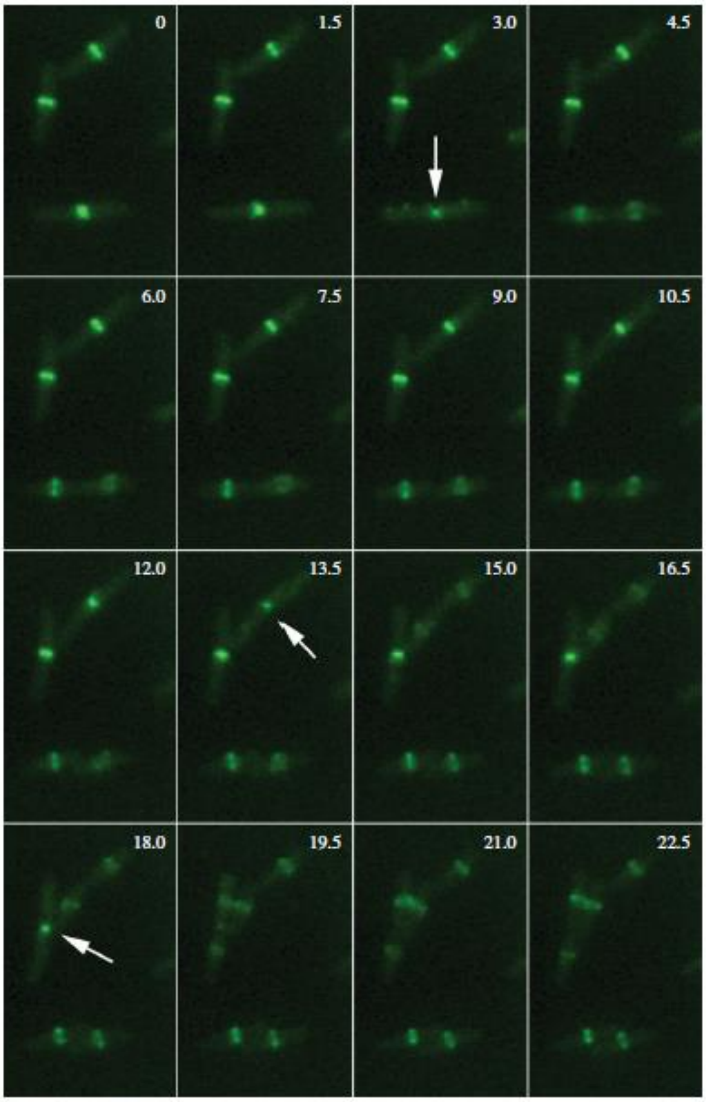

Figure 1.13: FtsZ dynamics in dividing *E. coli* cells. FtsZ-GFP is exogenously expressed as a dilute label in otherwise wildtype *E. coli*. FtsZ-GFP constricts down to a diffraction limited spot before it rapidly delocalises to the division sites. Elapsed time is shown in minutes. White arrows denote constricting Z-rings prior to septum completion.

1.9 FtsZ and Force Generation

It has also been suggested that the Z-ring plays an additional role in cell division, rather than simply acting as a scaffold for the recruitment of other divisome components. It has been proposed that the Z-ring may actually generate the force required to constrict the cytoplasmic membrane during cytokinesis. The idea that FtsZ forms the cytoskeletal framework of the Z-ring and may also generate constrictive force was first proposed in 1997 as the "Z-centric hypothesis" [126]. The rationale behind this hypothesis was (i) no motor molecules had been identified in bacteria, (ii) some bacteria lack homologs of the dozen accessory division proteins identified in *E. coli*, and (iii) GTP hydrolysis induces a straight to bent conformational change in the FtsZ protofilaments.

Two general classes of models exist that explain how the Z-ring may generate force. One suggests that if protofilaments can slide and increase the number of lateral bonds, this would decrease the circumference and constrict the Z-ring [127,128]. This model requires the Z-ring to be composed of long, continuous filaments and the energy to drive constriction is obtained from the increasing number of lateral bonds as the Z-ring condenses. However, recent evidence that individual monomers of FtsZ are immobile within the ring *in vivo*, and that FtsZ treadmills *in vitro* has made this hypothesis unlikely[116,125]. Filament bending is perhaps the simplest model to explain force generation. This model suggests that the FtsZ protofilaments have two preferred conformations that depend on whether the bound nucleotide is GTP or GDP. When GTP is bound, the protofilament is straight with zero bend between monomers. Conversely, when GDP is bound, a curved conformation is favoured with a 22° bend between monomers [129].

In vitro FtsZ has been shown to generate sufficient force to deform lipid tubules when an amphipathic helix was spliced onto the C-terminus to circumvent the need for a membrane anchor protein (Figure 1.14) [130]. Z-rings coincided with constrictions in the wall of the liposome and these constrictions relaxed when GTP was depleted from the system. Thus, *in vitro* FtsZ is capable of generating force in the absence of any other proteins. The "iterative pinching model" favours of filament bending. This model suggests that continuous cycles of polymerization, polymer bending and disassembly (promoted by the binding and hydrolysing of GTP) generates enough force to cause an inward pull on the cytoplasmic membrane [131]. However, it should be noted that for the iterative pinching model, individual filaments would be required to form laterally associated bundles. Without the formation of such bundles, individual protofilaments would be free to rotate on the membrane[1]. However, it has also been proposed that protein crowding may result in fluid cellular membranes bending [132]. Proteins that attach by either inserting a helix or binding lipid heads via an engineered tag are able to bend membranes when protein coverage exceeds ~20% [132]. Interestingly, GFP, an protein unrelated to membrane curvature, has been shown to cause membrane deformations when sufficiently concentrated [132]. Thus, the ability of FtsZ to act as a force generator still requires further investigation.

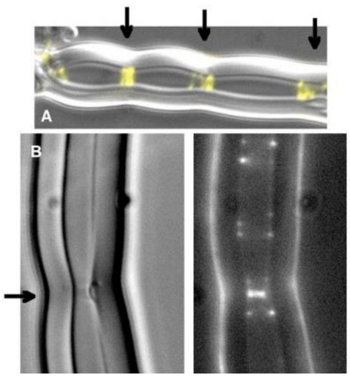

Figure 1.14: Z-rings are capable of deforming liposomes. (A) Fluorescent Z-rings are centred on constrictions in tubular liposomes. Arrows indicate Z-rings. **(B)** The constricting Z-ring indicated by the arrow forms a visible constriction. One the right side, this Z rings appears to have detached some inner layers of he multilamellar wall. **(C)** Z-rings are able to markedly constrict the tubular liposomes in 6 mins. Reproduced from [127.]

1.10 Stabilising the Z-ring

During the division period, FtsZ is known to interact with a number of proteins that modulate its activity. FtsZ's association with the cell membrane is crucial in order to maintain its structural integrity and exert constrictive force that it may generate. However, FtsZ itself has no direct affinity for the membrane and requires anchors to tether it in place. In *B. subtilis* both FtsA and SepF have been identified as functionally redundant membrane anchors. Individually, neither are essential though cells display pronounced division defects in the absence of either while deletions of both genes is lethal[133]. Other proteins such as ZapA and EzrA are thought to be positive and negative regulators of Z-ring formation respectively [134,135].

1.10.1 FtsA

Like FtsZ, FtsA is highly conserved among most bacteria and is often found upstream of FtsZ in an operon within the *dcw* cluster [136]. As stated previously FtsA co-localises with FtsZ and forms a ring like structure [57]. FtsA from *B. subtilis* has been shown to form dimers in solution and BTH assays have shown that FtsA can self-interact [137–140]. Like FtsZ, FtsA is a dynamic structure, and can self-assemble with FtsZ into dynamic vortices when reconstituted on artificial lipid tubules [125]. The crystal structure of FtsA from *Thermotoga maritima* revealed that it is structurally related to actin. The protein consists of two domains, both of which can be separated into two further subdomains. These domains form an interdomain cleft which contains a nucleotide binding site [12]. FtsA self-interaction is thought to be ATP dependent [137]. *In vitro,* FtsA from *Streptococcus pneumoniae* and *T. maritima* has been shown to polymerise into protofilaments [141,142]. BTH assays have confirmed the two are able to directly interact [143]. In *E. coli,* FtsA interacts with the extreme C-terminus of FtsZ [144]. Sequence alignments have confirmed that the extreme N-terminal of FtsA contains a membrane targeting amphipathic helix in a conserved motif. This is separated from the core protein by a flexible linker region. Deletion of the amphipathic helix causes FtsA to become non-functional under normal laboratory conditions [136]. Cell fractionation assays show that 30% of the cellular FtsA is present in the membrane fraction suggesting that FtsA does indeed bind to the membrane. In both *E. coli* and *B. subtilis* there is about a 5:1 ratio of FtsZ to FtsA and in *E. coli* this needs to be carefully maintained as over-expression of either has a toxic effect [145].

While in *B. subtilis* FtsA is not an essential gene, deletions result in filamentous cell growth and a higher proportion of non-functional Z-rings. This is in contrast to *E. coli* where deletion of FtsA is lethal. Though FtsA appears to form a ring-like structure when it co-localises with FtsZ, little is known about its ultra-structure *in vivo*.

1.10.2 SepF

In *B. subtilis* SepF (*ylmF*) is a division protein expressed from the ylm operon. Although not essential, electron microscopy (EM) has revealed that deletion of SepF results in strong septum deformations which are most evident in the early stages of septum synthesis [133]. Interestingly if either FtsA or EzrA are deleted alongside SepF, this results in synthetic lethality [146]. SepF is widely conserved amongst Gram-positive bacteria and cyanobacteria, but has not yet been discovered in Gram-negative bacteria[66,146]. Fluorescence microscopy indicates that SepF localises to the division site in an FtsZ dependent manner and colocalises with FtsZ. *In vitro,* SepF also forms regular ring-like structures with a diameter of about 40nm [147]. The crystal structure of SepF suggests that these rings must be composed of at least 80-

100 SepF molecules[13]. BTH assays have shave shown that FtsZ and SepF are capable of interacting and pull down assays have confirmed that SepF interacts with the extreme C-terminus of FtsZ [133,146]. *In vitro*, SepF has been shown to promote the assembly of FtsZ into tubules with an average dimeter of 48nm, close to that of the SepF rings, which are stacked perpendicular to FtsZ polymers [148]. However, these microtubular structures have not been observed *in vivo*. The crystal structure of SepF revealed that the conserved C-terminus of the protein interacts with FtsZ while the N-terminus contains the residues for membrane binding. Furthermore, purified SepF is able to recruit FtsZ to an artificial lipid membrane in a manner similar to FtsA [13]. Since SepF is able to perform three of the functions of FtsA (polymerisation, interaction with FtsZ and binding to the membrane) this suggests that it serves as an additional membrane anchor.

Later studies have suggested that membrane-binding amphipathic α-helix of SepF would be located on the inside of the SepF rings, and thus SepF may not form rings, but rather arcs that wrap over the leading edge of the nascent septa [13]. FtsZ filaments would then bind and align atop these SepF arcs [13]. However, it is unclear whether such arcs form *in vivo* as high resolution microscopy is unable to discern such structures due to the electron density of the bacterial cytoplasm [149]. However an argument for this model is that the diameter of SepF rings/arcs (41nm) is close to the thickness of the septal wall (43nm). Thus, as the SepF arcs would control the freedom of movement of FtsZ filaments, and by extension the PG synthetic machinery, the diameter of the SepF rings would control the thickness of the septum [149]. Indeed, a correlation between SepF ring diameter and septum thickness has been observed across multiple Gram -positive bacteria and the core domain of SepF is essential for function [149].

1.10.3 EzrA

Ezra was first identified in *B. subtilis* as a negative regulator of the Z-ring, preventing aberrant Z-ring formation at the poles [135]. Prior to division, EzrA is localised throughout the plasma membrane. Despite its apparent nature as a Z-ring antagonist, EzrA is paradoxically recruited to the Z-ring via a seven amino acid patch termed the QNR patch[150]. Cells that lack EzrA are significantly longer than wild-type cells which suggests that the division cycle is blocked, in addition to lowering the concentration of FtsZ required for Z-ring assembly and the ability of MinCD overproduction to inhibit this process [135,150–152]. Overexpression of EzrA to twice its native levels has also been shown to be sufficient to block Z-ring assembly [153]. Thus it would appear that FtsZ assembly is stabilised in the absence of EzrA.

However, despite the paradoxical nature of having a negative FtsZ-regulator present at the divisome, EzrA may play a role in maintaining the dynamic nature of the Z-ring [121]. For example, cells in which EzrA has been deleted are significantly longer than their wildtype counterparts, suggesting that the division cycle is delayed [135,151]. It is possible that this delay is due to increased stability of the Z-ring.

FtsZ and EzrA have been shown to directly interact *in vitro*, via a range of techniques in addition to showing the ability of EzrA to self-interact [153–155]. The interaction between FtsZ and EzrA is mediated through FtsZ's CTT[152]. Sedimentation assays and 90^o angle light scattering have demonstrated that EzrA is capable of inhibiting FtsZ protofilament formation in a concentration dependent manner [153–155]. Furthermore, by using a fluorescently conjugated nucleotide analogue, it has been shown that EzrA inhibits the polymerization of FtsZ at two distinct levels[151]. The first occurs at the monomeric level by reducing FtsZ's affinity for GTP. The second occurs at the polymeric level, increasing the rate of GTP hydrolysis.

Interestingly, a third role for EzrA has been observed in that it is required for the recruitment of the bifunctional penicillin-binding protein 1 (PBP1) to the divisome. Deletions of EzrA resulted in PBP1 failing to localise to the midcell during division [156].

1.10.4 ZapA

ZapA is a small protein 85 amino acids in length that was first identified in *B. subtilis* via a genome wide screen for proteins whose overexpression could overcome a lethal MinD overexpression [157]. Cells that lack ZapA are viable and display no phenotype in *B. subtilis* or *E. coli*, though conditional lethality is observed in the absence of EzrA in *B. subtilis*[157,158]. ZapA is an early divisome recruit and *in vitro* experiments have shown that ZapA promotes the formation of stable FtsZ filaments bundles when incubated together [134]. The crystal structure has revealed that the protein forms a pseudo-symmetric tetramer composed of a dimer pair that associate by coiled-coil interactions along the C-termini of individual subunits and forms two distal pairs of FtsZ-binding domains [134,159,160]. Interestingly, ZapA has been found to reduce the GTPase activity of FtsZ, suggesting it may reduce FtsZ polymerization dynamics [161–163]. Further *in vitro* studies have shown that despite the fact ZapA interacts only weakly and transiently with FtsZ, ZapA acts on FtsZ in a highly cooperative manner [164]. At low ZapA concentrations, FtsZ filament networks displayed low spatial order with fast reorganization dynamics. However, at high ZapA concentrations, FtsZ filament networks display a persistent state of high spatial order and slow reorganization[164]. Interestingly, despite the fact that the reorganization dynamics of the filament network were greatly slowed, the rate of FtsZ treadmilling was unchanged [164]. The authors suggest a model whereby ZapA spatially constrains FtsZ treadmilling trajectories to increase the precision of Z-ring assembly [164].

1.11 Positioning the Z-ring

One the most important aspects of cell division, is that it must occurs at the right time and place to ensure that it occurs between segregated nucleoids. In both *B. subtilis* and *E. coli* spatial control of Z-ring assembly is regulated by two distinct, albeit partially overlapping systems (Figure 1.2).

1.11.1 Nucleoid Occlusion

The first of these systems is nucleoid occlusion and this prevents Z-rings from forming over the DNA[165–167]. In *B. subtilis* a protein called Noc, which possesses a putative ParB-like fold participates in nucleoid occlusion, where as in *E. coli* SlmA, a member of the TetR family, is involved in the process[168–174]. Though neither gene is essential in their respective organisms, both are synthetically lethal with mutants in null *min* background [175].

Both Noc and SmlA localise to the nucleoid (Figure 2) where they each interact with specific DNA sequences located throughout the *B. subtilis* and *E. coli* nucleoids with the exception of the terminus-containing region (Ter) [168]. As Ter is the last chromosomal region to segregate [176], exclusion of Noc and SlmA from this region functions as a timing device to coordinate DNA segregation with division [168]. However it seems that Noc and SmlA act in different ways. For example, Noc has no known interaction with FtsZ. Rather it is known to interact with both the DNA and membrane and has been proposed to bring regions of the DNA to the membrane, sterically hindering FtsZ structures from forming at the division site [175]. It has recently been suggested that Noc may actually play a role in stabilising the Z-ring due to the observation that spiral-like FtsZ rings form over nucleoids in the absence of Noc [177]. These structures span out of pre-existing Z-rings but were locally depleted upon overexpression of ZapA [177]. In contrast, SlmA is known to have direct interaction with the CTT of FtsZ [173,174]. Interestingly, SlmA must be bound to the DNA in order to interact with FtsZ and it is throughout that SmlA forms extended assemblages on the DNA allowing it to bind the CTT of multiple FtsZ monomers and antagonise protofilament formation [168].

1.11.2 The Min System

The second system that is involved in the spatial positioning of the Z-ring is the Min system, and this prevents the formation of Z-rings at the cell poles. In *B. subtilis* DivIVA is responsible for localising the Min proteins to the cell poles (Figure 1.2A)[178,179]and is it thought to preferentially localise here as it is a negative curvature sensor [180]. MinJ is then recruited, acting as an adaptor for the recruitment of MinD to DivIVA at the cell poles. MinD then binds to the membrane itself due to the presence of a C-terminal amphipathic helix [181]. MinD is then capable of binding MinC directly, an important step due to the fact the MinC is the actual Z-ring antagonist[182,183]. It was originally thought that following localisation to the cell poles, the Min complex remained here, only inhibiting the formation of Z-rings at the poles. However, it is now known that a small proportion of the Min complex is recruited to the septum, prior to septation and the formation of the new cell poles [184]. This is thought to prevent more than one Z-ring forming at the midcell.

The Min system differs in *E. coli* as it lacks DivIVA and thus contains a third Min protein, MinE, to compensate [185]. As in *B. subtilis* MinD is capable of directly binding the membrane in addition to binding MinC [186,187]. In order to target the MinCD complex to the cell poles, MinE forms a ring that causes MinD to disassociate from the membrane and localise to the opposite pole (Figure 2B) [188,189]. This results in an oscillating pattern in which MinC is passenger[190,191]. In this system, the Min complex spends the majority of the time at the cell poles, with only a short time in transit (~10s) from pole to pole. Thus the average position of MinC is at the poles, leaving the midcell free for Z-ring formation [185].

1.12 Cell division across different phyla

Across all domains of life, successful division is essential in order to ensure the proper segregation of the genome and the cytoplasmic contents. A failure in division can result in either cell death or multi-nucleate or aneuploid cells [192–194]. Cell division via a contractile ring is almost a universal feature across all branches of cellular life, though higher plants are an exception [195]. For all organisms that utilize a contractile ring, cytokinesis can be broadly split into four stages. Firstly, the division site needs to be specified, secondly the components of the ring localise and assemble. Thirdly, the ring must then generate the constrictive force required to cleave the cell in two. Finally, the must disassemble allowing for separation of the daughter cells[195]. Whilst the majority of bacterial species, and many archaea, divide by the formation of the Z-ring, two of the five eukaryotic supergroups[196], Amoebozoa and Opisthokonta (which include fungi and animals) assemble a contractile ring composed of actin and myosin in a similar fashion to the Z-ring[197]. This ring forms perpendicular to the axis of the spindle apparatus[197].

Model eukaryotic organisms which utilize the cytokinetic ring include the fission yeast *Schizosaccharomyces pombe*, the budding yeast *Saccharomyces cerevisiae, Drosophila melanogaster* and the amoeba *Dictyostelium discoideum* . In these species, the cytokinetic ring is assembled in response to cell-cycle regulated signalling. F-actin accumulates at the division plane and, at the same time, myosin-II localises to the division plane in both F-actin- dependent and -independent manners [198–200]. Like the majority of bacterial species, these model organisms utilise an -outward-in method of division in which the contractile is assembled just underneath the membrane. The ring begins to contract, forming a cleavage furrow that slits the cell in two [195].

In contrast to the outward-in method of division employed by organisms which utilise a contractile ring for division, cytokinesis in most flowering plants occurs via the construction of new cell wall from the inside out. In such a case, a new cell plate is constructed through the fusion of Golgi-derived vesicles, which contribute the proteins, polysaccharides and membrane required. Rather than a contractile ring, a cytoskeletal phragmoplast is formed between the daughter nuclei and is composed of microtubules and actin filaments[201].

1.13 Research aims and objectives.

At the time of starting of this PhD project, the organisation and dynamics of FtsZ filaments within the Z-ring were poorly understood. This was largely due to the inherent difficultly of imaging the dynamics of division proteins. As such, the central work of this thesis involves the investigation of the dynamics of a number of key cell division proteins in the model Gram-positive organism *B. subtilis.*

The first objective of this project was the implementation of a method of vertically immobilising rod shaped cells to visualise the division machinery around the entire division septum. Using this method, the dynamics and organisation of FtsZ were examined.

Secondly, following our discovery that Z-ring is composed of multiple short filaments that treadmill bi-directionally around the division plane, this raised the question of how FtsZ filament dynamics change over the course of the cell cycle. As such, the vertical immobilisation technology was further refined in order to detect filament dynamics in dim, nascent rings and measure the dynamics of the FtsZ filaments within the Z-ring over different stages of the division cycle.

The final aim of this project was to use the developed technology in order to investigate how FtsZ modulating proteins move around the divisome to gain an insight into how the divisome works mechanistically.

Chapter 2 : A novel vertical immobilization imaging technique shows that FtsZ filaments treadmill bi-directionally around the division site in *B. subtilis*

2.1 Introduction

The majority of bacterial species are surrounded by a mesh-like PG sacculus which maintains cell shape in addition to opposing the cells high osmotic pressure. Gram-positive bacteria possess a single plasma membrane encased by a thick, multi-layered cell wall, allowing cells to maintain an osmotic pressure of approximately 20 atmospheres [4]. This makes cell division an exceptionally difficult mechanistic task- how does the cell cut itself in two without bursting?

Division is an extraordinary feat of molecular self-assembly whereby a nanoscale divisome machine is responsible for building a micron scale crosswall (septum) at the midcell in Gram-positive bacteria. How these divisome components work together to cleave the cell in two has remained elusive to scientists for decades, due to the difficulty in measuring protein organisation and dynamics in cells not much larger than the diffraction limit of light.

The core components of the bacterial divisome include the septal peptidoglycan (PG) synthases which build the septum, and the essential cell division protein FtsZ which polymerises into a dense Z-ring at the midcell [11,14]. Assembly of the Z-ring is the first recognizable event in bacterial cell division [65,202]. The Z-ring is often thought of as the master regulator of cell division, due to the fact that it serves as a scaffold, recruiting the core components of the divisome to the midcell [62,63]. As FtsZ itself has no direct affinity for the cell membrane, its requires anchors such as the actin-like FtsA to tether it to the cytoplasmic side of the membrane [12]. This allows the subsequent recruitment of PG synthases to the midcell, permitting the synthesis of the septal crosswall that cleaves the cell in two.

FtsZ is homologous to eukaryotic tubulin, both of which belong to a distinct family of GTPases which, despite significant differences in amino acid sequence, share a remarkably similar tertiary structure [203–205]. FtsZ monomers are able to assemble into protofilaments in a GTP dependent manner and these protofilaments are able to form higher order structures *in vitro* [100]. While the genetics and biochemistry of the divisome are reasonably well understood, how the divisome works mechanistically remains one of the great unknowns of bacterial cell division.

One of the most intriguing aspects of the Z-ring is its highly dynamic nature. FRAP experiments have shown that the Z-ring undergoes constant remodelling, rapidly exchanging FtsZ monomers between the Z-ring and the cytoplasmic pool [206,207]. The dynamic nature of the Z-ring is dependent on the intrinsic GTPase activity of FtsZ, as Z-rings with impaired GTPase activity recover much more slowly following photobleaching than their wildtype (wt) counterparts. In both *S. aureus* and *B. subtilis* the Z-ring was shown to undergo dramatic structural rearrangement throughout the constriction process [113]. This suggests that turnover is not just exchanging FtsZ monomers between the filament and the cytoplasmic pool, but also causing largescale reorganisation of the ring itself [113]. Interestingly, it was discovered that perturbing the GTPase activity of FtsZ, and thus subunit turnover, does not affect constriction rate in *E. coli*. Thus, it would appear that FtsZ turnover is not rate limiting for *E. coli*. Rather, it was suggested that cell wall synthesis was instead the rate limiting step [116].

In vitro, FtsA and FtsZ are able to self-assemble into highly dynamic cytoskeletal patterns that show directional motion when reconstituted onto an artificial lipid bilayers. Polymerisation of FtsZ into proto-filaments was again shown to require the binding of GTP, and ATP was required for FtsZ to associate with the membrane via FtsA. This directional motion was also dependent upon GTP hydrolysis as the addition of a non-hydrolysable form of GTP resulted in the formation of static bundles that did not re-organise. FtsZ was shown to move by treadmilling, a type of motion where an asymmetric filament undergoes plus-end polymerisation and minus-end depolymerisation, with monomers within the filament remaining stationary [208]. As such, we decided to turn our focus to why the Z-ring demonstrates rapid subunit turnover and significant structural rearrangement.

In order to assess the organisation and dynamics of FtsZ filaments *in vivo*, we developed a method of vertically immobilising *B. subtilis* cells in nanofabricated microchambers, allowing us to the observe the entirety of the Z-ring. From this, we discovered that the Z-ring is composed of multiple filaments which move bi-directionally around the division plane and the processive movement of FtsZ filaments continues well into active constriction. As part of a multi-lab collaboration, FtsZ filaments were observed to move by treadmilling as shown in previous *in vitro* experiments [208]; [209]. This was also shown to be true in *E .coli* in an independent study [210]. We also investigated the dynamics of the membrane anchor FtsA showing that, like FtsZ, FtsA forms a ring like structure of short filaments that move bi-directionally around the division plane. Collaborators also showed that FtsA treadmilled at the same speed as FtsZ and the dynamics of FtsA filaments were shown to be dependent upon FtsZ treadmilling [209]. As such, using FtsA as a proxy, we investigated the effects of nutrient availability on divisome dynamics and discovered that in both rich and poor media conditions, there was no significant difference in treadmilling speed.

2.2 Materials and Methods

2.2.1 Culture growth for vertical microhole immobilization

Strains of *B. subtilis* to be imaged by vertical microhole immobilization were streaked from -80°C freezer stocks onto NA plates and grown at 30°C overnight. Single colonies were transferred in liquid cultures of Time Lapse Medium (TLM) or PHMM and growth with agitation at 200rpm overnight at either 30°C (TLM[211]) or 22°C (PHMM[209]). The following morning TLM starter cultures were diluted into pre-warmed Chemically Defined Medium (CDM[211]) to a starting OD_{600} ~ 0.1, while PHMM starter cultures were diluted to a starting OD_{600} ~0.05, following which both liquid cultures were grown at 30°C until reaching the appropriate OD_{600}.

2.2.2 Genomic DNA extraction

Genomic DNA from *B. subtilis* was extracted using an adapted version of the Promega Wizard extraction method. In brief, one fresh colony of was inoculated into 3 ml LB. Cells were grown at 37°C (or 30°C if temperature sensitive) for approximately 5 hours, until cells has entered mid-exponential phase. The cultures were subsequently pelleted and resuspended in lysis buffer containing EDTA (50mM), lysozyme (10mg/ml) and RNase and incubated at 37°C for 30-60 minutes. Nuclei lysis solution was then added and the cells incubated at 80°C, after which the samples were cooled to room temperature. Protein precipitate was then added and, after vigorous vortexing, the samples were placed on ice for 10 minutes. Samples were then pelleted at 13000g for 10 minutes, after which the supernatant was transferred into 600 µL of isopropanol. Upon obtaining a visible mass of DNA, the samples were again centrifuged at 13000g for 10 minutes , after which the supernatant was removed, and the pellet washed in 70% ethanol. Following a final centrifuge at 13000g, the supernatant was removed, and the sample air dried for a short time to remove any remaining ethanol. Finally, the pellet was resuspended in 100 µL of Elution Buffer.

2.2.3 B. subtilis transformation.

B. sutbtilis cells were transformed by triggering chemical competence. In brief, a single colony was inoculated into minimal medium (MM: 10 mL SMM basic salts. *125 µL* 40% (w/v) glucose, *100 µL* 2% (w/v) tryptophan*, 60 µL* 1M $Mg_2SO_4.7H_2O$, *10 µL* 20% (w/v) casaminoacids, *5 µL* 2.2mg/ ml) and incubated overnight at 37°C. The following morning, the culture is diluted to OD_{600} ~0.2 in fresh, prewarmed MM and incubated at 37°C for 3 hours.

Following this, the culture is diluted 1:1 into pre-warmed starvation medium (SM: 10ml SMM basic salts, *125 µL* 40% (w/v) glucose, *60 µL* 1M $Mg_2SO_4.7H_2O$) and incubated for a further 2h at 37°C. After this, ~500ng of genomic DNA was added to *400 µL* of cells and incubated at 37°C for 1h. Cells are then plated on NA plates with the appropriate antibiotic and incubated overnight at 37°C.

2.2.4 Strain Construction

SH013 [*trpC2, ftsZ:: ftsZ-GFP::cat*] was created by transforming B. subtilis 168CA [trpC2] with genomic DNA from PAL642 (a gift from Petra Anne Levin).

SH033 [*trpC2, ftsZ:: ftsZ-GFP::cat, Δhag::aph(kan)*] was created by transforming SH013 with genomic DNA from PB5250 (obtained from BGSC catalogue number 1A842).

SH41 [*ftsAZ::mNeonGreen-15aa-ftsA-ftsZ-FtsA-FtsZ, Δhag::aph (kan)*] was created by transforming bAB167 with genomic DNA from PB5250 (obtained from BGSC catalogue number 1A842). bAB167 was provided by Ethan Garner.

SH42 [*ftsAZ::erm-ftsA-HaloTag(SW)-mNeonGreen- 15aa-ftsZ-cat-ftsA-FtsZ, Δhag::aph (Kan)*] was created by transforming bAB229 with genomic DNA from PB5250 (obtained from BGSC catalogue number 1A842). bAB229 was provided by Ethan Garner.

2.2.5 Microscopy.

Power density, exposure time and other key parameters are listed for each microscopy experiment in supplementary table 3.

FtsZ dynamics were imaged on a Nikon N-STORM inverted fluorescence microscope equipped with an NA 1.49 Nikon 100x TIRF objective, laser source (488 nm), additional 2.5x magnification optics and a 16 µm pixel Andor iXon DU897 EMCCD, giving a final pixel size at the image plane of 64 nm. Cells were illuminated via widefield or HilO, the latter of which was used to minimize background using an objective TIRF module (NIKON N-STORM module) using 488 nm laser excitation.

2.2.6 Vertical Immobilization

Agarose microholes were created by pouring molten 6% agarose (Invitrogen™ UltraPure™ Agarose) onto a silicon micropillar array. Patterned agarose was transferred into a Geneframe (Thermo Scientific AB-0577) mounted on a glass slide. The regions either side of the microholes were cut away, leaving a thin strip of agarose in the center of the Geneframe, to ensure sufficient oxygen. Cells at OD600~0.4 were concentrated 100x by centrifugation. 4 µL of sample was then loaded onto the agarose pad and a cover slip was placed on top.

VerCINI experiments were performed on cells in a *Δhag* mutant background, preventing undesirable cell rotation within the microholes by disabling flagellar motility. As a further control, immobilised cells were imaged in brightfield to ensure cells were not rotating within the agarose chambers.

2.2.7 HaloTag labeling

HaloTag labelling with Halo-TMR and JF- dyes. Full labeling of FtsA-HaloTag(SW) was obtained by incubating strain SH42 with 500 nM HaloTag-JF549 ligand for 15 min. Cells were pelleted, rinsed and washed in 1ml of fresh media

2.2.8 Dual colour imaging

Dual colour imaging was performed on a custom microscope. Cells were illuminated with a 488 nm laser (Obis) and/or a 561 nm laser (Obis) as indicated. A 100x TIRF objective (Nikon CFI Apochromat TIRF 100XC Oil) was used for all experiments. A 200 mm tube lens (Thorlabs TTL200) and Prime BSI sCMOS camera (Teledyne Photometrics) were used for imaging, giving effective image pixel size of 65 nm/pixel.

2.2.9 Data analysis – vertical microhole imaging.

Images were corrected for translational drift using the Fiji *StackReg* plugin. Cropped region of interest movies containing single in-focus cells were manually selected and exported for analysis. Each field of view (FOV) was compared to its brightfield counterpart to ensure each cell selected was not freely rotating. Tilted Z-rings were also excluded. Kymographs were automatically calculated along the circumference of individual Z rings using a custom MATLAB script. The best fitting circle for each Z ring was identified by least squares fitting, and the intensity around the circumference of the ring calculated with sub-pixel precision by bicubic interpolation. FtsA and FtsZ filament speed was measured manually by kymographs analysis, annotating filaments as lines in ImageJ and measuring the angle via an ImageJ script.

2.3 Results

2.3.1 Vertical immobilisation enables the Z-ring to be observed around the entire circumference of the cell.

FtsZ filament dynamics are difficult to observe *in vivo*. As rod shaped bacteria like *B. subtilis* lie flat on a coverslip, their division machinery is orientated perpendicular to the imaging plane, causing the Z-ring to be projected as a band at the midcell (Figure 2.1A). Not only are we limited to seeing a partial Z-ring, filament dynamics become even more difficult to observe as the Z-ring constricts and the filaments become more tightly packed together. While TIRF imaging is an useful technique for increasing the signal to noise ratio (SNR), only a thin slice of the cell is illuminated. This limits filament observations to pre-constricted Z-rings at the beginning of the cell division process [209,210]. Once the Z-ring has started to constrict, filaments will inevitably move out of the field of illumination. The above difficulties demonstrate the limitations of using a 2D approach to study a 3D structure orientated perpendicular to the XY plane. As such, we sought a way to visualise the Z-ring in its entirety, by rotating the division machinery into the imaging plane (Figure 2.1A)

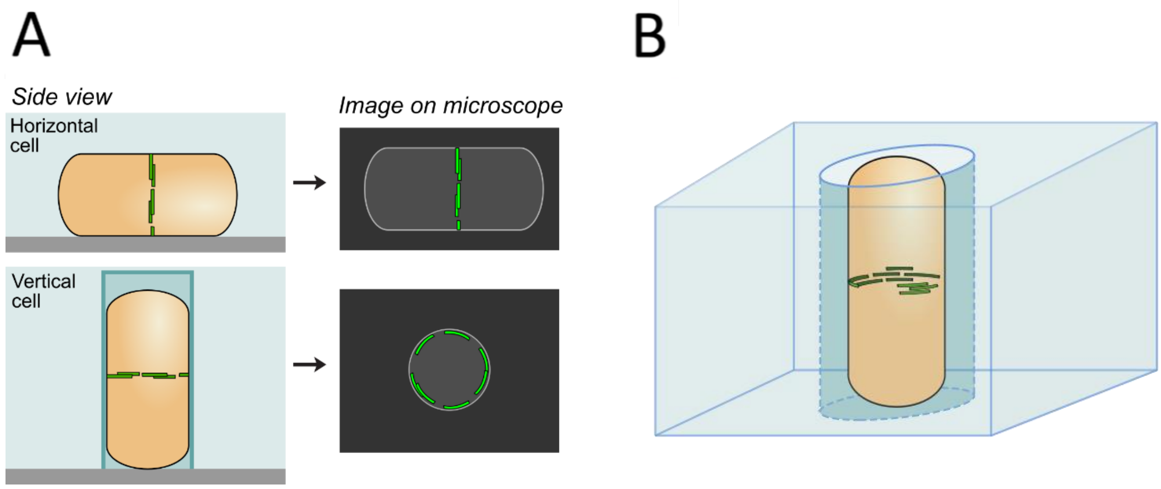

Figure 2.1: The inherent difficulties of Z-ring imaging. (A) Top, conventional imaging of rod shaped bacteria causes the Z-ring to be viewed as a band at the midcell. By trapping rod shaped cells vertically, we can visualise the division machinery in its entirety (bottom). **(B)** Diagrammatic representation of B. subtills trapped in an agarose microchamber. Adapted from[191]

To accomplish this, a method of vertically immobilising *B. subtilis* by trapping cells in agarose microchambers was developed (Figure 2.1B). Through a collaboration with the Dekker lab at TU Delft, an array of silicon micropillars was etched by e-beam lithography (Figure 2.2A)[209]. Using the pillars to pattern agarose, a series of microchambers was generated in which bacterial cells could be trapped. Briefly, microchambers were created by pouring molten agarose onto an array of silicon micropillars. The patterned agarose was then mounted onto a glass slide, with the regions either side being cut away, leaving a thin strip to ensure sufficient oxygen supply to the cells (Figure 2.2B). Cells were loaded onto the sample and a coverslip placed on top. This resulted in a number of cells being forced into the agarose microchambers causing them to "stand upright" (Figure 2.2C). Cells were grown in in CDM, a minimal medium selected as it has low autofluorescence, reduces the chaining phenotype of *B. subtilis* cells, and limits cells length to ensure they fit successfully into the microchambers [211]. As a further precaution, cells were imaged in a *Δhag* mutant background, preventing undesirable cell rotation within the microchambers by disabling flagellar motility. These steps allowed the successful immobilisation of *B. subtilis* cells in a vertical position, permitting top down imaging. This brought the division machinery into the imaging plane, allowing the Z-ring to be visualised around the entire circumference of the cell (Figure 2.2D).

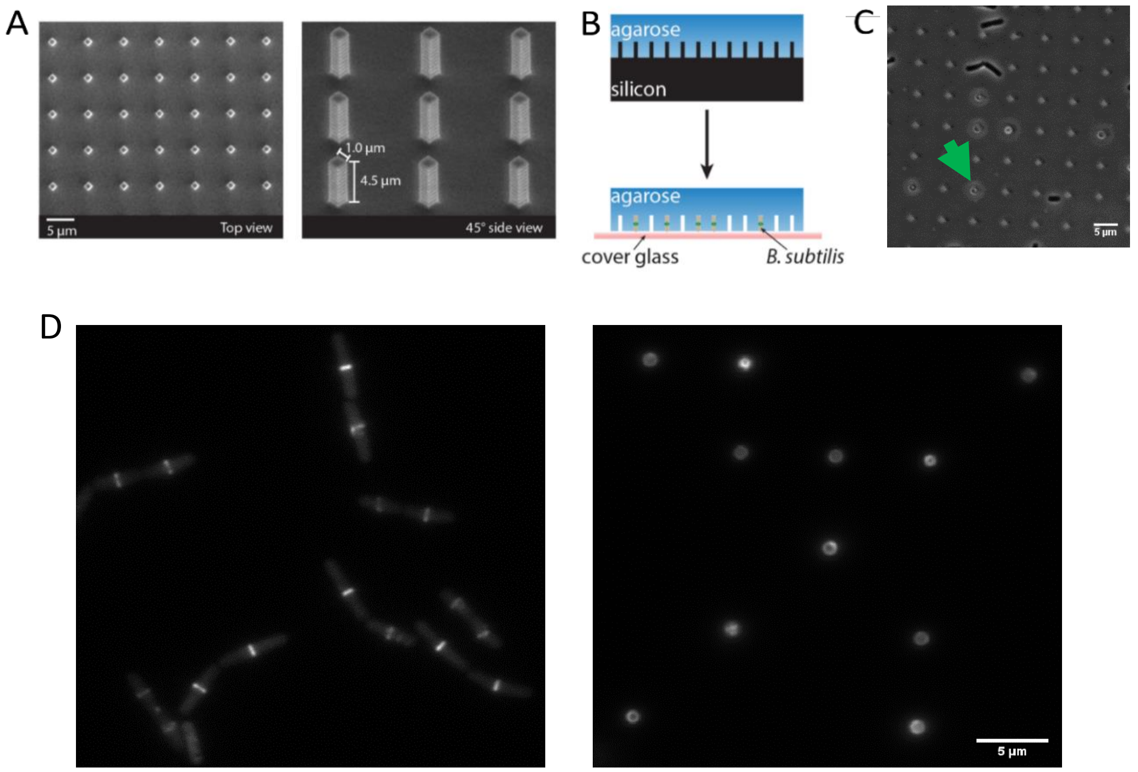

Figure 2.2: Vertical immobilisation workflow. (A) Scanning electron microscopy of silicon micropillars nanofabricated through electron-beam lithography and reactive-ion etching. **(B)** Schematic of the patterning process to produce agarose pads containing microholes. **(C)** Brightfield images of B. subtilis (SH33 [*trpC2, ftsZ:: ftsZ-GFP::cat, Δhag::aph(kan)]]*) inoculated in microholes. Green arrow shows vertically immobilised cell. **(D)** Comparison of Z-rings (SH33) between horizontal cells (left) and vertically immobilised cells (right).

2.3.2 FtsZ filaments move bi-directionally around the division plane

Following the successful immobilisation of cells within the agarose microchambers, the dynamics of FtsZ around the entire division plane could be imaged. This was achieved using a strain of *B. subtilis* that expressed an FtsZ-GFP fusion protein as the sole source of FtsZ from its native locus (SH33). Although this strain is known to have a temperature sensitive phenotype at 45^{o}C, it is otherwise functional [212]. By taking time-lapse images of FtsZ-GFP, kymographs were generated to visualise FtsZ filament dynamics. However due to the Z-ring being a dense structure, significant imaging optimisation was required in order to generate kymographs with a sufficient SNR to reliably interpret the dynamics. Initially, we sought to maximise temporal resolution by continuously imaging the Z-ring with 1s exposure for 2 mins. Kymographs were plotted to show two complete rotations around the line profile for ease of visualisation, allowing for straightforward visualisation of filaments crossing the 360^{o}, 0^{o} boundary. While this approach successfully generated kymographs in which the processive movement of FtsZ filaments could be observed, the low SNR made the faithful interpretation of the results difficult. For example, many of the filaments appeared to blur together, making it difficult to track single filaments, or bundles of filaments, within the cell (Figure 2.3A). To address the issue a compromise was reached by increasing exposure time, thus reducing temporal resolution, to increase the SNR while not increasing the rate of photobleaching (Figure 2.3B).

The Z-ring was shown to be composed of multiple FtsZ filaments which move bi-directionally around the division plane. Filaments were shown to be motile across a range of diameters, showing that they remained motile well into active constriction. Additionally, filament trajectories frequently crossed each other, indicating overlapping filaments. From these kymographs, we were also able to calculate that FtsZ filaments moved with a median velocity of 25nm/s (interquartile range, IQR, 22-28 nm/s, N=36).

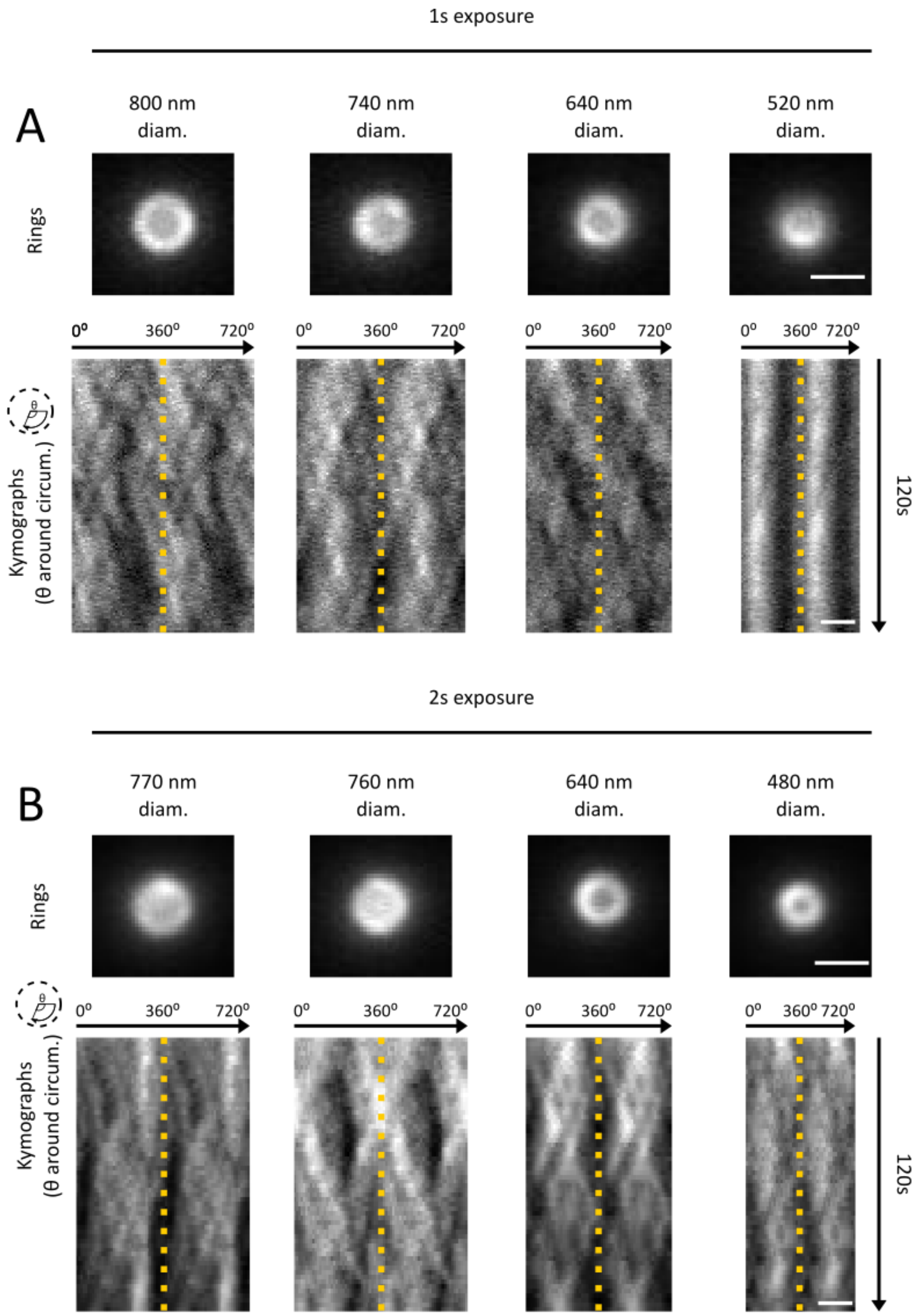

Figure 2.3: The Z-ring is composed of multiple filaments of FtsZ that move bi-directionally around the division plane. Representative images of Z-rings and associated kymographs of FtsZ-GFP (SH33 [*trpC2, ftsZ:: ftsZ-GFP::cat, Δhag::aph(kan)*]) dynamics in vertically-immobilised cells with low (**A**- exposure time 1s) and high (**B**-exposure time 2s) SNR . Scale bar 1 µm. Kymographs were obtained by fitting septal images to circles and plotting intensity values around the circumference of the cell for each frame of the time-lapse (1 frame/ s). Two full revolutions around the cell (0-720^{o}) are plotted side-by-side in each kymograph to resolve filament trajectories that pass 0^{o}/360^{o}, separated by yellow dotted lines

2.3.4 FtsA filaments colocalise and move with FtsZ filaments

The next objective was to image a strain expressing an mNeonGreen-FtsZ fusion protein as the sole source of FtsZ that was developed by collaborators (bAB185)[209]. It was originally thought that this strain was a functional replacement that lacked the temperature sensitive phenotype associated with the FtsZ-GFP strain in addition to using a fluorophore with better photophysical properties [213]. However, it was later discovered that an error by collaborators lead to us being provided with a strain expressing an FtsA-mNeonGreen sandwich fusion instead (bAB167). Like bAB185, it was originally thought that the FtsA-mNeonGreen fusion protein was a functional replacement. However, it has since been discovered that both of these strains have undergone a duplication event, resulting in these strains expressing two copies of the FtsAZ operon, one wt and the other with its respective fusion protein. Filament dynamics were not affected by this duplication[209], as will be discussed in the next chapter.

Thus the dynamics of the actin-like protein FtsA, which is required to tether FtsZ to the inner side of the cytoplasmic membrane in an ATP dependent fashion[214], were imaged instead. FtsA-mNeonGreen gave very poor SNR, surprising at the time given that mNeonGreen is a significantly brighter fluorophore than GFP [213]. This made it difficult to assess the dynamics of FtsA, as it was extremely difficult to pick out trajectories from the generated kymographs (Figure 2.4).

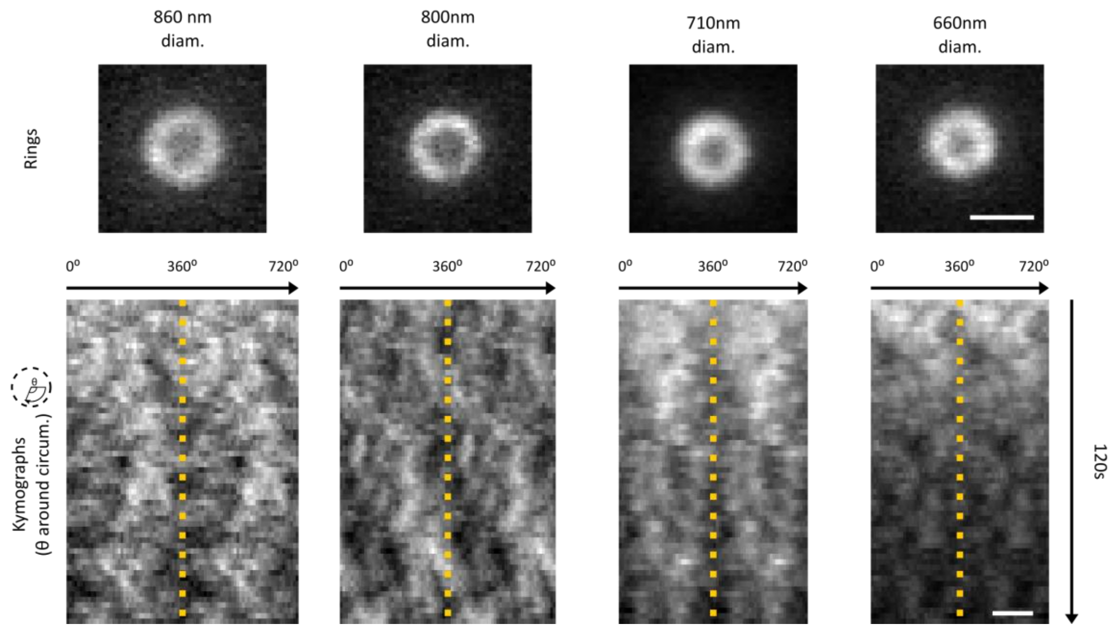

Figure 2.4: Initial FtsA filament dynamics were hindered by low SNR. Representative FtsA-rings and associated kymographs of FtsZ-GFP (SH41 *[ftsAZ::mNeonGreen-15aa-ftsA-ftsZ-FtsA-FtsZ, Δhag::aph (kan)*]) dynamics in vertically-immobilised cells when imaged in widefield. Scale bar 1 µm. Kymographs were obtained by fitting septal images to circles and plotting intensity values around the circumference of the cell for each frame of the time-lapse (1 frame/ s). Two full revolutions around the cell (0-720°) are plotted side-by-side in each kymograph to resolve filament trajectories that pass 0°/360°, separated by yellow dotted lines.

To combat the poor SNR, highly inclined and laminated optical sheet (HiLO) microscopy was implemented, which works by inclining the illumination beam and minimizing the illumination area. As the background is composed of out of focus light due to autofluorescence, reducing the illuminated range by inclining the beam reduces the background intensity. This results in an increase in signal while simultaneously reducing intensity of the background, increasing SNR. While the increase in SNR is not as great as in TIRF, HiLO allows structures throughout the entire depth of cells to be imaged [215] (Figure 2.5A-B).

A

B

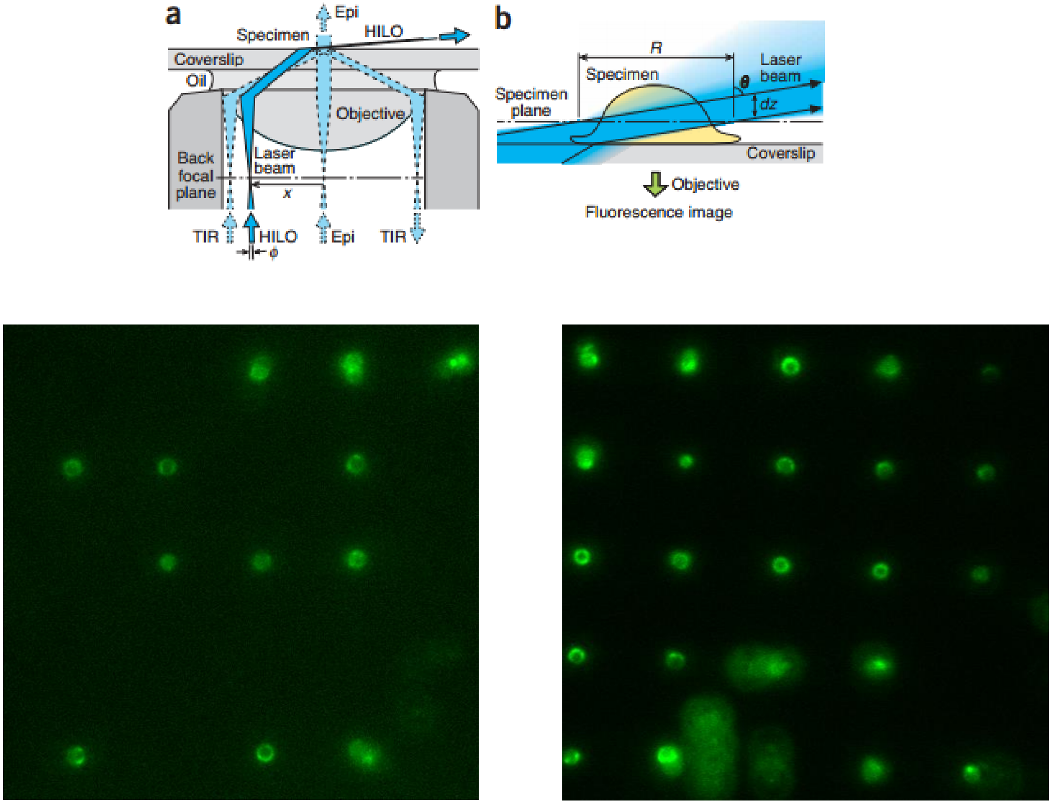

Figure 2.5: HiLO increases SNR. (A) Schematic representation on the principles of HiLO . Reproduced from[29]. **(B)** Widefield (left) and HLO (right) imaging of SH41 [*ftsAZ::mNeonGreen-15aa-ftsA-ftsZ-FtsA-FtsZ, Δhag::aph (kan)*].

After successfully increasing the SNR the dynamics of FtsA-mNeonGreen were then imaged. Like FtsZ, FtsA forms a ring composed of multiple short foci distributed around the circumference of the cell at the division site (Figure 2.6). These filaments also moved bi-directionally around the division plane and filaments moved with a median velocity of 41 nm/s (IQR 29-55 nm/s, N=111). This is higher than the observed speed of FtsZ filaments, however collaborators have shown that filaments of FtsA and FtsZ move with the same speed [209]. This is most likely an effect of the fusion proteins used. When mNeonGreen-FtsZ is expressed as a dilute label alongside its wildtype counterpart, FtsZ was shown to treadmill at 41 nm/s[216].

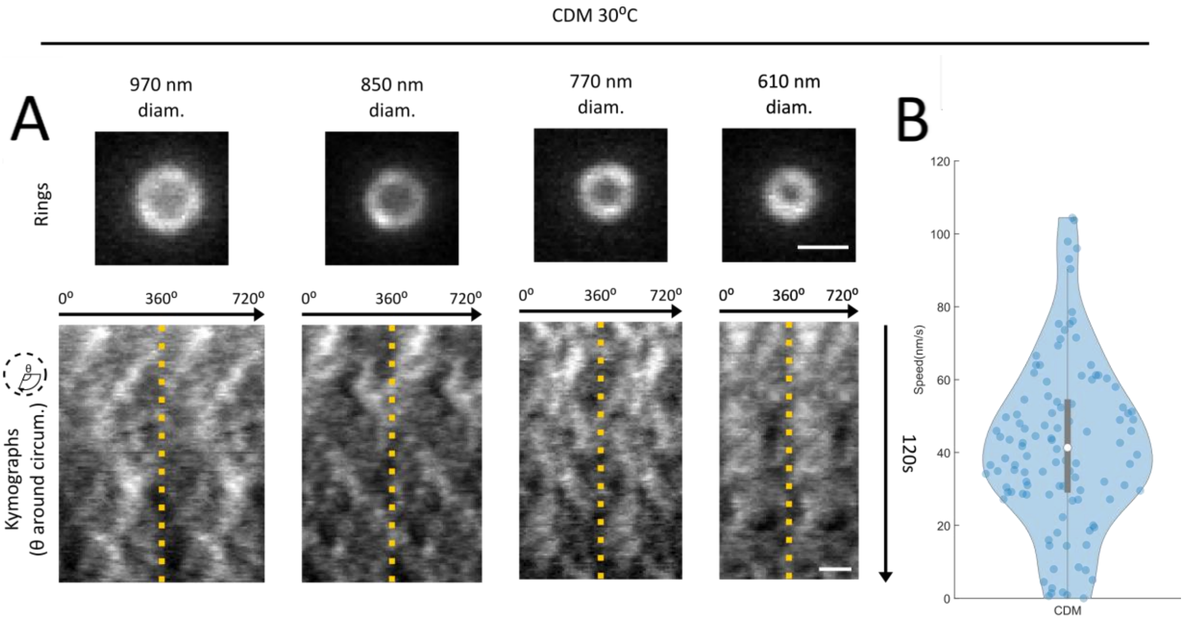

Figure 2.6: FtsA filaments move bi-directionally around the division plane. **(A)** Representative images of FtsA-rings and associated kymographs of FtsZ-GFP (SH41 [*ftsAZ::mNeonGreen-15aa-ftsA-ftsZ-FtsA-FtsZ, Δhag::aph (kan)*]) dynamics in vertically-immobilised cells. Scale bar 1 µm. Kymographs were obtained by fitting septal images to circles and plotting intensity values around the circumference of the cell for each frame of the time-lapse (1 frame/ s). Two full revolutions around the cell (0-720º) are plotted side-by-side in each kymograph to resolve filament trajectories that pass 0º/360º, separated by yellow dotted lines. **(B)** Violin plots of FtsA filament speed. White circles, median; grey lines, interquartile range.

Simultaneous dual colour imaging was conducted in order to assess how FtsA and FtsZ filament dynamics are coordinated. To do this, we used a strain which expressed both an mNeonGreen-FtsZ fusion and an FtsA-HaloTag fusion (SH42). In order to observe FtsA dynamics, we used JF-549 to fluorescently label the protein. As with the FtsA-mNeonGreen strain (SH41) we were initially under the impression that this strain utilised both FtsA-HaloTag and mNeonGreen-FtsZ as the sole sources of their respective proteins in the cell. However, we later discovered that this strain too suffered from a duplication resulting in the fusion proteins being expressed alongside their native counterparts [209]. The implications of the duplication will be discussed in the subsequent chapter, though the duplication was shown not to effect filament dynamics[209]. Filaments of FtsA and FtsZ colocalise and move together around the division site. Our results showed that static filaments of FtsZ also coincided with static filaments of FtsA. Motile filaments of FtsA and FtsZ moved with the same trajectory. This supports findings by collaborators that FtsZ and FtsA colocalise and move together (Figure 2.7) [209].

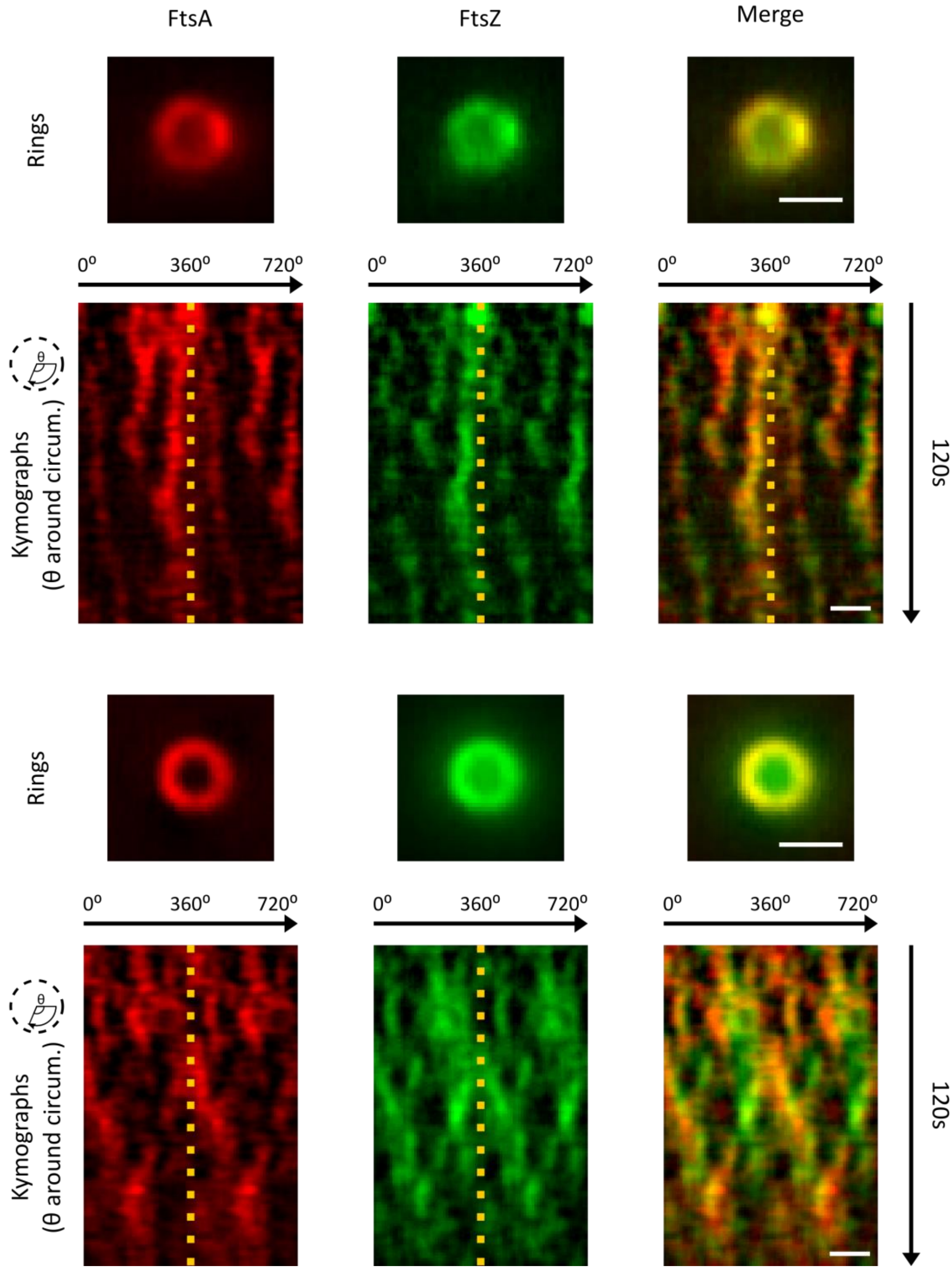

Figure 2.7: FtsA and FtsZ colocalise and move together around the division site. Simultaneous dual colour imaging shows that mNeonGreen-FtsZ and FtsA-HaloTag-JF549 (SH42 [*ftsAZ::erm-ftsA-HaloTag(SW)-mNeonGreen- 15aa-ftsZ-cat-ftsA-FtsZ, Δhag::aph (kan)*] colocalise and move together. Representative images of FtsA (red- FtsA-HaloTag-JF549) and FtsZ (green- mNeonGreen-FtsZ) rings and associated kymographs (SH42) dynamics in vertically-immobilised cells. Scale bar 1 µm. Kymographs were obtained by fitting septal images to circles and plotting intensity values around the circumference of the cell for each frame of the time-lapse (1 frame/ s). Two full revolutions around the cell (0-720^{o}) are plotted side-by-side in each kymograph to resolve filament trajectories that pass 0^{o}/360^{o}, separated by yellow dotted lines.

2.3.5 Filament dynamics are a result of treadmilling

Through work conducted by collaborators, individual monomers of FtsZ and FtsA were found to be stationary within a motile filaments (Fig. 2.8) [209]. This is consistent with previous measurements of single molecule FtsZ dynamics in live *E. coli* [116]. Together with our observation that FtsZ filaments are motile overall, this indicates that FtsZ treadmills, a process in which filament motility is achieved through plus-end polymerisation and minus-end depolymerisation while single monomers within the filament itself remain stationary (FIG 2.8). Furthermore, the treadmilling activity of FtsZ was observed both to depend on FtsZ GTPase activity, and to drive the motility of FtsA[209].

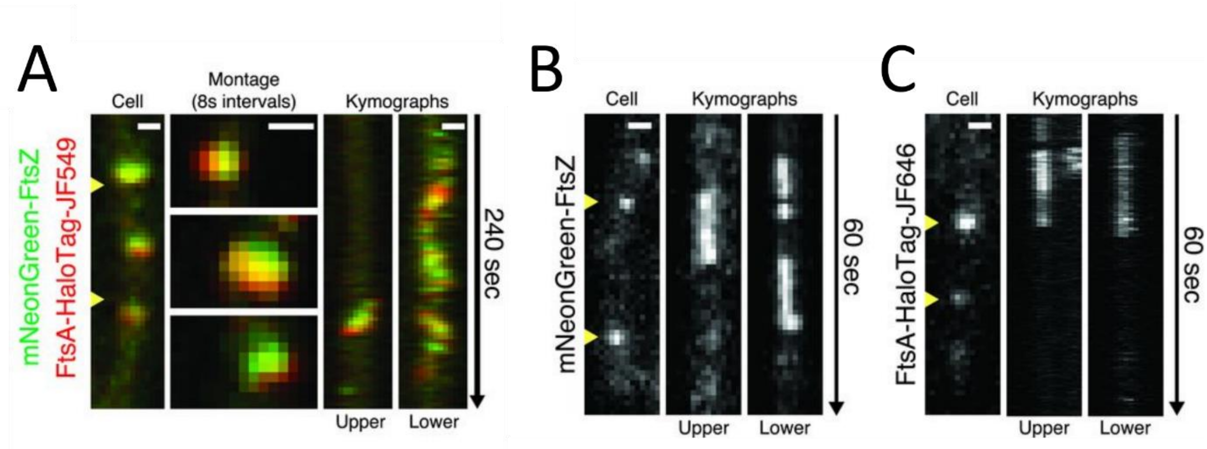

Figure 2.8: FtsZ filaments treadmill around the division site. (A) Filaments of FtsZ and FtsA colocalise and move together. **(B)** Single molecules of FtsZ are immobile at the division site. **(C)** Single molecules of FtsA are immobile at the division site[23]. Measurements conducted by collaborators and reproduced from[191].

2.3.6 Nutrient availability does not affect FtsZ treadmilling speed

We also investigated the effects of nutrient availability on division protein dynamics. We initially did so thinking we were using the mNeonGreen-FtsZ fusion (bAB185). However, as stated previously we later discovered we were in fact imaging FtsA-mNeonGreen (bAB167). Despite this, as FtsA and FtsZ colocalise and move with the same velocity, and with FtsZ driving the dynamics of FtsA, it is possible to use FtsA as a proxy. Thus we compared the treadmilling speed of FtsA filaments in rich and minimal media conditions. PHMM (equal parts CH and S750) is a rich media that promotes rod shaped morphology by reducing the chaining phenotype[209]. In nutrient rich conditions FtsA, and thus by extension FtsZ, was found to treadmill at a median speed of 44 nm/s (IQR 29-56 nm/s, N=62) thus not at a significantly faster rate than in nutrient limited conditions (Fig 2.9).

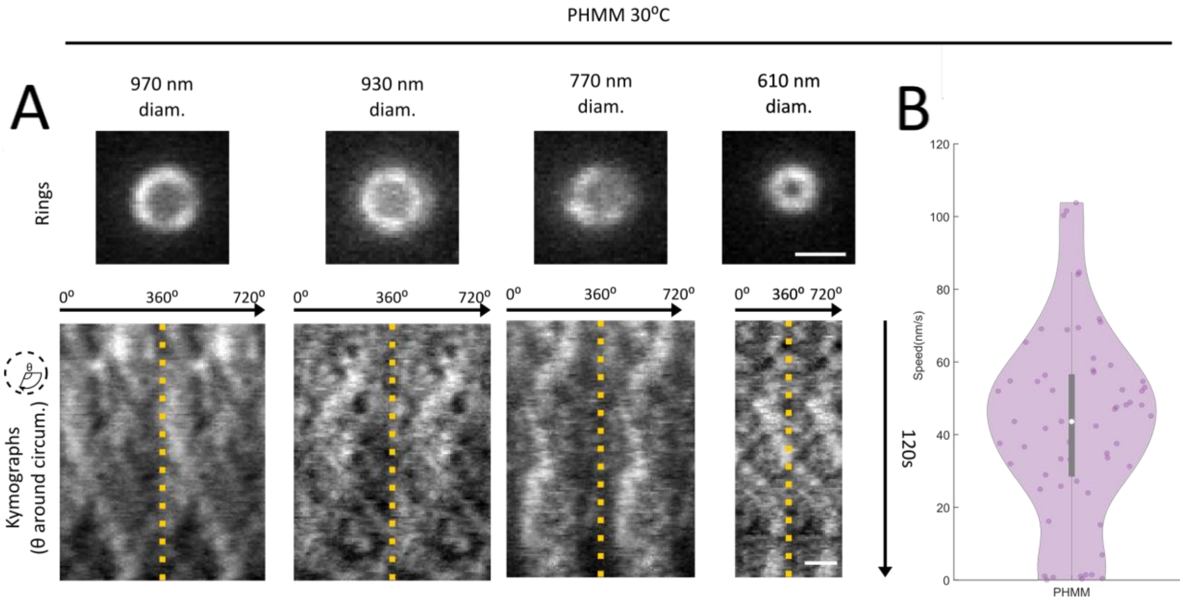

Figure 2.9: **FtsA filament treadmilling speed is unaffected by media composition.** **(A)** Representative images of FtsA-rings and associated kymographs of FtsZ-GFP (SH41 [*ftsAZ::mNeonGreen-15aa-ftsA-ftsZ-FtsA-FtsZ, Δhag::aph (kan)*]) dynamics in vertically-immobilised cells. Scale bar 1 µm. Kymographs were obtained by fitting septal images to circles and plotting intensity values around the circumference of the cell for each frame of the time-lapse (1 frame/ s). Two full revolutions around the cell (0-720°) are plotted side-by-side in each kymograph to resolve filament trajectories that pass 0°/360°, separated by yellow dotted lines. **(B)** Violin plots of FtsA filament speed. White circles, median; grey lines, interquartile range.

2.4. Discussion

2.4.1 Rational for vertical immobilisation

Division is an inherently dynamic process and gaining insights into the division machinery's organisation and dynamics will help reveal how the divisome works mechanistically. It has long been known that the Z-ring is a highly dynamic structure. FRAP experiments have shown that the Z-ring undergoes constant remodelling, exchanging subunits between the ring and cytoplasm and undergoing complete turnover in <10s [206,207]. Thus we sought to investigate the dynamic nature of the Z-ring and its role in cell division. However, imaging the organisation and dynamics of proteins in cells not much larger than the diffraction limit of light is an difficult task. *B. subtilis*, for example, is about 800nm in width, close to the 250nm diffraction limit of light [217].

The rod shaped morphology of cells like *B. subtilis* imposes additional obstacles in regards to studying the organisation and dynamics of division proteins. When imaged using conventional microscopy techniques, rod shaped cells lay flat on a coverslip. This causes the division machinery to be orientated perpendicular to the imaging plane. As such, the Z-ring appears as a dense band at the midcell, rather than a ring like structure that spans the circumference of the division site. Since widefield microscopy has an axial resolution of about 500nm, this limits observations to nascent rings- diffuse structures composed of sparse filaments distributed around the division site, prior to condensation into a mature dense ring. Following the initiation of constriction, the axial diffraction limit would render it impossible to resolve single filaments. Furthermore, as the Z-ring is visualised as a dense 2D-band when imaged by flat-pad microscopy, fluorescence from both the cytoplasmic FtsZ background and out of focus FtsZ filaments within the ring would degrade image quality resulting in poor SNR. This imposes another level of difficulty in tracking FtsZ filament dynamics. Although TIRF is able to increase the axial resolution to 50-100 nm[109], in addition to increasing the SNR[41], it also restricts the illumination depth, resulting in only a thin slice of the cell being illuminated close to the coverslip due to the exponential decay of the evanescent wave generated[41]. This again means that only the dynamics of the division machinery in the early stages of cytokinesis can be examined, as they eventually move out of the illumination area as constriction progresses.

One possible solution would have been to turn to super-resolution techniques. However, these techniques are often complex, and care must be taken when reconstructing images to avoid introducing artefacts. Localisation microscopy techniques such as PALM and STORM for example, are able to greatly increase resolution (XY ~10nm, Z ~20nm), circumventing the diffraction limit through stochastic localisation of single photoactivatable fluorophores [111,112]. However, these techniques are largely restricted to fixed, or single snapshots of live cells, due to their relatively lengthy acquisition time. Likewise, stimulated emission depletion (STED) microscopy is largely limited to fixed cell imaging due to the high illumination intensity required. Ideally, when imaging live cells, one would limit the light dose such that it does not elicit a physiological response[218]. Another possible solution would be to utilise structured illumination microscopy (SIM) which is much more amenable to live cell imaging due to lower light doses[219]. However, SIM only doubles the resolution when compared to epifluorescent widefield imaging, and SIM can fail if too much out of focus light is present[220].

Another possibility is single molecule tracking, a method in which a small number of isolated fluorophores are tracked within in a cell. This can be achieved through sub-stochiometric labelling of the proteins or the use of photoactivatable fluorophores [221]. This allows the overall organisation and dynamics of individual proteins to be tracked and this technique offers resolution of <30 nm (XY) and 100nm (Z). Single molecule tracking has previously been used to study the dynamics of the bacterial cytoskeletal protein MreB, a distant actin homologue[222]. MreB was observed to move perpendicular to the long axis of the cell driven by the motion of PG synthesis [222]. However, as individual monomers of FtsZ have been shown to be static within the ring *in vivo,* using this technique would not reveal whether the overall filament is motile. *In vitro* experiments have shown that FtsZ is capable of treadmilling, a type of asymmetric motion where plus-end polymerisation and minus-end depolymerisation results in overall filament movement while individual monomers remain stationary within the filament. While single molecule tracking has been used to highlight intriguing aspects of MreB filament motion such as pauses and reversals of signal monomers [222], the observation that FtsZ monomers are static within filaments means that this technique would be unable to reveal overall filament properties such as speed, lifetime and processivity.

Table 1. The principles of advanced microscopy techniques

Method	XY resolution (nm)	Z resolution (nm)	Principle	Advantages and disadvantages
SIM	100nm	250nm	Projection of spatially patterned illumination shifted through different angles and phases doubles lateral and axial resolution [219].	Uses light doses compatible with live cell imaging. Only doubles the effective resolution of conventional widefield imaging.
STED	50nm	100nm	Reduces the effective confocal spot size by projecting a depletion light to bring an excited fluorophore down to its ground state before it can emit a singnal[218]	High illumination intensity effectively limits this technique to fixed cells.
Single molecule tracking	<30nm	<100nm	Tracks a small number of individually labelled molecules within a cell[221].	Allows the overall organisation and dynamics of individual proteins to be tracked. For treadmilling filaments, single molecules tracking would be unable to elucidate overall filament properties.
PALM/STORM	10-40nm	20-100nm	Stochastic activation of photoactivatable fluorophores circumvents the diffraction barrier [111,112].	High spatial resolution. Extremely slow and thus is not useful for studying dynamics.
TIRF	250 nm	50-150 nm	Generation of an evanescent field illuminates a thin slice of the sample 100nm from the coverslip[41].	Dramatically increases SNR due to restricted illumination depth. Restricted illumination depth limits observations to 100nm above the coverslip.

In order to overcome these limitations, we developed a vertical immobilization method, causing rod shaped bacteria to "stand upright", rotating the division machinery into the imaging plane. This results in in the Z-ring being observed in its entirety around the entire circumference of the cell, rather than a dense band projected at the midcell (Figure 2.2D). While vertical immobilisation does not actually increase resolution, rotation of the Z-ring into the XY plane results in it being viewed at ~250nm resolution as opposed to ~500nm when imaged by conventional flat pad microscopy. Not only does this allow us to track the dynamics of FtsZ filaments around the entire circumference of the division site, but it also allows FtsZ filament dynamics to be observed in actively constricting cells.

2.4.2 FtsZ filaments treadmill bi-directionally around the division plane

Although it has long been known that the Z-ring is a highly dynamic structure, the organisation and dynamics of FtsZ filaments within the Z-ring has remained elusive. Using the novel vertical immobilisation technology described above, we discovered that the Z-ring is composed of multiple motile filaments which move bi-directionally around the division plane. Work by collaborators showed that individual monomers of FtsZ within the ring are static [209] in agreement with previous experiments [124]. Together these results show that FtsZ filaments move by treadmilling [209]. Simultaneously, it was discovered that FtsZ treadmills in an independent study in *E. coli*. Although FtsZ filaments had previously been shown to treadmill *in vitro* [208], it was unclear if this behaviour occurred *in vivo* or was simply an ability of FtsZ under strictly regulated conditions . Not only did we observe that FtsZ filaments are capable of treadmilling *in* vivo but we also demonstrated that this is the dominant behaviour of FtsZ filaments. Subsequently FtsZ treadmilling has since been observed in a number of other bacterial species [210,223,224]. This suggests that treadmilling is an intrinsic property of the FtsZ filaments, and its conserved nature suggests that treadmilling plays an essential role in cell division.

Bi-directional treadmilling of FtsZ filaments may also explain the complex “patch” dynamics observed by Strauss et al[113]. The authors observed that the Z-ring underwent significant structural rearrangement over time. Treadmilling filaments would cause not only exchange of subunits between the filament and the cytoplasmic pool, but also the actual position of the filaments themselves to change overtime. Additionally, bi-directional treadmilling may also explain the patchy, heterogenous organisation of the Z-ring [225]. Treadmilling of FtsZ filaments could stochastically cause aggregations of filaments in one region of the Z-ring, with a sparse distribution in other areas of the ring.

Despite the innovative work which showed that FtsZ is capable of treadmilling *in vitro,* demonstrating that it occurs under physiologically relevant conditions *in vivo* was no trivial task. *In vitro,* FtsZ was shown to self-assemble (alongside FtsA) into treadmilling vortices. Reconstituting Z-rings on an artificial bilayer not only orientates FtsZ into the imaging plane, it also allows the sample to be imaged via TIRF microscopy. This allowed Z-rings to be observed in their entirety with high SNR. Furthermore, rings were shown to be composed of bundles of FtsZ filaments which treadmilled in a single direction[208]. This is in contrast to *in vivo* where it is unknown if FtsZ filaments form large bundles, in addition to filaments treadmilling bi-directionally around the division plane[209]. This made observing FtsZ filament dynamics a difficult task. Not only are we limited to observing a partial Z-ring, but in mature rings filaments are constrained to an area ~100nm wide in mature rings[101], below the diffraction limit of light. This prevents us from resolving the dynamics of individual filaments within the ring limiting observations to isolated filaments of nascent rings. However, as described previously, the vertical immobilisation technology allowed us to combat this limitation.

The initial observation by Loose and Mitchison[125] that FtsZ can treadmill *in vitro* was surprising due to the fact that FtsZ was initially not considered a good candidate for treadmilling. The basic principle of treadmilling filaments is that the strength of intersubunit interfaces is made dynamic through nucleotide hydrolysis, and this is triggered by a nucleotide polymerisation reaction[226]. A nucleotide gradient would thus establish treadmilling, as the growing end of the filament would contain more triphosphate bound monomers, while the shrinking would contain more diphosphate bound monomers. In terms of FtsZ, it is known that polymerisation requires GTP and results in the activation of a subunits' GTPase ability, thus permitting hydrolysis of the bound nucleotide[106]. This would allow a nucleotide gradient to be established as the growing end would be more likely to contain GTP compared to the shrinking end, as these monomers have been present in the filament for longer.

A treadmilling filament is characterised by the preferential growth of the filament at one end, and shrinkage at the other [226], it requires a net difference in the polymerisation and depolymerisation rates between the plus- and minus-ends of the filament, meaning that the filaments has both structural and kinetic polarity. While FtsZ was known to have structural polarity in that the protofilament is formed via the head-to-tail association of individual monomers[104,105,227], the kinetic polarity was far more difficult to reconcile. Furthermore, treadmilling was assumed to require filaments to be multistranded, as lateral contacts between actin filaments changed the dissociation rates at the shrinking end of the filament [228,229].

In principle a polar filament such as FtsZ is capable of treadmilling with nucleotide hydrolysis alone[230], though three problems would prevent this process from being robust:

1. Oligomers would be formed at a higher frequency than larger filaments due to the fact that the association affinity is constant at each step.
2. Oligomers would fragment at interfaces where the bound nucleotide has been hydrolysed, at similar rates to the dissociation rate of the diphosphate containing end of the filament.
3. Oligomer association reactions at both ends would be identical as they have the same rate.

Thus the observation that FtsZ treadmills both *in vitro* and *in vivo* has spawned studies into discovering how this phenomenon occurs. FtsZ is known to possess two properties common to both actin and tubulin. The first is that FtsZ displays cooperative assembly, a feat not possible for a single-stranded, isodesmic filament composed of rigid subunits. Second, treadmilling was presumed to require multistrandedness, though it is unknown whether FtsZ forms such structures *in vivo.* Since the discovery that FtsZ treadmills, the crystal structure of FtsZ has resolved how a single stranded filament is able to cooperatively assemble and robustly treadmill[226].

In order to understand how a protofilament treadmills, one must divide the process into two stages: nucleation and elongation. Nucleation is the formation of a new protofilament from free monomers, after which monomers can freely associate and dissociate with the ends via a process known as elongation. When elongation occurs directionally, treadmilling can occur. As stated previously, FtsZ displays cooperative assembly,[99,100] yet it was not understood how this could occur with rigid subunits. By examining the crystal structure of FtsZ, Wagstaff *et al.* proved a long held hypothesis that FtsZ undergoes a conformational switch from a closed to open form as a result of polymerisation, explaining both cooperative assembly and treadmilling[226]. This confirmational change results in a rotation of the GTPase-activating domain relative to the GTP-binding domain, resulting in an increased affinity[226]. This causes FtsZ monomers to transition from a relaxed (R) to tense (T) state[231]. Free unassembled FtsZ monomers exists in the R form and have low self-association affinity while monomers within the polymer are in the high self-association T form, though it is thought a small number of free monomers also exist in the T form to facilitate nucleation[232]. The conformational switch from R to T form is intrinsically coupled to the association interface between consecutive monomers in filaments rather than their nucleotide state [226]. Thus switching between low and high affinity conformations can explain how FtsZ filaments display cooperative assembly and treadmilling.

Since FtsZ monomers are thought to primarily exist in the R form it would require substantial free energy to undergo the conformational switch to the T form [231]. However, when incorporated into a protofilament a monomer gains a protein-protein interface [231]. If the T conformation if able to provide a more stabilising interface than the R confirmation, this favourable negative free energy would compensate for the R to T change[231]. As such, this explains why protofilaments are formed as opposed to many oligomers. These changes in affinity also explain how treadmilling occurs. Monomers at the plus-end would be stabilised by being in the T state and possessing bound GTP resulting in strong association between subunits[231] . As such, this would make the-on rate greater than the off rate. Fragmentation of the filament would be prevented due to monomers in the middle of the filament, being sandwiched between two T-state monomers, locking them in the high affinity state, even when GTP hydrolysis has taken place [231]. Finally, the minus-end of the filament would have a greater off-rate as the interface is destabilised, due to it possessing only a single contact and bound GDP[231]. This may result in it switching back to its R state and rapidly dissociating from the filament.

It should be noted in the case of FtsZ, the ability of a single stranded filament to treadmill is a specific case where the nucleotide binding pocked forms part of the filament interface (for example a tubulin-like fashion) [226]. In this case, solvent exposed NDPs (nucleotide diphosphates) are rapidly exchanged with NTPs (nucleotide triphosphates). As NTP hydrolysis does not occur instantaneously, in addition to the interface being stronger than NDP interfaces, this explains how the growing end of the filament having a lower dissociation rate than the shrinking end.

Interestingly, FtsZ has been found to have the opposite kinetic polarity to microtubules [233]. This is surprising given the fact that FtsZ and tubulin are related. During the assembly of microtubules, the bound GTP of tubulin (top-end) is exposed at the plus-end. Incoming monomers then interact with the top-end via their T7 loop (bottom-end) [234]. In contrast to this, FtsZ has been shown to treadmill via bottom end growth in which the GTP-end of an incoming monomers interacts with the T7 loop of the top monomer in the filament [233]. Thus the conformational change induced by polymerisation causes the T7 loop to have a greater affinity for the GTP end of a monomer in either the R or T state.

2.4.3 Increasing SNR by HiLO

Initial imaging of FtsA yielded very poor SNR, making it difficult to assess the proteins dynamics. Thus, HiLO was implemented to combat this. When imaging by widefield epifluorescence, the excitation beam travels directly through the coverslip-sample interface[43]. This results in all of the fluorophores being excited. As such, out of focus light (i.e., fluorophores above and below the imaging plane) will contribute to the acquired fluorescence image in terms of background noise. Though TIRF is extensively used to reduce SNR, this technique only results in a thin slice, approximately 100 nm up from the coverslip, being illuminated due to the exponentially decaying evanescent wave that is generated[41]. As such, this wave could not penetrate deep enough into the sample to illuminate the Z-ring when vertically immobilised. HiLO was thus used as a substitute. In the most basic of terms, HiLO works on a similar principal to TIRF, that is, inclination of the illumination beam. However, in contrast to TIRF, HiLO inclines the beam at an angle lower than the critical angle (Figure 2.5A). Therefore, total internal reflection does not occur and structures can be imaged throughout the entire depth of the sample[215]. However, inclining the light beam in such a way reduces the amount of the sample that is illuminated. While in terms of bacterial cells, this inclination means that the whole cell is still illuminated and thus fusion proteins above and below the imaging plane would contribute to image noise, less of the agarose pad would be illuminated. This would greatly reduce autofluorescence of the media, increasing image quality [235].

2.4.4 FtsZ and FtsA colocalise and treadmill together

Kymographs produced from time-lapse images of FtsA-mNeonGreen showed that FtsA forms a ring like structure, with filaments moving bi-directionally around the division plane. Collaborators further showed that, like FtsZ, FtsA also treadmills [209]. Simultaneous 2 colour imaging showed that both FtsZ and FtsA colocalise and move together around the divisome. This was also shown by our collaborators [209] and is consistent with the observations that FtsA and FtsZ self-organise into dynamic cytoskeletal patterns *in vitro* [208]. FtsA is one of the proteins responsible for binding FtsZ to membrane, as the latter lacks any direct affinity.

FtsA binds to the membrane via its N-terminal amphipathic helix[12]. These structures show natural affinity for positive curvature and thus it is possible that this helps keep FtsA targeted to the division site. The observation that FtsA filaments treadmill alongside FtsZ may help keep FtsZ filaments tethered to the membrane for longer periods of time than a static anchor.

Interestingly, when FtsZ-GFP filament speeds (25 nm/s, IQR 22-28nm/s) are compared to FtsA-mNeonGreen filament speeds (41 nm/s, IQR 22-59 nm/s), we observe that FtsZ-GFP treadmills at a slower speed. This is most likely an effect of the fusion protein. When mNeonGreen-FtsZ is expressed as a dilute label alongside its wildtype counterpart, FtsZ filaments were shown to treadmill with a median velocity of 41 nm/s [216]. This suggests that the GFP tag is slowing down the treadmilling speeds of FtsZ filaments. Potentially, this is due to the fact that the GFP variant used in this fusion is the original GFP protein [212]. As such, the fluorescent protein is not monomeric. While the original GFP from *Aequorea victoria* is only weakly dimeric, having FtsZ filaments constrained to the membrane at the division site increases the likelihood that interactions between individual GFPs could occur [236]. This could cause aggregations of filaments, with the interactions potentially affecting the treadmilling speed. As mNeonGreen is known to be a monomeric protein[213], there should be no interaction between individual monomers. In order to assess this, one could conduct site directed mutagenesis in order to make GFP monomeric and assess the dynamics of the fluorescent protein.

2.4.5 Nutrient availability does not affect FtsZ dynamics.

Our collaborators also showed that FtsZ treadmilling drives FtsA dynamics. Inhibiting FtsZ treadmilling through chemical perturbation also caused FtsA filaments to become static[209]. Furthermore expression of an FtsZ mutant with impaired GTPase activity resulted in a reduction in speed of both FtsA and FtsZ filaments, with both filaments still treadmilling at the same speed as each other[209]. Due to the fact that FtsZ filaments treadmill at the same speed as FtsA filaments, in addition to FtsZ dictating the speed of the latter, we can use FtsA as a proxy for investigating the effects of nutrient availability on FtsZ dynamics. As tagging FtsZ with GFP appears to slow down filament speed, using FtsA as a proxy is advantageous as it eliminates this unfortunate effect. Cell division in *B. subtilis* is known to be subject to growth rate dependent regulation[237] and UgtP has been identified as a growth rate-dependent inhibitor of Z-ring assebmly[238]. UgtP is thought to inhibit Z-ring formation in order to ensure cells reach a critical mass before dividing. UgtP is known to be unregulated in cells cultured in rich media conditions, while down regulated and sequestered in nutrient limiting conditions[238]. Thus the dynamics of FtsA filaments were investigated in PHMM, a rich media with low autofluorescence that reduces the chaining of *B. subtilis* facilitating loading into the microholes. Our results show that nutrient availability has no effect on FtsA dynamics and thus, no effect on FtsZ dynamics. Thus this suggests that UgtP may simply prevent the assembly of protofilaments and thus the Z-ring itself, rather than affecting the overall treadmilling speed of filaments.

2.4.6 FtsZ treadmilling is required for synthase motion

Using SIM to image newly synthesised peptidoglycan, our collaborators observed that septal cell wall synthesis occurred at discrete mobile sites [209]. Single molecule tracking of the cell wall synthases PBP2B (*B. subtilis*)/PBP3 (*E. coli*) revealed that these proteins move processively around the division site. Not only was FtsZ treadmilling required for synthase motion, but the rate of FtsZ treadmilling also set the speed of individual synthases [209,210]. Thus FtsZ treadmilling is required for the motion of FtsA filaments and the synthases in addition to setting their speed. Furthermore, in *B. subtilis*, FtsZ treadmilling rate strongly affected septal constriction rate[209]. This would make sense, FtsZ treadmilling is rate limiting for synthase speed, and thus, is rate limiting for constriction.

However, treadmilling speed does not affect constriction rate in in *E. coli*. Although the treadmilling rate of FtsZ filaments sets the speed of individual synthases, it has no effect on the overall time of division [210]. This may be due to the fact that as *E. coli* only maintains a single layer of peptidoglycan, more control is required to prevent lysis when compared to the thick, multi-layered cell wall of *B. subtilis*. Furthermore, *E.coli* must coordinate constriction with the remodelling of its outer membrane, a feature which *B. subtilis* lacks. These factors could therefore act as additional brakes on cell division such that while FtsZ treadmilling is rate limiting for the speed of individual synthases, it is not rate limiting for the overall constriction process.

Thus in *B. subtilis* cell division is the result of discrete, motile enzyme filament complexes which are driven by FtsZ treadmilling and which build new septal PG in transit. FtsZ treadmilling creates long-range order from the local activity of the PG synthases, linking circumferential enzyme motion to the insertion of cell wall material. This proposes a model whereby FtsZ filaments act as an obligatory guide for septal synthases with the treadmilling of FtsZ being the rate limiting step for septal PG synthesis. Interestingly however, this model does not hold up for *S. aureus,* another Gram-positive organism. In this organism FtsZ treadmilling is dispensable following the initiation of constriction [223]. This is a somewhat surprising finding given that both *B. subtilis* and *S. aureus* belong to the same phylogenetic class. Potentially, this may reflect differences between the two species. On the other hand, a common mechanism may exists whereby FtsZ filament dynamics play different roles in different cell cycle stages. However, imaging FtsZ dynamics across the entire cell cycle is a difficult process. The vertical immobilisation technology presented here is not capable of imaging dim nascent rings due to high background caused by rapid photobleaching. As such, we further developed this technology, allowing us to track Z-dynamics in different cell cycle stages. This will be addressed in subsequent chapters.

2.4.7 Implications on force generation.

It has been suggested that the Z-ring may provide the force required for cytokinesis due to the fact that *in vitro* FtsZ is capable of forming rings or helices that can deform artificial lipid tubules [239,240]. A popular model for cytokinesis is the contractile ring model. Here the Z-ring would form a continuous ring from either a single continuous FtsZ filament or multiple overlapping short filaments [88]. The Z-ring would then generate sustained force around the entire circumference of the division site, through either GTPase induced filament bending, or sliding of multiple overlapping short FtsZ filaments. As individual monomers of FtsZ within the filament have previously been observed to be immobile [124], we have further provided evidence against a sliding filament model by showing filaments treadmill.

The model in which FtsZ treadmilling drives cell division through the action of motile cytoskeletal/synthase complexes, places constraints on how exactly the force required for cytokinesis is generated. For example, it is possible that FtsZ filaments are able to generate enough force to pull in on the membrane. This would be done through GTPase induced bending of the short treadmilling filaments. Importantly, this would only require transient force to be generated, as the synthases could reinforce these deformations by synthesising PG. As such, this would significantly reduce the force required to deform the membrane, when compared to a model in which the Z-ring generates sustained force around the entire circumference of the division site [241]. This model would require FtsZ filaments to form bundles via lateral interactions, as alternatively, filaments would be free to rotate on the membrane. Lateral interactions would constrain such movement. Alternatively, the synthase complex could be strong enough to sufficiently push in on the membrane, displacing it as it synthesis new PG. Additionally, a combination of filament pulling and synthase pushing may be required in order to generate sufficient force.

2.5 Conclusions and outlook

In this chapter, we established a method of vertically immobilising rod shaped bacteria, such that it causes them to sand upright. This brings the division machinery into the imaging plane, allowing it to be visualised in its entirety. I discovered that the Z-ring is composed of forms multiple, short motile filaments which move bi-directionally around the division site. Together with collaborators, we established that FtsZ treadmills in live *B. subtilis*[209]. FtsA was shown to colocalise and move with the same dynamics as FtsZ[209]. FtsZ has since been shown to treadmill in a number of other species [210,223,224]. It has also been shown that FtsZ drives the dynamics of both FtsA and the synthases involved in septal wall synthesis [209,210]. In *B. subtilis* FtsZ treadmilling was also shown to set the rate of cell division, and thus was thought to be rate limiting, yet this was not the case for *E. coli*[209,210].

Interestingly, in *S. aureus,* another Gram-positive organism, FtsZ is dispensable following the initiation of constriction[223]. This may reflect a genuine difference between organisms, or may indicate that FtsZ has different roles in different stages of the cell cycle. As such, it would be interesting to assess the dynamics of FtsZ across different stages of the cell cycle. However, the vertical immobilisation technology as presented in this chapter, is unable to detect dim nascent Z-rings. As such, it was necessary to further develop this technology before this question could be addressed.

Chapter 3 : Amendment to previous publication

3.1. Introduction

Over the course of this project, we became aware of problems regarding strains we had been using initially. Firstly, an inadvertent shipping error by collaborators lead us to image the dynamics of FtsA, as opposed to FtsZ. Furthermore, it was initially thought that the FtsA and FtsZ fusions created by collaborators were functional, single copy replacements. However, Western blots and WGS revealed that this was not the case. Rather, for strains expressing an FtsA and/or an FtsZ fusion created by collaborators, a duplication event lead to strains expressing the fusion protein alongside its native counterpart. Thus, neither the FtsA nor FtsZ fusions were acting as the sole source of their respective proteins in the cell.

As a result of these discoveries, a number of additional experiments and revisions has to be made in order to confirm that findings described in Chapter 2 had not been impacted. In this chapter, I will discuss how stain errors were identified, and the controls conducted by collaborators to ensure previous measurements had not been affected. I will also present additional characterisation performed on the FtsZ-GFP strain that is known to be a single copy replacement.

3.2 Materials and Methods

3.2.1 Culture growth for vertical microhole immobilization

Strains of *B. subtilis* to be imaged by vertical microhole immobilization were streaked from -80°C freezer stocks onto NA agar plates and grown at 30°C overnight. Single colonies were transferred in liquid cultures of Time Lapse Medium (TLM) or PHMM and growth with agitation at 200rpm overnight at either 30°C (TLM) or 22°C (PHMM). The following morning TLM starter cultures were diluted into pre-warmed Chemically Defined Medium (CDM) to a starting OD_{600} ~ 0.1, while PHMM starter cultures were diluted to a starting OD_{600} ~0.05, following which both liquid cultures were grown at 30°C until reaching the appropriate OD_{600}.

3.2.2 Genomic DNA extraction

Genomic DNA from *B. subtilis* was extracted using an adapted version of the Promega Wizard extraction method, In brief, one fresh colony of was inoculated into 3 ml LB. Cells were grown at 37°C (or 30°C if temperature sensitive) for approximately 5 hours, until cells has entered mid-exponential phase. The cultures were subsequently pelleted and resuspended in lysis buffer containing EDTA (50mM), lysozyme (10mg/ml) and RNase and incubated at 37°C for 30-60 minutes. Nuclei lysis solution was then added and the cells incubated at 80°C, after which the samples were cooled to room temperature. Protein precipitate was then added and, after vigorous vortexing, the samples were placed on ice for 10 minutes. Samples were then pelleted at 13000g for 10 minutes, after which the supernatant was transferred into 600 µL of isopropanol. Upon obtaining a visible mass of DNA, the samples were again centrifuged at 13000g for 10 minutes , after which the supernatant was removed, and the pellet washed in 70% ethanol. Following a final centrifuge at 13000g, the supernatant was removed, and the sample air dried for a short time to remove any remaining ethanol. Finally, the pellet was resuspended in 100 µL of Elution Buffer.

3.2.3 Plasmid purification.

Strains of *E. coli* from which a plasmid was to be extracted were streaked from -80°C freezer stocks onto LB agar plates containing 100 µg /ml ampicillin and incubated overnight at 37°C. Cells were subsequently grown overnight in LB supplemented with 100 µg /ml ampicillin and plasmids were purified using QIAprep Miniprep Kit® (Qiagen) according to manufacturers instructions. In brief, cells were pelleted by centrifugation and lysed under alkaline conditions. Lysates were then separated from the cell debris by centrifugation and the DNA was then bound to the QIAprep silica membrane. High salt buffer was used to remove RNA and proteins from the column, ad the DNA plasmid was elute using water at pH7.

3.2.4 B. subtilis transformation.

B. sutbtilis cells were transformed by triggering chemical competence. In brief, a single colony was inoculated into minimal medium (MM: 10 mL SMM basic salts. *125 µL* 40% (w/v) glucose, *100 µL* 2% (w/v) tryptophan*, 60 µL* 1M $Mg_2SO_4.7H_2O$, *10 µL* 20% (w/v) casaminoacids, *5 µL* 2.2mg/ ml) and incubated overnight at 37°C. The following morning, the culture is diluted to OD_{600} ~0.2 in fresh, prewarmed MM and incubated at 37°C for 3 hours. Following this, the culture is diluted 1:1 into pre-warmed starvation medium (SM: 10ml SMM basic salts, *125 µL* 40% (w/v) glucose, *60 µL* 1M $Mg_2SO_4.7H_2O$) and incubated for a further 2h at 37°C. After this, ~500ng of genomic DNA was added to *400 µL* of cells and incubated at 37°C for 1h. Cells are then plated on NA plates with the appropriate antibiotic and incubated overnight at 37°C.

3.2.5 Bacterial strain characterization

SH97 [trpC2, Δhag::aph(kan)] was created by transforming competent *B. subtilis 168CA* [*trpC2*] with genomic from PB5250 (obtained from BGSC catalogue number 1A842).

SH74 [*trpC2, ftsAZ:: ftsa-mNeonGreen-15aa-ftsZ-ftsAZ, Δhag::aph(kan)]* was created by transforming competent SH97 [*trpC2,* Δhag::aph(Kan)] with genomic DNA from bAB181[*ftsa-mNeonGreen-erm-15aaftsZ-cat, Δhag::aph(kan*] (supplied by Professor Ethan Garner). Resistance cassettes were looped out by pDR244 (obtained from BGSC catalogue number ECE274) as described by [242]. Colonies were subsequently straked onto LB, LB-MLS,LB-Cm and LB-Spec plates and incubated overnight at 45°C to confirm that only LB plates presented colonies.

SH211 (PY79 Δ*hag*) was constructed by transforming competent PY79 with genomic DNA extracted from strain PB5250. The antibiotic resistance cassette was removed using pDR224 as described previously.

SH130 (*PY79 Δhag ftsZ::ftsZ-gfp-cam*) was constructed by transforming competent SH211 competent cells with genomic DNA extracted from strain PL642.

3.2.6 Bacterial strain characterization

Strains were characterised by cell morphology analysis (Figure 3.5).

3.2.7 Cell morphology analysis

PY79 and SH130 cultures were prepared for imaging in CDM or PHMM as described above. Once the cultures had reached OD600 0.4-0.5, Nile Red was added to 200µl of cells to a working concentration of 1 µg/ml, and incubated at growth temperatures for 5 mins, prepared on agarose microscope slides as described below and cell morphology images recorded. Cell length was then manually determined using ImageJ.

3.2.8 Western blotting

PY79 and SH130 cultures were grown overnight in 2ml LB at 30^{o}C. The following morning, cultures were diluted to ~OD600 0.05 and grown at 30^{o}C until ~OD600 0.6. Cultures were centrifuged at 13,000 rpm for 2 minutes and the pellets resuspended in 104µL PBS plus peptidase inhibitor (Roche cOmplete™, Mini Protease Inhibitor Cocktail). Cells were then sonicated and 4X Laemmli Buffer and Dithiothreitol (DTT) added. Samples were heated at 80^{o}C for 10 minutes, following which the cells were centrifuged for 5 minutes at 14000 rpm. 20µL lysates were then separated by SDS PAGE in 4-12% Bis-Tris gels (Invitrogen™, NuPAGE™ and blotted (Trans-Blot Turbo Transfer System, BioRad) onto 0.45µm PVDF membrane. Primary polyclonal antibodies against FtsZ (Sigma, 1:10000 dilution) were coupled with HRP-conjugated polyclonal antibodies (anti-rabbit, Sigma). Samples were developed using Pierce™ ECL Western Blotting Substrate (Thermofisher) and imaged using an ImageQuant LAS 4000 mini Biomolecular Imager (GE Healthcare).

3.2.9 Growth curves

B. subtilis PY79 and variant strains were grown overnight in TLM or PHMM containing the relevant inducers. Overnight cells were diluted to an OD600 of 0.05 in either CDM or PHMM, respectively, and 200 µL were used in a 96-well microtiter plate. Growth was monitored for 12 hours using a FluoStar plate reader (BMG Labtech).

3.2.10 Polymerase chain reaction

For all PCR reactions Q5® High-Fidelity DNA Polymerase (New England BioLabs ®) was used.

Table 2: PCR reaction composition used

Component	Final Concentration
5X Q5 Reaction Buffer	1X
10 mM dNTPs	200 µM
Primers (both)	1 µM
Template DNA	< 1,000 ng
Q5 High-Fidelity DNA Polymerase	0.02 U/µl
Nuclease-Free Water	

Table 3: Thermocycling Conditions for a Routine PC

Step	Temperature	Time
Initial Denaturation	98°C	30 seconds
35 cycles:		
Denaturation	98°C	5-10 seconds
Annealing	50–72°C*	10–30 seconds
Elongation	72°C	30 seconds/kb
Final Elongation	72°C	2 minutes

* The optimal annealing temperature was calculated for each primer pair.

3.2.11 Microscopy

Power density, exposure time and other key parameters are listed for each microscopy experiment in supplementary table 3. All imaging was done using either a Nikon N-SIM/N-STORM inverted fluorescence microscope (Figure 3.5) or a custom-built inverted microscope (otherwise).

Nikon N-STORM. Cells were illuminated with a 488 nm line from an Argon Ion laser (CVI Melles-Griot). A 100x TIRF objective (Nikon CFI Apochromat TIRF 100XC Oil) was used for imaging and an Andor iXon DU897 EMCCD camera was used, with a 1.5 x OptoVar (Nikon) and standard Nikon tube lens, giving an effective image pixel size of 106 nm/pixel. Cells were illuminated via HiLO inclined illumination to minimise background using an objective TIRF module (Nikon N-STORM module) using 488 nm laser excitation.

Custom microscope. Cells were illuminated with a 488 nm laser (Obis) and/or a 561 nm laser (Obis) as indicated. A 100x TIRF objective (Nikon CFI Apochromat TIRF 100XC Oil) was used for all experiments except microfluidic VerCINI measurements where a 100x silicone immersion objective (CFI SR HP Plan Apochromat Lambda S 100XC Sil, Nikon) was used for deep focusing. A 200 mm tube lens (Thorlabs TTL200) and Prime BSI sCMOS camera (Teledyne Photometrics) were used for imaging, giving effective image pixel size of 65 nm/pixel. Imaging was done with a custom-built ring-TIRF module operated in ring-HiLO33 using a pair of galvanometer mirrors (Thorlabs) spinning at 200 Hz to provide uniform, high SNR illumination.

3.2.12 Vertical Immobilization

Agarose microholes were created by pouring molten 6% agarose onto a silicon micropillar array. Patterned agarose was transferred into a Geneframe (Thermo Scientific AB-0577) mounted on a glass slide. The regions either side of the microholes were cut away, leaving a thin strip of agarose in the center of the Geneframe, to ensure sufficient oxygen. Cells at OD600~0.4 were concentrated 100x by centrifugation. 4 µL of sample was then loaded onto the agarose pad and a cover slip was placed on top.

FtsZ dynamics were imaged at either 1 frame/s for 2 mins at 1.8 W/cm^2. VerCINI experiments were performed on cells in a *Δhag* mutant background, preventing undesirable cell rotation within the microholes by disabling flagellar motility. As a further control, immobilised cells were imaged in brightfield to ensure cells were not rotating within the agarose chambers.

3.2.13 Data analysis – vertical microhole imaging.

Images were corrected for translational drift using the Fiji *StackReg* plugin. Cropped region of interest movies containing single in-focus cells were manually selected and exported for analysis. Each field of view (FOV) was compared to its brightfield counterpart to ensure each cell selected was not freely rotating. Tilted Z-rings were also excluded. Kymographs were automatically calculated along the circumference of individual Z rings using a custom MATLAB script. The best fitting circle for each Z ring was identified by least squares fitting, and the intensity around the circumference of the ring calculated with sub-pixel precision by bicubic interpolation. FtsA and FtsZ filament speed was measured manually by kymographs analysis, annotating filaments as lines in ImageJ and measuring the angle via an ImageJ script.

3.3 Results

Prior to the collaboration described in chapter 2, our lab used *B. subtilis* 168 CA as the genetic background in which our experiments were conducted. However, due to the fact that collaborators used *B. subtilis* PY79, experiments were carried out in this background for the sake of continuity. Thus, following its completion it was desirable to backcross these strains into *B. subtilis* 168 CA. Initially, we thought that we were imaging bAB185, a strain which expressed an mNeonGreen-FtsZ fusion protein as the sole source of FtsZ in the cell. Instead, we discovered we were imaging bAB167, a strain expressing an FtsA-mNeonGreen fusion protein due to an inadvertent shipping error from our collaborators.

This error was first highlighted when the dynamics of mNeonGreen-FtsZ were imaged following introduction into wt *B. subtilis* 168 CA. As bAB185 is a markerless strain, we used the parental strain bAB181, which still contained the resistance cassettes, in order to introduce this construct into *B. subtilis* 168 CA via a backcross. Following the successful transformation, the strain was then imaged and it was here the first problems with the strains were highlighted.

When the dynamics of the fluorescently tagged protein in this strain were imaged, a dramatic difference was observed from the previous results. In the previous chapter, we established that the Z-ring is composed of multiple, short FtsZ filaments which move bi-directionally around the division plane. Initially, this was done using a well characterised strain expressing an FtsZ-GFP construct capable of functioning as the sole source of FtsZ in the cell, though the strain displays a temperature sensitive phenotype at 45^{o}C[135]. We found that this motion is due to FtsZ filament treadmilling[1]. Furthermore when we imaged what we thought was *B. subtilis* PY79 mNeonGreen-FtsZ (bAB185) but which we now know was FtsA-mNeonGreen (bAB167) using the vertical immobilisation technology, we also observed multiple filaments treadmilling bi-directionally.

In contrast, when I imaged the bAB181-derived mNeonGreen-FtsZ strain in *B. subtilis* 168CA, filament dynamics were dramatically altered. Rather than observing clear processive movements, the majority of the filaments were static (Figure 4.1B).

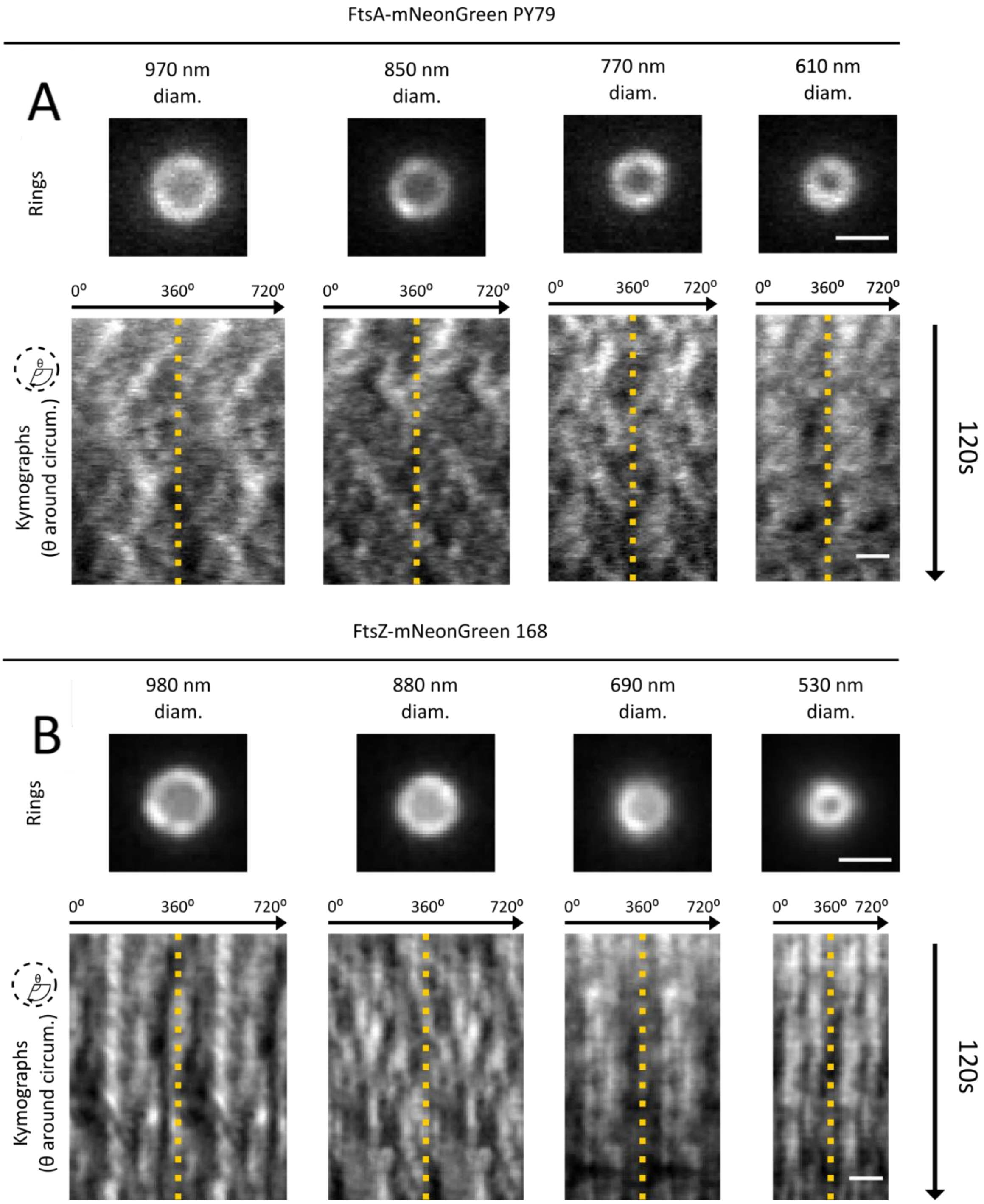

Figure 3.1: mNeonGreen-FtsZ filaments appear immobile at the division site. (A) FtsA filaments move progressively around the division site. Initially we were under the impression that we were imaging strain bAB185 (and thus the dynamics of mNeonGreen-FtsZ. However, it was later revealed that we were imaging FtsA-mNeonGreen (SH41 [*ftsAZ::mNeonGreen-15aa-ftsA-ftsZ-FtsAZ, Δhag::aph (kan)*]) was imaged instead. **(B)** mNeonGreen-FtsZ filaments (SH74 [*trpC2, ftsAZ:: ftsa-mNeonGreen-15aa-ftsZ-ftsAZ, Δhag::aph(kan)*]) are frequently observed as immotile at the division site. Kymographs were obtained by fitting septal images to circles and plotting intensity values around the circumference of the cell for each frame of the time-lapse (1 frame/ s). Two full revolutions around the cell (0-720º) are plotted side-by-side in each kymograph to resolve filament trajectories that pass 0º/360º, separated by yellow dotted lines.

In order to make sense of these confusing results, I conducted Western blots to determine the actual fusion protein we were observing using antibodies raised against FtsZ. Wildtype *B. subtilis* PY79 and SH33 (the well characterised stain expressing FtsZ-GFP[135] backcrossed into *B. subtilis* 168 CA) were used as controls and we requested that we be resent bAB185 to directly compare to the strain under question. I found that in the original experiments, the strain which we thought was bAB185 did not possess an FtsZ fusion protein (Figure 3.2A). The most natural conclusion was that we had been imaging FtsA-mNeonGreen instead, and thus a PCR was performed using primers that annealed within the FtsA construct, and based on band sizes we conclude that this is the case (Figure 3.2B). Primer pair oCJ154 and oCJ93 was used to amplify from the start of mNeonGreen to the end of FtsA resulting in a predicted band size of ~1.3kbp. Additionally oCJ154 and oCJ95 were used to amplify from the start of mNeonGreen to the end of FtsZ to give a predicted band size of ~2.5kbp.

It is also important to note that regardless of the inadvertent strain swap, it was also believed that bAB185 was a single copy replacement. However, the western blots indicated that that mNeonGreen-FtsZ was actually present as a minor speices in the cell. Thus I performed western blots on all strains we had used that possessed an FtsZ-fusion (bAB181, bAB185, bAB229, bGS31 -Figure 3.2D). However, I found the same pattern for these strains too - that mNeonGreen-FtsZ fusion proteins are expressed alongside wt FtsZ at low levels.

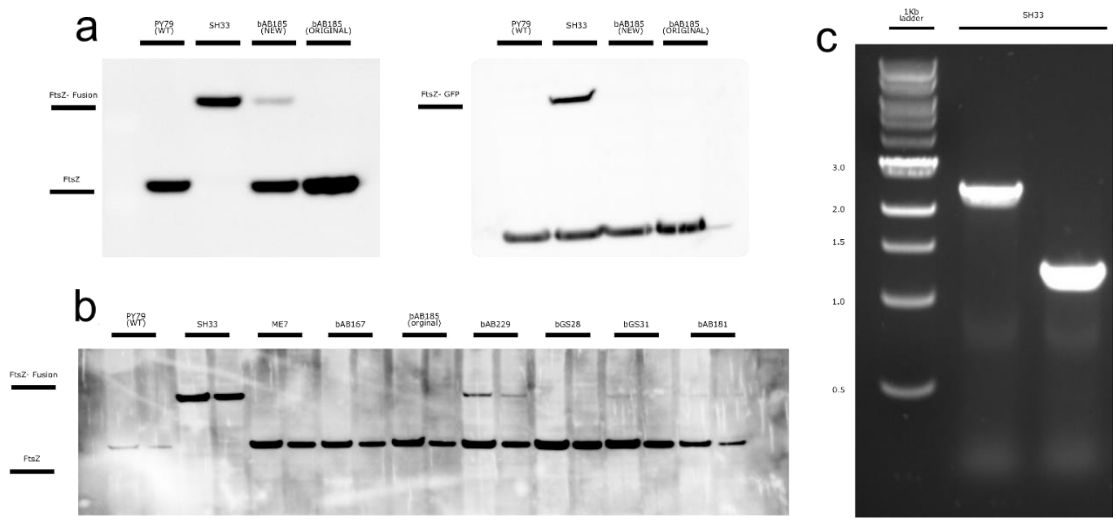

Figure 3.2: Characterisation of fusion proteins (A-B) Western blots of fluorescent fusion proteins used in this study 20 µL Lysate of SH130 was blotted alongside PY79. SH33 [*trpC2, ftsZ:: ftsZ-GFP::cat, Δhag::aph(kan)*], bAB185(new) [*trpC2, ftsAZ:: ftsa-mNeonGreen-15aa-ftsZ-ftsAZ*], bAB185 (original) [*ftsAZ::mNeonGreen-15aa-ftsA-ftsZ-FtsAZ*] . Genotypes of strains used in Western blot **(B)** can be found in Supplementary Table 1. Samples were incubated with specific polyclonal antibodies for FtsZ and or GFP. Bands were visualised by a chemiluminescence system. Lower bands of the GFP Western Blot are due to non-specific binding, a known problem with this particular antibody **(C)** Gel electrophoresis of amplified DNA fragments from that the “original bAB185” (SH33) as actually “bAB167” (SH41) [*ftsAZ::mNeonGreen-15aa-ftsA-ftsZ-FtsAZ*].

Due to these conflicting results, key strains were sent for whole genome sequencing which revealed that strains expressing FtsA and/or FtsZ fusion proteins at the native locus produced in the previous study had undergone a duplication event (Figure 5.3)[2]. As such, these strains expressed two copies of the FtsAZ operon. One of these operons was wt, while the second contained a fusion protein construct.

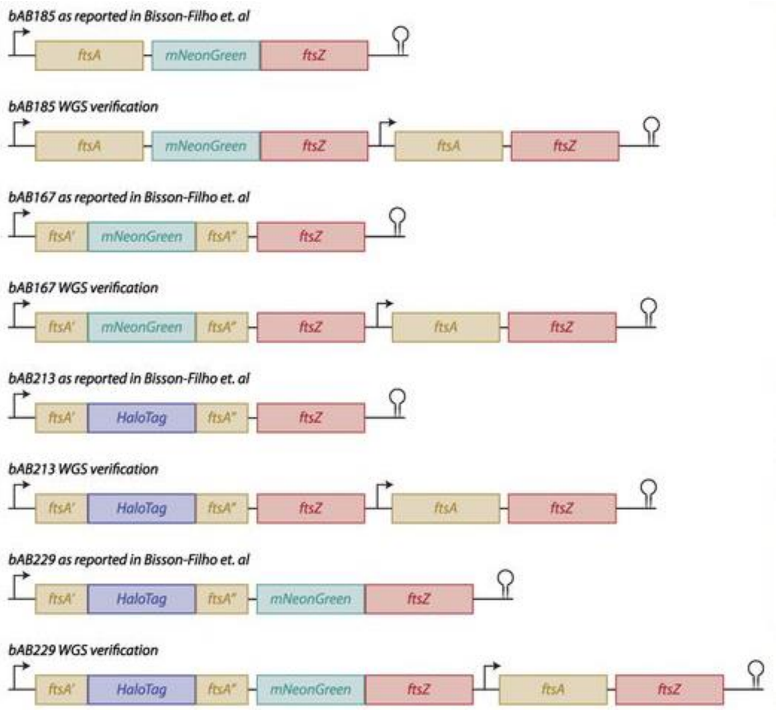

Figure 3.3 Multiple copies of ftsAZ detected by Illumina and Nanopore whole-genome sequencing. Reproduced from [224].

Thus in order to assess the functionality of the mNeonGreen-FtsZ and FtsZ-mNeonGreen fusion proteins, our collaborators assessed whether these fusions were capable of replacing their native counterparts in depletion strains (Figure 3.4A). The native FtsAZ operon was put under the control of the P_{xyl} promoter while a second copy containing either the FtsA-mNeonGreen or mNeonGreen-FtsZ fusion was integrated at *amyE*. It was observed that the mNeonGreen-FtsZ was unable to complement native FtsZ, although FtsA-mNeonGreen was able to complement its native counterpart. Historically, FtsA and FtsZ fusion proteins have been expressed as dilute labels alongside their wildtype versions due to the difficulty in creating functional replacements. As such, our collaborators also assessed whether dynamics of FtsA and FtsZ were affected by the duplication event.

To test if the duplications affected treadmilling speeds, our collaborators created different merodiploid strains which contained a second copy of the *ftsAZ* operon which contained fusion proteins (Table 3.1). These merodiploid strains were able to assemble competent Z-rings. Cells lengths of all of these strains were comparable as were treadmilling rates of both FtsA and FtsZ (Figure 3.4B and 3.4C)

Table 4: Mixed expression strains used to check the dynamics of treadmilling filaments

Strain	Genotype	Reference
bWM4	*amyE::erm-Phyperspank-ftsA- mNeonGreen(M10S)-15aa(v2)-ftsZ(opt)*	[2]
bAB431	*amyE::erm-Phyperspank-ftsA- msfGFP(SW)-ftsZ*	[1]
bAB434	*amyE::erm-Phyperspank-ftsA-msfGFP(SW)- ftsZ* *ftsAZ::cat-Pxyl-ftsAZ*	[2]
bAB229	*ftsAZ::erm-ftsA-HaloTag(SW)-mNeonGreen- 15aa-ftsZ-cat*	[1]
bAB429	*amyE::erm-Phyperspank-ftsA- Trunc_mNeonGreen(SW)-ftsZ*	[2]
SB168	*amyE::ftsAZ-cat::ftsA-gfp-ftsZ-kan*	[243]
bAB213	*ftsA::erm-ftsA-HaloTag(SW)-cat*	[1]
AH175	*thrC::Pspac-YFP-ftsZ-erm*	[244]
bAB185	*ftsAZ::ftsZ-mNeonGreen-15aa-ftsZ-fstAZ*	[1]
bAB167	*ftsAZ::ftsA-mNeonGreen(SW)-ftsAZ*	[1]
bAB221	*Native mNeonGreen-15aa-ftsZ* *amyE::erm-Physpank-ftsA-15aa-mNeonGreen- ftsZ*	[1]
bWM4	*amyE::erm-Phyperspank-ftsA- mNeonGreen(M10S)-15aa(v2)-ftsZ(opt)*	[2]

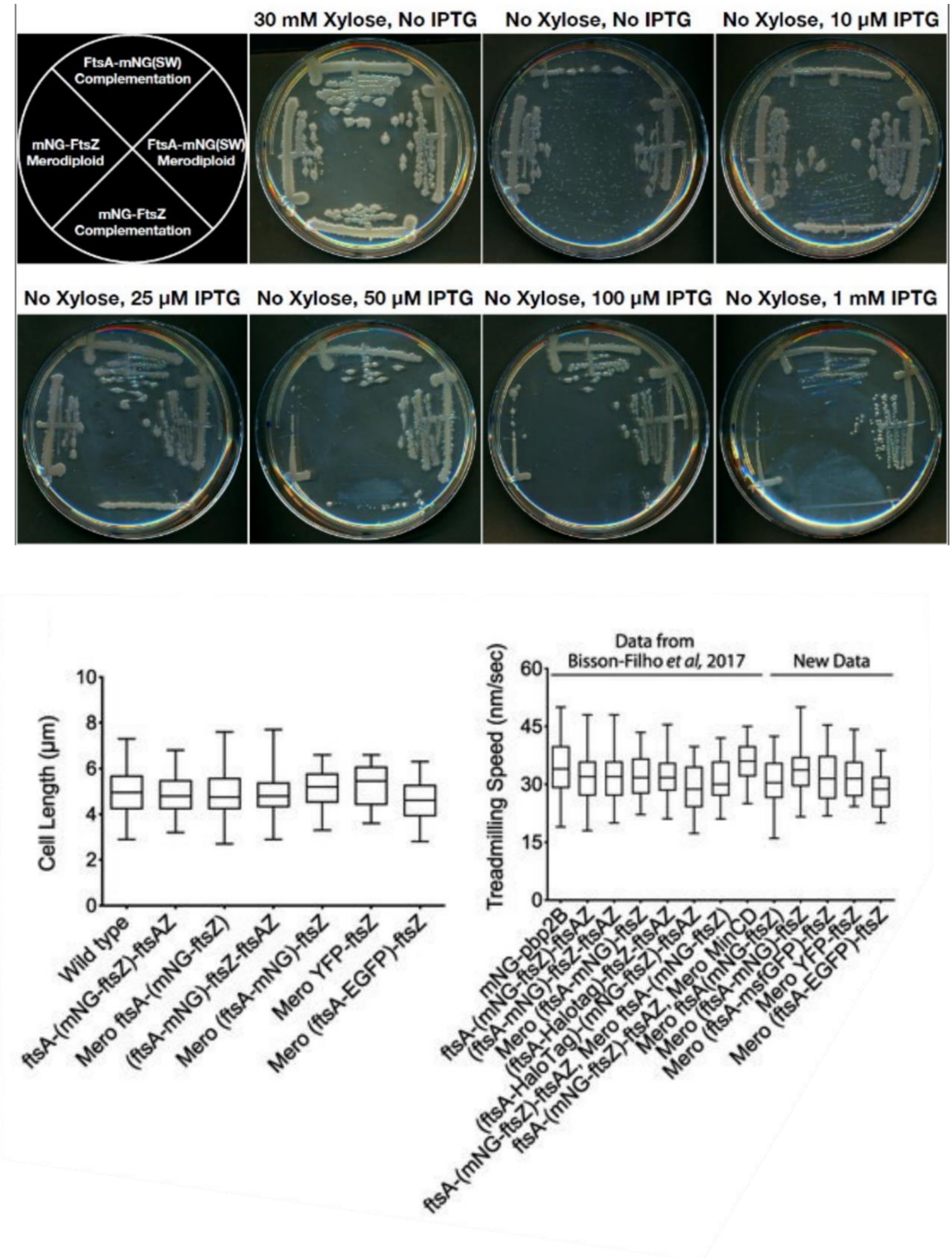

Figure 3.4: Characterisation of mixed expression strains. (A) complementation assay **(B)** Box plots from cell length distributions from duplication and merodiploid strains. **(C)** FtsAZ filament (and PBP2B single molecule) speeds present robust measurements across different strains despite the presence of the tagged divisome protein and fluorescent protein of choice. Strains used for measurements from Bisson-Filho et al. (2017) (left) and new data collected with different FtsAZ fusions from the literature (right). Reproduced from[224].

Due to the fact that mNeonGreen-FtsZ construct is unable to support native growth, we concluded that it was more desirable to use the FtsZ-GFP fusion protein previously established by Petra Levin and co-workers as this is able to replace FtsZ as the only source in the cell. We also decided to switch to using *B subtilis* PY79 as the genetic background for experiments. As such, SH13 (*trpC2, ftsZ::ftsZ-gfp-cat*) was backcrossed into SH211 (PY79 Δ*hag*), a strain of PY79 with a markerless *hag* knockout to prevent cell rotation in the microchambers. Thus, further characterisation was performed on the resulting strain SH130 *(PY79* Δ*hag ftsz::ftsz-gfp)*. Cell morphology analysis showed a mild elongation phenotype at 30°C and 37°C in both minimal and rich media conditions although growth rate was not impaired at either temperature. (Figure 3.5A-B). Correct integration was determined by PCR. Primer pairs (oCJ94 and oCJ95) were used to amplify a fragment from the end of FtsA to the end of FtsZ resulting in predicted band size of ~1.2kB. An additional primer pair (oCJ94 and oCJ06) were used to amplify from the end of FtsA to the end of GFP giving a band size of approximately 1.5kb (Figure 3.5C). Primers oCJ300 and oCJ301 were used to confirm deletion of *hag* (Figure 3.5D).

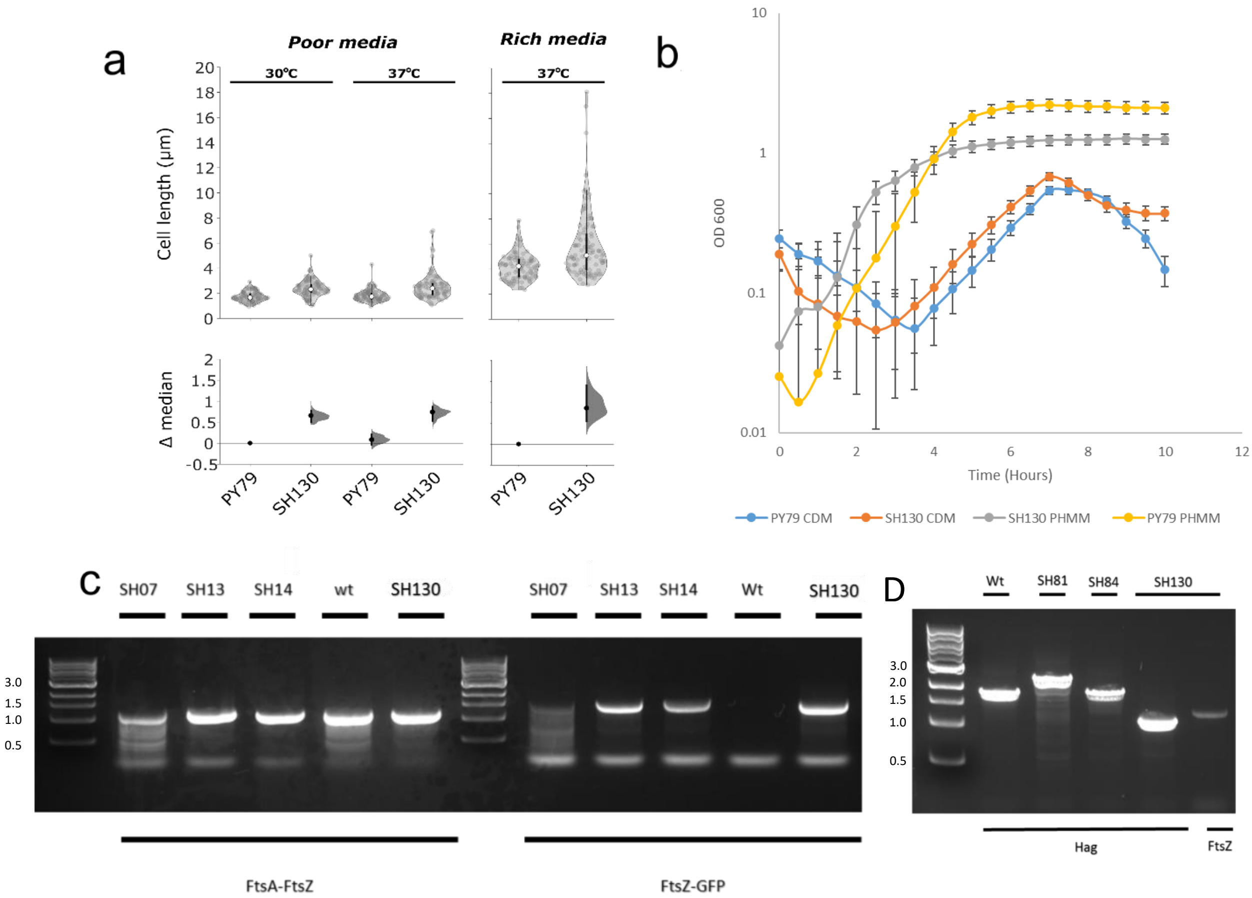

Figure 3.5: Characterisation of SH130 FtsZ-GFP (A) Cell length controls for SH130 in different growth conditions. The cell length of SH130 was measured by microscopy in different growth conditions and compared to PY79. Cells were grown in poor (CDM) or rich media (PHMM) at the indicated temperature. Violin plots: white circles, median; thick black lines, interquartile range; thin black lines, 1.5x interquartile range. DABEST plots: black circle, median difference between indicated conditions; black lines, 95% confidence interval of median difference. **(B)** Growth curves of strains under different growth conditions. Growth was monitored for 8 hours using a FluoStar plate reader (BMG Labtech) at the indicated temperature. Average values and standard deviations of triplicate repeats are plotted. Mutant strains grown in rich media (PHMM) at low and high temperatures compared to wild-type (PY79). **(C&D)** Gel electrophoresis confirming the correct integration of FtsZ-GFP in SH130 **(C)** and successful deletion of hag **(B).**

3.4 Discussion

Following the work described in the previous chapter, it became evident that there were a number of issues regarding the strains used to imagine the dynamics of FtsZ and FtsA. Originally we thought that microscopy experiments conducted in the previous chapter were done using single copy replacements of FtsZ or FtsA. This was the case for experiments done using a well-established FtsZ-GFP fusion protein[135], which subsequent Western blots confirmed was the sole source of FtsZ in the cell (Figure 3.1A). However we found multiple issues with other strains used in the study.

After investigation we concluded that our microscopy experiments of FtsZ dynamics in vertical cell immobilized cells were actually measurements of FtsA dynamics. We also found that all strains expressing FtsA and FtsZ fusion proteins at the native locus used in the study contained a duplication event led to these strains expressing two copies of the FtsAZ operon, one wildtype and one with the respective fusion protein. Our collaborators investigated whether the mNeonGreen-FtsZ and FtsA-mNeonGreen fusions were able to compliment native depletions. While cells were able to grow when expressing FtsA-mNeonGreen as the sole source of FtsA in the cell, cells expressing mNeonGreen-FtsZ were not viable in the absence of wildtype FtsZ. Control experiments were conducted to confirm that none of the conclusions of the published work were affected by these issues, and a correction confirming this conclusion has now been published[2]

FtsZ is a notoriously difficult protein to create a functional fusion protein of. Historically, live cell imaging of FtsZ has been achieved the exogenous expression of an FtsZ fusion protein as a dilute label alongside wildtype FtsZ[245]. However, Levin *et al.*[135] succeeded in creating a functional *ftsz-gfp* which could be incorporated into the genome, replacing the *ftsZ* gene. Later, Strauss *et al.* created a similar FtsZ fusion protein which they used to perform SIM imaging at 30^{o}C[113]. A functional FtsZ-GFP fusion was also created for *S. penumoniae* which was capable of acting as the sole source of FtsZ in the cell, which was subsequently followed by the development of a fully functional FtsZ-spDendra2 fusion protein [246,247]. However, in *E. coli* an FtsZ-GFP fusion protein is only capable of being expressed as a dilute label [120,248]. Although an FtsZ-YFP fusion protein has been developed that is able to function as the sole source of FtsZ in *E.coli* this is only possible following the generation of a suppressor mutation somewhere in genome [249]. Due to the fact that FtsZ's N-terminal contains the nucleotide binding pocket, it is not surprising that an N-terminal mNeonGreen-FtsZ fusion protein is unable to support native deletion. However, the exact cause of this fusion protein being non-functional is unclear as mNeonGreen-FtsZ is evidently able to localise and polymerise alongside wt FtsZ.

The Western blots that I performed indicate that the mNeonGreen-FtsZ fusion protein is expressed at much lower levels when compared to its wildtype counterpart in the duplication strain (bAB185), consistent with previous reports of the ability to express an non-complementary FtsZ fusion protein as a dilute label without obvious defects to the cell [248]. Thus this suggests mNeonGreen FtsZ- is able to act as a benign sub-stoichiometric marker, but at high concentrations it inhibits cell division.

Within the kymographs for mNeonGreen-FtsZ, the majority of filaments appear static, with only a minority treadmilling that are very difficult to distinguish. Although this is in apparent contradiction to our collaborators' results in which they determine that mNeonGreen-FtsZ is still capable of robust treadmilling, this is largely due to the method of measurement. Our collaborators measured the treadmilling dynamics of mNeonGreen-FtsZ using TIRF microscopy. As such, this limits measurements to the earliest Z-rings, that is diffuse nascent rings[1]. Static filaments are exceptionally difficult to distinguish via this method, as one would not know whether filaments are actually static, or if the ring is too dense to observe clear treadmilling. As such, this inherently biases the measurement to static motile filaments. The presence of FtsZ filament treadmilling in the bAB185 FtsZ-mNG(mero) strain has been independently confirmed by TIRF microscopy by another lab member (data not shown).

Characterisation of strains expressing FtsZ-GFP revealed only a mild elongation phenotype at 30^{o}C and 37^{o}C in both minimal and rich media conditions. However growth rate was not impaired in either media in either conditions. Gel electrophoresis confirmed the correct integration of the construct when introduced via a backcross and Western blots showed that FtsZ-GFP is expressed as the sole source of FtsZ in the cell. Due to the fact that FtsZ-GFP can support cell division as the sole cellular source of FtsZ with only a mild phenotype, it was decided to use this strain for future experiments.

3.5 Conclusions

In this chapter, I investigate and describe a number of issues with strains used in the previous chapter. Initially we were under the impression that all single colour strains imaged in the previous chapter were FtsZ- fusions. While this was true for FtsZ-GFP, an error lead to us imaging FtsA-mNeonGreen instead of mNeonGreen-FtsZ. Importantly, with the exception of FtsZ-GFP, the strains imaged in the previous chapter had undergone a duplication event, meaning they expressed two copies of the FtsAZ operon, one wildtype and the other with the respective fusion proteins. Collaborators also discovered that mNeonGreen-FtsZ was unable to support native depletion. While these results did not affect the overall findings[2], it was decided to use the sole copy FtsZ-GFP fusion going forward.

Chapter 4 : Development and Optimisation of Vertical Cell Imaging by Nanostructured Immobilisation (VerCINI) .

4.1 Introduction

FtsZ dynamics are difficult to observe *in vivo* and while TIRF is a useful tool for increasing SNR, the fact it only illuminates a thin slice of the septum limits observations to partial snapshots of filament dynamics in nascent Z-rings [209,210]. In the previous chapters a prototype approach of vertically immobilising rod shaped cells in nanofabricated chambers was developed, allowing continuous imaging of the entire division septum to overcome this problem. This allowed FtsZ filaments to be tracked around the entire division site even in dense, actively constricting rings. Implementing this method allowed us to discover that the Z-ring is composed of multiple short filaments that move bi-directionally around the division plane even during active constriction. Together with collaborators we found that FtsZ filaments treadmill, with GTP hydrolysis setting the rate of FtsZ depolymerisation and thus overall treadmilling speed [208–210].

However, the exact role of FtsZ treadmilling in cell division is uncertain. In *B. subtilis*, it was observed that perturbations to FtsZ treadmilling rate affected both the rate of constriction and the speed of individual septal cell wall synthases[209]. This lead to a model being proposed in which cell division was the result of a tightly coupled synthase-filament complex where FtsZ filaments act as obligatory guides and the rate limiting step for septal cell wall synthesis[209]. However, in *S. aureus* FtsZ treadmilling is dispensable following the initiation of constriction[223]- an interesting observation given that both of these organisms belong to the same phylogenetic class. While this may potentially represent a genuine difference between species, there may be a common mechanism where FtsZ treadmilling plays different roles in different stages of the cell cycle. Thus, it becomes desirable to measure how FtsZ dynamics alter across different stages of the cell cycle. Though the prototype vertical immobilisation technology described in the previous chapters was promising, it suffered from low signal, fast photobleaching and lacked the throughput required for cell cycle studies. As such, this prevented us from imaging FtsZ dynamics in nascent rings as their diffuse distribution of sparse filaments around the division site makes them inherently dim.

Thus, we entirely redesigned the vertical immobilisation method and workflow to address these issues. The new method allows ultrasensitive high-resolution imaging of FtsZ filament dynamics at all stages of the cell cycle, and this optimised method is now referred to as

VerCINI (Vertical Cell Imaging by Nanostructured Immobilisation). New features of the method include a high-throughput chip design, centrifugation loading, high SNR ring-HiLO illumination [250], imaging denoising[251], and custom septal localisation and background subtraction algorithms. This allowed extended time-lapse imaging of Z-rings over longer time scales, granting a more in depth view of filament dynamics within the ring. However, the major advantage of these optimisations was that it allowed the dynamics of FtsZ filaments within nascent Z-rings to be imaged, thus allowing us to image FtsZ dynamics across different stages of the division cycle.

4.2 Materials and Methods

4.2.1 Culture growth for vertical microhole immobilization

Strains of *B. subtilis* to be imaged by vertical microhole immobilization were streaked from -80°C freezer stocks onto LB agar plates and grown at 30°C overnight. Single colonies were transferred in liquid cultures of TLM and grown with agitation at 200rpm overnight at 30°C. The following morning TLM starter cultures were diluted into pre-warmed CDM to a starting OD_{600} ~ 0.1, grown at 30°C until reaching the appropriate ~0.4 OD_{600}.

4.2.2 Membrane Stain

SH130 cultures were prepared for imaging in CDM as described above. Once the cultures had reached OD_{600} 0.4-0.5, Nile Red was added to 200µl of cells to a working concentration of 1 µg/ml, and incubated at growth temperatures for 5 mins, and loaded onto into agarose microchambers as described in the optimized VerCINI loading below.

4.2.3 Microscopy.

Power density, exposure time and other key parameters are listed for each microscopy experiment in supplementary Table 1.3.

4.2.4 Original vertical immobilization experiments

Cells were imaged on a Nikon N-STORM inverted fluorescence microscope equipped with an NA 1.49 Nikon 100x TIRF objective, laser source (488 nm), additional 2.5x magnification optics and a 16 µm pixel Andor iXon DU897 EMCCD, giving a final pixel size at the image plane of 64 nm. Cells were illuminated via widefield or HilO, the latter of which was used to minimize background using an objective TIRF module (NIKON N-STORM module) using 488 nm laser excitation.

4.2.5 VerCINI imaging

Cells were imaged on a custom microscope with cells illuminated by a 488 nm laser (Obis) or a 561 nm laser (Obis) as indicated. A 100x TIRF objective (Nikon CFI Apochromat TIRF 100XC Oil) was used for all experiments except microfluidic VerCINI measurements where a 100x silicone immersion objective (CFI SR HP Plan Apochromat Lambda S 100XC Sil, Nikon) was used for deep focusing. A 200 mm tube lens (Thorlabs TTL200) and Prime BSI sCMOS camera (Teledyne Photometrics) were used for imaging, giving effective image pixel size of 65 nm/pixel. Cells were imaged using widefield, HiILO or ring-HilO as indicated. In order to achieve ring-Hilo a custom-built ring-TIRF module was operated in ring-HiLO [250] using a pair of galvanometer mirrors (Thorlabs) spinning at 200 Hz to provide uniform, high SNR illumination.

4.2.6 VerCINI sample preparation

Agarose microholes were created by pouring molten 6% agarose onto a silicon micropillar array. Patterned agarose was transferred into a Geneframe (Thermo Scientific AB-0577) mounted on a glass slide. The regions either side of the microholes were cut away, leaving a thin strip of agarose in the center of the Geneframe, to ensure sufficient oxygen.

4.2.7 Optimized loading

Cells at OD600 ~ 0.4 were concentrated 100x by centrifugation and added onto the agarose pad. 20µL of cells were then loaded into the microholes by centrifuging the mounted agarose pad with concentrated cell culture in an Eppendorf 5810 centrifuge with MTP/Flex buckets. Non-trapped cells were rinsed off with excess media.

4.2.8 Image Acquisition

FtsZ treadmilling dynamics were imaged at 1 frame/s (continuous exposure) for 2 mins at 1-8 W/cm2. After each field of view was imaged, a multi-slice Z-stack was taken at 500nm intervals to exclude tilted or improperly trapped cells, in addition to excluding Z-rings that have an adjacent Z-ring 1µm above or below the imaging plane. VerCINI experiments were performed on cells in a Δhag mutant background, preventing undesirable cell rotation within the microholes by disabling flagellar motility.

4.2.9 Pre-processing

Videos were denoised using the ImageJ plugin PureDenoise[251], which is based on wavelet decomposition. Key assumptions of the method are (i) local spatiotemporal similarity within the image (ii) absence of sharp discontinuities, guaranteed by diffraction-limited nature of the image. The denoising algorithm does not make any assumptions on the type of underlying biological structure.

Denoised videos were registered using the ImageJ plugin StackReg[252]. Image stacks of vertically immobilised cells were inspected to exclude tilted cells or out of focus FtsZ-rings, or FtsZ rings where a second Z-ring was closer than 1 um to the focal plane. Cropped region of interest movies containing single in-focus cells were manually selected and exported for analysis. An ImageJ package for VerCINI data processing is available (https://github.com/HoldenLab/Ring_Analysis_IJ).

4.2.10 VerCINI background subtraction, kymograph extraction, quantification

Custom software for quantitative cytoplasmic background subtraction and kymograph extraction was developed by Dr Séamus Holden for analysis of VerCINI movies (https://github.com/HoldenLab/ring-fitting2). Fluorescence images of isolated vertical cells were fitted to a joint explicit model for diffuse out-of-focus cytoplasmic background (Gaussian + Cauchy model) plus septal protein signal, modelled as a 12 sectored annulus with each sector of variable amplitude.

$$F(x,y) = Signal(x,y) + Bg(x,y)$$

Signal is calculated in polar coordinates, around the septal ring centre fit parameter (x_0, y_0), and then transformed into Cartesian coordinates. Signal is defined as

$$S(r,\theta) = A_i(\theta)\exp\left(-\frac{(r-R_0)^2}{2\sigma^2}\right),$$

where $A_i(\theta)$ defines a 12 sectored ring. Background is defined as

$$Bg(x,y) = a\exp\left(\frac{-((x-x_0)^2+(y-y_0)^2)}{2\sigma_{bg1}^2}\right) + b\frac{\sigma_{bg2}^2}{(x-x_0)^2+(y-y_0)^2+\sigma_{bg2}^2} + c.$$

This explicit model allowed accurate sub-pixel location of a circular line profile at the septal leading edge. Explicit subtraction of complex background signal also allowed septal intensity quantification. The background subtracted intensity along the circular line profile was then calculated for each frame and automatically plotted as a kymograph. Kymographs were plotted over the [0,720°] ie two complete revolutions around the line profile for ease of visualization, specifically to allow straightforward visualization of motile filaments crossing the 360°,0° boundary. For each cell, the Z-ring diameter was determined from the fitted model in the kymograph extraction step. Median septal intensity was calculated as the median value of all kymograph pixels from the first 60 image frames.

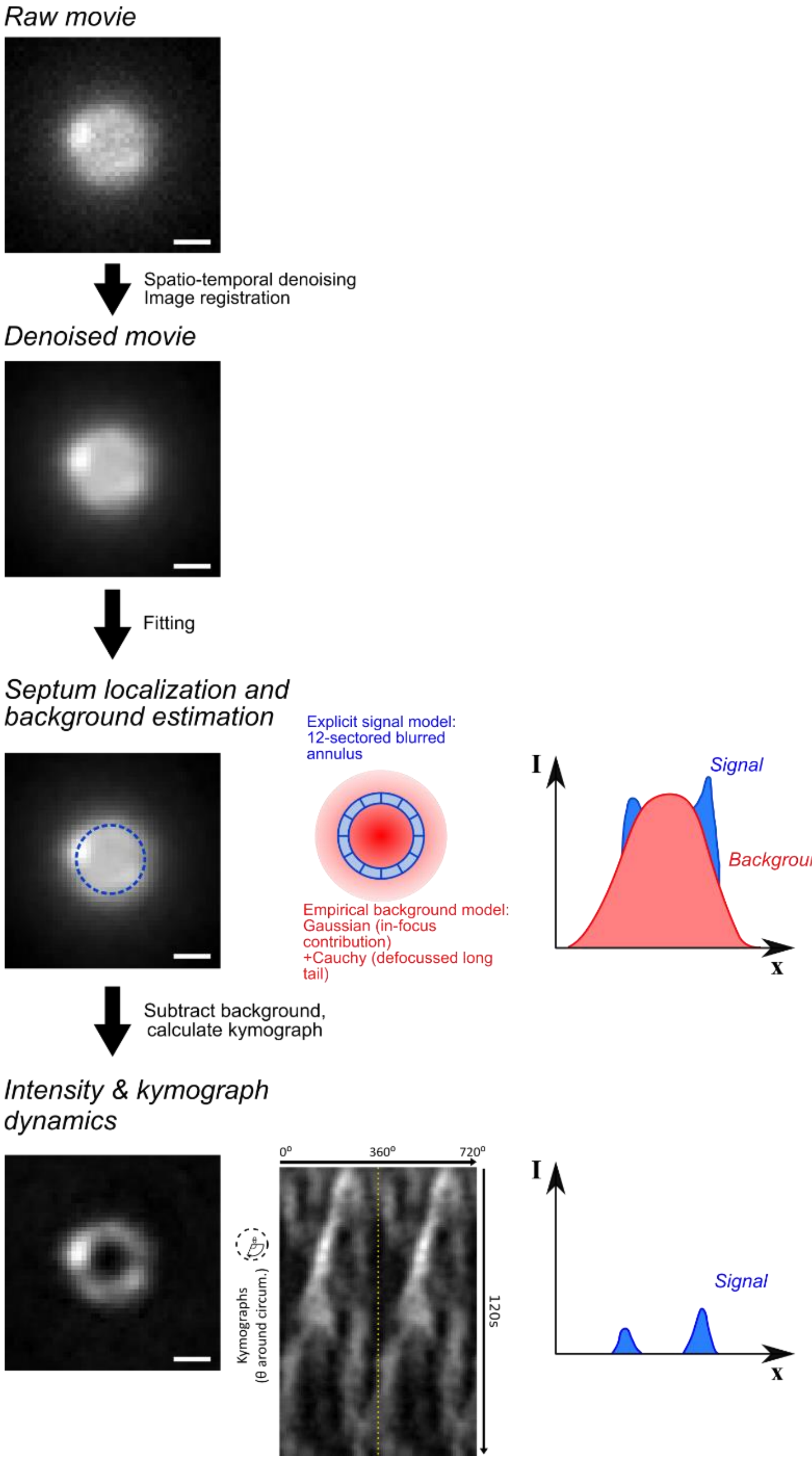

Figure 4.1: VerCINI image analysis workflow. Image processing of exemplar VerCINI data for FtsZ-GFP (SH130) strain. VerCINI movie is denoised and registered. Septal localisation is performed by fitting an explicit joint model of a multi-sector blurred annulus for localised signal, plus a mixed Gaussian Cauchy distribution for cytoplasmic background. Fitted background is then subtracted. Intensity around the fitted septal line profile is calculated to sub-pixel accuracy for each movie frame and plotted as a kymograph for further analysis. Scale bars 0.5 µm. Reproduced from [202].

4.2.11 FtsZ filament treadmilling analysis using VerCINI

We performed manual measurement of filament speed and processivity by kymograph analysis, annotating filaments as lines in ImageJ and then measuring the angle via ImageJ script. As the intensity range across kymographs is large, manual detection and analysis of filaments was aided by applying a ridge filter[253] to the kymograph which detects ridges in the image, independent of absolute intensity. The ridge filter consists of a Gaussian blur operation to set the feature scale and suppress noise (here 2 pixels, 130 nm), followed by calculation of the major eigenvalue of the Hessian matrix for each pixel, implemented as an ImageJ macro in the package listed above. Joint annotation of the ridge filtered and raw intensity kymograph was performed, allowing sensitive annotation of both bright and dim filaments.

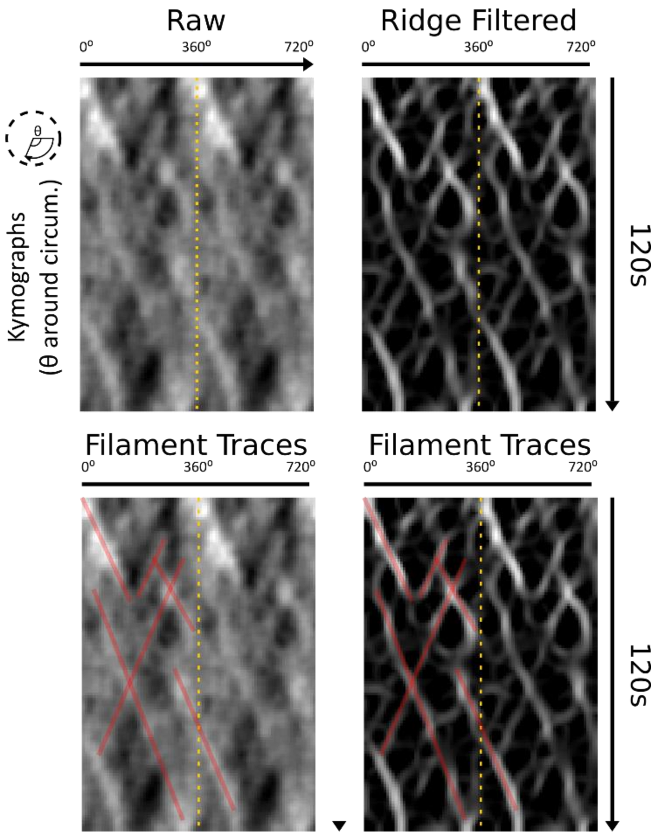

Figure 4.2: VerCINI FtsZ treadmilling dynamics analysis workflow. Ridge filter is applied to raw kymographs to detect filament trajectories independent of intensity. Filament trajectories are then manually traced with reference to both the raw and ridge-filtered kymographs; only filament trajectories clearly identifiable in both images were selected. Filament trajectories are exported, and filament speed, processivity and lifetime are calculated. Two full revolutions around the cell (0-720°) are plotted side-by-side in each kymograph to better show continuity of filament tracks as they pass 0°/360°, separated by yellow dotted lines. Red lines indicate all identified trajectories, shown only in the first of the two side-by-side kymographs. Reproduced from[202].

4.2. Results

4.2.1 Maximising the number of vertically immobilised cells in a single field of view

One of the major limitations of the prototype vertical immobilisation technology was the low throughput, as initially only an median of 6 cells per FOV (IQR=3-14, N=30 FOVs) were successfully immobilised (Figure 4.3). Thus it was desirable to increase the throughput in order to efficiently image FtsZ dynamics over different stages of the cell cycle. One of the first steps towards doing this was switching from an Nikon N-STORM inverted fluorescence microscope equipped with an Andor iXon DU897 EMCCD (electron multiplying charge-coupled device) camera to a custom built microscope with a Prime BSI sCMOS camera. The major advantage of this change is that the latter possess a 16x larger active pixel area. Though we crop down the FOV to ¼ size to ensure even illumination, this allows us to image a 4x larger FOV than previously. The use of an sCMOS camera also benefits from lower read noise, faster frame rate and higher dynamic range granting increased SNR[44].

A new silicon micropillar array was also designed by Dr Fabai Wu in which the micropillars possessed a range of diameters, in order to assess which diameters best facilitated loading of cells into microchambers, whilst being small enough to prevent movement of cells themselves. The initial silicon micropillars had a diameter of 0.8 µm and this proved to be inefficient for loading. As such, the new micropillar array had a range of diameters from 0.7 - 2.2 µm. Here, I assessed loading into different diameter microchambers to identify the micropillar widths that best facilitated loading (Figure 4.4). Time lapse videos were also taken to ensure that cells were indeed immobile within the holes. It was observed that micropillars with a width of 1.0-1.2 µm gave effective loading when compared to the previous incarnation of the microholes (Figure 4.3), but widths above this diameter resulted in cells moving within the holes. As such, a new array was etched by Dr Kevin Whitley so that all pillars would be 1.0-1.2 µm in width in addition to having the spacing between the pillars reduced. This combined with a camera capable of imaging a larger FOV allowed the successful immobilization of a median number of 50 cells per FOV (IQR= 31-58, N=30 FOVs) (Figure 4.3).

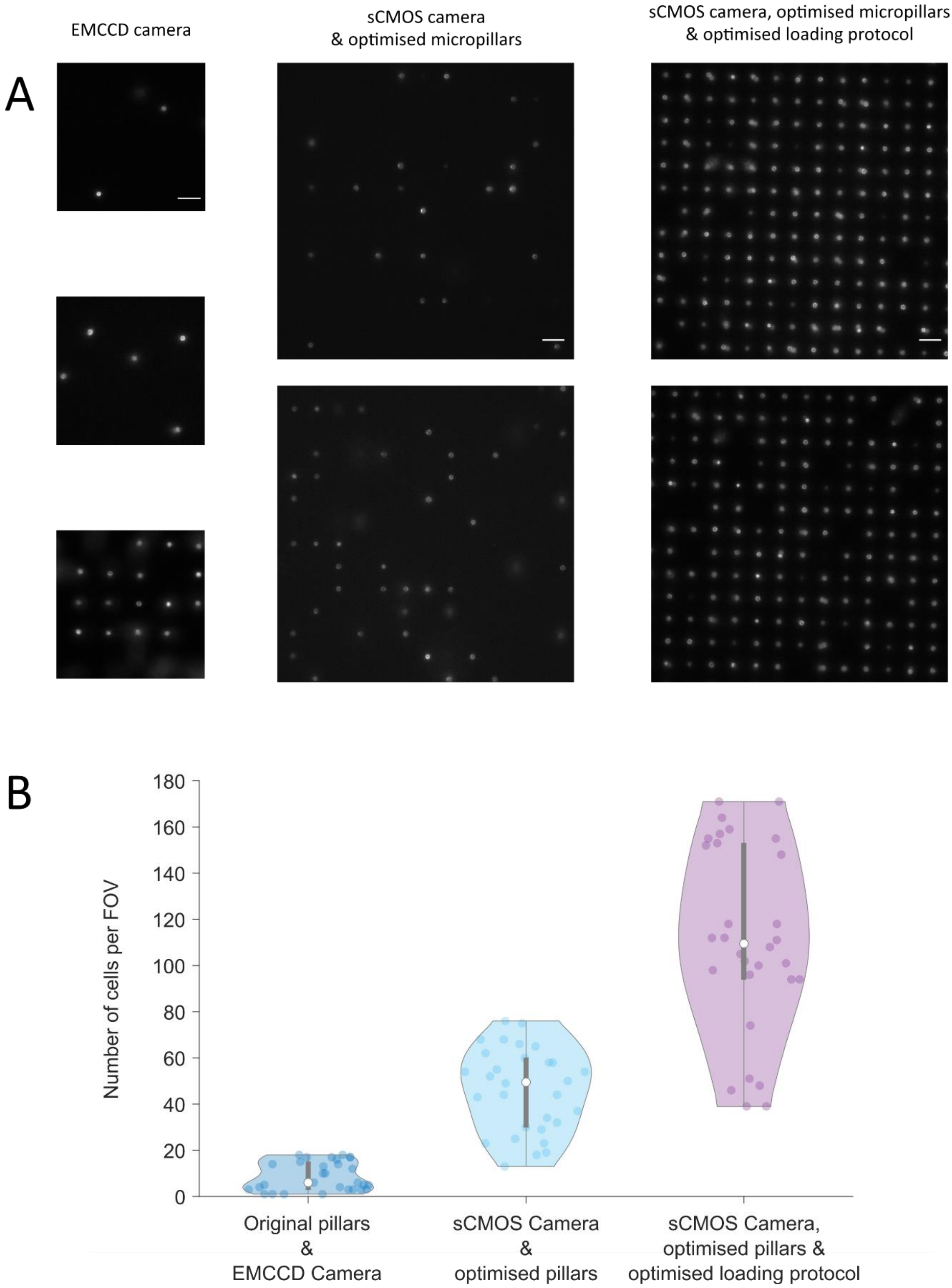

Figure 4.3: Quantification cell loading during the optimisation process. (A) Representative epifluorescence images of cells per FOV during different stages of method optimisation. The prototype microholes resulted in low numbers of cells fer FOV (left), optimising the micropillar width and using a camera capable of imaging a 4x larger FOV increased the bumber of cells per FOV. Optimising the loading process via centrifugation further increased the number of cells per FOV. **(B)** Quantification of cells per FOV. Violin plot: white circles, median; thick grey lines, interquartile range. Scale bar 5 µm.

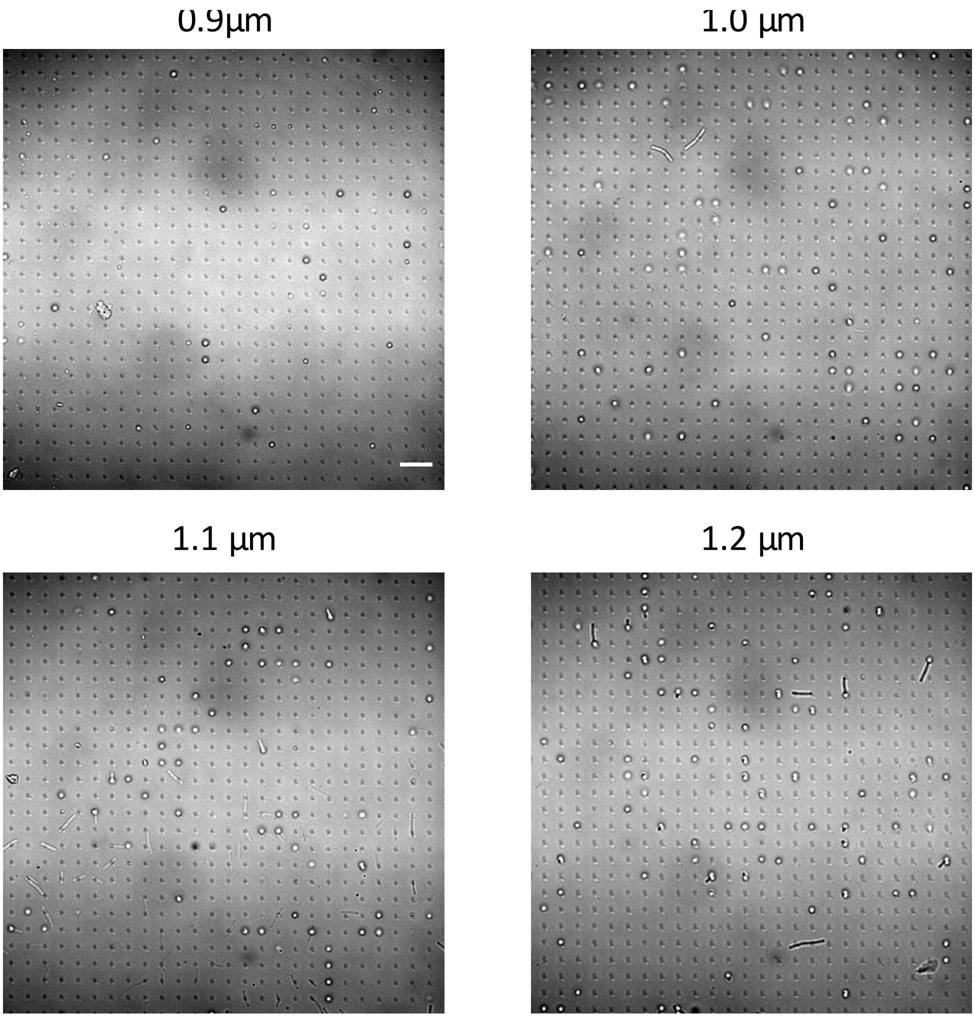

Figure 4.4: **Determination of the optimum micropillar diameters.** Representative brightfield images of cell loading into microchambers with different diameters. Scale bar 5 µm.

I developed and characterized a new loading VerCINI cell loading protocol which greatly increased loading efficiency of cells into the microchambers. Initially the samples were prepared by pouring 6% molten agarose onto the silicon pillar array. Once set, the patterned agarose was mounted onto a glass slide, with the edges of the agarose cut away to ensure sufficient oxygenation. After the cultures in CDM had reached OD_{600} ~0.4-0.5, they were pelleted and concentrated 100x and 4 µL was then loaded on top of the sample. A glass coverslip was then placed on top with the aim of forcing cells into the microchambers. However, this method of loading was extremely temperamental. Thus the approach was changed to centrifuge cells into the microholes. Cells were concentrated 100x in 20 µL and pipetted onto the patterned agarose pad. The sample was then secured onto a 96 well adapter, and covered loosely with a plastic coverslip to prevent the agarose pad from drying out. The sample was then centrifuged at 3200 g for 5 mins. Initially at this point, the plastic coverslip was removed and immediately replaced with glass coverslip and the sample sealed. However, it was observed that the 5 minute centrifugation resulted in the culture drying atop the pad. When imaged this resulted in a significant amount horizontal cells lying a top the agarose pad, obscuring the cells below (Figure 4.5). Thus if imaged with fluorescence microscopy this would degrade image quality of the vertical cells. For this reason, an extra step was included in which the agarose pad would be washed with fresh media. A complete diagrammatic representation of the VerCINI sample preparation can be seen in Figure 4.6. Taking all of the optimization steps into consideration (camera with a larger FOV, optimized micropillar array and centrifugation loading protocol), this resulted in the median number of cells successfully vertically immobilized increasing to 115 cells per FOV (IQR= 95-152, N=30 FOVs).

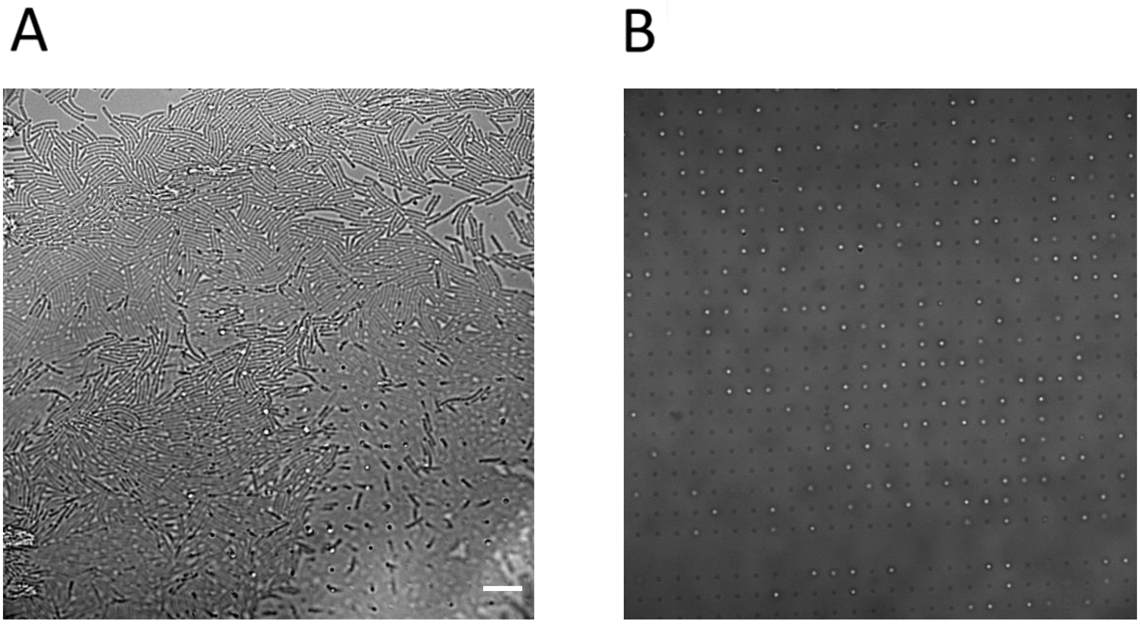

Figure 4.5: Rinsing the sample is imperative following centrifugation loading. (A) When the sample is centrifuged for 5 mins, the cultures dries atop the agarose pad causing cells horizontal cells to obscure vertically trapped cells. **(B)** Rinsing the agarose pad with fresh media is successfully able to remove horizontal cells. Scale bar 5 µm.

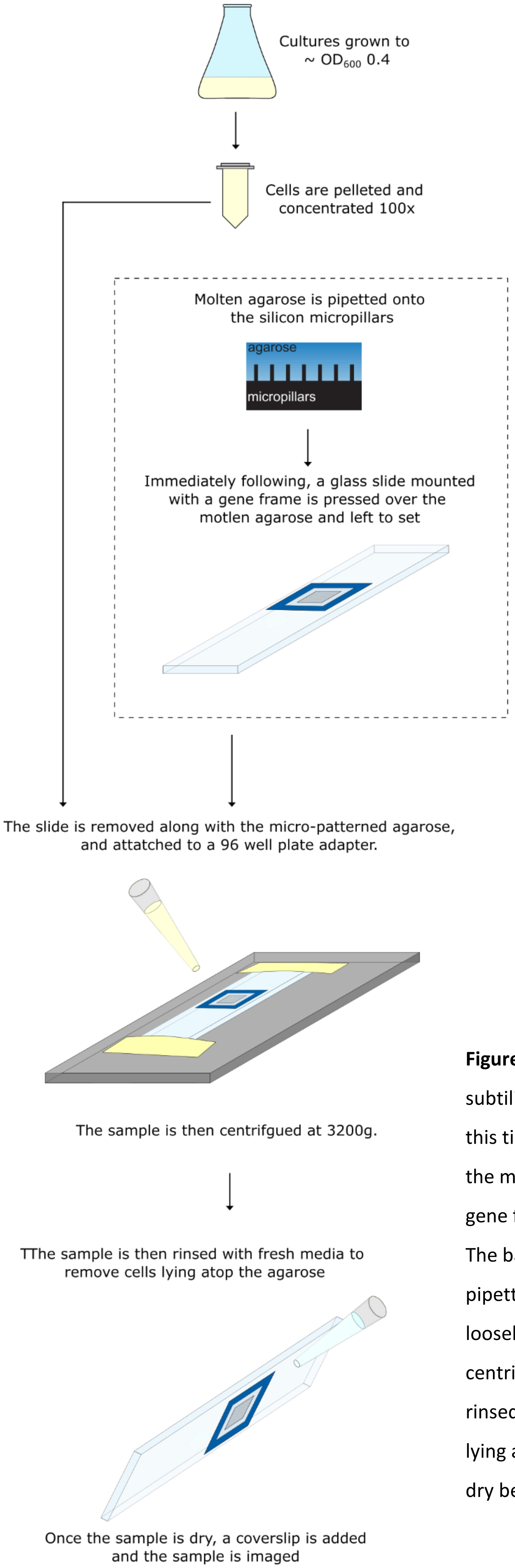

Figure 4.6: VerCINI sample preparation workflow. B. subtilis cultures are grown to an OD_{600} ~0.4-0.5. During this time, the agarose microholes are imprinted. Once the microchambers are formed and mounted into a gene frame, the slide is attached to a 96 well adapter. The bacterial culture is concentrated 100x and 20 µL is pipetted onto the microchambers. The sample is then loosely covered with a plastic cover slip and centrifuged at 3200g for 5 mins. The sample is then rinsed with fresh media to remove horizontal cells lying atop the microchambers. The sample is left to dry before being sealed with a glass coverslip.

4.2.2. Implementation and characterization of ring-HiLO

Once the loading into the microholes had been optimized, various methods of increasing the SNR were implemented. As stated in chapter 2, HiLO was used in order to reduce background and thus increase the SNR. However, there was concern that using this method may result in uneven illumination of the FOV, due to the fact that the inclined light beam results in the sample being illuminated from a single direction[215,254]. Thus ring-HiLO was implemented by Dr Séamus Holden as a method of rapidly rotating the inclined excitation beam around the focal plane thus illuminating the sample evenly from all directions (Figure 4.7) [250].

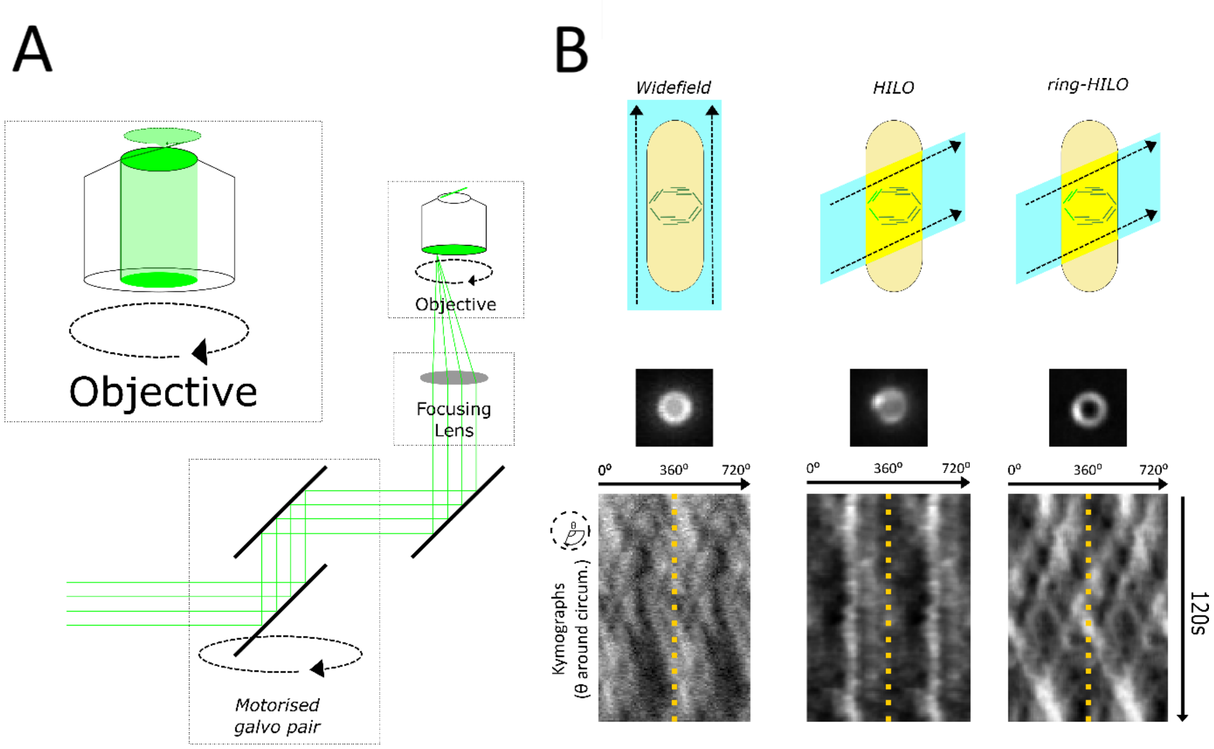

Figure 4.7: Ring-HiLO illuminates the sample evenly from all directions. (A) Schematic representation of ring-HiLO. A pair of motorised mirrors rapidly rotate the incident light beam around the back focal plane of the objective. This causes the light to propagate as a rapidly spinning light sheet. **(B)** Comparison of different illumination techniques. Widefield illumination illuminates the whole sample plane. Thus SNR is reduced by out of focus light from above and below the focal plane. HiLO inclines the illumination beam in order to limit the amount of sample which is illuminated, thus reducing noise. However, illumination occurs from a single direction, potentially introducing illumination artefacts. Ring-HiLO results in the sample being illuminated from all directions evenly.

Other methods of increasing the SNR were implemented by Dr Séamus Holden in the form of post-acquisition image processing in order to allow imaging under low light conditions, which would permit observations to be made over a longer time period. These included image denoising and background subtraction (see Methods). A schematic of the full VerCINI process can be seen in figure 4.8.

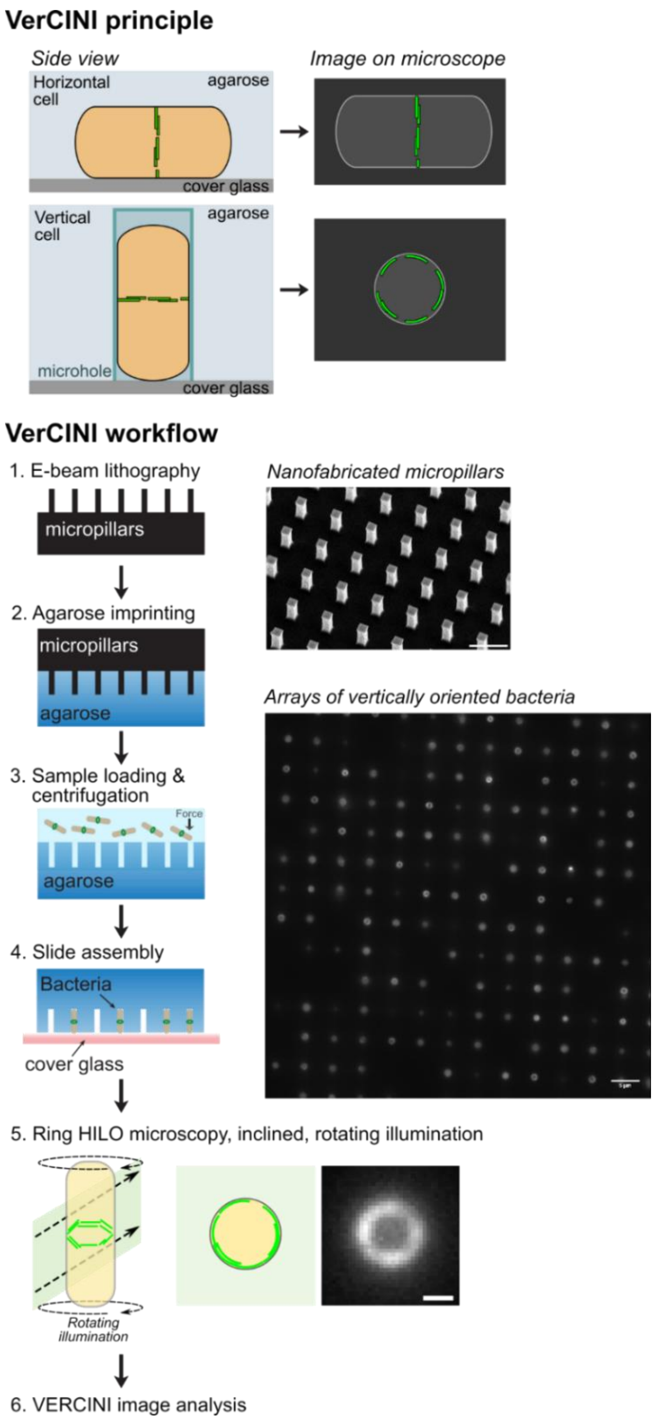

Figure 4.8: Principle and workflow for Vertical Cell Imaging by Nanostructured Immobilisation (VerCINI). Nanofabricated cell traps orient bacterial cells vertically on the microscope slide such that the division septum is oriented parallel to the microscope image plane. Silicon micropillars are fabricated by electron-beam lithography **(1)**. Micropillars are used as a mould for molten agarose **(2)**. Cells are loaded into agarose microholes by centrifugation **(3)** and assembled on a microscope slide **(4)**. Cells are imaged by ring HiLO microscopy for high signal-to-noise ratio and even illumination **(5)**. VerCINI data is then processed using a custom image analysis pipeline (Figure 4.1). Micropillar array imaged by Scanning Electron Microscopy. Vertically trapped bacteria expressing FtsZ-GFP (SH130) imaged ring HiLO fluorescence microscopy. Scale bars: 5 µm, top, middle images, 0.5 µm, bottom image.

Taken together, all of the optimization steps mentioned above allowed FtsZ-GFP dynamics to be measured over an extended time period. This was not previously possible as the prototype vertical immobilization workflow suffered from low signal and fast photobleaching. The rapid photobleaching meant that Z-rings could not be tracked over long periods of time as the loss of signal would be too great before the end of the acquisition period. In circumstances of fast photobleaching, one would usually reduce the laser intensity. However, as the samples already suffered from low signal, reducing the laser intensity would further reduce the SNR, making filament dynamics more difficult to track. Thus these optimizations were implemented as it was desirable to examine FtsZ dynamics over longer time scales in order to see if FtsZ filament dynamics evolved over time. These results showed that FtsZ filaments treadmill with a median velocity of 25 nm/s (IQR 14-33 nm/s, N=196). Interestingly, the dynamics could be split into motile and immotile population with ~20% of the filaments within the Z-rings being static (>10 nm/s) (Figure 4.19). When the kymographs are inspected, a range of filament dynamics within the Z-ring can be observed including filaments treadmilling with a constant velocity, static filaments, and filaments treadmilling with non-constant velocities. This may suggest there are factors responsible for regulating FtsZ filament dynamics, and this is investigated in detail in the next chapter.

The observation that treadmilling FtsZ filaments displayed a range of dynamics validated our approach of optimising the vertical immobilisation technology such that it could be used to image nascent Z-rings. As can be seen from figure 4.10, the increase in SNR observed when using the optimised VerCINI methodology when compared to the previous iteration, will allow us to probe the dynamics of FtsZ filaments in nascent rings, thus permitting us to investigate how FtsZ dynamics evolve over the division cycle.

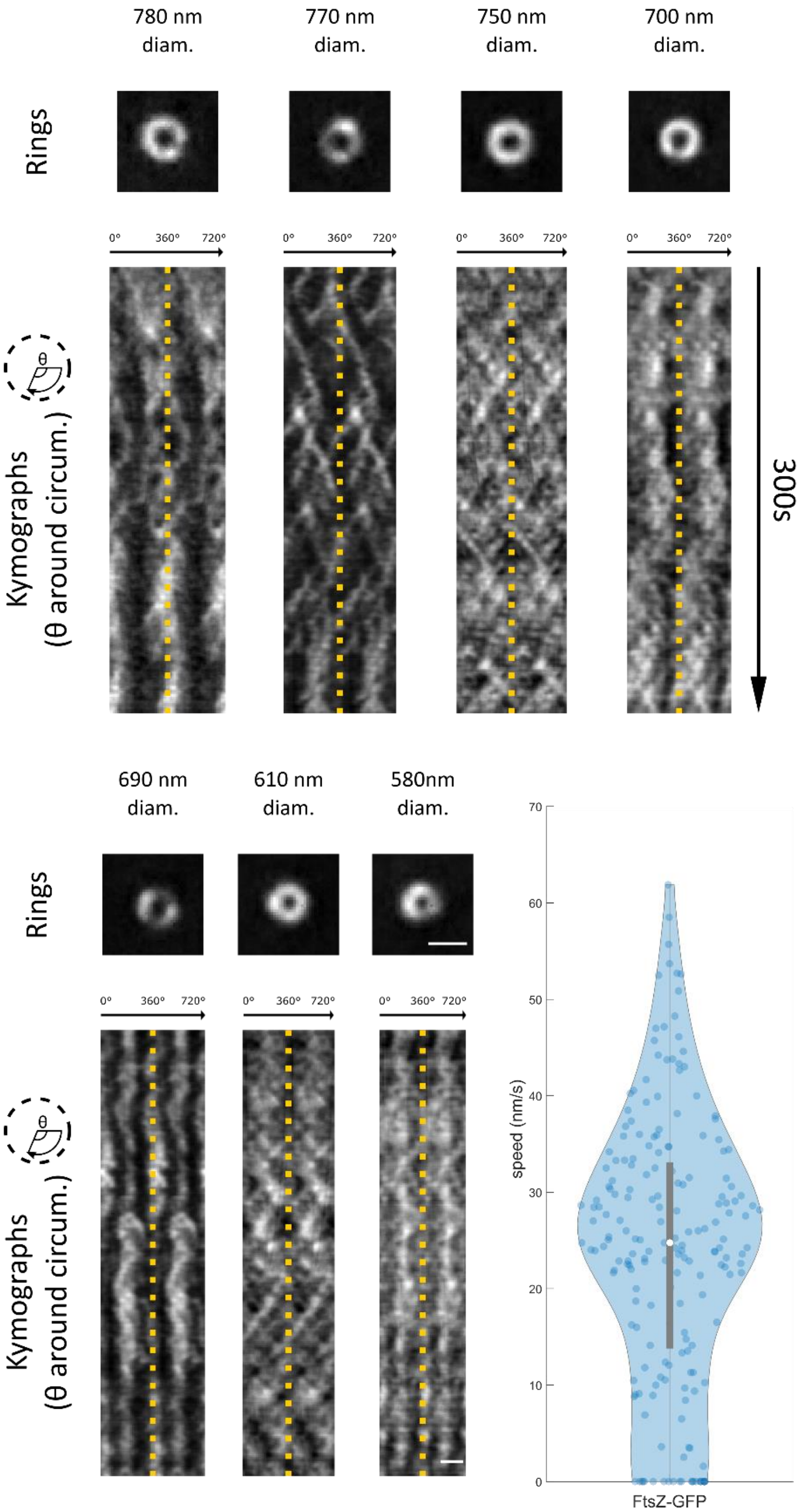

Figure 4.9 Extended time-lapse imaging of FtsZ-GFP. VerCINI microscopy of FtsZ filament dynamics imaged over a 10 min period (SH130 [*PY79 Δhag ftsZ::ftsZ-gfp-cam*]). A range of dynamics were observed including filaments treadmilling filaments at a continuous rate (750nm, 610nm, 580nm), stationary (780 nm, 700nm, 690nm, 580nm)and filaments and filaments with non-constant speeds (780nm, 750nm). Kymographs were obtained by fitting septal images to circles and plotting intensity values around the circumference of the cell for each frame of the time-lapse (1 frame/ 2s). Two full revolutions around the cell (0-720°) are plotted side-by-side in each kymograph to resolve filament trajectories that pass 0°/360°, separated by yellow dotted lines. Violin plot of FtsZ filament speed for each Z-ring phase. White circles, median; grey lines, interquartile range.

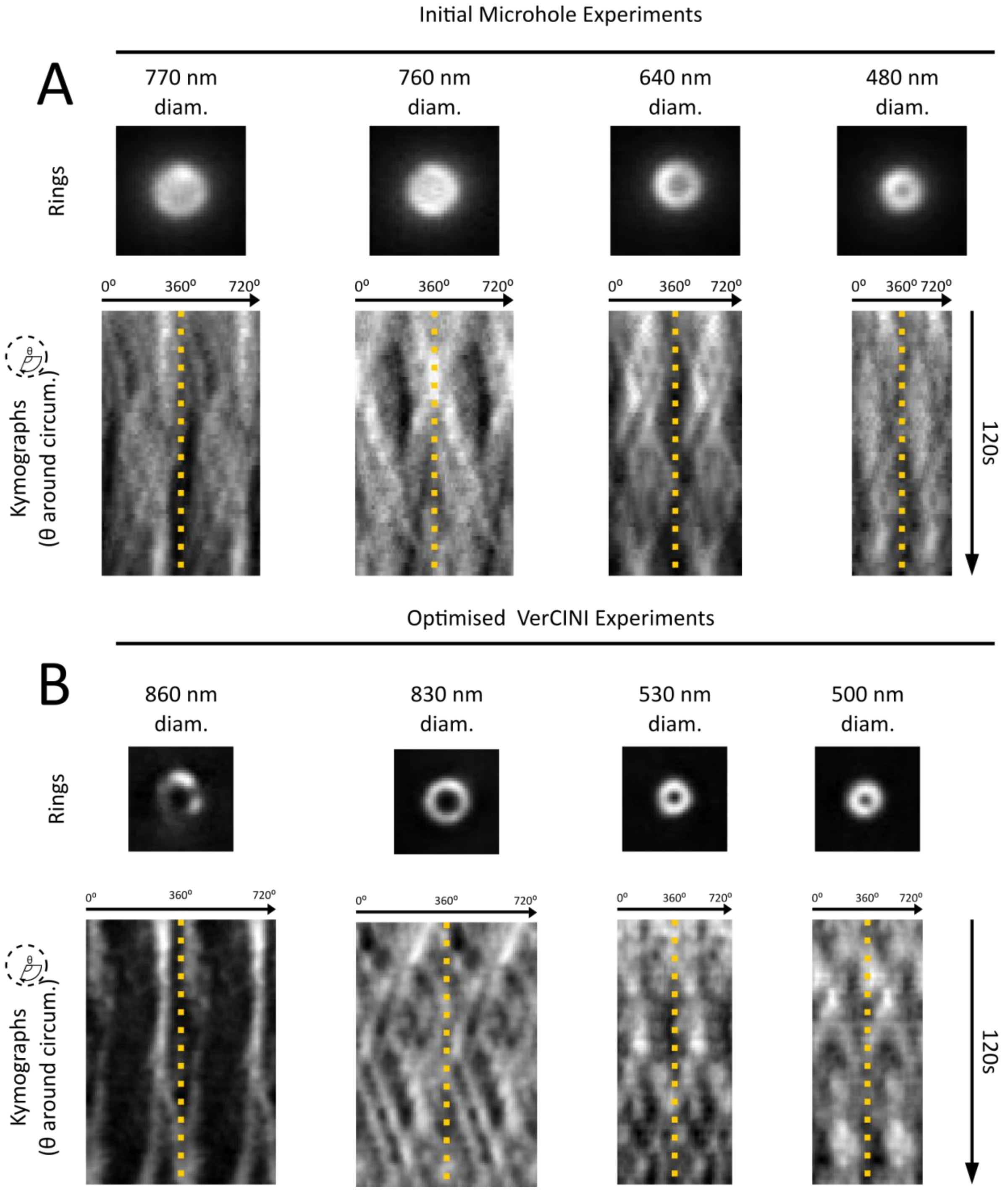

Figure 4.10: Comparison of initial vertical immobilisation results and optimised VerCINI. (A) Representative kymographs of FtsZ-GFP (SH33 [*trpC2, ftsZ:: ftsZ-GFP::cat, Δhag::aph(kan)*]) using the initial vertical immobilisation technology. **(B)** Representative kymographs of FtsZ-GFP (SH130 [*PY79 Δhag, ftsZ::ftsZ-gfp-cam*])using optimised VerCINI. Kymographs were obtained by fitting septal images to circles and plotting intensity values around the circumference of the cell for each frame of the time-lapse (**A-**1 frame/ 2s, **B-**1 frame/s). Two full revolutions around the cell (0-720°) are plotted side-by-side in each kymograph to resolve filament trajectories that pass 0°/360°, separated by yellow dotted lines. Violin plot of FtsZ filament speed for each Z-ring phase. White circles, median; grey lines, interquartile range.

4.4 Discussion

In chapter 2, I described a prototype vertical immobilisation technology that was used to trap *B. subtilis* cells in agarose microchambers. This enabled the Z-ring to be viewed in its entirety and allowed continuous imaging of the Z-ring over two minute time periods, in order to assess the dynamics of filaments within the ring. This allowed us to show that the Z-ring is composed of multiple filaments that treadmill bi-directionally around the division plane. Together with measurements taken by collaborators, FtsZ motion was observed to be a result of filaments treadmilling[2]. Initially we proposed a model in which FtsZ acts as an obligatory guide for septal synthases. In this model FtsZ treadmilling would be the rate limiting step PG synthesis[209]. However, it was later shown that FtsZ-treadmilling is dispensable following the initiation of constriction in *S. aureus*, another Gram-positive organism [223]. This suggested that FtsZ dynamics may play different roles indifferent stages of the cell cycle. Ergo, we sought to investigate the dynamics of FtsZ filaments over longer time scales and across different stages of the cell cycle.

Despite the benefits that the vertical immobilisation offered, the technology was still limited as it suffered from high background and fast photobleaching which made it incapable of imaging dim nascent rings. This prevented us from probing FtsZ dynamics across all stages of the division cycle. Another major limitation of this technique was that it suffered from low throughput. The diffuse nature of nascent rings makes them difficult to identify during the imaging process when utilising vertical immobilisation. This is because their dim nature makes it difficult to identify and differentiate the septum from the cytoplasmic background. Thus it is beneficial to have a high throughput technique to increase the number of cells in a single FOV, in order to maximise the chances of successfully capturing nascent rings.

4.4.1 Increasing the number of cells per FOV

I quantified the impact of the multiple approaches we undertook to maximize the number of cells in a single field of view. The first of these techniques was to switch from an EMCCD camera to an sCMOS camera. One of the major advantages of using an sCMOS camera is that is possess a 16x larger active pixel area. This allows a larger field of view to be imaged[44]. However, in addition to a larger field of view an sCMOS camera also offers a high dynamic range and the capability of imaging in low light conditions[49]. These are factors are vital for efficiently studying the dim nascent Z-rings, a necessity when wanting to quantify FtsZ filament dynamics in different stages on the cell cycle.

The second approach that was taken was a redesign of the silicon micropillar array used to generate the agarose microchambers. To accomplish this, I identified that agarose microchambers with a diameter of 1.0 -1.2 µm best facilitated efficient loading while still preventing cells from rotating within their chambers. As such, a new silicon micropillar array was collaboratively designed in which the overall size of the array was increased, while the spacing between the pillars was reduced. This would again allow more cells to fit in a single FOV. This new micropillar array was then etched by Dr Kevin Whitley. Combined with the larger camera, this was able to significantly increase the amount of cells obtained within a single view by an average of 733%.

Finally, I developed a new cell loading protocol for the microchambers. In the new protocol, rather than ineffectively forcing cells into the microholes by the addition of a coverslip, cells were centrifuged into the microchambers. Combining the centrifugation protocol I developed with larger camera size and optimized micropillars led to the overall loading rate increasing by an average of 1178% over the initial method.

4.4.2 The detrimental effects of phototoxicity and photobleaching

Imaging live cells is always a game of compromise. In order to obtain relevant data from a sample, the image must have sufficient contrast, spatial resolution and temporal resolution. All three of these factors are interlinked, it is not possible to change one without affecting the other two. The most common method of optimizing these factors is by increasing the samples exposure to light, either through increasing the intensity of the incident light beam, or increasing amount of time the sample is exposed to light. Yet care must be taken to keep cells happy when sat upon a microscope slide, and as free as possible from the deleterious effects of light. However phototoxicity is not the only concern, as one must also be careful not to photobleach the sample too rapidly, as this can lead to the loss of information gained from the imaging process. As it would be desirable to track the dynamics of FtsZ filaments over long timescales, to see how they evolve throughout the division, the detrimental effects of both phototoxicity and photobleaching must be taken into consideration.

Phototoxicity is an extremely important issue in microscopy. If one is not careful, the incident light beam can induce physical and chemical reactions due to it interacting with components of the cell[37,255,256]. One of the main contributing factors that makes phototoxicity so problematic is that it can directly damage intracellular components, or induce the production of harmful molecules either within the cell itself or its direct environment [257,258]. Perhaps the most obvious and well known example of light induced damage is by UV-light. The deleterious effects of UV-light include induction of the UV response leading to apoptosis in mammalian cells [259,260] and DNA strand breaks[261,262]. However, both UV-light and visible light are able to excite endogenous photoactive molecules such as tryptophan [263] and flavins [264]. Unfortunately, the fluorescent molecules that are imperative for labelling also exert phototoxic affects. This is due to the fact that when illuminated, photoactive molecules are capable of being excited to reactive states that can undergo redox reactions and thus produce ROS[265]. ROS are particularly problematic due to their broad range of effects which includes oxidizing proteins, lipids and DNA[255].

DNA damage can be taken as a prime example of the direct effects of phototoxicity on cell division dynamics. In *E. coli* DNA damage is known to induce the SOS response, which includes expression of SulA [266,267]. SulA is known to be an inhibitor of FtsZ preventing the formation of nascent Z-rings in addition to inducing the disassembly of existing Z-rings, even those undergoing active constriction[268–270] . This is thought to occur due to the binding of SulA to the base of the C-terminal domain of FtsZ, masking the T7 synergy loop, thus sequestering FtsZ monomers and preventing polymerization[269,271]. While SulA is not well conserved, YneA has been identified in *B. subtilis* as a protein produced through induction of the SOS-response that arrests cell division, though it appears to act at a later stage[97, 272]. Thus it is important to keep phototoxicity to a minimum when imaging Z-dynamics.

Photobleaching is the gradual decrease in fluorescence intensity cause by light-induced degradation of fluorophores [273]. This phenomenon occurs when a fluorophore undergoes photon-induced chemical damage and covalent modification, resulting in a permanent loss of fluorescence [274]. The amount of photobleaching increases over time and with incident light intensity [275]. Thus common methods of reducing phototoxicity and photobleaching are to reduce the intensity of the incident light, exposure time and acquisition time.

4.4.3 Optimizing imaging conditions

Reducing the incident light, exposure time and acquisition time will inevitably lower the SNR and as we wanted to image nascent Z-rings, which are inherently dim to begin with, several methods were implemented to combat this. In chapter 2, the implementation of HiLO was discussed as a method of increasing the SNR by inclining the incident light beam [215]. Here, the implementation of ring-HiLO is described as a method to ensure that the sample is evenly illuminated from all directions. As the ultimate aim of these optimization techniques is to quantify the dynamics of FtsZ filaments within the Z-ring across different stages of the cell cycle, this includes imaging nascent rings which are inherently dimmer than actively constructing rings. As such, ensuring the sample is evenly illuminated is imperative such that the SNR of nascent rings is not further reduced. Ring-HiLO is able to ensure that the sample is evenly illuminated through the action of a pair of motorized mirrors which rapidly spins the light beam around the back focal plane of the objective[250]. This results in the light propagating as a spinning light sheet, which rotates at such high speeds that the sample is evenly illuminated from all directions simultaneously.

Other methods that were implemented to increase the SNR took the form of post-acquisition imaging processing. The first such of these methods in the image processing pipeline is image denoising- a method of reducing the noise within data that is generated by the imperfectness of the sensors[251]. The second method used was background subtraction. During the division process, it has been suggested that around 30-40% of FtsZ is associated with the Z-ring, meaning there is a large cytoplasmic concentration[123,206] resulting in a high degree of background noise. Thus by measuring the intensity profile of cytoplasmic GFP, an algorithm for subtracting its contribution to the image was devised (see methods).

4.4.4 FtsZ filaments display a range of dynamics

All of the optimization steps described above allowed extended time-lapse imaging of the Z-ring to conducted. This allowed us to investigate the dynamics of FtsZ filaments over longer timescales. As observed in chapter 2, FtsZ-GFP was observed to treadmill with an average velocity of 25nm/s (IQR 14-33 nm/s). However, a range of filament dynamics were also observed over these longer timescales. These dynamics included filaments treadmilling at non-constant velocities. However one of the most intriguing observations was that FtsZ filament dynamics could be broadly split into two populations, mobile (80%) and immobile (20%). The amount of immobile filaments was surprising given the fact that FtsZ treadmilling has been observed to affect the rate of constriction in *B. subtilis*[209]*.* However, due to the observation that FtsZ treadmilling is dispensable following the onset of constriction in *S. aureus,* this may indicate that FtsZ treadmilling also plays different roles in different stages of the cell cycle in *B. subtilis.* Together, these results suggest that FtsZ dynamics may be regulated over different stages of the division cycle. The increase SNR achieved in the optimized VerCINI protocol will enable us to quantify the dynamics of FtsZ filaments across different stages of the cell cycle, even in dim nascent rings. The optimized loading protocol will further facilitate this by ensuring that a large number of cells per FOV will maximize chances of obtaining Z-rings in different stages of the division cycle.

4.5 Conclusions and outlook

In this chapter I described the optimization of the vertical immobilization technique developed in Chapter 2, in collaboration with other members of the lab. This technique is now capable of imaging with low light doses with high throughput. This imaging technique has been termed Vertical Cell Imaging by Nanostructured Immobilisation (VerCINI). However, it should be noted that this technique is not only applicable to imaging cell division proteins . This technique can also be used to study the dynamics of proteins that move circumferentially around the cell that are distributed throughout its length (e.g. MreB[276]), in addition to proteins that localize to the poles of rod shaped cells (e.g. TlpA[277]).

The observation that FtsZ displays a range of filament dynamics including motile and immotile filaments suggests that FtsZ treadmilling may play different roles in different stages of the cell cycle. While examining the dynamics of FtsZ filaments in different stages of the cell cycle would have been a difficult and arduous task, the optimised VerCINI workflow is able to overcome previous limitations. The increased throughput of the technique will ensure that a large number of cells in different cell division stages can be readily obtained. Furthermore, the image analysis pipeline developed by other members of the lab ensures that filaments in dim nascent rings can be observed.

Chapter 5 : FtsZ Treadmilling is essential for Z-ring condensation in *B. subtilis* cell division

5.1. Introduction

In previous chapters, I described a novel vertical immobilisation technique that allowed the Z-ring to be visualised in its entirety. This revealed that the Z-ring is composed of multiple short filaments of FtsZ that move bi-directionally around the division plane. FtsZ filament dynamics were shown to be the result of treadmilling, a type of motion where an asymmetric filaments end undergoes plus-end polymerisation and minus-end depolymerisation with GTP hydrolysis setting the rate of FtsZ depolymerisation and overall treadmilling speed[278–280]. FtsZ treadmilling dynamics are essential for cell division[280–283].

Despite this, the functional role of FtsZ treadmilling for cell division remains unsolved. In the Gram-positive *B. subtilis*, it was observed that constriction rate and synthase speed were dependent of the treadmilling speed of FtsZ filaments[279]. This lead us to propose an initial model in which cell division was the result of a tightly coupled motile filament-synthase complex, with FtsZ acting as an obligatory guide and rate limit step for PG synthesis. However, FtsZ was later found to be dispensable following the onset of constriction in *S. aureus,* despite both organisms belonging to the same phylogenetic class. This may represent a genuine difference between the two species, but it is also possible there is a common mechanism in which FtsZ plays a different role in different stages of the cell cycle. To date, it remains unclear how the role of treadmilling FtsZ filaments differs across the entire cell division process.

Thus, utilising the optimised VerCINI technology described in previous chapters, I investigated the dynamics of FtsZ filaments across all cell division stages at near single filament resolution.

5.2 Materials and Methods

5.2.1 Bacterial strains and growth conditions

Strains used in this study are listed in Supplementary Table 1. Strains were streaked from -80^{o}C freezer glycerol stocks onto Nutrient Agar (NA) plates containing the relevant antibiotics and/or inducers and grown overnight at 30^{o}C. Single colonies were transferred to liquid starter cultures in either TLM or PHMM media and grown with agitation at 200 rpm overnight at either 30^{o}C (TLM) or 22^{o}C (PHMM). The next day, TLM starter cultures were diluted to a starting OD_{600} of 0.1 in CDM, while PHMM starter cultures were diluted to a starting OD_{600} of 0.05 in PHMM, and these liquid cultures were grown at 30^{o}C or 37^{o}C with any required inducer until they reached the appropriate OD_{600}.

5.2.2 Microscopy

Power density, exposure time and other key parameters are listed for each microscopy experiment in Supplementary Table 1.3. All imaging was done using a custom-built inverted microscope (otherwise).

Custom microscope. Cells were illuminated with a 488 nm laser (Obis). A 100x TIRF objective (Nikon CFI Apochromat TIRF 100XC Oil) was used for all experiments. A 200 mm tube lens (Thorlabs TTL200) and Prime BSI sCMOS camera (Teledyne Photometrics) were used for imaging, giving effective image pixel size of 65 nm/pixel. Imaging was done with a custom-built ring-TIRF module operated in ring-HiLO [250] using a pair of galvanometer mirrors (Thorlabs) spinning at 200 Hz to provide uniform, high SNR illumination.

5.2.3 VerCINI

Agarose microholes were formed by pouring molten 6% agarose onto the silicon micropillar array. Patterned agarose was transferred into a Geneframe (Thermo Scientific) mounted on a glass slide, and excess agarose was cut away to ensure sufficient oxygen. Cells at $OD_{600} \sim$ 0.4 were concentrated 100x by centrifugation and added onto the agarose pad. Cells were then loaded into the microholes by centrifuging the mounted agarose pad with concentrated cell culture in an Eppendorf 5810 centrifuge with MTP/Flex buckets. Unloaded cells were rinsed off with excess media.

FtsZ treadmilling dynamics were imaged at 1 frame/s (continuous exposure) for 2 mins at 1-8 W/cm^2. After each field of view was imaged, a multi-slice Z-stack was taken at 500nm intervals to exclude tilted or improperly trapped cells, in addition to excluding Z-rings that have an adjacent Z-ring 1µm above or below the imaging plane. VerCINI experiments were performed on cells in a *Δhag* mutant background, preventing undesirable cell rotation within the microholes by disabling flagellar motility.

5.2.4 Microscopy of horizontal cells

Coverslips were first cleaned by treating with air plasma for 5 min. Slides were prepared as described previously[285]: Flat 2% agarose pads of either CDM or PHMM were prepared inside Geneframes (Thermo Scientific) and cut down to strips of 5 mm width to ensure sufficient oxygen supply to cells. Cell cultures were grown to OD_{600} between 0.2 and 0.4, when 0.5 µL of cell culture was spotted on the pad. Cells were allowed to adsorb to the pad for 30 s before a plasma-cleaned coverslip was placed on them. After spotting on agarose pads, cells were allowed to equilibrate within the microscope body for 15 min before being imaged. Cells were then imaged either by HiLO for time-lapse observation, with experimental parameters defined in supplementary table 3.

5.2.5 VerCINI data analysis

Pre-processing

Videos were denoised using the ImageJ plugin PureDenoise[251], which is based on wavelet decomposition. Key assumptions of the method are (i) local spatiotemporal similarity within the image (ii) absence of sharp discontinuities, guaranteed by diffraction-limited nature of the image. The denoising algorithm makes does not make any assumptions on the type of underlying biological structure.

Denoised videos were registered using the ImageJ plugin StackReg (REF). Image stacks of vertically immobilised cells were inspected to exclude tilted cells or out of focus FtsZ-rings, or FtsZ rings where a second Z-ring was closer than 1 um to the focal plane. Cropped region of interest movies containing single in-focus cells were manually selected and exported for analysis. An ImageJ package for VerCINI data processing is available (https://github.com/HoldenLab/Ring_Analysis_IJ).

VerCINI background subtraction, kymograph extraction, quantification

Custom software for quantitative cytoplasmic background subtraction and kymograph extraction was developed for analysis of VerCINI movies (https://github.com/HoldenLab/ring-fitting2). Fluorescence images of isolated vertical cells were fitted to a joint explicit model for diffuse out-of-focus cytoplasmic background

(Gaussian + Cauchy model) plus septal protein signal, modelled as a 12 sectored annulus with each sector of variable amplitude.

$$F(x, y) = Signal(x, y) + Bg(x, y)$$

Signal is calculated in polar coordinates, around the septal ring centre fit parameter (x_0, y_0), and then transformed into Cartesian coordinates. Signal is defined as

$$S(r, \theta) = A_i(\theta) \exp\left(-\frac{(r - R_0)^2}{2\sigma^2}\right),$$

where $A_i(\theta)$ defines a 12 sectored ring. Background is defined as

$$Bg(x, y) = a \exp\left(\frac{-((x - x_0)^2 + (y - y_0)^2)}{2\sigma_{bg1}^2}\right) + b \frac{\sigma_{bg2}^2}{(x - x_0)^2 + (y - y_0)^2 + \sigma_{bg2}^2} + c.$$

This explicit model allowed accurate sub-pixel location of a circular line profile at the septal leading edge. Explicit subtraction of complex background signal also allowed septal intensity quantification. The background subtracted intensity along the circular line profile was then calculated for each frame and automatically plotted as a kymograph. Kymographs were plotted over the [0,720°] ie two complete revolutions around the line profile for ease of visualization, specifically to allow straightforward visualization of motile filaments crossing the 360°,0° boundary. For each cell, the Z-ring diameter was determined from the fitted model in the kymograph extraction step. Median septal intensity was calculated as the median value of all kymograph pixels from the first 60 image frames.

FtsZ filament treadmilling analysis using VerCINI

We performed manual measurement of filament speed and processivity by kymograph analysis, annotating filaments as lines in ImageJ and then measuring the angle via ImageJ script. As the intensity range across kymographs is large, manual detection and analysis of filaments was aided by applying a ridge filter to the kymograph which detects ridges in the image, independent of absolute intensity. The ridge filter consists of a Gaussian blur operation to set the feature scale and suppress noise (here 2 pixels, 130 nm), followed by calculation of the major eigenvalue of the Hessian matrix for each pixel, implemented as an ImageJ macro in the package listed above. Joint annotation of the ridge filtered and raw intensity kymograph was performed, allowing sensitive annotation of both bright and dim filaments.

5.2.6 Horizontal cell image analysis
Pre-processing.

Images were denoised and registered as described above.

Cell segmentation and tracking of division protein localization.

MicrobeJ[286] was used to track individual FtsZ -rings and export their centroid coordinates for analysis. To do this, image backgrounds were first subtracted using a sliding paraboloid window of 50 pixels and all frames were converted to 8-bit for easier thresholding.

For analysis of FtsZ ring dynamics over the entire division process, from nascent Z-ring assembly to late constriction (Figure 1), it was necessary to robustly detecting diffuse patchy FtsZ-rings. We trained the machine learning segmentation tool Ilastik[287] to detect cell outlines with fluorescence images of cells labelled with FtsZ. For detection of diffuse Z-rings, we applied a large Gaussian blur filter to the images, and then multiplied this by the Ilastik-segmented binary image, which had the effect of separating any overlap of Z-rings between adjacent cells.

An intensity-based threshold detection was applied in MicrobeJ, a threshold was selected manually for each field of view using MinError. Additional area and length thresholds (Area: [0.08 Inf] μm^2, Length: [0.02 1.8] µm) were established to exclude objects in fields of view that were not rings. Tracks shorter than 7 frames were excluded. Data was then exported for analysis in MATLAB.

Quantification of division protein septal localization

Custom MATLAB software was developed to measure the diameters and intensities of Z-rings obtained from either MicrobeJ or Ilastik. Each frame of each individual ring was first segmented using a multi-level threshold to distinguish the septum, cytoplasm, and background. The septal axis and the cell axis were identified using the segmented image, and the image was rotated such that pixels were aligned along these axes. Line profiles of Z-rings were obtained by averaging pixel values along the septal axis ±2 pixels to reduce noise. Diameter were then obtained by fitting line profiles to a toy model that describes a circle of uniform intensity rotated to be orthogonal to the axis of the imaging plane. Septal density was calculated as the total intensity along the lateral line profile, divided by the ring circumference to reduce single frame noise. Septal density was used in place of total intensity, in order to compare to the septal intensity measurements obtained during the VerCINI experiments. Axial thickness was estimated by fitting an axial line profile to an analytical super-Gaussian and calculating the full-width half maximum.

5 3 Results:

5.3.1 Z-rings at the division site have three main phases: nascent, mature, and constricting.

The organisation of FtsZ filaments during cell division in *B. subtilis* was observed by conventional time-lapse imaging of horizontal cells expressing the FtsZ-GFP fusion protein[212], that was characterised in previous chapters. Upon initial assembly, FtsZ filaments form a diffuse structure at the midcell, which undergoes rapid condensation into a dense band before constriction is initiated (Figure 5.1A). These changes in structure were quantified by measuring the Z-rings dimensions (axial thickness and diameter) and septal density (the total septal intensity divided by the fitted Z-ring circumference) in each frame. Septal density was calculated instead of total intensity as the former is directly comparable to septal intensities measured by VerCINI. Traces of diameter, axial thickness and septal density were each aligned by the start time of constriction (Figure 5.1B). This revealed that there are three distinct phases to the Z-ring that were classified as “nascent”, “mature”, and “constricting”.

By inspecting the ring thickness plot (Figure 5.1B) in addition to a plot of ring thickness vs diameter (Figure 5.1C), it was observed that nascent Z-rings have large variable thicknesses which is consistent with their composition of sparse FtsZ filaments. These nascent rings then condense to form a dense mature Z-ring with thicknesses of 300-250 nm (Figure 5.1C). This corresponds approximately to the thickness of a diffraction limited structure.

Z-rings were classified as “Nascent”, “Mature” and “Constricting” as follows (Figure 5.11b-c):

- Nascent Z-rings: ring thickness > 400nm, not constricting (time after initiation < 0)
- Mature Z-rings: ring thickness < 400nm, not constricting (time after initiation < 0)
- Constricting Z-ring: actively constricting (time after initiation > 0)

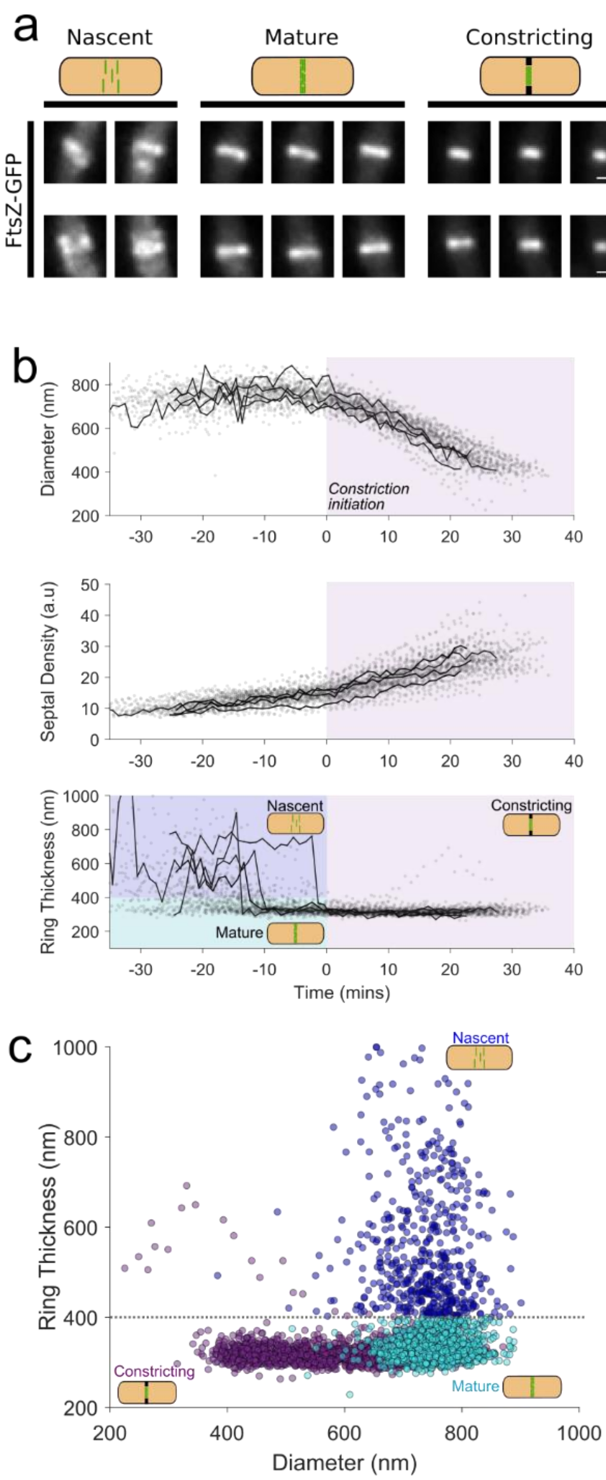

Figure 5.1: FtsZ filament organisation and dynamics throughout the division cycle. (a) *Exemplar images of FtsZ-GFP (SH130 [PY79 Δhag ftsZ::ftsZ-gfp-cam]). Filament organisation over the division cycle, classified by division phase.* ***(b)*** *Quantification of FtsZ-ring diameter, ring thickness and septal density (septal intensity divided by ring circumference) over cell cycle from time-lapse microscopy data. Nascent Z-rings have large axial width (ring thickness) due to the diffuse distribution of filaments, which condense into a thin mature Z-ring, followed by constriction initiation. Traces are temporally aligned relative to the start time of constriction (Methods). Grey scatter points represent all data points, black lines show individual, representative traces.* ***(c)*** *Classification of Z-ring stage via ring thickness and relative septal diameter. Nascent Z-rings (blue) have a ring thickness greater than 400 nm (dashed line) and unconstricted septum. Mature rings (cyan) have a ring thickness less than 400 nm*

5.3.2 Septal density and Z-ring diameter are sufficient parameters to classify Z-rings when imaging using VerCINI .

As outlined in previous chapters, Z-ring dynamics are difficult to observe *in vivo,* with TIRF illumination limiting observations to partial snapshots of filament dynamics in nascent cells [288,289]. Thus the optimised VerCINI was used in order to assess the dynamics of FtsZ filaments in different stages of the cell cycle. However, classification of Z-ring phase is much more difficult when imaging cells by VerCINI when compared to horizontal cells as the former lacks the long term time-lapse and high resolution axial thickness information that is required to trivially assess Z-ring state. As septal intensity has been observed to steadily increase throughout cell division (figure 5.1B), this was used alongside Z-ring diameter in order to assess whether these parameters could determine Z-phase for VerCINI data based on calibration from the horizontal cell data.

Septal density was plotted against diameter for all cell data points classified into Z-ring phase, using the previous analysis of axial thickness against constriction state (Figure 5.2A). Significantly constricted Z-rings were able to be trivially separated from other Z-ring phases based on diameter alone (Figure 5.2A; constricting Z-rings < 700 nm, purple circles). Unconstricted mature and nascent Z-rings (Supplementary Figure 6a; cyan circles, mature Z-rings; blue circles, nascent Z-rings), together with constricting Z-rings that had not yet constricted a large amount (Figure 5.2A; constricting Z-rings > 700 nm, purple circles), showed a large distribution of fitted diameters around 800 nm.

A kernel density plot was produced of the septal density for all Z-rings that has a diameter > 700nm to assess if phases of unconstricted Z-rings could be separated using intensity alone (Figure 5.2A right). It was observed that the intensity distribution for each Z-ring phase formed distinct peaks. However, there was significant overlap between these peaks when the measurements were based on horizontal cells alone.

Thus, it was next assessed whether the increased intensity resolution granted by VerCINI would be sufficient so separate Z-rings intro their distinct phases (Figure 5.2B). Median septal intensity was plotted against the fitted Z-ring diameter for each Z-ring imaged by VerCINI and this resulted in a similar intensity-diameter distribution to the horizontal cell data. The observed un-constricted cell diameter was slightly larger (~900nm) when imaged using VerCINI due to the more direct method of measuring septal diameter (i.e. fitting an entire circle compared to a tilted, projected circle).

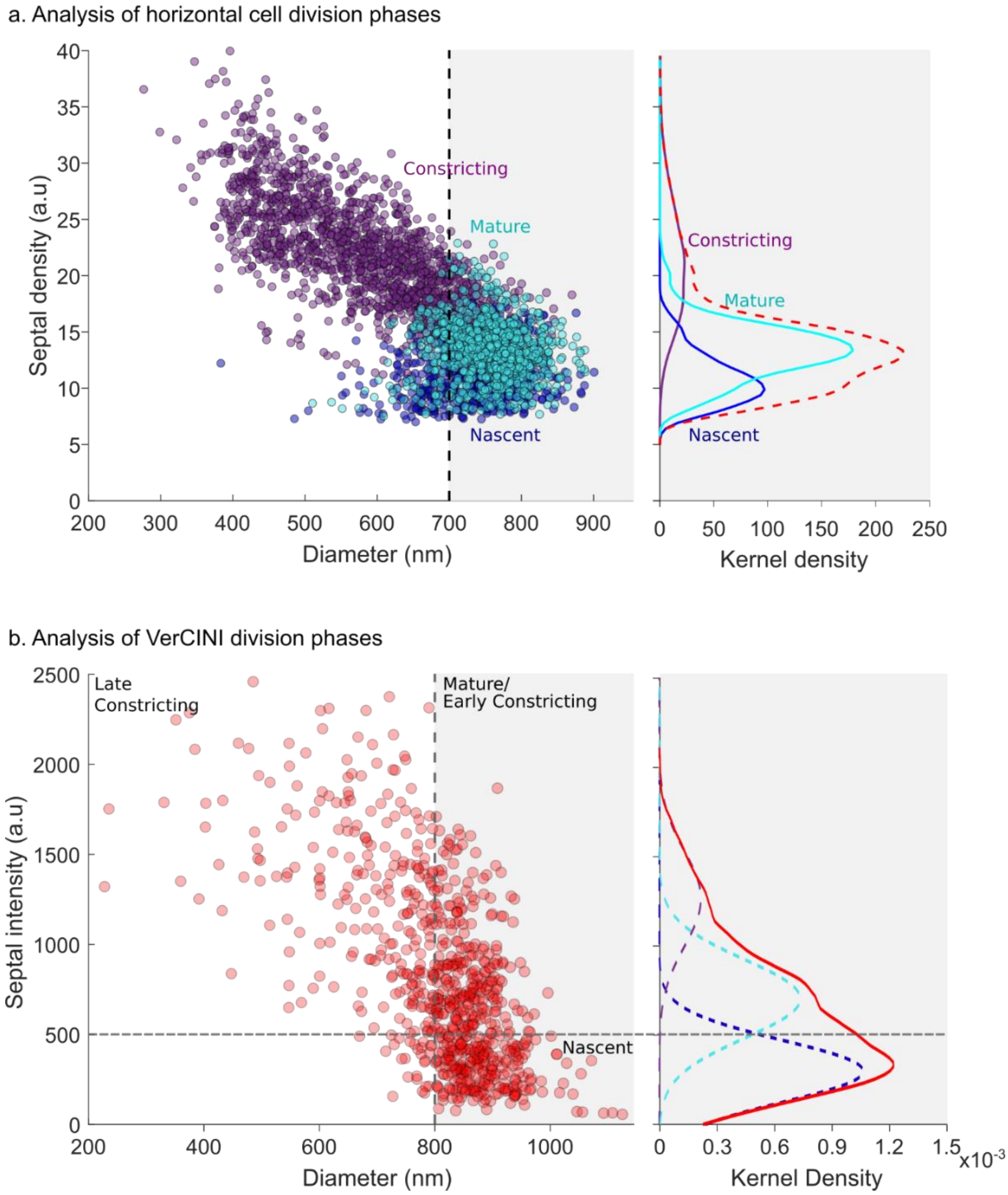

Figure 5.2: Classification of Z-ring state for horizontal and vertical cells. **(a)** Septal density and diameter of Z-rings for time lapse microscopy of horizontal cells. Z-ring phase classified as constricting (purple), mature (cyan) or nascent (magenta) based on Z-ring thickness and time-lapse analysis of constriction state (Figure XX). Kernel density plot (right) of septal density for highlighted grey region of septal density-diameter plot (left). Continuous lines show kernel density estimates of septal density for each separate Z-ring phase. Red dashed line indicates sum of all 3 distributions. **(b)** Septal density and diameter of Z-rings for vertical cells imaged by VerCINI. Cells in each identified quadrant were classified as nascent, mature/ early constricting or late constricting Z-rings based on septal intensity and diameter, calibrated against horizontal cell time lapse analysis (Supplementary Note 3). Kernel density plot (right, red dashed line) of VerCINI septal intensity for highlighted grey region of septal density-diameter plot. Dashed lines show contribution of nascent (blue), mature (cyan) and constricting (purple) to observed septal intensity distribution, as estimated by fitting a 3 Gaussian model to the data.

It was observed that, like the horizontal cell analysis, Z-rings that were significantly constricted were able to be separated from other data points based upon their diameter. Thus these Z-rings were classified as “late constricting” (diameter <800nm). The kernel density for all Z-ring septal intensities with a diameter greater than 800nm was then calculated (Figure 5.2B, left, red line). As with the horizontal cell measurements, a broad distribution of 3 overlapping peaks was observed. Thus based on the horizontal cell data, 3 Gaussian peaks were fitted to the data as a method of estimating the degree of overlap between nascent, mature and constricting Z-ring intensity distributions (Figure 5.2B, purple, cyan, magenta dashed lines). The results showed that there was greater separation between the nascent and mature Z-ring populations when imaged using VerCINI rather than as horizontal cells. This is consistent with the presence of a large diameter, dim intensity cluster in the intensity-diameter plot of VerCINI data (Figure 5.2B, left).

Using a threshold of 500 AU (arbitrary units) intensity as the crossover point of the mature and nascent Z-ring populations allows robust classification of different cell divisions stages in the VerCINI data with little overlap, as estimated from the 3 fitted populations: nascent Z-rings (84% nascent Z-rings, 16% mature Z-rings and 0% early constricting Z-rings) and mature/early constricting Z-rings (62% mature Z-rings, 27% early constricting Z-rings, 10% nascent Z-rings). Based on this analysis, we classified VerCINI Z-ring state as follows:

- Nascent Z-rings: ring diameter > 800nm, septal intensity < 500 AU,
- Mature/early constricting Z-rings: ring thickness > 800nm, septal intensity > 500 AU,
- Constricting Z-ring: ring thickness < 800nm, septal intensity > 500 AU.

The spatiotemporal organisation of the Z-ring when visualised using VerCINI was consistent with the morphology of horizontal cells. Nascent Z-rings were patchy and these rings frequently contained large gaps (Figure 5.3A and Figure 5.4A). Mature/early constricting and late constricting Z-ring were dense structures that were continuous to the attainable resolution of the technique (Figure 5.3B-C and Figure 5.4B-C).

5.2.3 VerCINI microscopy reveals FtsZ filament dynamics are division stage regulated and FtsZ treadmilling drives filament encounter in nascent Z-rings

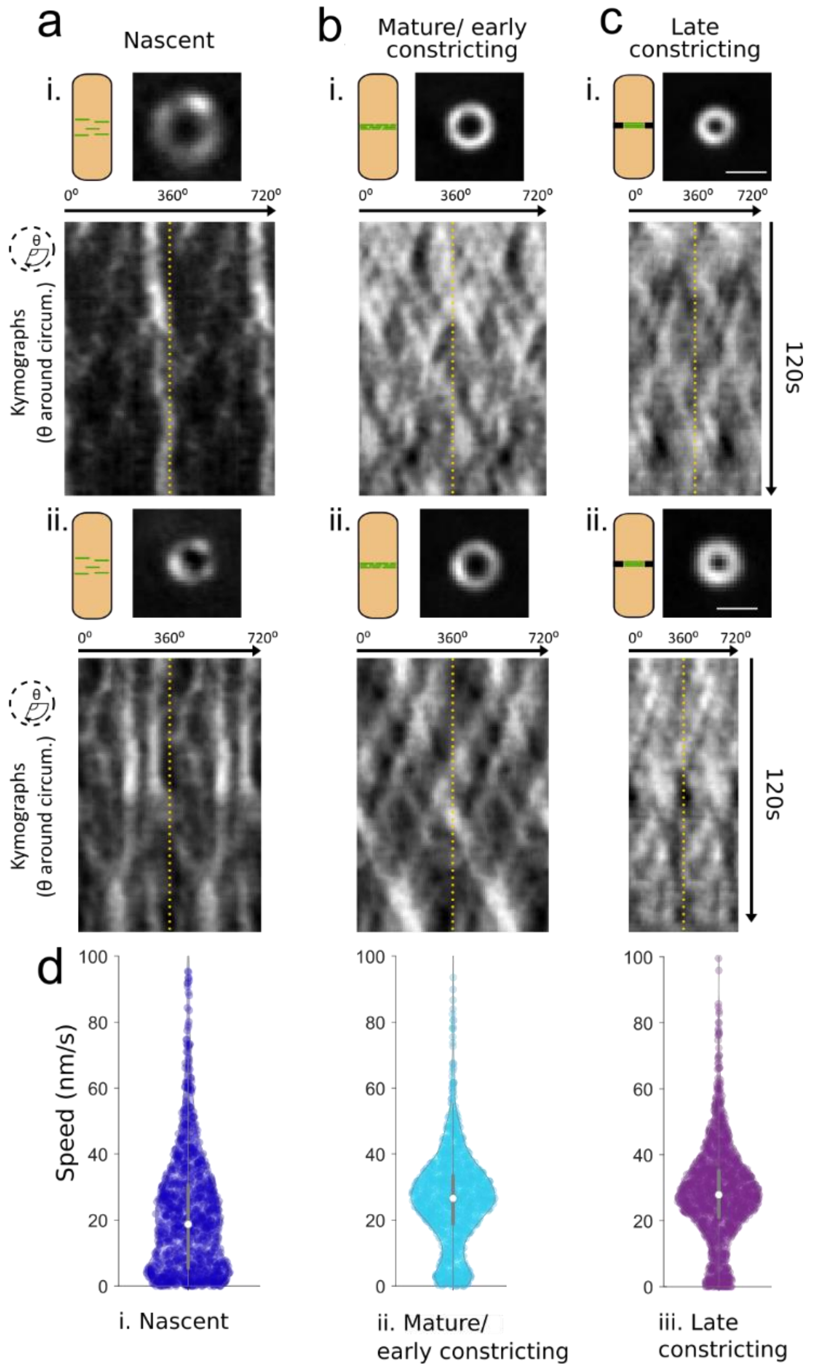

Figure 5.3: (a-c) VerCINI microscopy of FtsZ filament dynamics for each Z-ring phase, two representative examples per phase (i-ii), *(SH130 [PY79 Δhag ftsZ::ftsZ-gfp-cam]).* Nascent Z-rings are composed of sparse filaments diffusely distributed around the circumference of the cell, and a large fraction of static FtsZ filaments. Mature and constricting Z-rings possess a more uniform distribution of FtsZ filaments around the division site, with most filaments treadmilling. Images of septa show the first frame in kymographs (t=0 s). Kymographs were obtained by fitting septal images to circles and plotting intensity values around the circumference of the cell for each frame of the time-lapse (1 frame/ s). Two full revolutions around the cell (0-720°) are plotted side-by-side in each kymograph to resolve filament trajectories that pass 0°/360°, separated by yellow dotted lines. **(d)** Violin plots of FtsZ filament speed for each Z-ring phase. White circles, median; grey

The VerCINI experiments revealed that in nascent Z-rings, FtsZ filaments are distributed sparsely and are a mixture of motile and static filaments (Figures 5.3 and 5.4A, 35% immobile, filament speed < 10 nm/s) resulting in a lower average filament speed with a broad distribution (median 19 nm/s, interquartile range, IQR, 5-31, N=526). Interestingly, two or more FtsZ filaments were often observed colliding, which lead to filament aggregation and temporary arrest of those filaments involved (Figure 5.4A). FtsZ filament aggregation by lateral filament interactions is required to bundle FtsZ filaments and condense the Z-ring[22–26]. These data show that FtsZ treadmilling can drive filament aggregation by promoting the filament encounters required for lateral interactions.

Following the condensation of the Z-ring, a drop in the number of immobile filaments was observed in mature/ early constricting rings which resulted in a significant increase in the average filament speed with a narrower spread of speeds (15% immobile, median 27 nm/s, IQR 19-34, N=1053; Figure 5.3B and Figure 5.4B). Filament speeds in late constricting Z-rings were similar to those of mature/early constricting Z-rings (13% immobile, median speed 28 nm/s, IQR 21-36, N=1677; Figure 5.3C and 5.4C). As a result of the decreased population of static filaments, FtsZ filaments in mature and constructing Z-rings, on average, traversed twice the distance around the division site when compared to those in nascent rings (Figure 5.5B). FtsZ filament life time (the time that filaments spend bound at the septum) was observed to be similar across each of the three division stages. Thus although the FtsZ filaments in nascent Z-rings are less dense and motile, their bound lifetime remains similar (Figure 5.5c).

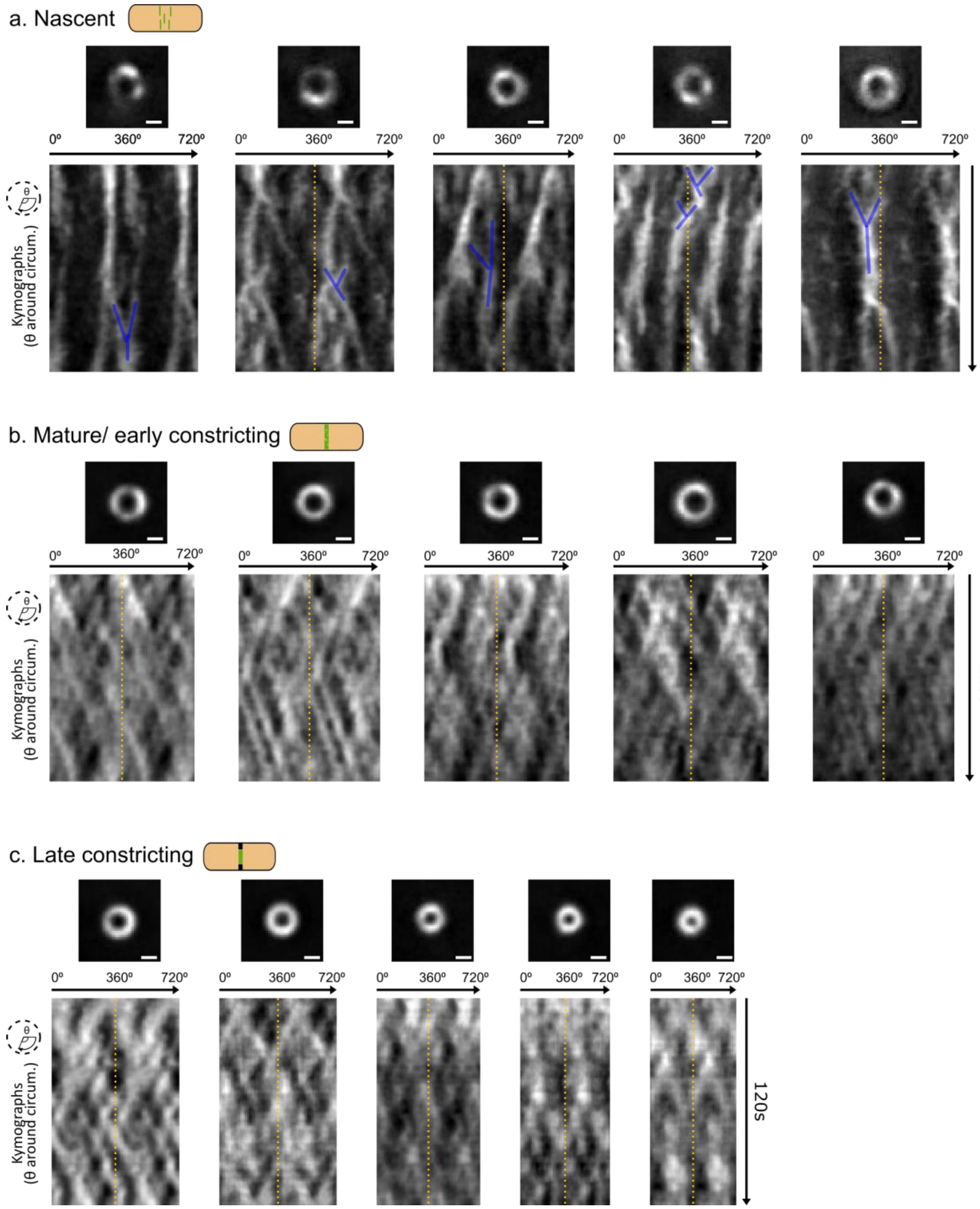

Figure 5.4: Z-ring dynamics in each cell division phase, nascent (a), mature/ early constricting (b) and late constricting (c) imaged by VerCINI. Images are snapshots of Z-ring *(SH130 [PY79 Δhag ftsZ::ftsZ-gfp-cam]).* organisation at beginning of time lapse. Kymographs are plotted around Z-ring circumference, with a complete line profile around the circumference repeated twice side-by-side to allow visualisation of filament trajectories which cross the 0^{o}-360^{o} boundary; yellow dashed line indicates beginning of repeated kymograph. Blue lines indicate examples of FtsZ filament interaction. Scale bar 0.5 µm

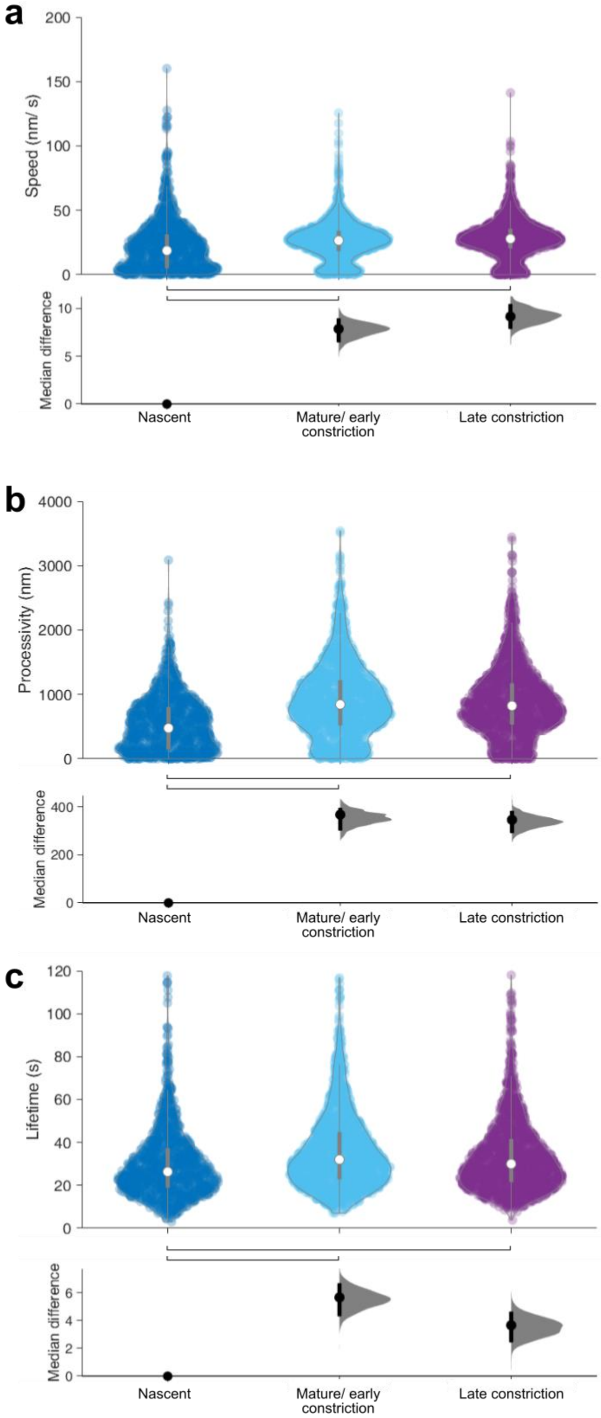

Figure 5.5: Quantification of FtsZ-GFP (SH130) filament dynamics for cells imaged by VerCINI, with DABEST analysis of median difference for each cell cycle stage. (a) Speed distribution of filaments (as presented Figure 5.3D, with additional DABEST analysis). **(b)** Filament processivity (distance filament treadmills around septal circumference). **(c)** Filament lifetime (time bound to septum). Violin plot: white circles, median; thick grey lines, interquartile range; thin grey lines, 1.5x interquartile range. DABEST plot: black circle, median difference between indicated conditions; black lines, 95% confidence interval of median difference.

5.4 Discussion

Using optimised VerCINI methodology described in previous chapters, I showed that FtsZ filament dynamics and organisation evolve over the course of the division cycle and can be split into three distinct phases: nascent, mature, and constricting.

Conventional imaging of horizontal cells revealed that FtsZ filaments initially form a diffuse structure at the division site, which rapidly condense into a dense narrow band after which constriction initiates. Imaging the cells horizontally granted access to three main Z-ring descriptors, diameter, axial thickness and septal density. By quantifying these measurements, three distinct phases of the Z-ring were observed: nascent, mature and constricting. During the nascent Z-ring stage, sparse FtsZ filaments transiently assemble at the midcell over a wide region. This is consistent with previous reports[282,290–292]. FtsZ filaments then undergo rapid condensation into a thin mature ring which remains unconstricted for a time, but gradually increases in intensity. The Z-ring then begins constricting until division is finished. The thickness of the mature ring was observed to be about 300-350nm wide, consistent with the thickness of a diffraction limited structure in this system.

As I wanted observe the dynamics of FtsZ filaments across these different Z-ring stages, attention was turned back to the optimised VerCINI method that has been explained in previous chapters. However, classifying Z-ring phase by VerCINI is more difficult than by horizontal time-lapse as the former lacks long term time-lapse and high resolution axial thickness. As it had been observed that the septal density steadily increases throughout cell division, the horizontal cell data was used as a calibration tool to see if septal density and Z-ring diameter could be used to determine Z-ring phase for the VerCINI data.

It was observed that significantly constricted Z-rings could be easily separated from other Z-ring phases using diameter alone. Intensity profiles revealed three distinct peaks, though significant overlap was observed for nascent, mature and constricting rings that had not constricted to a great degree. Thus for horizontal cells, intensity alone is insufficient to accurately separate between the populations. However, VerCINI offers greater intensity resolution and because of this, three distinct peaks corresponding to nascent, mature and constricting were observed with little overlap when the intensity distributions were plotted. This supports the conclusion the Z-rings can be classified based on diameter and septal intensity.

Classifying the stages of different Z-rings was advantageous as it allowed the dynamics of FtsZ filaments within the ring to be assessed across different stages in the division cycle for the first time. Using VerCINI, we observed that in nascent rings, FtsZ filaments are sparsely distributed with a mixture of static and motile filaments (35% immobile, filament speed < 10 nm/s). This resulted in a lower average FtsZ filament speed with large spread (median 19 nm/s, interquartile range, IQR, 5-31, N=526).

The difference in dynamics observed between nascent and both mature and constricting rings suggests that FtsZ filament dynamics may be regulated throughout different stages of the division cycle. One potential reason for these differences is that FtsZ is intrinsically capable of regulating its own dynamics. FtsZ has been observed to assemble into straight, or slightly curved, protofilaments under physiological salt and buffer conditions[99]. GTP binding and hydrolysis were identified as key factors in driving polymer dynamics. Furthermore, it was observed that increasing Mg^{2+} or Ca^{2+} concentration induces formation of filaments which are more stable in addition to forming thick bundles by lateral interactions and reducing polymer disassembly [99].

Loose and Mitchison[208] first demonstrated that FtsZ is capable of treadmilling on supported lipid bilayers. Treadmilling was shown to require sufficient local concentrations of FtsZ, GTP binding and hydrolysis and association to the membrane via the anchor FtsA[208]. Interestingly, FtsZ filaments were shown to treadmill at similar rates to those observed *in vivo* (~30nm/s)[288,289], further suggesting that FtsZ is able to regulate its own dynamics. Cooperative assembly and treadmilling of a single stranded FtsZ filament has been proposed to be a result of FtsZ undergoing a conformational switch between an open and close formation as a result of polymerisation[226]. Thus it is possible that the switch to robust treadmilling in mature and constricting rings is due to a critical local concentration of FtsZ monomers being reached at the division site, facilitating nucleation and directional elongation of FtsZ filaments.

Further evidence of FtsZ being able to regulate its own dynamics is supported by the observation that when FtsZ is fused to a membrane targeting sequence (FtsZ-MTS), it is capable of treadmilling on supported lipid bilayers under a narrow range of Mg^{2+} concentrations [293]. Below these concentrations FtsZ is unable to bind GTP and above these concentrations FtsZ forms dense, mesh-like bundles with increased single-molecule residence times [293]. Treadmilling has not been observed in these structures, but the filaments are still known to be dynamic [293]. The formation of these structures is likely due to high concentrations of Mg^{2+} inducing increased filament budling. Similar hyper-bundled structures have been observed when the C-terminal linker (CTL) is deleted from *C. crescentus* [294]. Thus, FtsZ treadmilling appears rely on local concentrations of monomers, GTP and Mg^{2+} at the membrane. Interestingly however, FtsZ-MTS from *C. crescentus* has not been observed to treadmill directionally on supported lipid bilayers. Discrete clusters are instead observed that undergo rapid formation and disassembly[294]. This suggests that intrinsic proclivity of FtsZ to treadmill may differ between species.

The C-terminal domain of FtsZ contains the C-terminal Peptide (CTC), a disordered C-terminal linker (CTL) which separates the CTC from the GTPase domain, and a short variable sequence at the extreme C-terminus (CTV). The C-terminal has also been proposed to influence filament dynamics[295]. *In vitro* studies of FtsZ with its CTL deleted (ΔCTL) has shown a propensity of FtsZ to form bundles of polymers with greater stability when compared to wildtype FtsZ from *C. crescentus* [96,294,296] and *B. subtilis*[297]. When the CTL is deleted *in vivo* it results in aberrant Z-ring morphology and cell division in *B. subtilis*, *E. coli*, and *C. crescentus* [296,298–300]. Thus the CTL potentially plays a role in regulating the filament interactions and FtsZ dynamics. In condensed mature and actively constricting Z-rings when FtsZ filaments are in close proximity, the CTL may play in role in preventing over bundling of filaments which would increase the stability of filaments and prevent treadmilling.

However the potential exists for other factors to regulate the dynamics of FtsZ. FtsZ is known to have binding partners that regulate its localisation and structures in cells, in addition to filament dynamics and structure in purified *in vitro* systems.Thus, the regulation of FtsZ dynamics is potentially due to a complex network of interaction by a number of FtsZ binding proteins. Further investigation into their function is required in order to understand how this regulation occurs and the start of this investigation will be described in the next chapter.

However, another key question is the significance of the different dynamics in different stages of the division cycle. It is currently unclear if the static filaments observed within nascent rings display any relevant biological function. It is possible that these structures may serve as stable nucleation sites that facilitate directional elongation of FtsZ filament on the cell membrane. It is however, easier to infer the significance of the treadmilling filaments observed in this study. As stated previously, one of the most interesting observations was that in nascent rings, filament interactions were commonly observed, with two or more filaments colliding, leading to aggregation and temporary motion arrest. Previous studies have shown that FtsZ filament aggregation by lateral filament interactions is required to bundle FtsZ filaments and condense the Z-ring[96,98,164,298,301]. This is significant as it shows bi-directional FtsZ treadmilling can drive filament aggregation by increasing the likelihood of filament encounters. Parallel work by other members of the lab showed that chemical arrest of treadmilling results in Z-ring condensation being completely abolished[216]. This suggests that filament interaction is essential for condensation into the mature rings. Furthermore, these results also suggest that Z-ring condensation also promotes the switch to robust treadmilling due to the decrease in static filament population observed in mature and constricting rings. Thus filament interactions may induce robust treadmilling.

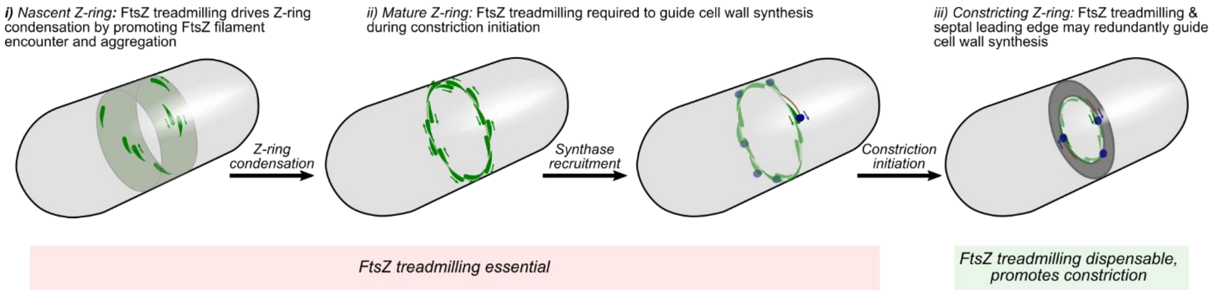

Figure 5.6: Model for function of FtsZ treadmilling in Z-ring assembly and septal constriction.

It had previously been shown that one of the roles of motile FtsZ filaments was to guide the septal PG synthases[279,280]. Research from our lab has also shown that FtsZ treadmilling is essential during the constriction initiation phase, but is not required afterwards [216]. This is in agreement with a previous studying showing that FtsZ treadmilling is dispensable following the onset of constriction in *S. aureus*[281]. Thus it is likely that FtsZ treadmilling is required during the initiation of constriction in order to guide the synthases around the division site in the absence of a defined septum. Z-ring condensation will result in the concentration of the division machinery to a small area and as condensation promotes efficient treadmilling, this may indirectly promote efficient constriction initiation by increasing the fraction of treadmilling filaments that are available to guide cell wall synthases (Figure 5.6)[290].

5.5 Conclusions and future outlook

In this chapter, I presented how VerCINI can be used as a powerful tool for ultra-sensitive measurement of cell division protein dynamics. This revealed that Z-ring undergoes three distinct phases during the division cycle: nascent, mature and constructing rings. Interestingly, nascent rings were observed to contain a large population of static filaments and a broad range of treadmilling speeds. Following condensation into a mature ring, FtsZ filaments demonstrated robust treadmilling and similar dynamics were observed in actively constricting rings.

Interestingly, filament interactions were also observed in the form of collisions, leading to aggregation and temporary arrest of the filaments involved. Parallel work by members of the lab showed that treadmilling is essential for condensation into a mature ring. This suggest that treadmilling enables FtsZ filaments to increase their likelihood of filament interactions leading to lateral interaction and the formation of the mature Z-ring.

The observation that FtsZ treadmilling is essential for the condensation of the Z-ring and thus formation of the mature divisome adds key mechanistic information to our understanding of how bacterial cell division occurs. The observation that FtsZ treadmilling drives its own condensation by promoting filament interactions brings into question the roles of the FtsZ regulatory proteins such as FtsA, SepF, EzrA and ZapA and how they act throughout the division cycle. The presence of a large population of static filaments in nascent rings suggests that the ability of FtsZ to treadmill through different stages of the division cycle is actively regulated. As we have now established VerCINI as an useful tool for studying the intricate dynamics of division proteins, we can utilise this methodology in order to examine the dynamics of key FtsZ modulating proteins relative to FtsZ itself in order to elucidate their dynamics at the divisome. Gaining an understanding of how these proteins move around the division site may give insights into their regulatory roles and this is investigated in the next chapter.

Chapter 6 : Imaging the in vivo dynamics of the FtsZ associated proteins

6.1 Introduction:

In the previous chapters I described the development of VerCINI (Vertical Cell Imaging by Nanostructured Immobilisation), a method of vertically immobilising rod shaped bacteria in order to visualise the division septum in its entirety. Using this technique, I showed that the Z-ring is composed of multiple short filaments which treadmill bi-directionally around the division plane.

Following this, I characterised the dynamics of FtsZ filaments over different stages of the cell cycle, and discovered that the Z-ring has three distinct phases: nascent, mature and constricting. Initially, FtsZ filaments form a diffuse structure at the midcell (nascent) before undergoing rapid condensation forming a dense band at the division site (mature) after which constriction is initiated.

A large population of static filaments was observed in the nascent rings, and in these rings, FtsZ filaments often collide and aggregate. Chemical arrest of treadmilling was found to completely abolish Z-ring condensation[216]. Thus FtsZ treadmilling is able to drive filament interactions by allowing FtsZ to search the division site and efficiently encounter each other. Thus both FtsZ treadmilling and filament interactions by lateral aggregations are essential for condensation of the Z-ring.

Due to the fact that FtsZ showed different dynamics in different stages of the cell cycle, I investigated the dynamics of a number of FtsZ-interacting proteins that are known to modulate its activity. Previously I observed that FtsA localises to the division site and forms a ring composed of multiple short filaments which colocalise and moves together with FtsZ around the division site[288]. FtsA is known to bind the C-terminal peptide (CTC) of FtsZ and tether it to the cytoplasmic membrane, as FtsZ has no direct affinity for the membrane itself [12]. FtsZ filaments dynamics were also shown to drive the dynamics of FtsA[288].

In order to identify potential regulators of FtsZ filament dynamics, I imaged the dynamics of DivIVA, SepF and EzrA at high spatiotemporal resolution by VerCINI. As FtsZ filaments have been observed to possess different dynamics in different stages of the division cycle, potential regulators could be identified if their dynamics also change throughout this period.

While DivIA does not directly interact with FtsZ itself, it is known to localise the Min system in *B. subtilis*, which prevents the formation of aberrant Z-rings at the cell poles[302]. However, a small amount of DivIVA also localises to the leading edge of constriction, likely to ensure that only a single Z-ring forms at the division site. Previous studies have indicated that DivIVA forms static structures as the midcel[302]. Thus, the static foci formed by DivIVA should serve as a crucial control for identifying other static components of the division machinery.

SepF is a redundant membrane anchor alongside FtsA in *B. subtilis*. While *sepF*-null mutants are viable and only have a mild division defect[303,304], these cells possess abnormally thick septa and in some cases cell separation is initiated before septal completion[304]. It has been proposed that SepF controls septal thickness by forming arcs that span the leading edge of the septa and are orientated perpendicular to FtsZ filaments[149]. This suggests that SepF may also be a static component of the bacterial division machinery, tethering FtsZ to the membrane at a precise location at division site, while clamping the growing septum in order to control its thickness.

EzrA is known to be a negative cell regulator of FtsZ with *ezrA*-null mutants showing increased indices of Z-rings in the cell[150,152,153,212]. In these mutants additional Z-rings are frequently observed at the cell poles, suggesting that EzrA may serve a Min-like function. Interestingly, EzrA deletions are synthetically lethal with SepF[304] suggesting it may play multiple roles in cell division .

The results obtained in this chapter show that both DivIVA and SepF form static foci. Interestingly, EzrA has both motile and static filaments with the majority of filaments becoming static following the initiation of constriction. The possible implications of these observations for Z-associated proteins (ZAPs) function are discussed.

6.2 Materials and methods

6.2.1 Bacterial strains and growth conditions

Strains used in this study are listed in Supplementary Table 1. Strains were streaked from -80°C freezer glycerol stocks onto Nutrient Agar (NA) plates containing the relevant antibiotics and/or inducers and grown overnight at 30°C. Single colonies were transferred to liquid starter cultures in either TLM or PHMM media and grown with agitation at 200 rpm overnight at either 30°C (TLM) or 22°C (PHMM). The next day, TLM starter cultures were diluted to a starting OD_{600} of 0.1 in CDM, while PHMM starter cultures were diluted to a starting OD_{600} of 0.05 in PHMM, and these liquid cultures were grown at 30°C or 37°C with any required inducer until they reached the appropriate OD_{600}. SepF was induced with 0.1% 1 hour before imaging as previously reported for this strain [304] .

6.2.2 Strain construction

SH136 ([*divIVA::divIVA-mCherry2::cat,* Δ*hag*]) was constructed by transforming with SH211 with genomic DNA from strain SH14.

SH137 ([*amyE::sepF-gfp-spec,* Δ*hag*]*)* was constructed by transforming with SH211 with genomic DNA from strain 4181 provided by Dr Richard Daniels.

SH138 ([*ezrA::ezrA-gfp-cat,* Δ*hag*]*)* was constructed by transforming with SH211 with genomic DNA from strain 3312 provided by Dr Richard Daniels .

SH211 ([PY79 Δ*hag*]) was constructed by transforming competent PY79 with genomic DNA extracted from strain PB5250, using standard protocols[305]. The antibiotic resistance cassette was removed using pDR224 as described previously[306].

6.2.3 Microscopy

Power density, exposure time and other key parameters are listed for each microscopy experiment in supplementary Table 1.3. All imaging was done using a custom-built inverted microscope.

Custom microscope. Cells were illuminated with a 488 nm laser (Obis) and/or a 561 nm laser (Obis) as indicated. A 100x TIRF objective (Nikon CFI Apochromat TIRF 100XC Oil) was used for all experiments except microfluidic VerCINI measurements where a 100x silicone immersion objective (CFI SR HP Plan Apochromat Lambda S 100XC Sil, Nikon) was used for deep focusing. A 200 mm tube lens (Thorlabs TTL200) and Prime BSI sCMOS camera (Teledyne Photometrics) were used for imaging, giving effective image pixel size of 65 nm/pixel. Imaging was done with a custom-built ring-TIRF module operated in ring-HiLO33 using a pair of galvanometer mirrors (Thorlabs) spinning at 200 Hz to provide uniform, high SNR illumination.

6.2.4 VerCINI

Agarose microholes were formed by pouring molten 6% agarose onto the silicon micropillar array. Patterned agarose was transferred into a Geneframe (Thermo Scientific) mounted on a glass slide, and excess agarose was cut away to ensure sufficient oxygen. Cells at OD600 ~ 0.4 were concentrated 100x by centrifugation and added onto the agarose pad. Cells were then loaded into the microholes by centrifuging the mounted agarose pad with concentrated cell culture in an Eppendorf 5810 centrifuge with MTP/Flex buckets. Unloaded cells were rinsed off with excess media.

Protein dynamics were imaged at 1 frame/s (continuous exposure) for 2 mins. After each field of view was imaged, a multi-slice Z-stack was taken at 500nm intervals to exclude tilted or improperly trapped cells, in addition to excluding protein rings that have an adjacent ring 1µm above or below the imaging plane. VerCINI experiments were performed on cells in a Δhag mutant background, preventing undesirable cell rotation within the microholes by disabling flagellar motility.

6.2.5 VerCINI data analysis

Pre-processing Videos were denoised using the ImageJ plugin PureDenoise[251], which is based on wavelet decomposition. Key assumptions of the method are (i) local spatiotemporal similarity within the image (ii) absence of sharp discontinuities, guaranteed by diffraction-limited nature of the image. The denoising algorithm makes does not make any assumptions on the type of underlying biological structure.

Denoised videos were registered using the ImageJ plugin StackReg[252]. Image stacks of vertically immobilised cells were inspected to exclude tilted cells or out of focus rings, or rings where a second ring was closer than 1 um to the focal plane. Cropped region of interest movies containing single in-focus cells were manually selected and exported for analysis. An ImageJ package for VerCINI data processing is available (https://github.com/HoldenLab/Ring_Analysis_IJ).

VerCINI background subtraction, kymograph extraction, quantification

Custom software for quantitative cytoplasmic background subtraction and kymograph extraction was developed for analysis of VerCINI movies (https://github.com/HoldenLab/ring-fitting2). Fluorescence images of isolated vertical cells were fitted to a joint explicit model for diffuse out-of-focus cytoplasmic background (Gaussian + Cauchy model) plus septal protein signal, modelled as a 12 sectored annulus with each sector of variable amplitude.

$$F(x,y) = Signal(x,y) + Bg(x,y)$$

Signal is calculated in polar coordinates, around the septal ring centre fit parameter (x_0, y_0), and then transformed into Cartesian coordinates. Signal is defined as

$$S(r,\theta) = A_i(\theta)\exp\left(-\frac{(r-R_0)^2}{2\sigma^2}\right),$$

where $A_i(\theta)$ defines a 12 sectored ring. Background is defined as

$$Bg(x,y) = a\exp\left(\frac{-((x-x_0)^2+(y-y_0)^2)}{2\sigma_{bg1}^2}\right) + b\frac{\sigma_{bg2}^2}{(x-x_0)^2+(y-y_0)^2+\sigma_{bg2}^2} + c.$$

This explicit model allowed accurate sub-pixel location of a circular line profile at the septal leading edge. Explicit subtraction of complex background signal also allowed septal intensity quantification. The background subtracted intensity along the circular line profile was then calculated for each frame and automatically plotted as a kymograph. Kymographs were plotted over the [0,720°] ie two complete revolutions around the line profile for ease of visualization, specifically to allow straightforward visualization of motile filaments crossing the 360°,0° boundary. For each cell, the Z-ring diameter was determined from the fitted model in the kymograph extraction step. Median septal intensity was calculated as the median value of all kymograph pixels from the first 60 image frames.

Protein dynamics analysis using VerCINI

We performed manual measurement of protein speed and processivity by kymograph analysis, annotating proteins as lines in ImageJ and then measuring the angle via ImageJ script. As the intensity range across kymographs is large, manual detection and analysis of filaments was aided by applying a ridge filter[253] to the kymograph which detects ridges in the image, independent of absolute intensity. The ridge filter consists of a Gaussian blur operation to set the feature scale and suppress noise (here 2 pixels, 130 nm), followed by calculation of the major eigenvalue of the Hessian matrix for each pixel, implemented as an ImageJ macro in the package listed above. Joint annotation of the ridge filtered and raw intensity kymograph was performed, allowing sensitive annotation of both bright and dim filaments.

6.3 Results

DivIVA dynamics were obtained by imaging a strain expressing a DivIVA-mCherry2 construct (SH136). As expected, DivIVA localised to the division site forming a ring like structure that spanned the entirety of the midcell. DivIVA was also found to be static throughout different stages of the cell cycle (Figure 6.1 and 6.4A). This is consistent with previous findings that DivIVA forms a marker of the cell poles and division septum [182,184,302]. DivIVA is also long lived at the division and tracks were most often observed spanning the entity of the kymographs (Figure 6.1). Though these results indicate that DivIVA has a median lifetime of 113s (IQR 64-117s N=188), this estimate is likely limited by the total imaging time (120s). As one would expect due to the static nature of the DivIVA-ring at the division site, DivIVA did not processively move around the division site.

The dynamcis of SepF were found to be similar to DivIVA. SepF dynamics were obtained by imaging a strain expressing a SepF-GFP fusion protein under the control of a xylose promter integrated at *amyE* alongside wt (SH137)[307]. The results show that SepF froms static foci at the midcell across a range of diameters. This suggests that SepF is static throughout the enitre cell cycle and thus does not move processively around the division site (Figure 6.2 and Figure 6.4). Like DivIVA, SepF was often to be found to be static throughout the entiry of the aquistion perid and had a median lifetime of 114s (IQR 91-116, N=160). Again, this is likely limited by the total imaging time (120s).

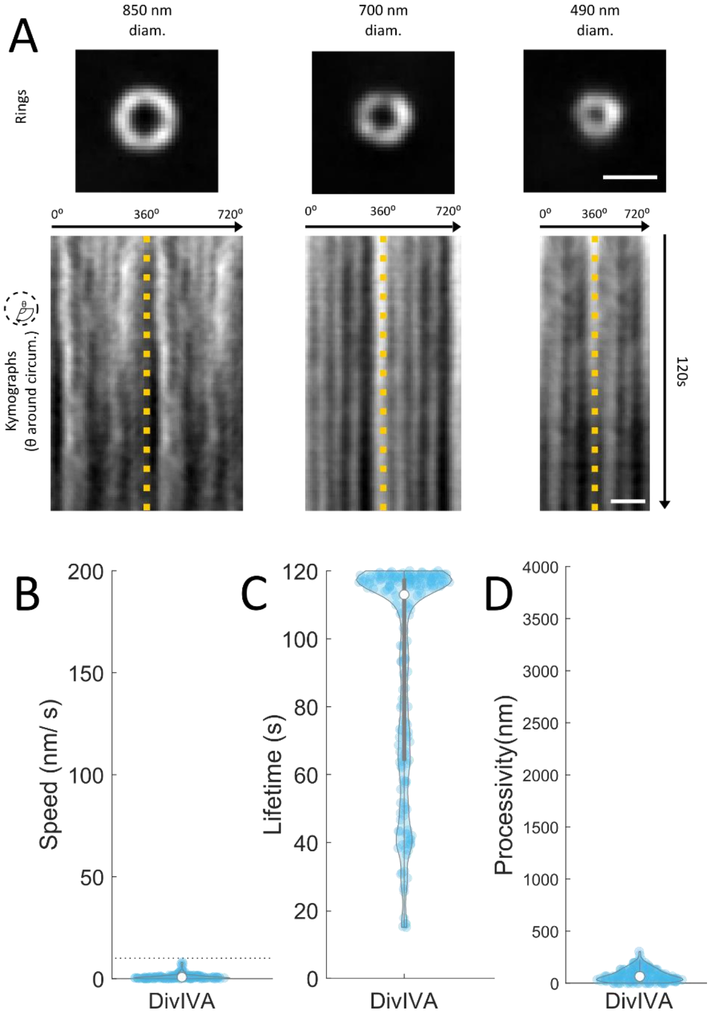

Figure 6.1: **DivIVA is static at the midcell**. **(A)** Representative kymographs of DivIVA-mcherry2 dynamics (SH136 [*(divIVA::divIVA-mCherry2::cat, Δhag)]*). Kymographs were obtained by fitting septal images to circles and plotting intensity values around the circumference of the cell for each frame of the time-lapse (1 frame/ s). Two full revolutions around the cell (0-720°) are plotted side-by-side in each kymograph to resolve filament trajectories that pass 0°/360°, separated by yellow dotted lines. **(B)** Speed distribution, **(C)** Filament lifetime (time bound to septum). **(D)** Filament processivity (distance filament treadmills around septal circumference). Violin plot: white circles, median; thick grey lines, interquartile range; thin grey lines, 1.5x interquartile range.

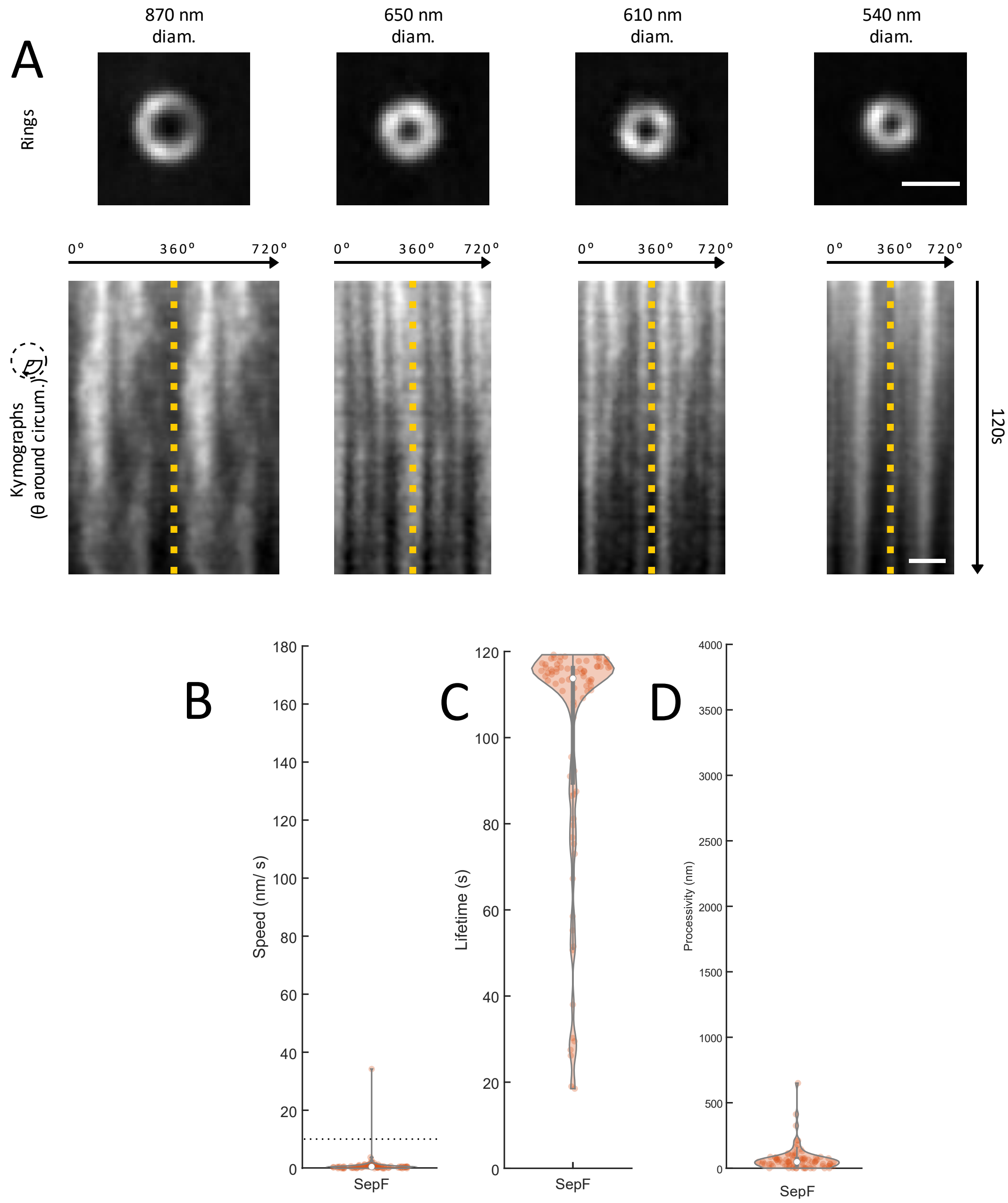

Figure 6.2: **SepF is static at the midcell**. Representative kymographs of SepF-GFP dynamics (SH137 [*amyE::sepF-gfp-spec, Δhag*]). Kymographs were obtained by fitting septal images to circles and plotting intensity values around the circumference of the cell for each frame of the time-lapse (1 frame/ s). Two full revolutions around the cell (0-720°) are plotted side-by-side in each kymograph to resolve filament trajectories that pass 0°/360°, separated by yellow dotted lines. **(B)** Speed distribution, **(C)** Filament lifetime (time bound to septum). **(D)** Filament processivity (distance filament treadmills around septal circumference). Violin plot: white circles, median; thick grey lines, interquartile range; thin grey lines, 1.5x interquartile range. SepF was induced with 0.1% 1 hour before imaging.

EzrA dynamics were obtained by imaging an EzrA-GFP fusion protein that acted as the sole source of EzrA in the cell (SH138). The dynamics of EzrA are arguably the most interesting of the proteins imaged in the chapter. Kymographs revealed that EzrA was neither truly static nor motile, showing a mixed population (70% static, 30% motile). Thus EzrA moves with a low median velocity of 5 nm/s (IQR 2-13 nm/s, N=857) and a median lifetime of 19s (IQR 28-40s, N=587). Thus, due to the low speed of EzrA it also has a low median processivity 152 nm (IQR-65-336 nm). Interestingly the dynamics of EzrA seemed to be regulated by division stage. Rings with a diameter greater than 800nm showed a mixed population of static and motile foci, however, below 800 nm the vast majority of filaments become static (Figure 6.3B).

As DivIVA is known to be a static component of the division machinery, we used the speed measurements obtained from imaging this protein in order to define static components of the divisome. As such, we define a static foci as one which moves with a speed below 10 nm/s. Using this measurement, we were thus able to robustly separate static and motile EzrA populations. When the median speeds of the motile EzrA population were determined (median 23nm/s, IQR 15-33 nm/s, N=257) this was found to be similar to the average treadmilling speed of FtsZ (median 25nm/s, IQR 15-33nm/s).

As would be expected, static EzrA populations display very low processivity (median processivity 90nm, IQR 30-160nm, N=600) compared to motile EzrA (median processivity 480nm, IQR 350-670nm). Static EzrA assemblies also displayed a longer lifetime than motile assemblies (static median lifetime 30s, IQR22-46s; motile median lifetime 20 s, IQR 22-46s).

As can be seen from Figure 6.4 DivIVA and SepF display similar dynamics in terms of speed, lifetime and processivity, consistent with their suggested role as structural divisome components. FtsZ filaments and EzrA display similar lifetimes, but EzrA displays many more static filaments and thus a lower processivity. Due to the observation that FtsA displays a similar speed distribution as FtsZ (Chapter 2) this suggests that the FtsZ associated proteins can be split into three categories; motile (FtsZ and FtsA), static (SepF) and mixed populations (EzrA).

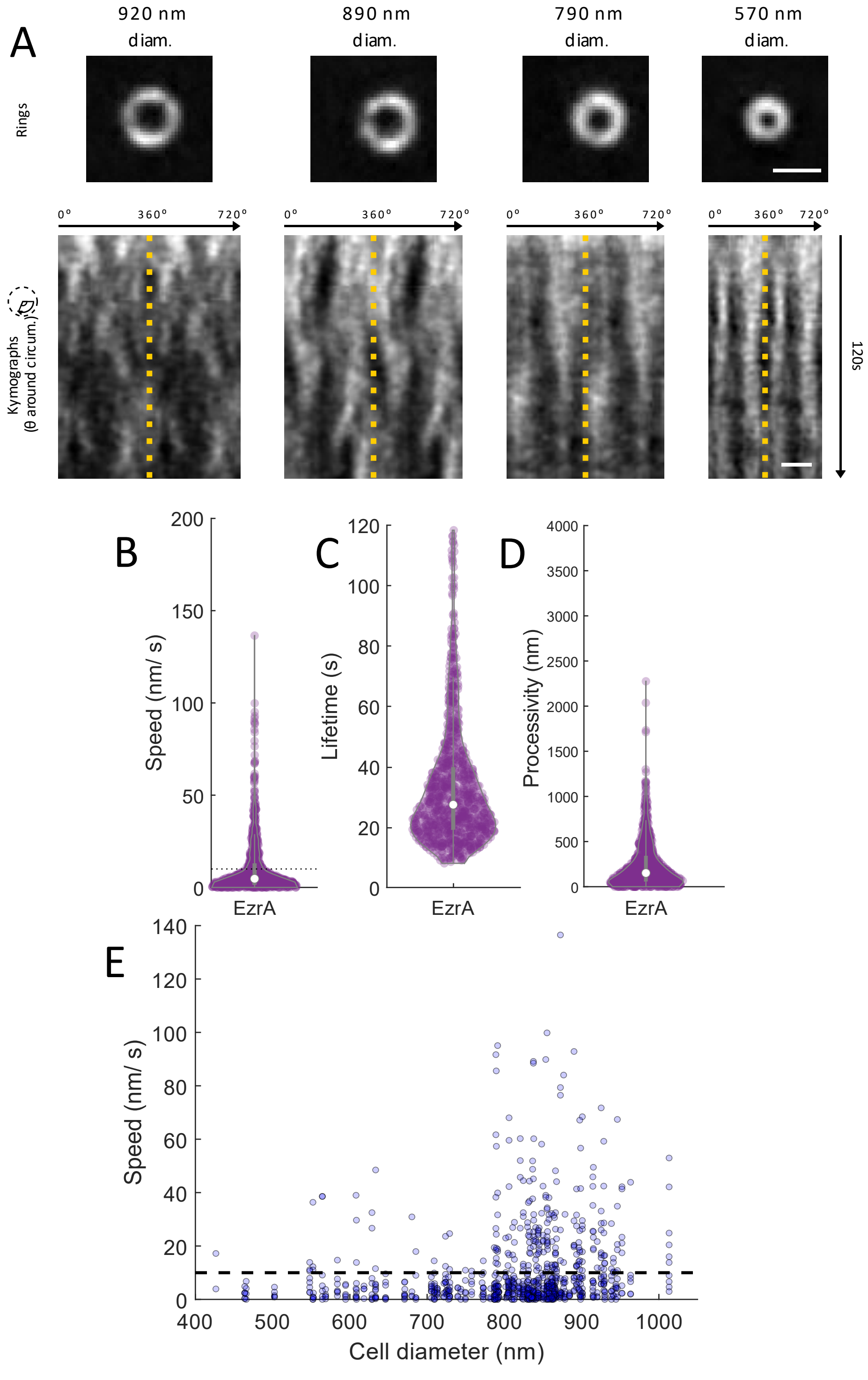

Figure 6.3: EzrA dynamics have mixed populations. **(A)**Representative kymographs of EzrA-GFP dynamics (SH138 *[ezrA::ezrA-gfp-cat, Δhag])* Kymographs were obtained by fitting septal images to circles and plotting intensity values around the circumference of the cell for each frame of the time-lapse (1 frame/ s). Two full revolutions around the cell (0-720°) are plotted side-by-side in each kymograph to resolve filament trajectories that pass 0°/360°, separated by yellow dotted lines. **(B)** Speed distribution, **(C)** Filament lifetime (time bound to septum). **(D)** Filament processivity (distance filament treadmills around septal circumference). Violin plot: white circles, median; thick grey lines, interquartile range; thin grey lines, 1.5x interquartile range. **(E)** EzrA dynamics are seemingly abolished following constriction initiation.

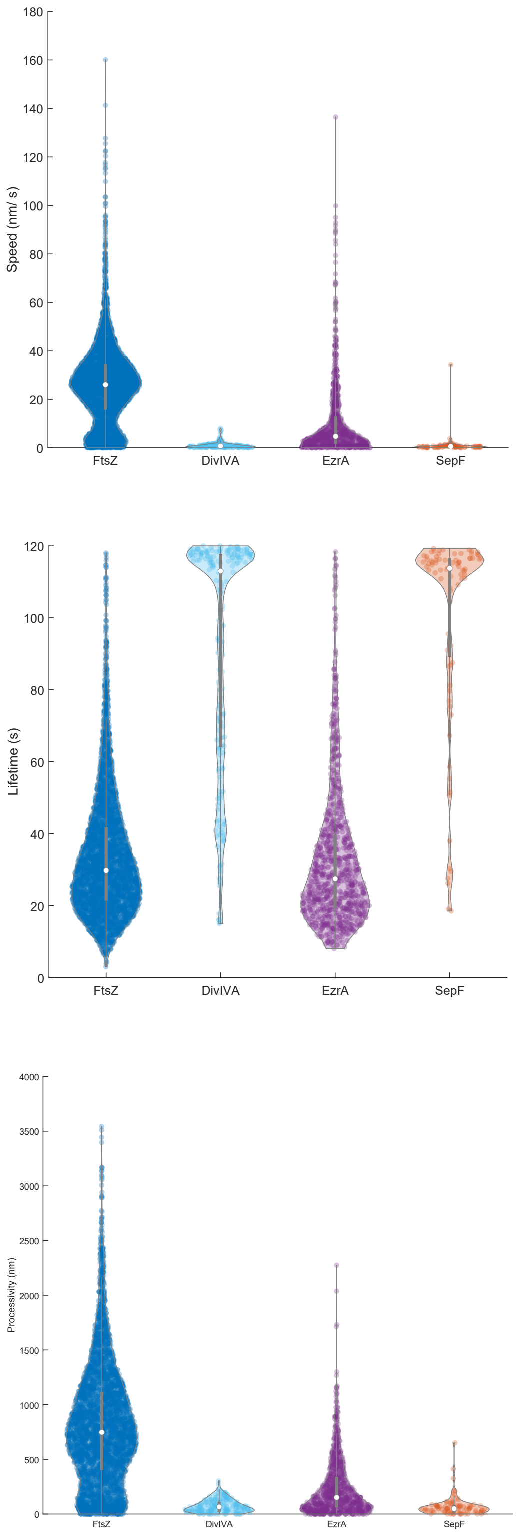

Figure 6.4 Comparisons of FtsZ modulating protein dynamics. Violin plot: white circles, median; thick grey lines, interquartile range; thin grey lines, 1.5x interquartile range.

6.5 Discussion

In this chapter, I imaged the dynamics of three FtsZ associated proteins (ZAPs) with the aim of identifying candidates that may regulate FtsZ filament dynamics across different stages of the division cycle. Over the course of this PhD project, I imaged the dynamics of FtsZ, FtsA, DivIVA, SepF and EzrA and observed that the dynamics of these division proteins can be broadly split into three different categories. The first of these groups is the dominantly motile Z-associated proteins which includes FtsA and FtsZ itself. The second group is the static architectural divisome proteins and includes DivIVA and SepF. As a negative curvature sensor DivIVA is known to localise to the cells poles and the leading edge of invagination in order to localise the Min proteins, which prevent aberrant Z-ring formation [179,180,302]. SepF is thought to be a redundant membrane anchor alongside FtsZ in Gram-positive bacteria and Cyanobacteria[148,307]. However SepF is also thought to act as a molecular clamp in order to control septum thickness[149] . The third category includes proteins that are neither fully motile or static, which currently includes only the negative FtsZ regulator EzrA.

6.5.1 DivIVA and SepF form static structures, consistent with their suggested roles as architectural division proteins

Although DivIVA does not interact directly with FtsZ, it is responsible for localising the Min system and thus plays an important role in the regulation of the Z-ring[178,179]. Kymographs of DivIVA protein dynamics revealed that DivIVA forms static long-lived structures close to the division site consistent with previous studies[308]. The observation that DivIVA is static at the midcell is also consistent with its proposed function during the division process. As DivIVA has an intrinsic affinity for the negatively curved membrane, it readily localises to the cell poles [180,309]. Here it recruits MinJ, which acts as a bridging protein for the recruitment of MinD[182,183]. However, a small amount of DivIVA also localises to negatively curved regions of the growing septum in order to prevent the formation of multiple additional Z-rings following the start of the constriction process[310]. These measurements also act as useful technical control for measurement of other ZAP protein dynamics as an observation of a static stable protein at mid cell. The observation that the DivIVA ring constricts is also consistent with pervious results in the literature as Eswaramoorthly observed DivIVA-GFP rings associated with the septum steadily decreased in diameter [308].

We also observed that SepF forms static structures in live cells, which also supports its suggested roles during the division process. SepF has been proposed to be an redundant membrane anchor alongside FtsA. It has also been suggested that SepF forms arc-like filaments which align perpendicularly over the leading edge of the division septa acting as a molecular clamp to control septum thickness[149]. If SepF does in fact form arcs that align perpendicularly to the nascent septum this may explain its static and long lived dynamics. It is possible that while acting as a molecular clamp to control the thickness of the septum, SepF may additionally act in a similar fashion to the ballast of a railway track, with FtsZ filaments assemble on top of SepF arc like rails, a fitting analogy as FtsZ also acts as a guide for the synthesis machinery. This could also result in SepF aiding in keeping the Z-ring in the correct position. While FtsZ-treadmilling would still be essential for driving filament interactions which lead to condensation of the Z-ring to a tight band at the midcell, SepF arcs could prevent the Z-ring from moving position following its assembly, or preventing the Z-ring from slanting. This may also explain the fact that deletions of *sepF* result in highly deformed septa. While both FtsA and SepF act as membrane anchors, FtsA moves alongside FtsZ. Thus as the dynamics of FtsA rely on the treadmilling activity of FtsZ, FtsA may not keep FtsZ "locked" into position as well as the static SepF, explaining the deformed septum in its absence. Despite this, *ftsA* null mutants display a more pronounced phenotype suggesting it may be the more important anchor. It is likely that both SepF and FtsA work in tandem, having overlapping roles in tethering FtsZ to the membrane in addition to distinct roles that contribute to efficient cell division.

6.5.2 EzrA displays of a mixed population of static and motile dynamics in pre-constricted rings.

Of the protein dynamics imaged in this chapter EzrA is perhaps the most intriguing yet confusing. EzrA is a spectrin-like protein[311] and though its exact role in cell division is unclear, it is thought to be a negative regulator of the Z-ring by preventing Z-ring formation[153,212]. While DivIVA and SepF were found to form static structures, and FtsA has previously been shown to localise and co-treadmill with FtsZ, EzrA fits into neither of these categories. Kymographs of EzrA dynamics revealed mixed static and motile populations. The majority of EzrA tracks become static once the ring diameter decreased below 800nm, while prior to this a mixed population of static and motile filaments was observed. As EzrA is known to be a negative regulator of the Z-ring [212], its presence at the midcell throughout the division period seems contradictory. Thus the fact that EzrA displays a range of dynamics suggests that it displays multiple roles throughout the division cycle. This is supported by the observation that EzrA switched to a majority of static filaments following the initiation of constriction. EzrA may potentially move around the division site, destabilising FtsZ filaments prior to the initiation of constriction. Following a signal that it is time to divide, EzrA may then form static assemblies performing a function analogous to the Min system.

6.5.3 The dynamics of FtsZ binding proteins still to be determined

An additional regulator of FtsZ is ZapA and although the dynamics of this protein were not able to be imaged during the course of this project, its role in modulating FtsZ filaments warrants discussion. Purified ZapA has been shown to cause FtsZ filaments to form stable, multifilament bundles *in vitro* under specific conditions [157,301]. These observations lead to an initial model being proposed whereby ZapA acts as an FtsZ stabiliser, causing filaments to bundle by promoting lateral interactions and slowing subunit turnover. However, a recent study by has indicated that ZapA does not alter the dynamics of FtsZ on supported lipid bilayers *in vitro* [164]*.* Instead, ZapA was shown to align FtsZ filaments in parallel. This resulted in filament bundles straightening and stabilizing[164]. As such, the spatial order and spatiotemporal persistence of the large scale filament network was increased. Thus it possible that ZapA aids in condensation of the Z-ring. ZapA may help in aligning FtsZ filaments in a parallel fashion from their diffuse and stochastic distribution around division site. It is possible that FtsZ and ZapA work cooperatively to stimulate ZapA recruitment and the formation of the mature, condensed Z-ring. ZapA is known to form a tetramer and, because of its central four-helix structure, it is assumed that the ZapA tetramer is a rigid structure [164]. Due to the ZapA tetramers inflexibility, it has been suggested that the only way all four binding domains of the tetramer could be in contact with an FtsZ monomer would be if filaments were aligned in a straight and parallel fashion[164]. We observed treadmilling FtsZ filaments in nascent rings colliding and interacting, it is thus possible that when this occurs, ZapA would straighten the filaments and organise them in a parallel fashion, helping to define the position of the mature Z-ring, and thus providing spatial order. As such, investigating the dynamics of ZapA in *in vivo* would provide invaluable insights into its *in vivo* role in FtsZ regulation.

FtsA is the best characterised membrane anchor and is a well conserved actin homologue that binds to the CTC of FtsZ, tethering it to the membrane via its N-terminal amphipathic helix [248]. ,I measured the dynamics of FtsA (chapter 2), which colocalises and moves with

FtsZ, supported by evidence that FtsZ and FtsA form co-assemblies capable of treadmilling on supported lipid bi-layers[125]. Furthermore, the treadmilling activity of FtsZ has been shown to drive the dynamics of FtsA[1]. Co-treadmilling of FtsA with FtsZ would allow FtsZ to stay associated with the membrane for longer periods. This is due to the fact that as FtsZ has no direct affinity for the membrane, its bridging contact would move with it, allowing it to stay associated in transit. Although the speeds of FtsA were determined in the previous chapter, this was done with a strain that had undergone a duplication event as described in chapter 3. As such, other measurements such as processivity and lifetime were not conducted due to the unreliability of measurements associated with this strain. Thus it would beneficial in future work to remeasure the dynamics of FtsA with a functional, single copy replacement.

6.5 Conclusions and future outlook

During this chapter I imaged the dynamics of DivIVA, SepF and EzrA, proteins that have each been suggested to play a role in modulating the dynamics of FtsZ filaments. The results obtained show that DivIVA and SepF were static at the division site, consistent with their proposed role as architectural division proteins. However, it is clear that many questions remain regarding the exact nature of the FtsZ modulating proteins. The observation that EzrA shows a mixed population of static and immobile filaments in pre-constricted rings, before switching to a predominantly static population may suggest it plays a role in regulating FtsZ filaments dynamics in the early stages of cell division, however, much work remains to unravel the biological significance of these observations. Ideally, dual colour imaging would could be conducted to effectively correlate the different dynamics of EzrA to the nascent, mature and constricting phases that Z-rings undergo.

Additional future work should involve imaging the dynamics of ZapA and a native FtsA replacement *in vivo* in order to observe its affects in FtsZ dynamics in the cell. Furthermore the dynamics of FtsZ in the absence of FtsA, SepF, EzrA and ZapA should be investigated using VerCINI. However, this should be conducted alongside conventional flat pad imaging in order to investigate if processes such at the time to condense Z-ring are affected. Additionally, localisation microscopy could be conducted on these deletions, both with VerCINI and flat-pad imaging to investigate the effects of the Z-associated proteins on Z-ring ultra-structure.

Chapter 7 : General discussion and outlook

Bacterial cell division is an inherently dynamic process. A remarkable feat of molecular self-assembly, cell division occurs by the action of a nanoscale divisome machine which builds a micron-scale wall at the midcell known as the septum. The core components of the divisome include the septal cell wall synthases which insert new PG to build the septum and the almost universally essential cytoskeletal tubulin homologue FtsZ which polymerises into a dense Z-ring composed of short filaments at the division site [109,113,119]. One of the Z-ring's major functions is to act as a scaffold, recruiting the proteins essential for the formation of the mature divisome[97].

It is well established that the Z-ring is a highly dynamic structure with FRAP experiments showing that the Z-ring undergoes constant remodelling. Subunits are readily exchanged between the ring and the cytoplasm with the Z-ring undergoing complete turnover in <10s[206,207]. To elucidate the key mechanistic principles of bacterial cell division, we attempted to solve why midcell FtsZ displays rapid turnover *in vivo.*

7.1 The benefits of vertical immobilisation

The organisation and dynamics of proteins in bacteria are difficult to measure as their cells are not much larger than the diffraction limit of light. Imaging the division machinery of rod shaped cells like *B. subtilis* is further complicated by the fact they lay flat on a coverslip. This rotates the division machinery out of the imaging plane, causing it to be projected as a dense 2D-band at the midcell. As conventional widefield microscopy has an axial resolution of ~500nm[312], measurements of FtsZ dynamics would be limited to nascent Z-rings- diffuse structures composed of isolated filaments prior to condensation into a mature ring. Once the Z-ring has begun to constrict, the axial diffraction limit would make it impossible to resolve individual FtsZ filaments. Furthermore, as the Z-ring is projected as a 2D-band, tracking individual filaments is hindered by low SNR due to the fluorescence from out of focus filaments within the ring, and cytoplasmic FtsZ, contributing to the background noise. This makes it difficult to identify filament dynamics from the noisy cell background. Although TIRF microscopy is able to increase the SNR and increase axial resolution to 50-100nm [109], observation of FtsZ filament dynamics would again be limited to rings in the earliest stages on constriction. This is because the evanescent wave generated during TIRF imaging decays exponentially and thus only penetrates about 100nm into the sample [41]. As such, the Z-ring would inevitably move out of the illumination field during the constriction process.

We resolved the above problems by vertically immobilising cells in nanofabricated chambers[1]. Silicon micropillars were used to micropattern agarose, resulting in the formation of microchambers in which cells could be trapped. This technique allows the rod-shaped bacteria to stand up-right instead of lying flat on the coverslip. This results in the division machinery being rotated into the imaging plane, allowing the Z-ring to be viewed in its entirety. While this technique does not increase the optical resolution of the microscope, rotation of the Z-ring into the XY plane allows its entire circumference to be visualized at ~250nm resolution, as opposed to the 500nm resolution when viewed by conventional microscopy. This allows us to probe the dynamics of FtsZ filaments around the entire circumference of the division site, even in actively constricting cells. Using this technique also circumvents the need for super-resolution microscopy techniques that often require higher light doses and image reconstruction which increases the possibility of imaging artefacts being introduced.

7.2 Treadmilling is a conserved and intrinsic property of the FtsZ filament

As stated previously, a major advantage of the vertical immobilisation technology was that it allowed us to investigate the dynamics of individual FtsZ filaments in actively constricting rings, a feat that had not previously been achieved *in vivo*. Imaging using this technology revealed that the Z-ring is composed of multiple filaments that move bi-directionally around the division plane, with these dynamics continuing in dense, actively constricting rings[1]. Together, with the findings that individual subunits are immobile, this showed that FtsZ motion is the result of treadmilling [1]. Simultaneously, FtsZ filaments were shown to treadmill in a parallel study in *E. coli* [210]*.* Although FtsZ had previously been shown to treadmill *in vitro*[125]*,* it was unclear if this represented FtsZ's true behaviour *in vivo* or simply an ability of FtsZ under strictly regulated conditions. Interestingly, not only was FtsZ observed to treadmill *in vivo*, but this was the dominant behaviour of filaments, with over 80% the filaments undergoing treadmilling. This was significant as filament treadmilling is a difficult property to achieve and as treadmilling was the dominant behaviour observed, suggesting that it may play an essential role during the division process. This is further supported by the observation that FtsZ has been observed to treadmill in a range of other bacterial species including both *S. aureus* and *S. pneumoniae* [223,224]*.* This suggests that treadmilling is an intrinsic property of FtsZ and its conserved nature indicates it is essential to its function across a diverse range of organisms.

Treadmilling of cytoskeletal filaments is a useful property as it allows the filament to push or pull molecules in a cell in the absence of motor proteins, provided end-tracking mechanisms or co-factors exist[226]. Despite this, the initial observation that FtsZ is capable of treadmilling *in vitro* was surprising as FtsZ was not thought of as a good candidate for treadmilling behaviour. This is because robust treadmilling is not achievable for an isodesmic filament that is composed of rigid subunits[226]. Since the discovery that FtsZ treadmills, several studies have been published with models explaining how both cooperative assembly and treadmilling occurs for a single stranded filament. One of the key steps in developing these models was the observation that FtsZ is able to undergo a confirmational shape change as a result of filament polymerisation [226]. These models suggest that polymerisation of FtsZ results in a confirmational shape change from a relaxed (R) to tense (T) structure with monomers having a greater affinity for other subunits when in the T state [231,232]. Thus the conformational switch increases the affinity of monomers within the filament for other monomers of FtsZ, regardless of whether they are in the R or T state.

This conformational switch also explains why the filament does not fragment, allowing treadmilling to be a robust process. Monomers within the filament would be held in their high affinity T-state regardless of the bound nucleotide, due to their interactions with two other FtsZ monomers locking them in this form. On the other hand, the nucleotide at the shrinking end of the filament would be the most likely to dissociate as it possess only a single protein-protein interaction and is more likely to have to hydrolysed GTP.

Another significant implication of bi-directional treadmilling is that it also explains the patchy, heterogeneous organisation of the Z-ring. Previous super resolution microscopy studies suggest that the Z-ring is a loose , patchy toroidal band that is about 80-100nm thick radially [115,117,313]. The bi-directional treadmilling of FtsZ filaments around the division plane would lead to stochastic aggregations as well as gaps in the Z-ring, explaining why super-resolution imaging of the Z-ring has shown regions of high and low FtsZ intensity. Filament treadmilling would also explain the large scale reorganisation of the Z-ring that was observed by Strauss *et al* [113] when using 3D-SIM to investigate the Z-rings of *B. subtills* and *S. aureus*. Previous *in vivo* studies on FtsZ dynamics revealed that individual subunits were stationary, arguing against the model in which FtsZ filaments were capable over traversing the division site by filament sliding[124]. Treadmilling however reconciles how individual subunits can be static while the Z-ring still displays largescale re-organisation.

7.3 FtsZ-treadmilling is required for synthase motion

During this project, as part of a collaboration it was shown that FtsZ treadmilling was required for the dynamics of both FtsA and PBP2B[1]. This was simultaneously shown in *E. coli*[210]*.* FtsZ treadmilling was required for synthase motion in addition to setting the speed of individual synthases. In *B. subtilis*, modulating the speed of FtsZ treadmilling was observed to affect the rate of septal constriction.

Interestingly however, altering the speed of FtsZ treadmilling did not affect constriction time in *E. coli*. Although the treadmilling rate of FtsZ filaments sets the speed of individual synthases, it has no effect on the overall time of division [210]. This may be due to the fact that as *E. coli* only maintains a single layer of peptidoglycan, more control is required to prevent lysis when compared to the thick, multi-layered cell wall of *B. subtilis*. Furthermore, *E.coli* must coordinate constriction with the remodelling of its outer membrane, a feature which *B. subtilis* lacks. These factors could therefore act as additional brakes on cell division such that while FtsZ treadmilling is rate limiting for the speed of individual synthases, it is not rate limiting for the overall constriction process.

7.4 Implications on force generation

One of the key outstanding questions regarding cell division is how the divisome is able to generate the constrictive force required to oppose the cell's high turgor pressure. The observation that FtsZ treadmills also has significant implications for its suggested role as a force generator. One of the historically favoured models of Z-ring force generation is the contractile ring model. In this model, the Z-ring would form a continuous ring from either a single continuous filament or multiple overlapping short filaments[314]. The Z-ring would then be capable of generating sustained force around the entire division site by GTPase induced filament bending or by the sliding of multiple, overlapping filaments. However, as individual monomers within the Z-ring are stationary, filaments do not slide, and thus a sliding filament model is not compatible if FtsZ is a force generator.

In terms of force generation, the observation that treadmilling FtsZ filaments facilitate cell division through the action of motile cytoskeletal-synthase complexes imposes specific constraints on a Z-centric force generation hypothesis. This is because a treadmilling filament would be unable to generate sustained force on the membrane. However, this problem could be circumvented by the PG synthases incorporating new PG to reinforce these deformations. This would allow treadmilling filaments to transiently deform the membrane through GTP-induced bending of short, treadmilling filaments. Importantly, this model would require FtsZ filaments to form lateral interactions as single filaments would be free to rotate on the membrane upon bending. Alternatively, the synthase complex alone may provide enough force to push in on the membrane, utilising FtsZ as a passive guide for localisation at the midcell. Additionally, a combination of these two scenarios may exist, with the FtsZ filament and synthase complex working in tandem to produce the force required to deform the membrane.

7.5 Initial model of *B. subtilis* cell division

Cell division in *B. subtilis* is the result of discrete, motile enzyme-filament complexes driven by FtsZ treadmilling. This results in new septal PG being built in transit, with FtsZ creating long-range order from the local activity of PG synthases, linking circumferential enzyme motion to the insertion of cell wall. This lead to us proposing an initial model in which FtsZ acts as an obligatory guide for septal synthases. In this model FtsZ treadmilling would be the rate limiting step for PG synthesis. However, it was later shown that FtsZ-treadmilling is dispensable following the initiation of constriction in *S. aureus*, another Gram-positive organism [223]. This suggested that FtsZ dynamics may play different roles in different stages of the division cycle. Ergo, we sought to investigate the dynamics of FtsZ across different stages of the division cycle.

7.6 Identification of strain issues

After initial classification of FtsZ and FtsA dynamics, we became aware of a number of issues regarding the strains used to collect these measurements. Initially we were under the impression that all single colour experiments conducted in chapter 2 were FtsZ measurements. However, after investigation, we determined that the microscopy experiments conducted to determine the dynamics of mNeonGreen-FtsZ were actually performed on FtsA-mNeonGreen. Furthermore, we originally thought that the FtsA and FtsZ fusion proteins used in chapter 2 were single copy replacements. Although this was the case for the well-established and characterised FtsZ-GFP fusion protein[212], we discovered that all strains expressing mNeonGreen or HaloTag fusions had undergone a duplication event. This resulted in strains expressing two copies of the FtsAZ operon, one wildtype and one with the respective fusion protein.

Western blots revealed that the actual strain expressing mNeonGreen-FtsZ expressed this construct alongside wildtype FtsZ though at much lower levels. As such, all strains used in chapter 2 were sent for whole genome sequencing and this confirmed that the strains expressing mNeonGreen or HaloTag fusions has undergone a duplication event. Our collaborators then assessed weather these constructs were capable of complimenting native deletions. While cells were viable and displayed normal morphology when expressing FtsA-mNeonGreen as the sole source of FtsA in the cell, mNeonGreen-FtsZ was unable to compliment native deletion. As such, our collaborators performed crucial control experiments to confirm that the findings of the published work were not affected by these issues. A correction confirming this conclusion has now been published[2].

Due to these issues, I further characterised the FtsZ-GFP strain (SH13). Western blots confirmed that FtsZ-GFP was the sole source of FtsZ in the cell. Furthermore, although this strain displayed a mild elongation phenotype at 30^{o}C and 37^{o}C in both minimal and media conditions, growth rate was not impaired in either media, in either conditions[216]. Thus due to the fact that FtsZ-GFP can support growth with only a mild elongation phenotype, this construct was used for future experiments.

7.7 Functionality of fluorescent fusion proteins

One point that became evident over the course of this thesis was the observation that FtsZ is a notoriously difficult protein to create a functional fluorescent variant of, as demonstrated by the duplication event that occurred when attempting to make FtsZ-mNeonGreen fusion proteins. This difficulty is also highlighted throughout the literature. Initially, carboxyl and amino terminal fusions were created in order to observe localisation and dynamics of FtsZ in live *E. coli* cells[248]. However, neither of these fusion proteins were able to act as the sole source of FtsZ in the cell. Instead. Correct localisation was only observed when expressed at a concentration lower that that of wild-type FtsZ[248]. As such, this suggests that these FtsZ fusions were able to localise and copolymerise with wild-type FtsZ but when expressed at higher levels some function of the filament is interfered with.

Despite this, Levin *et al.* successfully created a of FtsZ-GFP fusion protein that was capable as acting as the sole source of FtsZ in the cell though strains expressing this construct exhibited a temperature sensitive phenotype[212]. Strauss *et al.* later created a similar FtsZ-GFP fusion protein which they utilised for SIM imaging[131] and Fluerie et al also incorporated *ftsZ-gfp* into the genome of *S. pneumoniae*[246] . However, the creation of fluorescent proteins with improved photo-physical properties created an intriguing conundrum for those whishing to study the Z-ring by fluorescent microscopy- is possible to create new, functional FtsZ-fusion proteins with improved fluorescence properties. This was achieved by Jacq *et al*. who successfully created an FtsZ-spDenda2 fusion protein for the use of PALM analysis in *S. pneumoniae* [247].

Thus, attempts to were made by collaborators to produce an mNeonGreen-FtsZ fusion protein due to mNeonGreen being three to five times brighter than GFP[213]. As such, this would translate to a higher signal, potentially allowing the use of lower laser intensities meaning less perturbation to the cell. However, as indicated by the results, mNeonGreen-FtsZ was unable to compliment native FtsZ and would only support cell growth when expressed alongside its native counterpart. The difficulties in creating functional FtsZ fusions likely arises from the importance of both the N- and C-terminal domain of FtsZ. The N-terminal domain possess the nucleotide binding pocket while the C-terminal domain possess the CTC essential for membrane binding, in addition to the CTL which is thought to play a role in filament bundling[202]. Interestingly, the ability of the FtsZ-GFP fusion protein to be able to act as the sole source of FtsZ in the cell may relate to the fact that the GFP used in these experiments is not monomeric. As such, this may compensate for a decreased propensity for filaments to bundle when a C-terminal fusion is used. To assess this, a point mutation would be made within the GFP region to convert it to its monomeric form.

Due to the difficulties in creating classical N- and C-terminal FtsZ fusions, attempts have been made to search for a better site of insertion through the creation of sandwich fusions. Previous success with sandwich fusions has been shown bu Bendezú *et al.* used this concept to insert red fluorescent protein (RFP) onto one of the surface-exposed loops of MreB, allowing for genomic replacement of the native counterpart[315]. Moore *at al.* probed several regions within FtsZ from *E. coli* and discovered one internal site, G55-Q56, in which several different FPs could be inserted and the gene inserted into the genome[245]. This suggests that similar regions may exist in FtsZ from different species, allowing for the creation of FtsZ fusion protein, allowing the Z-ring to be imaged by super resolution techniques.

7.8 Optimising of vertical immobilisation methodology.

Despite the success in showing that FtsZ filaments treadmill throughout the division process using a prototype vertical immobilisation technology, this technique was limited as it had low throughput and suffered from high background and fast photobleaching which made it incapable of imaging dim nascent rings. This was a major limitation as it prevented us from probing FtsZ dynamics across all stages of the division cycle. Thus, the entirety of the method was redesigned in order to address these issues and allow ultrasensitive, high-resolution imaging of FtsZ dynamics with high throughout though different stages of the cell cycle.

As stated, one of the major limitations of the vertical immobilization technology was the low throughput due to inefficient loading into the microholes. The dim and diffuse nature of nascent ring makes them difficult to identify during image acquisition. As one cannot visualise the entire length of the cell, it difficult to differentiate a nascent ring from the cytoplasmic background. Thus it is difficult to determine if the division site of nascent rings is in the imaging plane. It is not until image analysis that such rings are able to be identified. Furthermore, preparation of the microholes is a time consuming process and once the cells are loaded onto the sample, one has roughly an hour to complete the imaging before cells start growing out of the agarose microchambers. Thus, maximising the number of cells in a single FOV is advantageous as it increases the chances of imaging nascent rings.

Thus we applied multiple factors in order to improve the throughput of this technique. The first was using switching from an EMCCD camera to an sCMOS that possesses a 16x larger active pixel area allowing more of the microhole array to be imaged in a single FOV. However it should be noted the image size was cropped to 1/4 of this size, as the full size FOV could not currently be evenly illuminated. However, this still enabled us to image a 4x larger FOV. Another major advantage of this switch is that an sCMOS cameras possess a broader dynamics range, making them ideal for imaging in low light conditions[44,49]. As such, this instrument is beneficial when attempting to image the dynamics of dim nascent rings.

The silicon micropillars themselves were also redesigned. I identified the optimum diameter of the silicon micropillars that resulted in trapped cells that were unable to rotate. Following this a new design of micropillars was discussed which utilised the optimum diameter that I identified. Additionally, the overall size of the micropillar array was increased, while the space between individual pillars was decreased. This new design was then refined and etched by Dr Kevin Whitley. I also developed a new loading protocol of cells into the microchambers. In the new protocol, rather than ineffectively attempting to force cells into the microholes by the addition of a coverslip, cells were centrifuged into the microchambers. Combining the centrifugation protocol with larger camera size and optimised micropillar diameters led to loading rate increasing by 1178% over the initial method.

It has been suggested that around 30-40% of FtsZ is in the Z-ring meaning there is a large cytoplasmic concentration[123,206], resulting in a high degree of background noise. This is especially problematic when attempting to image the dynamics of nascent Z-rings. Ring-HilO illumination [316], image denoising [251] and custom septal localisation and background subtraction algorithms were implemented to combat the low SNR of nascent rings by Dr Séamus Holden. I performed the experimental comparison of the different illumination methods to determine that ring-HilO resulted in the best illumination.

In chapter 2, I described how it was necessary to implement HiLO microscopy in order to improve the SNR ratio, to faithfully determine the dynamics of division proteins. When a sample is imaged by conventional widefield microscopy, the entire sample plane is illuminated, resulting in all fluorophores being excited. As such, out of focus light from both autofluorescence and fluorophores above and below the imaging plane contribute to the background noise thus degrading image quality. As previously described, while TIRF microscopy is able to dramatically increase the SNR, only a thin slice of the cell is illuminated close to the coverslip[41]. Thus to combat the poor SNR HiLO was used as a substitute. Like TIRF, HiLO works by inclining the illumination, but in the latter's case the angle of inclination is below the critical angle so total internal reflection does not occur. Inclination of incident light in such a manner reduces the amount of the sample that is illuminated[215]. For organisms the size of bacterial cells the entire cell is still illuminated, however less of the agarose pad is exposed to the excitation beam and thus the background noise is reduced. Thus, while HiLO does not offer as great an increase in SNR when compared to TIRF, its major advantage is that it allows structures to be imaged throughout the entire length of the cell.

In order to optimise the illumination method further, Dr Séamus Holden implemented ring-HiLO as part of the optimised VerCINI protocol. Ring-HiLO differs from HiLO as the former utilises a pair of motorised mirrors to rapidly rotate the excitation beam around the back of the objective [316]. This results in the excitation beam propagating as a spinning light sheet which rotates at high speeds. While offering the same benefits in terms of increasing the SNR as HiLO, ring-HiLO over-comes potential illumination differences in a FOV when the sample is illuminated from a single direction. By rapidly spinning the incident light around the sample plane, we can ensure that that the sample is evenly illuminated from all directions simultaneously. This is imperative when trying to assess the dynamics of nascent rings, as the effects of uneven illumination could be detrimental to their classification.

These optimisation steps allowed us to develop a powerful tool enabling ultrasensitive, high resolution imaging of FtsZ filament dynamics and we named this technique VerCINI (Vertical

Cell Imaging by Nanostructured Immobilisation). This allows the dynamics of dim structures to be investigated that may otherwise be masked by poor SNR.

7.9 FtsZ filament dynamics are regulated throughout the division cycle

As the optimised VerCINI methodology was now capable of imaging dim nascent rings, this meant we could assess the dynamics of FtsZ across different stages of the division cycle in a high throughout fashion. We performed conventional flat-pad imaging in order to assess the assembly dynamics of FtsZ. It was observed that initially FtsZ forms a diffuse structure at the midcell which undergoes a rapid condensation reaction forming a dense band at the division site, followed by the initiation of constriction. We quantified these changes in Z-ring structure in terms of Z-ring dimensions (ring thickness and diameter) and septal density in each frame. The time traces of these measurements revealed three distinct phases that we classified as “nascent”, “mature” and “constricting”.

During the nascent stage, low density filaments transiently assemble at the midcell over a wide region. This is consistent with previous reports [224,292,314,317]. Following this, FtsZ filaments undergo a rapid condensation reaction forming the thin, mature Z-ring. This was found to be 300-350nm in width.

We subsequently used septal density and diameter in order to characterise the Z-rings observed using VerCINI into their three previously defined stages and assessed the dynamics of FtsZ filaments in each stages. Interestingly, we observed that nascent Z-rings possessed a large population of static filaments (~35% immobile filaments). As would be expected, the presence of many static filaments resulted in nascent rings being, on average, less processive then mature and actively constricting rings. Following condensation intro a mature ring, the percentage of immotile filaments decreased resulting in the median treadmilling speed and processivity of FtsZ filaments significantly increasing. Similar results were observed for actively constricting rings.

One of the most interesting observations is that in nascent rings, filament interactions in the form of collisions between 2 or more filaments were frequently observed. These collisions resulted in aggregation of the filaments and arrest of their dynamics. Previous studies have shown that FtsZ filament aggregation by lateral filament interactions is required to bundle FtsZ filaments and condense the Z-ring[96,98,164,298,301]. Thus bi-directional FtsZ treadmilling appears to drive filament aggregation by increasing the likelihood of filament collisions such that they can laterally interact. Parallel work conducted by Dr Kevin Whitley revealed that chemical arrest of treadmilling prevents Z-ring condensation [216]. This suggests that filament interactions are essential for condensation into a mature ring, with condensation itself promoting a switch to robust treadmilling due to the decrease in static filaments observed within mature and constricting rings. This suggests FtsZ treadmilling may permit filaments to search the midcell for lateral interaction partners with treadmilling thus driving condensation.

The observation that FtsZ filaments exhibit different dynamics in nascent rings when compared to mature and constricting rings suggests that dynamics may be actively regulated throughout the division cycle. FtsZ is potentially responsible for regulating its own dynamics. When FtsZ was first shown to treadmill on supported lipid bilayers *in vitro*, sufficient local concentrations of FtsZ, GTP binding and hydrolysis and association to the membrane via the FtsA were required in order for this process to occur [208]. Furthermore, *in vitro* FtsZ was observed to treadmill at similar rates to those observed *in vivo,* given further credit to the notion that FtsZ is able to regulate its own dynamics. Thus a proportion of the static filaments present at the division site may be due to a lack of free FtsZ monomers localised to the region. Once a critical concentration is reached, the Z-ring can condense and a switch to robust treadmilling occurs.

FtsZ may also possess intrinsic properties to prevent over-bundling of filaments, as this would result in hyper stable structures that are unable to treadmill. When FtsZ is fused to a membrane targeting sequence (MTS), FtsZ-MTS has been shown to be capable of treadmilling on supported lipid bi-layers without an additional membrane anchor, but only under a narrow range of Mg^{2+} concentrations [293]. When the concentration of Mg^{2+} is too low, FtsZ is unable to bind GTP. When the concentration of Mg^{2+} is too high, FtsZ forms dense mesh-like structures with increased single-molecule residence times in which treadmilling has not been observed, though the structures themselves are still dynamic[293]. This suggests that for robust treadmilling to occur, FtsZ requires local concentrations of monomer, GTP and Mg^{2+} at the membrane in addition to an anchor and a mechanism to prevent over bundling. It should be noted however, that FtsZ-MTS from *C. crescentus* has not been observed to treadmill on supported lipid bilayers, suggesting that inherent inclination to treadmill may differ between species.

The C-terminal Linker (CT) has been suggested to prevent over bundling and inhibition of treadmilling filaments[295]. *In vitro* studies in which the CTL of FtsZ has been deleted (ΔCTL) has shown that filaments display an increased proclivity to bundle into dense structures. These bundles also display greater stability when compared to wildtype FtsZ from *C. crescentus* and *B. subtilis* [96,294,296,297.]. *In vivo* when the CTL is deleted aberrant Z-ring morphology and cell division are observed in *B. subtilis*, *E. coli*, and *C. crescentus* [296,298–300].

Thus, it would appear that FtsZ possess its own intrinsic methods to regulate its own dynamics. However, FtsZ is also known to possess a number of binding partners that regulate its localisation and structures in cells in addition to filament dynamics and structure in *in vitro* systems. In *B. subtills* these include the membrane anchors FtsA[64,123,208,300] and SepF[13,307,318] in addition to positive and negative FtsZ regulators ZapA [134,162–164] and EzrA[135,150,154] respectively. Thus other candidates exist that may regulate the dynamics of FtsZ filaments *in vivo.*

7.10 The dynamics of FtsZ associated proteins can be broadly split into three categories

I investigated the *in vivo* dynamics of the key FtsZ proteins FtsA, SepF, EzrA and DivIVA. From the results obtained, it appears that the dynamics of the FtsZ associated division proteins can be broadly split into three categories which correlate to their function. The first of these categories is the dominantly motile group which includes the proteins FtsZ and FtsA. Both of these proteins have been observed to move processively around the division site [208,279]. As has been explained extensively throughout this thesis, the dynamics of FtsZ have been shown to be essential for synthase motion, filament interaction and Z-ring condensation [216,279,280]. FtsA is known to tether FtsZ to the cell membrane and has also been shown to colocalise and move with FtsZ. The second group of dynamics are the static architectural proteins, and these include DivIVA and SepF. DivIVA is a negative curvature sensor and thus preferentially localises to the cell poles and the leading edge of constriction where it recruits the Min proteins in order to prevent incorrect Z-ring localisation [179,180,302]. SepF has been suggested to act as a molecular clamp in order to regulate the thickness of the division septum. Finally, the third category displays dynamics which are neither truly static or motile and this currently only includes EzrA, a negative regulator of the Z-ring that also prevents incorrect localisation falls into this group[212].

Although the DivIVA does not interact directly with the divisome, it localises and the leading site of constriction, and the cell pole, in order to recruit the Min system to prevent aberrant Z-ring formation[178,179]. DivIVA is largely thought to form static assemblies [302], and thus this provides us with a crucial control for defining static components of the divisome. As no DivIVA was shown to move with a speed of 10nm/s, we set this as a threshold for classifying a division protein as static.

FtsA is potentially the most well characterised FtsZ binding protein and as stated previously is known to tether FtsZ to the cell membrane. FtsA is well conserved actin homologue which binds to the CTC of FtsZ, and interacts with the membrane via its N-terminal amphipathic helix[248]. Imaging the dynamics of FtsA has revealed that it also forms a ring like-structure composed of multiple filaments that move bi-directionally around the division plane. Measurements taken by collaborators showed that like FtsZ, individual monomers of FtsA are stationary, suggesting that it too treadmills around the division plane [279]. Using simultaneous dual colour imaging we found that FtsA and FtsZ colocalise and move together around the division plane, a finding that was corroborated by collaborators.[288] This is further supported by the observation that both FtsZ and FtsA co-assemble into dynamic vortices *in vitro* [278]. *In vivo* it has further been shown that FtsZ treadmilling dynamics drive the dynamics of FtsA, with FtsA moving at the same speed as FtsZ[279]. The observation that FtsA filaments treadmill alongside FtsZ may help keep FtsZ filaments tethered to the membrane for longer periods of time than a static anchor. With static anchors, FtsZ filament association with the membrane would be dependent on encountering a static structural anchor around the division site. However, if an anchor is able travel alongside FtsZ, this would allow filaments to be kept in association with the membrane for longer periods of time, potentially aiding in efficient septum synthesis during the initial stages of constriction.

In addition to FtsA, *B. subtilis* is also thought to possess an additional, redundant membrane anchor SepF as both display polymerisation, FtsZ binding and membrane binding [13,146,148]. Like FtsA, SepF also binds to the CTC of FtsZ and binds the membrane via its N-terminal amphipathic helix. Despite not being essential, deleting SepF results in highly deformed septa, which indicates that SepF may also play additional roles during the cell division process[307]. One of these roles is the control of septum thickness[149]. Although SepF has been observed to form large rings with an internal diameter of ~40nm *in vitro*[13], it has been suggested that *in vivo* SepF likely forms arc-like as the amphipathic helix is likely on the inside of the SepF rings[319]. It has been proposed that SepF may control the width of the septum by acting as a molecular clamp, forming arc like structures perpendicular to the growing seetum[149]. Support for this model derives from the observation that the diameter of the SepF rings formed *in vitro* are close in with to the septum[319]. Furthermore, chimeric SepF proteins that, *in vitro*¸ form rings with different widths corresponded *in vivo,* with altered septum thickness when expressed. Thus the observation that SepF forms static foci supports its role as an architectural division protein. While acting as a molecular clamp to control the septum thickness, SepF may also form a secondary role as a membrane anchor, helping to keep the Z-ring constrained to a narrow region of the division site. This may also explain why deletion of SepF results in deformed septa, as the Z-ring would be no longer locked in position, but would be free to tilt. However, *ftsA* null mutants display a far more pronounced phenotypes, suggesting that FtsA is the more important membrane anchor. It is likely that both FtsA and SepF work in tandem to tether FtsZ to the membrane and keep it localised to the correct position.

Conclusions and Future Work.

Over the course of this PhD I, along with Dr Séamus Holden and Dr Kevin Whitley, developed a method of vertically immobilising rod shaped bacteria such as *B. subtilis* in order to visualise the division machinery in its entirety. This provided a high throughput, ultrasensitive, high-resolution technique for imaging division protein dynamics though different stages of the cell cycle.

Using this technique, I showed that the Z-ring is composed of multiple filaments which move bi-directionally around the division plane. Together, with measurements taken by collaborators, we showed that FtsZ filaments move by treadmilling. I then quantified FtsZ filament organization across the entire division cycle and observed that the Z-ring could be split into three distance phases: nascent, mature and constricting. Initially, the Z-ring is diffuse structure composed of spare filaments distributed around the midcell. The Z-ring then undergoes a rapid condensation reaction to form a thin, dense mature Z-ring following which construction is initiated.

By quantifying the dynamics of FtsZ filaments in each stage of the division cycle I observed that nascent rings contain a large population of static filaments and a broad distribution of treadmilling filament speeds. Following condensation into a mature ring, the percentage of static filaments reduces and filaments display robust treadmilling with a narrow distribution of speeds. These dynamics continue during active constriction. The difference in dynamics between nascent rings and mature and constricting rings suggest that FtsZ filaments dynamics may be regulated according to cell division stage. Interestingly, interactions between two or more filaments were frequently observed in nascent rings, leading to aggregation and arrest of the filaments involved. Parallel work by Dr Kevin Whitley showed that FtsZ treadmilling is essential for condensation by chemically perturbing FtsZ treadmilling activity[216]. This suggests that treadmilling allows FtsZ to actively search the division site for other filaments in order to laterally interact with and thus promote condensation.

I further imaged the dynamics of a number FtsZ interacting proteins including FtsA, SepF, EzrA and DivIVA in order to screen for treadmilling regulators. As had previously been observed *in vitro*[283] and as confirmed by collaborators[279], FtsA colocalised and moved with FtsZ. Collaborators also showed that the treadmilling dynamics of FtsZ drives the dynamics of FtsA. Both DivIVA and SepF were observed to form static structures at the division consistent with their suggested role as architectural division proteins. Interestingly, EzrA was observed to display a mix of motile and static structures in pre-constricted rings, before switching to predominantly static assemblies. This suggests that EzrA may play a role in regulating the dynamics of FtsZ filaments between nascent rings and mature and constricting rings.

Overall, the results in this thesis demonstrate that FtsZ treadmills *in vivo*, and FtsZ treadmilling is essentially for formation of the mature divisome. Additionally, the Z-ring undergoes three distinct phases during the division cycle: nascent, mature and constricting, The observation of a large population of static filaments in nascent rings that is followed by a switch to robust treadmilling following condensation into a mature ring, suggests that FtsZ filament dynamics are regulated over the cell cycle.

In future work, the roles of the FtsZ binding proteins should be investigated in greater depth. Due to the observation that EzrA displays a mixed population of static and motile filaments in pre-constructed rings, it would be beneficial to conduct simultaneous 2 colour imaging alongside FtsZ, in order to further classify these dynamics between nascent, mature and constricting phases. Furthermore, it would be beneficial to image the dynamics of the FtsZ binding protein ZapA, which was unable to be conducted in the timescale of this project.

Additionally, further information about the mechanistic roles of the FtsZ binding proteins could be obtained by investigating the dynamics and ultrastructure of the Z-ring in deletion backgrounds. In terms of dynamics, both conventional flat-pad imaging and VerCINI should be combined in in order to assess not only the dynamics of individual FtsZ filaments in the absence of specific FtsZ associated proteins, but also the effects on condensation. In terms of super resolution microscopy, localisation microscopy techniques such as PALM could be conducted again using flat-pad and VerCINI. This would allow the effects that the FtsZ-associated proteins exert on Z-ring ultra-structure. VerCINI imaging would permit the distribution of filaments around the entire division site to be examined, while flat pad imaging would provide information on the Z-ring thickness.

Finally, in order to investigate the exact role of filament interactions, SIM could be combined with VerCINI in order to visualise the dynamics of FtsZ filaments around the division plane at ~100nm resolution. Again, this could be combined with FtsZ-associated protein deletions, but also with FtsZ self-interaction mutants, in order to investigate the proclivity of FtsZ to regulate dynamics *in vivo.*

1. Bisson-Filho, A. W. *et al.* Treadmilling by FtsZ filaments drives peptidoglycan synthesis and bacterial cell division. *Science* **355**, 739–743 (2017).
2. Science, A. A. for the A. of. Erratum for the Report: “Treadmilling by FtsZ filaments drives peptidoglycan synthesis and bacterial cell division” by A. W. Bisson-Filho, Y.-P. Hsu, G. R. Squyres, E. Kuru, F. Wu, C. Jukes, Y. Sun, C. Dekker, S. Holden, M. S. VanNieuwenhze, Y. V. Brun, E. C. Garner. *Science* **367**, (2020).
3. Typas, A., Banzhaf, M., Gross, C. A. & Vollmer, W. From the regulation of peptidoglycan synthesis to bacterial growth and morphology. *Nat. Rev. Microbiol.* **10**, 123–136 (2011).
4. Whatmore, A. M. & Reed, R. H. Determination of turgor pressure in Bacillus subtilis: a possible role for K+ in turgor regulation. *J. Gen. Microbiol.* **136**, 2521–2526 (1990).
5. Gueiros-Filho. Cell Division. in *Bacillus: Cellular and Molecular Biology* (Caister Academic Press, 2007).
6. Labischinski, H., Goodell, E. W., Goodell, A. & Hochberg, M. L. Direct proof of a ‘more-than-single-layered’ peptidoglycan architecture of Escherichia coli W7: a neutron small-angle scattering study. *J. Bacteriol.* **173**, 751–756 (1991).
7. Deng, Y., Sun, M. & Shaevitz, J. W. Direct Measurement of Cell Wall Stress Stiffening and Turgor Pressure in Live Bacterial Cells. *Phys. Rev. Lett.* **107**, 158101 (2011).
8. Egan, A. J. F. & Vollmer, W. The physiology of bacterial cell division. *Ann. N. Y. Acad. Sci.* **1277**, 8–28 (2013).
9. Erickson, H. P. How bacterial cell division might cheat turgor pressure – a unified mechanism of septal division in Gram-positive and Gram-negative bacteria. *BioEssays News Rev. Mol. Cell. Dev. Biol.* **39**, (2017).
10. Harry, E., Monahan, L. & Thompson, L. Bacterial cell division: the mechanism and its precison. *Int. Rev. Cytol.* **253**, 27–94 (2006).
11. Errington, J., Daniel, R. A. & Scheffers, D.-J. Cytokinesis in bacteria. *Microbiol. Mol. Biol. Rev. MMBR* **67**, 52–65, table of contents (2003).

12. van den Ent, F. & Löwe, J. Crystal structure of the cell division protein FtsA from Thermotoga maritima. *EMBO J.* **19**, 5300–5307 (2000).

13. Duman, R. *et al.* Structural and genetic analyses reveal the protein SepF as a new membrane anchor for the Z ring. *Proc. Natl. Acad. Sci.* **110**, E4601–E4610 (2013).

14. Scheffers, D.-J., Jones, L. J. F. & Errington, J. Several distinct localization patterns for penicillin-binding proteins in Bacillus subtilis. *Mol. Microbiol.* **51**, 749–764 (2004).

15. Hirota, Y., Ryter, A. & Jacob, F. Thermosensitive mutants of E. coli affected in the processes of DNA synthesis and cellular division. *Cold Spring Harb. Symp. Quant. Biol.* **33**, 677–693 (1968).

16. Rowlett, V. W. & Margolin, W. The bacterial divisome: ready for its close-up. *Philos. Trans. R. Soc. Lond. B. Biol. Sci.* **370**, (2015).

17. Bi, E. & Lutkenhaus, J. FtsZ ring structure associated with division in Escherichia coli. *Nature* **354**, 161–164 (1991).

18. Rosenthal, C. K. The beginning: Invention of the microscope. *Nat. Cell Biol.* **11**, S6–S6 (2009).

19. Hooke, R., Allestry, J. & Martyn, J. *Micrographia, or, Some physiological descriptions of minute bodies made by magnifying glasses :with observations and inquiries thereupon*. 1–323 (Printed by Jo. Martyn and Ja. Allestry, printers to the Royal Society ... , 1665). doi:10.5962/bhl.title.904.

20. Leeuwenhoek, A. van. *The selected works of Antony van Leeuwenhoek: containing his microscopical discoveries in many of the works of nature*. (Arno Press, 1977).

21. Schneider, J. P. & Basler, M. Shedding light on biology of bacterial cells. *Philos. Trans. R. Soc. B Biol. Sci.* **371**, (2016).

22. Cremer, C. & Masters, B. R. Resolution enhancement techniques in microscopy. *Eur. Phys. J. H* **38**, 281–344 (2013).

23. ZEISS Microscopy Online Campus | Microscopy Basics | Kohler Illumination. http://zeiss-campus.magnet.fsu.edu/articles/basics/kohler.html.

24. Abbe, E. VII.—On the Estimation of Aperture in the Microscope. *J. R. Microsc. Soc.* **1**, 388–423 (1881).

25. Ishikawa-Ankerhold, H. C., Ankerhold, R. & Drummen, G. P. C. Advanced Fluorescence Microscopy Techniques—FRAP, FLIP, FLAP, FRET and FLIM. *Molecules* **17**, 4047–4132 (2012).

26. Vogelsang, J. *et al.* A reducing and oxidizing system minimizes photobleaching and blinking of fluorescent dyes. *Angew. Chem. Int. Ed Engl.* **47**, 5465–5469 (2008).

27. Thorley, J. A., Pike, J. & Rappoport, J. Z. Super-resolution Microscopy. in *Fluorescence Microscopy* 199–212 (Elsevier, 2014). doi:10.1016/B978-0-12-409513-7.00014-2.

28. Fluorescence Microscopy – the Magic of Fluorophores and Filters. *Bitesize Bio* https://bitesizebio.com/33529/fluorescence-microscopy-the-magic-of-fluorophores-and-filters/ (2017).

29. Drummen, G. P. C. Fluorescent Probes and Fluorescence (Microscopy) Techniques — Illuminating Biological and Biomedical Research. *Molecules* **17**, 14067–14090 (2012).

30. Rusk, N. The fluorescence microscope: First fluorescence microscope, First epifluorescence microscope, The dichroic mirror. *Nat. Cell Biol.* **11**, S8–S9 (2009).

31. Schleede. Die Fluoreszenzanalyse in der Mikrochemie. Von Max Haitinger. Verlag Emil Haim u. Co., Wien und Leipzig 1937. Preis geh. RM. 8,–. *Angew. Chem.* **51**, 898–898 (1938).

32. Coons, A. H. & Kaplan, M. H. LOCALIZATION OF ANTIGEN IN TISSUE CELLS. *J. Exp. Med.* **91**, 1–13 (1950).

33. van Ooij, C. Recipe for fluorescent antibodies: Immunofluorescence. *Nat. Cell Biol.* **11**, S10–S11 (2009).

34. Js, P. The use of a vertical illuminator with interchangeable dichroic mirrors for fluorescence microscopy with incidental light. *Z. Wiss. Mikrosk. Mikrosk. Tech.* **68**, 129–142 (1967).

35. White, J. G., Amos, W. B. & Fordham, M. An evaluation of confocal versus conventional imaging of biological structures by fluorescence light microscopy. *J. Cell Biol.* **105**, 41–48 (1987).

36. *Handbook of Biological Confocal Microscopy*. (Springer US, 2006). doi:10.1007/978-0-387-45524-2.

37. Icha, J., Weber, M., Waters, J. C. & Norden, C. Phototoxicity in live fluorescence microscopy, and how to avoid it. *BioEssays* **39**, 1700003 (2017).

38. Schneckenburger, H. *et al.* Light exposure and cell viability in fluorescence microscopy. *J. Microsc.* **245**, 311–318 (2012).

39. Gorgidze, L. A., Oshemkova, S. A. & Vorobjev, I. A. Blue light inhibits mitosis in tissue culture cells. *Biosci. Rep.* **18**, 215–224 (1998).

40. Rösner, J. *et al.* Minimizing photodecomposition of flavin adenine dinucleotide fluorescence by the use of pulsed LEDs. *J. Microsc.* **264**, 215–223 (2016).

41. Axelrod, D. Cell-substrate contacts illuminated by total internal reflection fluorescence. *J. Cell Biol.* **89**, 141–145 (1981).

42. Tonzani, S. TIRF: imaging at the cellular edge: TIRF microscopy. *Nat. Cell Biol.* **11**, S16–S16 (2009).

43. Mattheyses, A. L., Simon, S. M. & Rappoport, J. Z. Imaging with total internal reflection fluorescence microscopy for the cell biologist. *J. Cell Sci.* **123**, 3621–3628 (2010).

44. EMCCD vs sCMOS Cameras | A Comparison - Andor Learning Centre. *Oxford Instruments* https://andor.oxinst.com/learning/view/article/comparing-scmos.

45. Digital Imaging in Optical Microscopy - Concepts in Digital Imaging - Dynamic Range | Olympus Life Science. https://www.olympus-lifescience.com/en/microscope-resource/primer/digitalimaging/concepts/dynamicrange/.

46. Meiniel, W., Olivo-Marin, J. & Angelini, E. D. Denoising of Microscopy Images: A Review of the State-of-the-Art, and a New Sparsity-Based Method. *IEEE Trans. Image Process.* **27**, 3842–3856 (2018).

47. Introduction to Charge-Coupled Devices (CCDs). *Nikon's MicroscopyU* https://www.microscopyu.com/digital-imaging/introduction-to-charge-coupled-devices-ccds.

48. Cameras for fluorescence imaging: A comparative guide. *Scientifica* https://www.scientifica.uk.com/learning-zone/cameras-for-fluorescence-imaging.

49. sCMOS Technology - What is sCMOS. *Oxford Instruments* https://andor.oxinst.com/learning/view/article/scmos-technology-what-is-scmos.

50. Anderson, L. K. Sequential Immunofluorescent Light Microscopy and Electron Microscopy of Recombination Nodules During Meiotic Prophase I. in *Meiosis* (ed. Stuart, D. T.) 187–216 (Springer, 2017). doi:10.1007/978-1-4939-6340-9_10.

51. Harry, E. J., Pogliano, K. & Losick, R. Use of immunofluorescence to visualize cell-specific gene expression during sporulation in Bacillus subtilis. *J. Bacteriol.* **177**, 3386–3393 (1995).

52. Levin, P. A. & Losick, R. Transcription factor Spo0A switches the localization of the cell division protein FtsZ from a medial to a bipolar pattern in Bacillus subtilis. *Genes Dev.* **10**, 478–488 (1996).

53. Addinall, S. G., Bi, E. & Lutkenhaus, J. FtsZ ring formation in fts mutants. *J. Bacteriol.* **178**, 3877–3884 (1996).

54. Addinall, S. G. & Lutkenhaus, J. FtsA is localized to the septum in an FtsZ-dependent manner. *J. Bacteriol.* **178**, 7167–7172 (1996).

55. Chalfie, M., Tu, Y., Euskirchen, G., Ward, W. W. & Prasher, D. C. Green fluorescent protein as a marker for gene expression. *Science* **263**, 802–805 (1994).

56. Webb, C. D., Decatur, A., Teleman, A. & Losick, R. Use of green fluorescent protein for visualization of cell-specific gene expression and subcellular protein localization during sporulation in Bacillus subtilis. *J. Bacteriol.* **177**, 5906–5911 (1995).

57. Ma, X., Ehrhardt, D. W. & Margolin, W. Colocalization of cell division proteins FtsZ and FtsA to cytoskeletal structures in living Escherichia coli cells by using green fluorescent protein. *Proc. Natl. Acad. Sci. U. S. A.* **93**, 12998–13003 (1996).

58. Swulius, M. T. & Jensen, G. J. The Helical MreB Cytoskeleton in Escherichia coli MC1000/pLE7 Is an Artifact of the N-Terminal Yellow Fluorescent Protein Tag. *J. Bacteriol.* **194**, 6382–6386 (2012).

59. Snapp, E. Design and Use of Fluorescent Fusion Proteins in Cell Biology. *Curr. Protoc. Cell Biol. Editor. Board Juan Bonifacino Al* **CHAPTER**, Unit-21.4 (2005).

60. Osawa, M. & Erickson, H. P. FtsZ from Divergent Foreign Bacteria Can Function for Cell Division in Escherichia coli. *J. Bacteriol.* **188**, 7132–7140 (2006).

61. Weiss, D. S. *et al.* Localization of the Escherichia coli cell division protein Ftsl (PBP3) to the division site and cell pole. *Mol. Microbiol.* **25**, 671–681 (1997).

62. Wang, L., Khattar, M. K., Donachie, W. D. & Lutkenhaus, J. FtsI and FtsW are localized to the septum in Escherichia coli. *J. Bacteriol.* **180**, 2810–2816 (1998).

63. Buddelmeijer, N., Aarsman, M. E. G., Kolk, A. H. J., Vicente, M. & Nanninga, N. Localization of Cell Division Protein FtsQ by Immunofluorescence Microscopy in Dividing and Nondividing Cells of Escherichia coli. *J. Bacteriol.* **180**, 6107–6116 (1998).

64. Addinall, S. G. & Lutkenhaus, J. FtsA is localized to the septum in an FtsZ-dependent manner. *J. Bacteriol.* **178**, 7167–7172 (1996).

65. Gamba, P., Veening, J.-W., Saunders, N. J., Hamoen, L. W. & Daniel, R. A. Two-Step Assembly Dynamics of the Bacillussubtilis Divisome. *J. Bacteriol.* **191**, 4186–4194 (2009).

66. Errington, J., Daniel, R. A. & Scheffers, D.-J. Cytokinesis in Bacteria. *Microbiol. Mol. Biol. Rev.* **67**, 52–65 (2003).

67. Karimova, G., Dautin, N. & Ladant, D. Interaction Network among Escherichia coli Membrane Proteins Involved in Cell Division as Revealed by Bacterial Two-Hybrid Analysis. *J. Bacteriol.* **187**, 2233–2243 (2005).

68. Di Lallo, G., Fagioli, M., Barionovi, D., Ghelardini, P. & Paolozzi, L. Use of a two-hybrid assay to study the assembly of a complex multicomponent protein machinery: bacterial septosome differentiation. *Microbiology* **149**, 3353–3359 (2003).

69. Maggi, S. *et al.* Division protein interaction web: identification of a phylogenetically conserved common interactome between Streptococcus pneumoniae and Escherichia coli. *Microbiology* **154**, 3042–3052 (2008).

70. Alexeeva, S., Gadella, T. W. J., Verheul, J., Verhoeven, G. S. & Den Blaauwen, T. Direct interactions of early and late assembling division proteins in Escherichia coli cells resolved by FRET. *Mol. Microbiol.* **77**, 384–398 (2010).

71. Busiek, K. K., Eraso, J. M., Wang, Y. & Margolin, W. The Early Divisome Protein FtsA Interacts Directly through Its 1c Subdomain with the Cytoplasmic Domain of the Late Divisome Protein FtsN. *J. Bacteriol.* **194**, 1989–2000 (2012).

72. Buddelmeijer, N. & Beckwith, J. A complex of the Escherichia coli cell division proteins FtsL, FtsB and FtsQ forms independently of its localization to the septal region. *Mol. Microbiol.* **52**, 1315–1327 (2004).

73. Sievers, J. & Errington, J. The Bacillus subtilis cell division protein FtsL localizes to sites of septation and interacts with DivIC. *Mol. Microbiol.* **36**, 846–855 (2000).

74. Robichon, C., King, G. F., Goehring, N. W. & Beckwith, J. Artificial Septal Targeting of Bacillus subtilis Cell Division Proteins in Escherichia coli: an Interspecies Approach to the Study of Protein-Protein Interactions in Multiprotein Complexes. *J. Bacteriol.* **190**, 6048–6059 (2008).

75. Daniel, R. A., Noirot-Gros, M.-F., Noirot, P. & Errington, J. Multiple Interactions between the Transmembrane Division Proteins of Bacillus subtilis and the Role of FtsL Instability in Divisome Assembly. *J. Bacteriol.* **188**, 7396–7404 (2006).

76. Noirclerc-Savoye, M. *et al.* In vitro reconstitution of a trimeric complex of DivIB, DivIC and FtsL, and their transient co-localization at the division site in Streptococcus pneumoniae. *Mol. Microbiol.* **55**, 413–424 (2005).

77. Daniel, R. A. & Errington, J. Intrinsic instability of the essential cell division protein FtsL of Bacillus subtilis and a role for DivIB protein in FtsL turnover. *Mol. Microbiol.* **36**, 278–289 (2000).

78. Wadenpohl, I. & Bramkamp, M. DivIC Stabilizes FtsL against RasP Cleavage. *J. Bacteriol.* **192**, 5260–5263 (2010).

79. Daniel, R. A., Harry, E. J., Katis, V. L., Wake, R. G. & Errington, J. Characterization of the essential cell division gene ftsL (yllD) of Bacillus subtilis and its role in the assembly of the division apparatus. *Mol. Microbiol.* **29**, 593–604 (1998).

80. Liu, B., Persons, L., Lee, L. & de Boer, P. A. J. Roles for both FtsA and the FtsBLQ subcomplex in FtsN-stimulated cell constriction in Escherichia coli. *Mol. Microbiol.* **95**, 945–970 (2015).

81. Tsang, M.-J. & Bernhardt, T. G. A role for the FtsQLB complex in cytokinetic ring activation revealed by an ftsL allele that accelerates division. *Mol. Microbiol.* **95**, 925–944 (2015).

82. Resolution. *Nikon's MicroscopyU* https://www.microscopyu.com/microscopy-basics/resolution.

83. Beiträge zur Theorie des Mikroskops und der mikroskopischen Wahrnehmung. *Arch. Für Mikrosk. Anat.* (1873) doi:10.1007/BF02956174.

84. Huang, B., Babcock, H. & Zhuang, X. Breaking the Diffraction Barrier: Super-Resolution Imaging of Cells. *Cell* **143**, 1047–1058 (2010).

85. Airy, G. B. On the Diffraction of an Object-glass with Circular Aperture. *Trans. Camb. Philos. Soc.* **5**, 283 (1835).

86. Weiss, S. Shattering the diffraction limit of light: A revolution in fluorescence microscopy? 3.

87. Cole, R. W., Jinadasa, T. & Brown, C. M. Measuring and interpreting point spread functions to determine confocal microscope resolution and ensure quality control. *Nat. Protoc.* **6**, 1929–1941 (2011).

88. Erickson, H. P., Anderson, D. E. & Osawa, M. FtsZ in Bacterial Cytokinesis: Cytoskeleton and Force Generator All in One. *Microbiol. Mol. Biol. Rev.* **74**, 504–528 (2010).

89. Nogales, E., Wolf, S. G. & Downing, K. H. Structure of the αβ tubulin dimer by electron crystallography. *Nature* **391**, 199–203 (1998).

90. Buske, P. J. & Levin, P. A. Extreme C Terminus of Bacterial Cytoskeletal Protein FtsZ Plays Fundamental Role in Assembly Independent of Modulatory Proteins. *J. Biol. Chem.* **287**, 10945–10957 (2012).

91. Hanukoglu, I. Proteopedia: Rossmann fold: A beta-alpha-beta fold at dinucleotide binding sites. *Biochem. Mol. Biol. Educ. Bimon. Publ. Int. Union Biochem. Mol. Biol.* **43**, 206–209 (2015).

92. Oliva, M. A., Cordell, S. C. & Löwe, J. Structural insights into FtsZ protofilament formation. *Nat. Struct. Mol. Biol.* **11**, 1243–1250 (2004).

93. Scheffers, D. J., de Wit, J. G., den Blaauwen, T. & Driessen, A. J. Substitution of a conserved aspartate allows cation-induced polymerization of FtsZ. *FEBS Lett.* **494**, 34–37 (2001).

94. Vaughan, S., Wickstead, B., Gull, K. & Addinall, S. G. Molecular Evolution of FtsZ Protein Sequences Encoded Within the Genomes of Archaea, Bacteria, and Eukaryota. *J. Mol. Evol.* **58**, 19–29 (2004).

95. Buske, P. J., Mittal, A., Pappu, R. V. & Levin, P. A. An intrinsically disordered linker plays a critical role in bacterial cell division. *Semin. Cell Dev. Biol.* **0**, 3–10 (2015).

96. Sundararajan, K. & Goley, E. D. The intrinsically disordered C-terminal linker of FtsZ regulates protofilament dynamics and superstructure in vitro. *J. Biol. Chem.* **292**, 20509–20527 (2017).

97. Adams, D. W. & Errington, J. Bacterial cell division: assembly, maintenance and disassembly of the Z ring. *Nat. Rev. Microbiol.* **7**, 642–653 (2009).

98. Huecas, S. *et al.* Self-Organization of FtsZ Polymers in Solution Reveals Spacer Role of the Disordered C-Terminal Tail. *Biophys. J.* **113**, 1831–1844 (2017).

99. Romberg, L., Simon, M. & Erickson, H. P. Polymerization of FtsZ, a Bacterial Homolog of Tubulin. Is Assembly Cooperative? *J. Biol. Chem.* **276**, 11743–11753 (2001).

100. Caplan, M. R. & Erickson, H. P. Apparent cooperative assembly of the bacterial cell division protein FtsZ demonstrated by isothermal titration calorimetry. *J. Biol. Chem.* **278**, 13784–13788 (2003).

101. Chen, Y., Bjornson, K., Redick, S. D. & Erickson, H. P. A Rapid Fluorescence Assay for FtsZ Assembly Indicates Cooperative Assembly with a Dimer Nucleus. *Biophys. J.* **88**, 505–514 (2005).

102. Wang, X. & Lutkenhaus, J. The FtsZ protein of Bacillus subtilis is localized at the division site and has GTPase activity that is dependent upon FtsZ concentration. *Mol. Microbiol.* **9**, 435–442 (1993).

103. Mukherjee, A. & Lutkenhaus, J. Dynamic assembly of FtsZ regulated by GTP hydrolysis. *EMBO J.* **17**, 462 (1998).

104. Mukherjee, A. & Lutkenhaus, J. Guanine nucleotide-dependent assembly of FtsZ into filaments. *J. Bacteriol.* **176**, 2754–2758 (1994).

105. Erickson, H. P., Taylor, D. W., Taylor, K. A. & Bramhill, D. Bacterial cell division protein FtsZ assembles into protofilament sheets and minirings, structural homologs of tubulin polymers. *Proc. Natl. Acad. Sci.* **93**, 519–523 (1996).

106. Bramhill, D. & Thompson, C. M. GTP-dependent polymerization of Escherichia coli FtsZ protein to form tubules. *Proc. Natl. Acad. Sci. U. S. A.* **91**, 5813 (1994).

107. D, P., M, I., A, N., Hp, E. & Y, M. FtsZ condensates: an in vitro electron microscopy study. *Biopolymers* vol. 91 https://pubmed.ncbi.nlm.nih.gov/19137575/ (2009).

108. Lu, C., Stricker, J. & Erickson, H. P. FtsZ from Escherichia coli, Azotobacter vinelandii, and Thermotoga maritima--quantitation, GTP hydrolysis, and assembly. *Cell Motil. Cytoskeleton* **40**, 71–86 (1998).

109. Holden, S. Probing the mechanistic principles of bacterial cell division with super-resolution microscopy. *Curr. Opin. Microbiol.* **43**, 84–91 (2018).

110. Li, Z., Trimble, M. J., Brun, Y. V. & Jensen, G. J. The structure of FtsZ filaments in vivo suggests a force-generating role in cell division. *EMBO J.* **26**, 4694–4708 (2007).

111. Betzig, E. Imaging intracellular fluorescent proteins at nanometer resolution. *Science* **313**, 1642–1645 (2006).

112. Rust, M. J., Bates, M. & Zhuang, X. Sub-diffraction-limit imaging by stochastic optical reconstruction microscopy (STORM). *Nat. Methods* **3**, 793–796 (2006).

113. Strauss, M. P. *et al.* 3D-SIM Super Resolution Microscopy Reveals a Bead-Like Arrangement for FtsZ and the Division Machinery: Implications for Triggering Cytokinesis. *PLOS Biol.* **10**, e1001389 (2012).

114. Biteen, J. S., Shapiro, L., Moerner, W. E. & Goley, E. D. Three-Dimensional Super-Resolution Imaging of the Midplane Protein FtsZ in Live Caulobacter crescentus Cells Using Astigmatism. *ChemPhysChem* **13**, 1007–1012 (2012).

115. Holden, S. J. *et al.* High throughput 3D super-resolution microscopy reveals Caulobacter crescentus in vivo Z-ring organization. *Proc. Natl. Acad. Sci.* **111**, 4566–4571 (2014).

116. Coltharp, C., Buss, J., Plumer, T. M. & Xiao, J. Defining the rate-limiting processes of bacterial cytokinesis. *Proc. Natl. Acad. Sci.* 201514296 (2016) doi:10.1073/pnas.1514296113.

117. Lyu, Z., Coltharp, C., Yang, X. & Xiao, J. Influence of FtsZ GTPase activity and concentration on nanoscale Z-ring structure in vivo revealed by three-dimensional Superresolution imaging. *Biopolymers* **105**, 725–734 (2016).

118. Szwedziak, P., Wang, Q., Bharat, T. A. M., Tsim, M. & Löwe, J. Architecture of the ring formed by the tubulin homologue FtsZ in bacterial cell division. *eLife* **3**, e04601 (2015).

119. Yao, Q. *et al.* Short FtsZ filaments can drive asymmetric cell envelope constriction at the onset of bacterial cytokinesis. *EMBO J.* **36**, 1577–1589 (2017).

120. Sun, Q. & Margolin, W. FtsZ Dynamics during the Division Cycle of Live Escherichia coli Cells. *J. Bacteriol.* **180**, 2050 (1998).

121. Stricker, J., Maddox, P., Salmon, E. D. & Erickson, H. P. Rapid assembly dynamics of the Escherichia coli FtsZ-ring demonstrated by fluorescence recovery after photobleaching. *Proc. Natl. Acad. Sci.* **99**, 3171–3175 (2002).

122. Anderson, D. E., Gueiros-Filho, F. J. & Erickson, H. P. Assembly Dynamics of FtsZ Rings in Bacillus subtilis and Escherichia coli and Effects of FtsZ-Regulating Proteins. *J. Bacteriol.* **186**, 5775–5781 (2004).

123. B, G., D, S. & W, M. The ftsA* gain-of-function allele of Escherichia coli and its effects on the stability and dynamics of the Z ring. *Microbiology (Reading, England)* vol. 153 https://pubmed.ncbi.nlm.nih.gov/17322202/ (2007).

124. Niu, L. & Yu, J. Investigating Intracellular Dynamics of FtsZ Cytoskeleton with Photoactivation Single-Molecule Tracking. *Biophys. J.* **95**, 2009–2016 (2008).

125. Loose, M. & Mitchison, T. J. The bacterial cell division proteins FtsA and FtsZ self-organize into dynamic cytoskeletal patterns. *Nat. Cell Biol.* **16**, 38–46 (2014).

126. Erickson, H. P. FtsZ, a tubulin homologue in prokaryote cell division. *Trends Cell Biol.* **7**, 362–367 (1997).

127. Lan, G., Daniels, B. R., Dobrowsky, T. M., Wirtz, D. & Sun, S. X. Condensation of FtsZ filaments can drive bacterial cell division. *Proc. Natl. Acad. Sci.* **106**, 121–126 (2009).

128. Hörger, I., Velasco, E., Rivas, G., Vélez, M. & Tarazona, P. FtsZ Bacterial Cytoskeletal Polymers on Curved Surfaces: The Importance of Lateral Interactions. *Biophys. J.* **94**, L81–L83 (2008).

129. Erickson, H. P., Taylor, D. W., Taylor, K. A. & Bramhill, D. Bacterial cell division protein FtsZ assembles into protofilament sheets and minirings, structural homologs of tubulin polymers. *Proc. Natl. Acad. Sci.* **93**, 519–523 (1996).

130. Osawa, M., Anderson, D. E. & Erickson, H. P. Reconstitution of Contractile FtsZ Rings in Liposomes. *Science* **320**, 792–794 (2008).

131. Strauss, M. P. *et al.* 3D-SIM Super Resolution Microscopy Reveals a Bead-Like Arrangement for FtsZ and the Division Machinery: Implications for Triggering Cytokinesis. *PLoS Biol* **10**, e1001389 (2012).

132. Stachowiak, J. C. *et al.* Membrane bending by protein–protein crowding. *Nat. Cell Biol.* **14**, 944–949 (2012).

133. Ishikawa, S., Kawai, Y., Hiramatsu, K., Kuwano, M. & Ogasawara, N. A new FtsZ-interacting protein, YlmF, complements the activity of FtsA during progression of cell division in Bacillus subtilis. *Mol. Microbiol.* **60**, 1364–1380 (2006).

134. Low, H. H., Moncrieffe, M. C. & Löwe, J. The crystal structure of ZapA and its modulation of FtsZ polymerisation. *J. Mol. Biol.* **341**, 839–852 (2004).

135. Levin, P. A., Kurtser, I. G. & Grossman, A. D. Identification and characterization of a negative regulator of FtsZ ring formation in Bacillus subtilis. *Proc. Natl. Acad. Sci. U. S. A.* **96**, 9642–9647 (1999).

136. Pichoff, S. & Lutkenhaus, J. Tethering the Z ring to the membrane through a conserved membrane targeting sequence in FtsA. *Mol. Microbiol.* **55**, 1722–1734 (2005).

137. Feucht, A., Lucet, I., Yudkin, M. D. & Errington, J. Cytological and biochemical characterization of the FtsA cell division protein of Bacillus subtilis. *Mol. Microbiol.* **40**, 115–125 (2001).

138. Pichoff, S. & Lutkenhaus, J. Identification of a region of FtsA required for interaction with FtsZ. *Mol. Microbiol.* **64**, 1129–1138 (2007).

139. Shiomi, D. & Margolin, W. Dimerization or oligomerization of the actin-like FtsA protein enhances the integrity of the cytokinetic Z ring. *Mol. Microbiol.* **66**, 1396–1415 (2007).

140. Rico, A. I., García-Ovalle, M., Mingorance, J. & Vicente, M. Role of two essential domains of Escherichia coli FtsA in localization and progression of the division ring. *Mol. Microbiol.* **53**, 1359–1371 (2004).

141. Lara, B. *et al.* Cell division in cocci: localization and properties of the Streptococcus pneumoniae FtsA protein. *Mol. Microbiol.* **55**, 699–711 (2005).

142. Szwedziak, P., Wang, Q., Freund, S. M. & Löwe, J. FtsA forms actin-like protofilaments. *EMBO J.* **31**, 2249–2260 (2012).

143. Yan, K., Pearce, K. H. & Payne, D. J. A Conserved Residue at the Extreme C-Terminus of FtsZ Is Critical for the FtsA-FtsZ Interaction in Staphylococcus aureus. *Biochem. Biophys. Res. Commun.* **270**, 387–392 (2000).

144. Erickson, H. P. The FtsZ protofilament and attachment of ZipA—structural constraints on the FtsZ power stroke. *Curr. Opin. Cell Biol.* **13**, 55–60 (2001).

145. Dai, K. & Lutkenhaus, J. The proper ratio of FtsZ to FtsA is required for cell division to occur in Escherichia coli. *J. Bacteriol.* **174**, 6145–6151 (1992).

146. Hamoen, L. W., Meile, J.-C., De Jong, W., Noirot, P. & Errington, J. SepF, a novel FtsZ-interacting protein required for a late step in cell division. *Mol. Microbiol.* **59**, 989–999 (2006).

147. Gündoğdu, M. E. *et al.* Large ring polymers align FtsZ polymers for normal septum formation. *EMBO J.* **30**, 617–626 (2011).

148. Król, E. *et al.* Bacillus subtilis SepF Binds to the C-Terminus of FtsZ. *PLOS ONE* **7**, e43293 (2012).

149. Wenzel, M. *et al.* Controlling septum thickness by a large protein ring. *bioRxiv* 771139 (2020) doi:10.1101/771139.

150. Haeusser, D. P., Garza, A. C., Buscher, A. Z. & Levin, P. A. The division inhibitor EzrA contains a seven-residue patch required for maintaining the dynamic nature of the medial FtsZ ring. *J. Bacteriol.* **189**, 9001–9010 (2007).

151. Kawai, Y. & Ogasawara, N. Bacillus subtilis EzrA and FtsL synergistically regulate FtsZ ring dynamics during cell division. *Microbiol. Read. Engl.* **152**, 1129–1141 (2006).

152. Levin, P. A., Schwartz, R. L. & Grossman, A. D. Polymer Stability Plays an Important Role in the Positional Regulation of FtsZ. *J. Bacteriol.* **183**, 5449–5452 (2001).

153. Haeusser, D. P., Schwartz, R. L., Smith, A. M., Oates, M. E. & Levin, P. A. EzrA prevents aberrant cell division by modulating assembly of the cytoskeletal protein FtsZ. *Mol. Microbiol.* **52**, 801–814 (2004).

154. Chung, K.-M., Hsu, H.-H., Yeh, H.-Y. & Chang, B.-Y. Mechanism of regulation of prokaryotic tubulin-like GTPase FtsZ by membrane protein EzrA. *J. Biol. Chem.* **282**, 14891–14897 (2007).

155. Singh, J. K., Makde, R. D., Kumar, V. & Panda, D. A membrane protein, EzrA, regulates assembly dynamics of FtsZ by interacting with the C-terminal tail of FtsZ. *Biochemistry* **46**, 11013–11022 (2007).

156. Claessen, D. *et al.* Control of the cell elongation–division cycle by shuttling of PBP1 protein in Bacillus subtilis. *Mol. Microbiol.* **68**, 1029–1046 (2008).

157. Gueiros-Filho, F. J. & Losick, R. A widely conserved bacterial cell division protein that promotes assembly of the tubulin-like protein FtsZ. *Genes Dev.* **16**, 2544–2556 (2002).

158. Johnson, J. E., Lackner, L. L., Hale, C. A. & de Boer, P. A. ZipA is required for targeting of DMinC/DicB, but not DMinC/MinD, complexes to septal ring assemblies in Escherichia coli. J. Bacteriol. 186, 2418–2429 (2004) - Google Search. https://www.google.com/search?q=Johnson%2C+J.+E.%2C+Lackner%2C+L.+L.%2C+Hale%2C+C.+A.+%26+de+Boer%2C+P.+A.+ZipA+is+required+for+targeting+of+DMinC%2FDicB%2C+but+not+DMinC%2FMinD%2C+complexes+to+septal+ring+assemblies+in+Escherichia+coli.+J.+Bacteriol.+186%2C+2418%E2%80%932429+(2004)&rlz=1C1CHBF_en-GBGB864GB864&oq=Johnson%2C+J.+E.%2C+Lackner%2C+L.+L.%2C+Hale%2C+C.+A.+%26+de+B

oer%2C+P.+A.+ZipA+is+required+for+targeting+of+DMinC%2FDicB%2C+but+not+DMinC%2FMinD%2C+complexes+to+septal+ring+assemblies+in+Escherichia+coli.+J.+Bacteriol.+186%2C+2418%E2%80%932429+(2004)&aqs=chrome..69i57.1470j0j4&sourceid=chrome&ie=UTF-8.

159. Mohammadi, T. *et al.* The GTPase Activity of Escherichia coli FtsZ Determines the Magnitude of the FtsZ Polymer Bundling by ZapA in Vitro. *Biochemistry* **48**, 11056–11066 (2009).

160. Roach, E. J., Kimber, M. S. & Khursigara, C. M. Crystal structure and site-directed mutational analysis reveals key residues involved in Escherichia coli ZapA function. *J. Biol. Chem.* **289**, 23276–23286 (2014).

161. Small, E. *et al.* FtsZ polymer-bundling by the Escherichia coli ZapA orthologue, YgfE, involves a conformational change in bound GTP. *J. Mol. Biol.* **369**, 210–221 (2007).

162. Galli, E. & Gerdes, K. FtsZ-ZapA-ZapB interactome of Escherichia coli. *J. Bacteriol.* **194**, 292–302 (2012).

163. Pacheco-Gómez, R. *et al.* Tetramerization of ZapA is required for FtsZ bundling. *Biochem. J.* **449**, 795–802 (2013).

164. Caldas, P. *et al.* Cooperative ordering of treadmilling filaments in cytoskeletal networks of FtsZ and its crosslinker ZapA. *Nat. Commun.* **10**, 5744 (2019).

165. Woldringh, C. L. *et al.* Role of the nucleoid in the toporegulation of division. *Res. Microbiol.* **141**, 39–49 (1990).

166. Woldringh, C. L., Mulder, E., Huls, P. G. & Vischer, N. Toporegulation of bacterial division according to the nucleoid occlusion model. *Res. Microbiol.* **142**, 309–320 (1991).

167. Woldringh, C. L. The role of co-transcriptional translation and protein translocation (transertion) in bacterial chromosome segregation. *Mol. Microbiol.* **45**, 17–29 (2002).

168. Schumacher, M. A. & Zeng, W. Structures of the nucleoid occlusion protein SlmA bound to DNA and the C-terminal domain of the cytoskeletal protein FtsZ. *Proc. Natl. Acad. Sci.* **113**, 4988–4993 (2016).

169. Wu, L. J. & Errington, J. Coordination of cell division and chromosome segregation by a nucleoid occlusion protein in Bacillus subtilis. *Cell* **117**, 915–925 (2004).

170. Tonthat, N. K. *et al.* SlmA forms a higher-order structure on DNA that inhibits cytokinetic Z-ring formation over the nucleoid. *Proc. Natl. Acad. Sci.* **110**, 10586–10591 (2013).

171. Cho, H., McManus, H. R., Dove, S. L. & Bernhardt, T. G. Nucleoid occlusion factor SlmA is a DNA-activated FtsZ polymerization antagonist. *Proc. Natl. Acad. Sci.* **108**, 3773–3778 (2011).

172. Cho, H. & Bernhardt, T. G. Identification of the SlmA Active Site Responsible for Blocking Bacterial Cytokinetic Ring Assembly over the Chromosome. *PLOS Genet.* **9**, e1003304 (2013).

173. Du, S. & Lutkenhaus, J. SlmA Antagonism of FtsZ Assembly Employs a Two-pronged Mechanism like MinCD. *PLOS Genet.* **10**, e1004460 (2014).

174. Du, S., Park, K.-T. & Lutkenhaus, J. Oligomerization of FtsZ converts the FtsZ tail motif (conserved carboxy-terminal peptide) into a multivalent ligand with high avidity for partners ZipA and SlmA. *Mol. Microbiol.* **95**, 173–188 (2015).

175. Adams, D. W., Wu, L. J. & Errington, J. Nucleoid occlusion protein Noc recruits DNA to the bacterial cell membrane. *EMBO J.* **34**, 491–501 (2015).

176. Deghorain, M. *et al.* A defined terminal region of the E. coli chromosome shows late segregation and high FtsK activity. *PloS One* **6**, e22164 (2011).

177. Yu, Y., Zhou, J., Gueiros-Filho, F., Kearns, D. B. & Jacobson, S. C. *Noc corrals migration of FtsZ protofilaments during cytokinesis in* Bacillus subtilis. http://biorxiv.org/lookup/doi/10.1101/2020.08.27.271361 (2020) doi:10.1101/2020.08.27.271361.

178. Cha, J. H. & Stewart, G. C. The divIVA minicell locus of Bacillus subtilis. *J. Bacteriol.* **179**, 1671–1683 (1997).

179. The Bacillus subtilis DivIVA protein targets to the division septum and controls the site specificity of cell division - Edwards - 1997 - Molecular Microbiology - Wiley Online Library. https://onlinelibrary.wiley.com/doi/abs/10.1046/j.1365-2958.1997.3811764.x.

180. Lenarcic, R. *et al.* Localisation of DivIVA by targeting to negatively curved membranes. *EMBO J.* **28**, 2272–2282 (2009).

181. Szeto, T. H., Rowland, S. L., Rothfield, L. I. & King, G. F. Membrane localization of MinD is mediated by a C-terminal motif that is conserved across eubacteria, archaea, and chloroplasts. *Proc. Natl. Acad. Sci.* **99**, 15693–15698 (2002).
182. Bramkamp, M. *et al.* A novel component of the division-site selection system of Bacillus subtilis and a new mode of action for the division inhibitor MinCD. *Mol. Microbiol.* **70**, 1556–1569 (2008).
183. Patrick, J. E. & Kearns, D. B. MinJ (YvjD) is a topological determinant of cell division in Bacillus subtilis. *Mol. Microbiol.* **70**, 1166–1179 (2008).
184. Gregory, J. A., Becker, E. C. & Pogliano, K. Bacillus subtilis MinC destabilizes FtsZ-rings at new cell poles and contributes to the timing of cell division. *Genes Dev.* **22**, 3475–3488 (2008).
185. Rowlett, V. W. & Margolin, W. The Min system and other nucleoid-independent regulators of Z ring positioning. *Front. Microbiol.* **6**, (2015).
186. de Boer, P., Crossley, R. & Rothfield, L. The essential bacterial cell-division protein FtsZ is a GTPase. *Nature* **359**, 254–256 (1992).
187. Hu, Z. & Lutkenhaus, J. A conserved sequence at the C-terminus of MinD is required for binding to the membrane and targeting MinC to the septum. *Mol. Microbiol.* **47**, 345–355 (2003).
188. Hu, Z., Gogol, E. P. & Lutkenhaus, J. Dynamic assembly of MinD on phospholipid vesicles regulated by ATP and MinE. *Proc. Natl. Acad. Sci.* **99**, 6761–6766 (2002).
189. Raskin, D. M. & de Boer, P. A. J. The MinE Ring: An FtsZ-Independent Cell Structure Required for Selection of the Correct Division Site in E. coli. *Cell* **91**, 685–694 (1997).
190. Raskin, D. M. & Boer, P. A. J. de. MinDE-Dependent Pole-to-Pole Oscillation of Division Inhibitor MinC in Escherichia coli. *J. Bacteriol.* **181**, 6419–6424 (1999).
191. Raskin, D. M. & Boer, P. A. J. de. Rapid pole-to-pole oscillation of a protein required for directing division to the middle of Escherichia coli. *Proc. Natl. Acad. Sci.* **96**, 4971–4976 (1999).
192. Storchova, Z. & Pellman, D. From polyploidy to aneuploidy, genome instability and cancer. *Nat. Rev. Mol. Cell Biol.* **5**, 45–54 (2004).

193. Li, R. Cytokinesis in development and disease: variations on a common theme. *Cell. Mol. Life Sci.* **64**, 3044–3058 (2007).

194. Normand, G. & King, R. W. Understanding Cytokinesis Failure. in *Polyploidization and Cancer* (ed. Poon, R. Y. C.) 27–55 (Springer, 2010). doi:10.1007/978-1-4419-6199-0_3.

195. Cheffings, T. H., Burroughs, N. J. & Balasubramanian, M. K. Actomyosin Ring Formation and Tension Generation in Eukaryotic Cytokinesis. *Curr. Biol. CB* **26**, R719–R737 (2016).

196. Burki, F. The Eukaryotic Tree of Life from a Global Phylogenomic Perspective. *Cold Spring Harb. Perspect. Biol.* **6**, a016147 (2014).

197. Mangione, M. C. & Gould, K. L. Molecular form and function of the cytokinetic ring. *J. Cell Sci.* **132**, (2019).

198. Wu, J.-Q., Kuhn, J. R., Kovar, D. R. & Pollard, T. D. Spatial and Temporal Pathway for Assembly and Constriction of the Contractile Ring in Fission Yeast Cytokinesis. *Dev. Cell* **5**, 723–734 (2003).

199. Dean, S. O., Rogers, S. L., Stuurman, N., Vale, R. D. & Spudich, J. A. Distinct pathways control recruitment and maintenance of myosin II at the cleavage furrow during cytokinesis. *Proc. Natl. Acad. Sci.* **102**, 13473–13478 (2005).

200. Motegi, F., Mishra, M., Balasubramanian, M. K. & Mabuchi, I. Myosin-II reorganization during mitosis is controlled temporally by its dephosphorylation and spatially by Mid1 in fission yeast. *J. Cell Biol.* **165**, 685–695 (2004).

201. Smith, L. G. Divide and conquer: cytokinesis in plant cells. *Curr. Opin. Plant Biol.* **2**, 447–453 (1999).

202. Adams, D. W. & Errington, J. Bacterial cell division: assembly, maintenance and disassembly of the Z ring. *Nat. Rev. Microbiol.* **7**, 642–653 (2009).

203. Erickson, H. P. FtsZ, a prokaryotic homolog of tubulin? *Cell* **80**, 367–370 (1995).

204. Löwe, J. & Amos, L. A. Crystal structure of the bacterial cell-division protein FtsZ. *Nature* **391**, 203–206 (1998).

205. Nogales, E., Wolf, S. G. & Downing, K. H. Structure of the αβ tubulin dimer by electron crystallography. *Nature* **391**, 199–203 (1998).

206. Anderson, D. E., Gueiros-Filho, F. J. & Erickson, H. P. Assembly dynamics of FtsZ rings in Bacillus subtilis and Escherichia coli and effects of FtsZ-regulating proteins. *J. Bacteriol.* **186**, 5775–5781 (2004).

207. Stricker, J., Maddox, P., Salmon, E. D. & Erickson, H. P. Rapid assembly dynamics of the Escherichia coli FtsZ-ring demonstrated by fluorescence recovery after photobleaching. *Proc. Natl. Acad. Sci.* **99**, 3171–3175 (2002).

208. Loose, M. & Mitchison, T. J. The bacterial cell division proteins FtsA and FtsZ self-organize into dynamic cytoskeletal patterns. *Nat. Cell Biol.* **16**, 38–46 (2014).

209. Bisson-Filho, A. W. *et al.* Treadmilling by FtsZ filaments drives peptidoglycan synthesis and bacterial cell division. *Science* **355**, 739–743 (2017).

210. Yang, X. *et al.* GTPase activity-coupled treadmilling of the bacterial tubulin FtsZ organizes septal cell wall synthesis. *Science* **355**, 744–747 (2017).

211. de Jong, I. G., Beilharz, K., Kuipers, O. P. & Veening, J.-W. Live Cell Imaging of Bacillus subtilis and Streptococcus pneumoniae using Automated Time-lapse Microscopy. *J. Vis. Exp. JoVE* (2011) doi:10.3791/3145.

212. Levin, P. A., Kurtser, I. G. & Grossman, A. D. Identification and characterization of a negative regulator of FtsZ ring formation in Bacillus subtilis. *Proc. Natl. Acad. Sci.* **96**, 9642–9647 (1999).

213. Hostettler, L. *et al.* The Bright Fluorescent Protein mNeonGreen Facilitates Protein Expression Analysis *In Vivo*. *G3amp58 GenesGenomesGenetics* **7**, 607–615 (2017).

214. Feucht, A., Lucet, I., Yudkin, M. D. & Errington, J. Cytological and biochemical characterization of the FtsA cell division protein of Bacillus subtilis. *Mol. Microbiol.* **40**, 115–125 (2001).

215. Tokunaga, M., Imamoto, N. & Sakata-Sogawa, K. Highly inclined thin illumination enables clear single-molecule imaging in cells. *Nat. Methods* **5**, 159–161 (2008).

216. Whitley, K. D. *et al.* FtsZ treadmilling is essential for Z-ring condensation and septal constriction initiation in Bacillus subtilis cell division. *bioRxiv* 2020.07.01.182006 (2020) doi:10.1101/2020.07.01.182006.

217. Hell, S. W. Far-field optical nanoscopy. *Science* **316**, 1153–1158 (2007).

218. Hell, S. W. & Wichmann, J. Breaking the diffraction resolution limit by stimulated emission: stimulated-emission-depletion fluorescence microscopy. *Opt. Lett.* **19**, 780–782 (1994).

219. Gustafsson, M. G. L. Surpassing the lateral resolution limit by a factor of two using structured illumination microscopy. *J. Microsc.* **198**, 82–87 (2000).

220. Cox, S. Super-resolution imaging in live cells. *Dev. Biol.* **401**, 175–181 (2015).

221. Manley, S. *et al.* High-density mapping of single-molecule trajectories with photoactivated localization microscopy. *Nat. Methods* **5**, 155–157 (2008).

222. Garner, E. C. *et al.* Coupled, Circumferential Motions of the Cell Wall Synthesis Machinery and MreB Filaments in B. subtilis. *Science* **333**, 222–225 (2011).

223. Monteiro, J. M. *et al.* Peptidoglycan synthesis drives an FtsZ-treadmilling-independent step of cytokinesis. *Nature* (2018) doi:10.1038/nature25506.

224. Perez, A. J. *et al.* Movement dynamics of divisome proteins and PBP2x:FtsW in cells of Streptococcus pneumoniae. *Proc. Natl. Acad. Sci.* **116**, 3211–3220 (2019).

225. Holden, S. J. *et al.* High throughput 3D super-resolution microscopy reveals Caulobacter crescentus in vivo Z-ring organization. *Proc. Natl. Acad. Sci. U. S. A.* **111**, 4566–4571 (2014).

226. Wagstaff, J. M. *et al.* A Polymerization-Associated Structural Switch in FtsZ That Enables Treadmilling of Model Filaments. *mBio* **8**, (2017).

227. Oliva, M. A., Cordell, S. C. & Löwe, J. Structural insights into FtsZ protofilament formation. *Nat. Struct. Mol. Biol.* **11**, 1243–1250 (2004).

228. Narita, A. Minimum requirements for the actin-like treadmilling motor system. *BioArchitecture* **1**, 205–208 (2011).

229. Narita, A. Merits of the double-stranded form of the actin filament revealed by structures of the filament ends. *Commun. Integr. Biol.* **4**, 692–695 (2011).

230. Wegner, A. Head to tail polymerization of actin. *J. Mol. Biol.* **108**, 139–150 (1976).

231. Corbin, L. C. & Erickson, H. P. A Unified Model for Treadmilling and Nucleation of Single-Stranded FtsZ Protofilaments. *Biophys. J.* **119**, 792–805 (2020).

232. Andreu, J. M. How Protein Filaments Treadmill. *Biophys. J.* **119**, 717–720 (2020).

233. Du, S., Pichoff, S., Kruse, K. & Lutkenhaus, J. FtsZ filaments have the opposite kinetic polarity of microtubules. *Proc. Natl. Acad. Sci.* **115**, 10768–10773 (2018).

234. Desai, A. & Mitchison, T. J. Microtubule Polymerization Dynamics. *Annu. Rev. Cell Dev. Biol.* **13**, 83–117 (1997).

235. Jaeger, P. A., McElfresh, C., Wong, L. R. & Ideker, T. Beyond Agar: Gel Substrates with Improved Optical Clarity and Drug Efficiency and Reduced Autofluorescence for Microbial Growth Experiments. *Appl. Environ. Microbiol.* **81**, 5639–5649 (2015).

236. Margolin, W. The Price of Tags in Protein Localization Studies. *J. Bacteriol.* **194**, 6369–6371 (2012).

237. Weart, R. B. & Levin, P. A. Growth Rate-Dependent Regulation of Medial FtsZ Ring Formation. *J. Bacteriol.* **185**, 2826–2834 (2003).

238. Weart, R. B. *et al.* A Metabolic Sensor Governing Cell Size in Bacteria. *Cell* **130**, 335–347 (2007).

239. Osawa, M. & Erickson, H. P. Liposome division by a simple bacterial division machinery. *Proc. Natl. Acad. Sci.* **110**, 11000–11004 (2013).

240. Osawa, M., Anderson, D. E. & Erickson, H. P. Reconstitution of Contractile FtsZ Rings in Liposomes. *Science* **320**, 792–794 (2008).

241. Lan, G., Wolgemuth, C. W. & Sun, S. X. Z-ring force and cell shape during division in rod-like bacteria. *Proc. Natl. Acad. Sci.* **104**, 16110–16115 (2007).

242. Koo, B.-M. *et al.* Construction and Analysis of Two Genome-Scale Deletion Libraries for Bacillus subtilis. *Cell Syst.* **4**, 291-305.e7 (2017).

243. Ben-Yehuda, S. & Losick, R. Asymmetric cell division in B. subtilis involves a spiral-like intermediate of the cytokinetic protein FtsZ. *Cell* **109**, 257–266 (2002).

244. Handler, A. A., Lim, J. E. & Losick, R. Peptide inhibitor of cytokinesis during sporulation in Bacillus subtilis. *Mol. Microbiol.* **68**, 588–599 (2008).

245. Moore, D. A., Whatley, Z. N., Joshi, C. P., Osawa, M. & Erickson, H. P. Probing for Binding Regions of the FtsZ Protein Surface through Site-Directed Insertions: Discovery of Fully Functional FtsZ-Fluorescent Proteins. *J. Bacteriol.* **199**, (2017).

246. Fleurie, A. *et al.* Interplay of the Serine/Threonine-Kinase StkP and the Paralogs DivIVA and GpsB in Pneumococcal Cell Elongation and Division. *PLOS Genet.* **10**, e1004275 (2014).

247. Jacq, M. *et al.* Remodeling of the Z-Ring Nanostructure during the Streptococcus pneumoniae Cell Cycle Revealed by Photoactivated Localization Microscopy. *mBio* **6**, e01108-15 (2015).

248. Ma, X., Ehrhardt, D. W. & Margolin, W. Colocalization of cell division proteins FtsZ and FtsA to cytoskeletal structures in living Escherichia coli cells by using green fluorescent protein. *Proc. Natl. Acad. Sci. U. S. A.* **93**, 12998–13003 (1996).

249. Osawa, M. & Erickson, H. P. FtsZ from Divergent Foreign Bacteria Can Function for Cell Division in Escherichia coli. *J. Bacteriol.* **188**, 7132–7140 (2006).

250. Ellefsen, K. L., Dynes, J. L. & Parker, I. Spinning-Spot Shadowless TIRF Microscopy. *PLOS ONE* **10**, e0136055 (2015).

251. Luisier, F., Vonesch, C., Blu, T. & Unser, M. Fast interscale wavelet denoising of Poisson-corrupted images. *Signal Process.* **90**, 415–427 (2010).

252. Thevenaz, P., Ruttimann, U. E. & Unser, M. A pyramid approach to subpixel registration based on intensity. *IEEE Trans. Image Process.* **7**, 27–41 (1998).

253. Eberly, D., Gardner, R., Morse, B., Pizer, S. & Scharlach, C. Ridges for image analysis. *J. Math. Imaging Vis.* **4**, 353–373 (1994).

254. Introduction To Light Sheet Microscopy. *Teledyne Photometrics* https://www.photometrics.com/learn/light-sheet-microscopy/introduction-to-light-sheet-microscopy.

255. Tosheva, K. L., Yuan, Y., Matos Pereira, P., Culley, S. & Henriques, R. Between life and death: strategies to reduce phototoxicity in super-resolution microscopy. *J. Phys. Appl. Phys.* **53**, 163001 (2020).

256. Laissue, P. P., Alghamdi, R. A., Tomancak, P., Reynaud, E. G. & Shroff, H. Assessing phototoxicity in live fluorescence imaging. *Nat. Methods* **14**, 657–661 (2017).

257. Dixit, R. & Cyr, R. Cell damage and reactive oxygen species production induced by fluorescence microscopy: effect on mitosis and guidelines for non-invasive fluorescence microscopy. *Plant J. Cell Mol. Biol.* **36**, 280–290 (2003).

258. Logg, K., Bodvard, K., Blomberg, A. & Käll, M. Investigations on light-induced stress in fluorescence microscopy using nuclear localization of the transcription factor Msn2p as a reporter. *FEMS Yeast Res.* **9**, 875–884 (2009).

259. Devary, Y., Rosette, C., DiDonato, J. A. & Karin, M. NF-kappa B activation by ultraviolet light not dependent on a nuclear signal. *Science* **261**, 1442–1445 (1993).

260. Rehemtulla, A., Hamilton, C. A., Chinnaiyan, A. M. & Dixit, V. M. Ultraviolet radiation-induced apoptosis is mediated by activation of CD-95 (Fas/APO-1). *J. Biol. Chem.* **272**, 25783–25786 (1997).

261. Peak, M. J. & Peak, J. G. Single-strand breaks induced in Bacillus subtilis DNA by ultraviolet light: action spectrum and properties. *Photochem. Photobiol.* **35**, 675–680 (1982).

262. Peak, M. J., Peak, J. G. & Carnes, B. A. Induction of direct and indirect single-strand breaks in human cell DNA by far- and near-ultraviolet radiations: action spectrum and mechanisms. *Photochem. Photobiol.* **45**, 381–387 (1987).

263. Brem, R., Macpherson, P., Guven, M. & Karran, P. Oxidative stress induced by UVA photoactivation of the tryptophan UVB photoproduct 6-formylindolo[3,2-b]carbazole (FICZ) inhibits nucleotide excision repair in human cells. *Sci. Rep.* **7**, 4310 (2017).

264. Eichler, M., Lavi, R., Shainberg, A. & Lubart, R. Flavins are source of visible-light-induced free radical formation in cells. *Lasers Surg. Med.* **37**, 314–319 (2005).

265. Kilian, N. *et al.* Assessing photodamage in live-cell STED microscopy. *Nat. Methods* **15**, 755–756 (2018).

266. Huisman, O. & D'Ari, R. An inducible DNA replication–cell division coupling mechanism in E. coli. *Nature* **290**, 797–799 (1981).

267. Huisman, O., D'Ari, R. & Gottesman, S. Cell-division control in Escherichia coli: specific induction of the SOS function SfiA protein is sufficient to block septation. *Proc. Natl. Acad. Sci.* **81**, 4490–4494 (1984).

268. Justice, S. S., García-Lara, J. & Rothfield, L. I. Cell division inhibitors SulA and MinC/MinD block septum formation at different steps in the assembly of the Escherichia coli division machinery. *Mol. Microbiol.* **37**, 410–423 (2000).

269. Mukherjee, A., Cao, C. & Lutkenhaus, J. Inhibition of FtsZ polymerization by SulA, an inhibitor of septation in Escherichia coli. *Proc. Natl. Acad. Sci.* **95**, 2885–2890 (1998).

270. Bi, E. & Lutkenhaus, J. Cell division inhibitors SulA and MinCD prevent formation of the FtsZ ring. *J. Bacteriol.* **175**, 1118–1125 (1993).

271. Cordell, S. C., Robinson, E. J. H. & Lowe, J. Crystal structure of the SOS cell division inhibitor SulA and in complex with FtsZ. *Proc. Natl. Acad. Sci. U. S. A.* **100**, 7889–7894 (2003).

272. Kawai, Y., Moriya, S. & Ogasawara, N. Identification of a protein, YneA, responsible for cell division suppression during the SOS response in Bacillus subtilis. *Mol. Microbiol.* **47**, 1113–1122 (2003).

273. Magidson, V. & Khodjakov, A. Circumventing photodamage in live-cell microscopy. *Methods Cell Biol.* **114**, (2013).

274. Fluorophore Photobleaching Literature References. *Nikon's MicroscopyU* https://www.microscopyu.com/references/fluorophore-photobleaching.

275. Kalies, S., Kuetemeyer, K. & Heisterkamp, A. Mechanisms of high-order photobleaching and its relationship to intracellular ablation. *Biomed. Opt. Express* **2**, 805–816 (2011).

276. Garner, E. C. *et al.* Coupled, circumferential motions of the cell wall synthesis machinery and MreB filaments in B. subtilis. *Science* **333**, 222–225 (2011).

277. Transmembrane protein sorting driven by membrane curvature | Nature Communications. https://www.nature.com/articles/ncomms9728.

278. Loose, M. & Mitchison, T. J. The bacterial cell division proteins FtsA and FtsZ self-organize into dynamic cytoskeletal patterns. *Nat. Cell Biol.* **16**, 38–46 (2014).

279. Bisson-Filho, A. W. *et al.* Treadmilling by FtsZ filaments drives peptidoglycan synthesis and bacterial cell division. *Science* **355**, 739–743 (2017).

280. Yang, X. *et al.* GTPase activity–coupled treadmilling of the bacterial tubulin FtsZ organizes septal cell wall synthesis. *Science* **355**, 744–747 (2017).

281. Monteiro, J. M. *et al.* Peptidoglycan synthesis drives an FtsZ-treadmilling-independent step of cytokinesis. *Nature* (2018) doi:10.1038/nature25506.

282. Perez, A. J. *et al.* Movement dynamics of divisome proteins and PBP2x:FtsW in cells of Streptococcus pneumoniae. *Proc. Natl. Acad. Sci.* **116**, 3211–3220 (2019).

283. Baranova, N. *et al.* Diffusion and capture permits dynamic coupling between treadmilling FtsZ filaments and cell division proteins. *Nat. Microbiol.* **5**, 407–417 (2020).

284. Coltharp, C., Buss, J., Plumer, T. M. & Xiao, J. Defining the rate-limiting processes of bacterial cytokinesis. *Proc. Natl. Acad. Sci.* 201514296 (2016) doi:10.1073/pnas.1514296113.

285. de Jong, I. G., Beilharz, K., Kuipers, O. P. & Veening, J.-W. Live Cell Imaging of Bacillus subtilis and Streptococcus pneumoniae using Automated Time-lapse Microscopy. *J. Vis. Exp.* (2011) doi:10.3791/3145.

286. Ducret, A., Quardokus, E. M. & Brun, Y. V. MicrobeJ, a tool for high throughput bacterial cell detection and quantitative analysis. *Nat. Microbiol.* **1**, 1–7 (2016).

287. Berg, S. *et al.* ilastik: interactive machine learning for (bio)image analysis. *Nat. Methods* **16**, 1226–1232 (2019).

288. Bisson-Filho, A. W. *et al.* FtsZ filament capping by MciZ, a developmental regulator of bacterial division. *Proc. Natl. Acad. Sci.* **112**, E2130–E2138 (2015).

289. Yang, D., Jennings, A. D., Borrego, E., Retterer, S. T. & Männik, J. Analysis of factors limiting bacterial growth in PDMS mother machine devices. *Front. Microbiol.* **9**, (2018).

290. Monahan, L. G., Robinson, A. & Harry, E. J. Lateral FtsZ association and the assembly of the cytokinetic Z ring in bacteria. *Mol. Microbiol.* **74**, 1004–1017 (2009).

291. Erickson, H. P., Anderson, D. E. & Osawa, M. FtsZ in Bacterial Cytokinesis: Cytoskeleton and Force Generator All in One. *Microbiol. Mol. Biol. Rev.* **74**, 504–528 (2010).

292. Walker, B. E., Männik, J. & Männik, J. Transient Membrane-Linked FtsZ Assemblies Precede Z-Ring Formation in Escherichia coli. *Curr. Biol.* **30**, 499-508.e6 (2020).

293. Ramirez-Diaz, D. A. *et al.* Treadmilling analysis reveals new insights into dynamic FtsZ ring architecture. *PLOS Biol.* **16**, e2004845 (2018).

294. Sundararajan, K., Vecchiarelli, A., Mizuuchi, K. & Goley, E. D. Species- and C-terminal linker-dependent variations in the dynamic behavior of FtsZ on membranes in vitro. *Mol. Microbiol.* **110**, 47–63 (2018).

295. Barrows, J. M. & Goley, E. D. FtsZ dynamics in bacterial division: What, how, and why? *Curr. Opin. Cell Biol.* **68**, 163–172 (2021).

296. Sundararajan, K. *et al.* The bacterial tubulin FtsZ requires its intrinsically disordered linker to direct robust cell wall construction. *Nat. Commun.* **6**, 7281 (2015).

297. Cohan, M. C., Eddelbuettel, A. M. P., Levin, P. A. & Pappu, R. V. Dissecting the Functional Contributions of the Intrinsically Disordered C-terminal Tail of Bacillus subtilis FtsZ. *J. Mol. Biol.* **432**, 3205–3221 (2020).

298. Buske, P. J. & Levin, P. A. A flexible C-terminal linker is required for proper FtsZ assembly in vitro and cytokinetic ring formation in vivo. *Mol. Microbiol.* **89**, 249–263 (2013).

299. Gardner, K. A. J. A., Moore, D. A. & Erickson, H. P. The C-terminal linker of Escherichia coli FtsZ functions as an intrinsically disordered peptide. *Mol. Microbiol.* **89**, 264–275 (2013).

300. Barrows, J. M., Sundararajan, K., Bhargava, A. & Goley, E. D. FtsA Regulates Z-Ring Morphology and Cell Wall Metabolism in an FtsZ C-Terminal Linker-Dependent Manner in Caulobacter crescentus. *J. Bacteriol.* **202**, (2020).

301. Dajkovic, A., Pichoff, S., Lutkenhaus, J. & Wirtz, D. Cross-linking FtsZ polymers into coherent Z rings. *Mol. Microbiol.* **78**, 651–668 (2010).

302. Eswaramoorthy, P. *et al.* Cellular Architecture Mediates DivIVA Ultrastructure and Regulates Min Activity in Bacillus subtilis. *mBio* **2**, e00257-11 (2011).

303. Ishikawa, S., Kawai, Y., Hiramatsu, K., Kuwano, M. & Ogasawara, N. A new FtsZ-interacting protein, YlmF, complements the activity of FtsA during progression of cell division in Bacillus subtilis. *Mol. Microbiol.* **60**, 1364–1380 (2006).

304. Hamoen, L. W., Meile, J.-C., de Jong, W., Noirot, P. & Errington, J. SepF, a novel FtsZ-interacting protein required for a late step in cell division. *Mol. Microbiol.* **59**, 989–999 (2006).

305. Harwood, C. R. & Cutting, S. M. *Molecular biological methods for Bacillus*. (Wiley, 1990).

306. Koo, B.-M. *et al.* Construction and Analysis of Two Genome-Scale Deletion Libraries for Bacillus subtilis. *Cell Syst.* **4**, 291-305.e7 (2017).

307. Hamoen, L. W., Meile, J.-C., De Jong, W., Noirot, P. & Errington, J. SepF, a novel FtsZ-interacting protein required for a late step in cell division. *Mol. Microbiol.* **59**, 989–999 (2006).

308. Eswaramoorthy, P. *et al.* Cellular Architecture Mediates DivIVA Ultrastructure and Regulates Min Activity in Bacillus subtilis. *mBio* **2**, (2011).

309. Ramamurthi, K. S. & Losick, R. Negative membrane curvature as a cue for subcellular localization of a bacterial protein. *Proc. Natl. Acad. Sci.* **106**, 13541–13545 (2009).

310. Bach, J. N., Albrecht, N. & Bramkamp, M. Imaging DivIVA dynamics using photo-convertible and activatable fluorophores in <i>Bacillus subtilis</i> *Front. Microbiol.* **5**, (2014).

311. Cleverley, R. & Lewis, R. EzrA: a spectrin-like scaffold in the bacterial cell division machinery. *Microb. Cell* **2**, 59–61.

312. Huang, B., Babcock, H. & Zhuang, X. Breaking the Diffraction Barrier: Super-Resolution Imaging of Cells. *Cell* **143**, 1047–1058 (2010).

313. Coltharp, C. & Xiao, J. Superresolution microscopy for microbiology. *Cell. Microbiol.* **14**, 1808–1818 (2012).

314. Erickson, H. P., Anderson, D. E. & Osawa, M. FtsZ in bacterial cytokinesis: cytoskeleton and force generator all in one. *Microbiol. Mol. Biol. Rev. MMBR* **74**, 504–528 (2010).

315. Bendezú, F. O., Hale, C. A., Bernhardt, T. G. & de Boer, P. A. J. RodZ (YfgA) is required for proper assembly of the MreB actin cytoskeleton and cell shape in E. coli. *EMBO J.* **28**, 193–204 (2009).

316. Ellefsen, K. L., Dynes, J. L. & Parker, I. Spinning-Spot Shadowless TIRF Microscopy. *PLOS ONE* **10**, e0136055 (2015).

317. Monahan, L. G., Robinson, A. & Harry, E. J. Lateral FtsZ association and the assembly of the cytokinetic Z ring in bacteria. *Mol. Microbiol.* **74**, 1004–1017 (2009).

318. Król, E. *et al.* Bacillus subtilis SepF Binds to the C-Terminus of FtsZ. *PLOS ONE* **7**, e43293 (2012).

319. Duman, R. *et al.* Structural and genetic analyses reveal the protein SepF as a new membrane anchor for the Z ring. *Proc. Natl. Acad. Sci.* **110**, E4601–E4610 (2013).

320. Kunst, F. *et al.* The complete genome sequence of the gram-positive bacterium Bacillus subtilis. *Nature* **390**, 249–256 (1997).

321. Youngman, P. J., Perkins, J. B. & Losick, R. Genetic transposition and insertional mutagenesis in Bacillus subtilis with Streptococcus faecalis transposon Tn917. *Proc. Natl. Acad. Sci. U. S. A.* **80**, 2305–2309 (1983).

Appendix I: Supplementary tables

Supplementary Table 1: Strain genotypes

Strain	Genotype	Reference
168 CA	BS168 CA- *trpC2*	[320]
PY79	Prototroph	[321]
PL642	JH642 *ftsZ::ftsZ-gfp-cat*	[135]
PB5250	BS168 *trpC2 Δhag::kan*	[242]
3312	BS168 *trpC2,ezrA::ezrA-gfp-cat*	[65]
4181	BS168 *amy::Pxyl-sepF-gfp spc*	[307]
SH14	BS168 *trpC2, divIVA::divIVA-mCherry2::cat*	Marc Braumkamp unpublished
ME7	PY79 *pbp2B::mNeonGreen-15aa-pbp2B*	
bAB167	PY79 *ftsAZ::mNeonGreen-15aa-ftsA-ftsZ-ftsA-ftsZ*	[1]
bAB181	PY79 *ftsAZ::erm-ftsA-mNeonGreen-15aa-ftsZ-ftsA-ftsZ-cat*	[1]
bAB185	*PY79* *ftsAZ:: ftsA-mNeonGreen-15aa- ftsZ-ftsA-ftsZ*	[1]
bAB229	*PY79* ftsAZ::erm-ftsA-HaloTag(SW)-mNeonGreen-15aa-ftsZ-ftsA-ftsZ-cat	[1]
bGS28	*PY79* *pbp2B::erm-Phyperspank-HaloTag-15aa-pbp2B*	[1]
bGS31	*PY79* *pbp2B::erm-Phyperspank-HaloTag-15aa-pbp2B*	[1]
SH13	trpC2, ftsZ::ftsZ-gfp-cat	[1]
SH41	ftsAZ::mNeonGreen-15aa-ftsA-ftsZ-FtsA-FtsZ, Δhag::aph (Kan)]	[1]
SH42	ftsAZ::erm-ftsA-HaloTag(SW)-mNeonGreen- 15aa-ftsZ-cat-ftsA-FtsZ, Δhag::aph (Kan)	This work
SH74	*BS168CA* *trpC2, ftsAZ:: ftsa-mNeonGreen-15aaftsZ,* Δhag::aph(Kan)	This work
SH97	*trpC2,* Δhag::aph(Kan)	This work
SH130	PY79 *Δhag ftsZ::ftsZ-gfp-cam*	This work
SH136	*BS168CA* *trpC2 divIVA::divIVA-mCherry2-cat, Δhag*	This work
SH137	*amyE::sepF-gfp-spec, Δhag*	This work
SH138	*ezrA::ezrA-gfp-cat, Δhag*	This work
SH211	PY79 *Δhag*	This work
ECE274	*E. coli* *Ap* *Sp* *(pDR244)*	[242]

Supplementary Table 2: Table of sample sizes. N.D indicates when the number of filaments were not quantified.

Figure Number	No. data points	No Cells
2.3A	ND	22
2.3B	35 filaments	10
2.4	ND	69
2.6	111	32
2.7	ND	130
2.8	62	30
3.1A	111	32
3.1B	ND	178
3.5A PY79 30C poor media	98 cells	98
3.5A SH130 30C poor media	98 cells	98
3.5A PY79 37C poor media	98 cells	98
3.5A SH130 37C poor media	98 cells	98
3.5A PY79 37C rich media	98 cells	98
3.5A SH130 37C rich media	98 cells	98
4.3 A EMMCD	30 FOV	262
4.3 A SCMOS and Optimised micropillars	30 FOV	1384
4.3 A SCMOS, Optimised micropillars & centrifugation	30 FOV	3551
4.10		
5.1A	61 cells	61
5.1B	3526 data points	61
5.1C nascent rings	526 data points	61
5.1C mature rings	1053 data points	61
5.1C constricting rings	1677 data points	61
5.2A	3256 data points	61
5.2B	766 rings	766
5.3A-C	ND	766
5.3D nascent rings	1066 filaments	234
5.3D mature/ early constricting rings	1588 filaments	254
5.3D late constricting rings	1538 filaments	766
6.1	188	54
6.2	160	64
6.3	857	127

Supplementary Table 3: Microscopy acquisition parameters.

Figure Number	Microscope Configuration	Wavelength and power density	Exposure time & Acquisition interval	Image Pixel Size
2.2D (LEFT)	Nikon NSTORM microscope, Widefield illumination	488 nm 1.8 W/cm^2	1 second exposure, 1 frame/s	64 nm
2.2D (RIGHT)	Nikon NSTORM microscope, Widefield illumination	488 nm 1.8 W/cm^2	1 second exposure, 1 frame/s	64 nm
2.3A	Nikon NSTORM microscope, Widefield illumination	488 nm 1.8 W/cm^2	1 second exposure, 1 frame/s	64 nm
2.3B	Nikon NSTORM microscope, Widefield illumination	488 nm 1.8 W/cm^2	2 second exposure, 1 frame/2s	64nm
2.4	Nikon NSTORM microscope, Widefield illumination	488 nm 1.8 W/cm^2	1 second exposure, 1 frame/s	64nm
2.5B	Nikon NSTORM microscope, Widefield illumination	488 nm 1.8 W/cm^2	1 second exposure, 1 frame/s	64nm
2.5C	Nikon NSTORM microscope, HiLO illumination	488 nm 1.8 W/cm^2	1 second exposure, 1 frame/s	64nm
2.6	Nikon NSTORM microscope, HiLO illumination	488 nm 1.8 W/cm^2	1 second exposure, 1 frame/s	64nm

2.7	Custom inverted microscope, HiLO illumination	488 nm 1.8 W/cm^2 561 nm 1-8 W/cm^2	1 second exposure, 1 frame/s	65nm
2.9	Nikon NSTORM microscope, HiLO illumination	488 nm 1.8 W/cm^2	1 second exposure, 1 frame/s	65nm
3.1A	Custom inverted microscope, HiLO illumination	488 nm 1.8 W/cm^2	1 second exposure, 1 frame/s	65nm
3.1B	Custom inverted microscope, HiLO illumination	488 nm 1.8 W/cm^2 561 nm, 1.2 W/cm^2	1 second exposure, 1 frame/s	64nm
4.2A EMCCD camera	Nikon NSTORM microscope, HiLO illumination	488 nm 1.8 W/cm^2	1 second exposure, 1 frame/s	64nm
4.2A sCMOS camera & optimised micropillars	Custom inverted microscope, HiLO illumination	488 nm 1.8 W/cm^2	1 second exposure, 1 frame/s	65nm
4.2A EMCCD camera & centrifugation	Custom inverted microscope, HiLO illumination	488 nm 1.8 W/cm^2	1 second exposure, 1 frame/s	65nm
4.8	Custom inverted microscope, HiLO illumination	561 nm, 1.2 W/cm^2	1 second exposure, 1 frame/s	65nm
4.10	Custom inverted microscope, HiLO illumination	488 nm 0.9 W/cm^2	1 second exposure, 1 frame/2s	64nm
5.1A	Custom inverted microscope, ring HiLO illumination	488 nm 1.8 W/cm^2	1 second exposure, 1 frame/min	65 nm
5.3A	Custom inverted microscope, ring HiLO illumination	488 nm 1.8 W/cm^2	1 second exposure, 1 frame/min	65 nm

5.3B	Custom inverted microscope, ring HiLO illumination	488 nm 1.8 W/cm^2	1 second exposure, 1 frame/min	65 nm
5.3C	Custom inverted microscope, ring HiLO illumination	488 nm 1.8 W/cm^2	1 second exposure, 1 frame/min	65 nm
5.4A	Custom inverted microscope, ring HiLO illumination	488 nm 1.8 W/cm^2	1 second exposure, 1 frame/min	65 nm
5.4B	Custom inverted microscope, ring HiLO illumination	488 nm 1.8 W/cm^2	1 second exposure, 1 frame/min	65 nm
5.4C	Custom inverted microscope, ring HiLO illumination	488 nm 1.8 W/cm^2	1 second exposure, 1 frame/min	65 nm
6.1A	Custom inverted microscope, ring HiLO illumination	561 nm, 1.2 W/cm^2	1 second exposure, 1 frame/min	65 nm
6.2A	Custom inverted microscope, ring HiLO illumination	488 nm 1.8 W/cm^2	1 second exposure, 1 frame/min	65 nm
6.3A	Custom inverted microscope, ring HiLO illumination	488 nm 5.6 W/cm^2	1 second exposure, 1 frame/min	65 nm

Supplementary Table 4: Antibiotic concentration used in this study

Antibiotic	Concentration
Ampicillin	100µg/ml
Chloramphenicol	5µg/ml
Spectinomycin	60µg/ml
Erythromycin *	1µg/ml
Kanamycin	5µg/ml
Lincomycin *	25µg/ml

Primer	Sequence
oCJ06	GTAGAGCTCATCCATGCCATGTG
oCJ93	CTATTCCCAAAACATGCTTAATAG
oCJ95	TTAGCCGCGTTTATTACG
oCJ154	ATGGTTTCGAAAGGAGAGGAG
oCJ300	GACAATATTGACTATGGCAGAGCC
oCJ301	GCCGCATAAAAATCAAGCCACCG

Appendix II: Media, Buffers and Solutions

Growth cultures

LB broth (1l)

Component	Volume	Final conc (%)
Casein	10 g	0.1
Yeast extract	5 g	0.05
NaCl	5 g	0.05
dH2O	1000 ml	

Spizizen minimal medium (SMM)

Component	Volume	Final conc (%)
(NH4)2SO$_4$	2.0 g	0.2
K_2HPO_4	14.0 g	1.4
KH_2PO_4	6.0 g	0.6
Na-Citrate•2H_2O	1.0 g	0.1
$MgSO_4$•7H^2O	200 mg	0.02
dH2O	995 ml	

Time lapse medium (TLM)

Component	Volume	Final conc (%)
SMM	100ml	
Glucose (40% w/v)	1.3 ml	0.52
Casamino acids (20% w/v)	100µL	0.002
Tryptophan (0.2%)	0.1 ml	0.02

Chemically defined medium (CDM)

Component	Volume	Final conc (%)
SMM	100ml	
Glucose (40% w/v)	100µL	0.04
Glutamic acid monosodium salt (10%w/v)	350µL	0.035
Tryptophan (2%)	6µL	0.00012
Modified metal mix	300µL	
$MnCl_2$	75µL	

Modified metal mix

Component	Volume	Final conc (mg/ml)	Final conc (mM)
HCl (2mM)	10ml		
$MgCl_2$•$6H_2O$	400mg	40	200 [Mg^{2+}]
$CaCl_2$•$2H_2O$	100mg	10	68 [Ca^{2+}]
$MnCl_2$•$2H_2O$ (100mg/ml)	100µL	1	5 [Mn^{2+}]
$ZnCl_2$ (10mg/ml)	15µL	0.015	0.072 [Zn^{2+}]
Thiamine hydrochloride (10mg/ml)	70µL	0.070	0.072 [Thiamine]
$FeCl_3$•$2H_2O$ (10mg/ml)	135µL	0.135	0.5 [Fe^{2+}]

1X PHMM medium (100ml)

CH I + II	47.5ml
CH III	1.5ml
CH IV	500µL
Tryptophan (0.2% w/v)	500µL
$S7_{50}$ salts (10X)	5ml
Modified metal mix	500µL
Glutamate (1M)	1ml
Glucose (20% w/v)	1ml
MgCl2 (2M)	5ml
dH_2O	37.5 ml

$S7_{50}$Salts (10X) (1L)

Component	Volume	Final Concentration (mM)
MOPS (free acid)	104.7g	500
$(NH_4)_2SO_4$	13.2g	100
KH_2PO_4	6.8g	50
ddH_2O	To 1L	

- Adjust pH to 7.0 with 50% KOH

CH I & II (2L)

Component	Volume
Casein Hydrolysate	20g
L-glutamate (sodium salt) (monohydrate)	9.4g
L-asparagine (monohydrate)	3.2g
L-alanine	2.5g
KH_2PO_4	2.72g
NH_4Cl	2.68g
Na_2SO_4	1ml (2000X stock)
NH_4NO_3	1ml (2000X stock)
$FeCl_3 \cdot 6H_2O$	1ml (2000X stock)
ddH_2O	To 2L

- Adjust pH to pH7.0 with 1N NaOH (~25ml for 4L)

CH III (1L)

Component	Volume	Final conc (%)
$CaCl_2 \cdot 2H_2O$	0.66g	0.066
$MgSO_4$	1.21g	0.121
ddH_2O	To 1L	

CH IV (1L)

Component	Volume	Final conc (%)
$MnSO_4 \cdot H_2O$	1.67g	0.0167
ddH_2O	To 1L	

Minimal Media (MM)

SMM	10ml
Glucose (40% w/v)	120µL
Tryptophan (0.2%)	100µL
$Mg_2SO \cdot 7H_2O$ (1M)	60µL
Casamino acids (20% w/v)	10µL
Fe-citrate (2.2mg/ml)	5µL

Starvation media

SMM	10ml
Glucose (40% w/v)	120µL

Mg_2SO_4• $7H_2O$ (1M)	60µL

Western blotting

Transfer buffer (1x) (1L)

Component	Volume	Final conc (%)
Tris	36.3g	3.63
Glycine	22.5g	2.25
Tricine	25.0g	2.50
SDS	0.5g	0.05
EDTA	0.73g	0.073

PBST (1X) (1L)

PBS (1X)	1L
Tween20	10ml

MES buffer (1X)

NuPAGE MES SDS (20x)	20ml
ddH_{2o}	980ml

Appendix III: Published works

Alexandre Wilson Bisson Filho, Yen-Pang Hsu, Georgia Squyres, Erkin Kuru, Fabai Wu, Calum Jukes, Cees Dekker, Séamus Holden, Michael VanNieuwenhze, Yves Brun, Ethan Garner, Treadmilling by FtsZ filaments drives peptidoglycan synthesis and bacterial cell division. Science, 355, 739-743 (2017).

Kevin D. Whitley*, Calum Jukes*, Nick Tregidgo, Eleni Karinous, Pedro Almada, Yann Cesbron, Ricardo Henriques, Cees Dekker, and Séamus Holden, FtsZ treadmilling is essential for Z-ring condensation and septal constriction initiation in *Bacillus subtilis* cell division. *Nat Commun* **12,** 2448 (2021). https://doi.org/10.1038/s41467-021-22526- *Equal author contribution.

Erratum 17 January 2020. See Erratum on pages 6-10.

REPORT

BACTERIAL DIVISION

Treadmilling by FtsZ filaments drives peptidoglycan synthesis and bacterial cell division

Alexandre W. Bisson-Filho,[1]‡ Yen-Pang Hsu,[2]‡ Georgia R. Squyres,[1]‡ Erkin Kuru,[2*]‡ Fabai Wu,[3]† Calum Jukes,[4] Yingjie Sun,[1] Cees Dekker,[3]§ Seamus Holden,[4]§ Michael S. VanNieuwenhze,[2,5]§ Yves V. Brun,[6]§ Ethan C. Garner[1]§

The mechanism by which bacteria divide is not well understood. Cell division is mediated by filaments of FtsZ and FtsA (FtsAZ) that recruit septal peptidoglycan-synthesizing enzymes to the division site. To understand how these components coordinate to divide cells, we visualized their movements relative to the dynamics of cell wall synthesis during cytokinesis. We found that the division septum was built at discrete sites that moved around the division plane. FtsAZ filaments treadmilled circumferentially around the division ring and drove the motions of the peptidoglycan-synthesizing enzymes. The FtsZ treadmilling rate controlled both the rate of peptidoglycan synthesis and cell division. Thus, FtsZ treadmilling guides the progressive insertion of new cell wall by building increasingly smaller concentric rings of peptidoglycan to divide the cell.

In most bacteria, cell division involves the inward synthesis of peptidoglycan (PG), creating a septum that cleaves the cell in two. The location of the septal PG synthases is regulated by filaments of the tubulin homolog FtsZ, which associate with the cytoplasmic side of the membrane via the actin-like FtsA and other factors. FtsZ forms membrane-associated filaments with FtsA (FtsAZ) (*1*, *2*). Together, they form a dynamic structure, the Z ring, which encircles the cell at the future division site (*3*) and recruits PG synthases and other proteins involved in cytokinesis (*4*). Once the division machinery is mature, the Z ring constricts while the associated synthases build the septum that partitions the cell in two.

We do not have a clear understanding of how the components of cell division interact in space and time to carry out cytokinesis, as we have been unable to observe the dynamics of each component relative to each other or to the structure they build: The organization and dynamics of FtsZ filaments within the Z ring remain ill-defined; it is not known how FtsAZ filaments control the activity of PG synthases; and the dynamics of septal PG synthesis have never been directly observed. To gain insight into how these components work together to divide bacteria, we visualized the dynamics of septal PG synthesis in

[1]Molecular and Cellular Biology, Faculty of Arts and Sciences Center for Systems Biology, Harvard University, Cambridge, MA 02138, USA. [2]Department of Molecular and Cellular Biochemistry, Indiana University, Bloomington, IN 47405, USA. [3]Department of Bionanoscience, Kavli Institute of Nanoscience Delft, Delft University of Technology, Netherlands. [4]Centre for Bacterial Cell Biology, Institute for Cell and Molecular Biosciences, Newcastle University, Newcastle upon Tyne NE2 4AX, UK. [5]Department of Chemistry, Indiana University, Bloomington, IN 47405, USA. [6]Department of Biology, Indiana University, Bloomington, IN 47405, USA.
*Present address: Department of Genetics, Harvard Medical School, Boston, MA 02115, USA. †Present address: Division of Geology and Planetary Sciences, California Institute of Technology, Pasadena, CA 91125, USA. ‡These authors contributed equally to this work. **§Corresponding author. Email: egarner@g.harvard.edu (E.C.G.); mvannieu@indiana.edu (M.S.V.); ybrun@indiana.edu (Y.V.B.); seamus.holden@newcastle.ac.uk (S.H.); c.dekker@tudelft.nl (C.D.)**

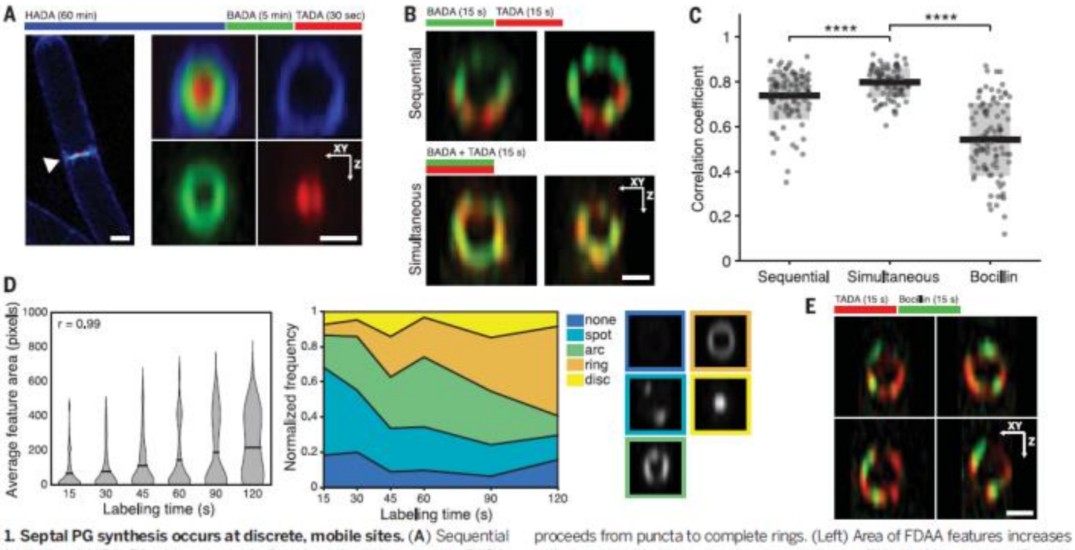

Fig. 1. Septal PG synthesis occurs at discrete, mobile sites. (**A**) Sequential FDAA labeling (HADA, 7-hydroxycoumarin-3-carboxylic acid–D-alanine; BADA, BODIPY FL-D-alanine; TADA, TAMRA–D-alanine) of division septa shows outside-in synthesis (arrowhead). (Right) 90° rotations of septa. (**B**) Sites of PG synthesis move around the septum. (**C**) Correlation coefficient of overlap between colors (yellow) in (B) and (E). Line, mean; box, SD. ****$P < 0.0001$. (**D**) FDAA labeling proceeds from puncta to complete rings. (Left) Area of FDAA features increases with pulse length. Lines, mean; r, correlation coefficient of the means. (Center) Blinded classification of FDAA features at various pulse lengths. (Right) Representative images of septal PG structures. (**E**) Sites of PG synthesis are offset from synthetic enzymes. Colored bars indicate time course of FDAA labeling. All images were taken with 3D-SIM. Scale bars, 0.5 μm.

Erratum 17 January 2020. See Erratum on pages 6-10.

relation to the movements of FtsAZ filaments and the septal PG synthase Pbp2B in the Gram-positive *Bacillus subtilis*.

To assess the dynamics of septal PG synthesis, we sequentially pulse-labeled growing cells with different colors of fluorescent D-amino acids (FDAAs) (table S1), which are incorporated into PG (*5*) by the D,D-transpeptidation activity of penicillin-binding proteins (PBPs) (*6*). Three-dimensional (3D)–structured illumination microscopy (3D-SIM) showed that sequential three-color FDAA pulse-labeling resulted in bull's-eye patterns at the division plane (Fig. 1A), demonstrating that the septum is progressively synthesized inward from the cell surface. Short, sequential pulses of two FDAA colors resulted in discrete spots or arcs distributed around the septum, with the colors more offset than for cells pulsed simultaneously (Fig. 1, B and C, and fig. S1, A and B). Thus, PG synthesis occurs at discrete sites that move around the division plane.

We next observed how discrete sites of PG synthesis develop into a complete division septum by labeling cells with FDAAs with increasing pulse durations. Both the total amount of labeling and the area of labeled regions increased with pulse duration (Fig. 1D, left, and fig. S2, A to C). Following short pulses, septa contained discrete spots or arcs (fig. S1C). As pulse duration increased, these arcs elongated and gradually transitioned into complete rings at longer pulses (Fig. 1D, right). As expected, PG synthesis inhibitors reduced FDAA incorporation (fig. S2D). To explore the location of the PG synthases relative to newly incorporated PG, we followed short FDAA pulses with Bocillin, which labels active PBPs (*7*) while inactivating them. The Bocillin signal was offset from the newly synthesized PG (Fig. 1, C and E), suggesting that the PG synthases also move around the division plane.

We next examined the motions of the division-specific PG synthases and their associated cytoskeletal polymers. Total internal reflection fluorescence microscopy (TIRFM) of a functional mNeonGreen-FtsZ fusion expressed from the native locus (fig. S3, A to E, and tables S2 and S3) revealed directional movements within newly assembled Z rings (Fig. 2A and movie S1).

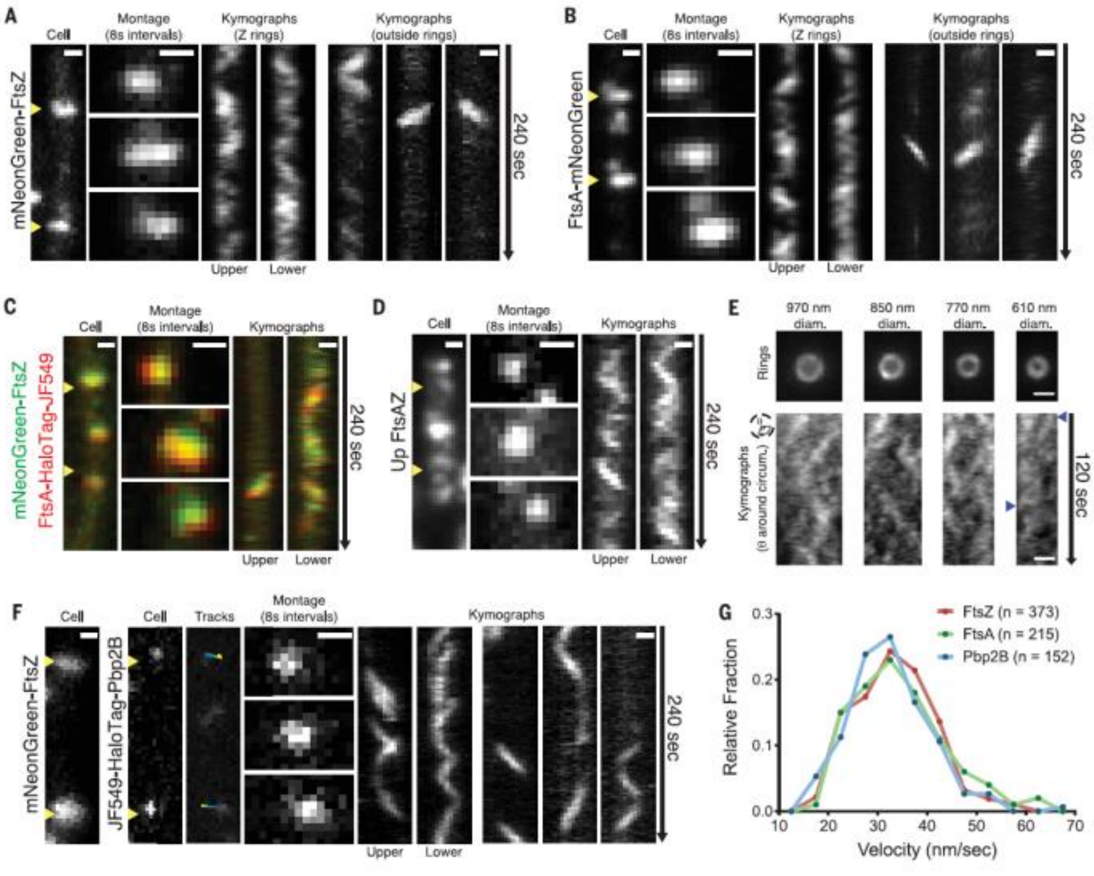

Fig. 2. FtsAZ and Pbp2B move directionally around the division site. (**A**) mNeonGreen-FtsZ (bAB185) shows directional motion inside (left) and outside (right) the Z ring; montage at 8-s intervals. (**B**) FtsA-mNeonGreen (bAB167) shows directional motion inside (left) and outside (right) the ring. (**C**) mNeonGreen-FtsZ and FtsA-HaloTag-JF549 (bAB229) colocalize and move together. Yellow is the overlap of green and red. (**D**) FtsAZ overexpression [100 μM isopropyl β-D-1-thiogalactopyranoside (IPTG) in bAB221] creates increased FtsZ filaments showing directional motion outside the Z ring. (**E**) Vertically immobilized cells (SH41) show multiple, independent mNeonGreen-FtsZ filaments moving in both directions around the division site. Cropped rings and radial kymographs in early (left), middle (center), and late (right) divisional stages. Blue arrowheads indicate directional FtsZ tracks. (**F**) Single molecules of Pbp2B (bGS31, 15-min incubation of 50 pM JF549) move directionally around the division site. Blue to yellow indicates trajectory time. Kymographs drawn at yellow arrowheads. Scale bars, 0.5 μm. (**G**) Velocity distributions of FtsA filaments, FtsZ filaments, and single Pbp2B molecules.

Erratum 17 January 2020. See Erratum on pages 6-10.

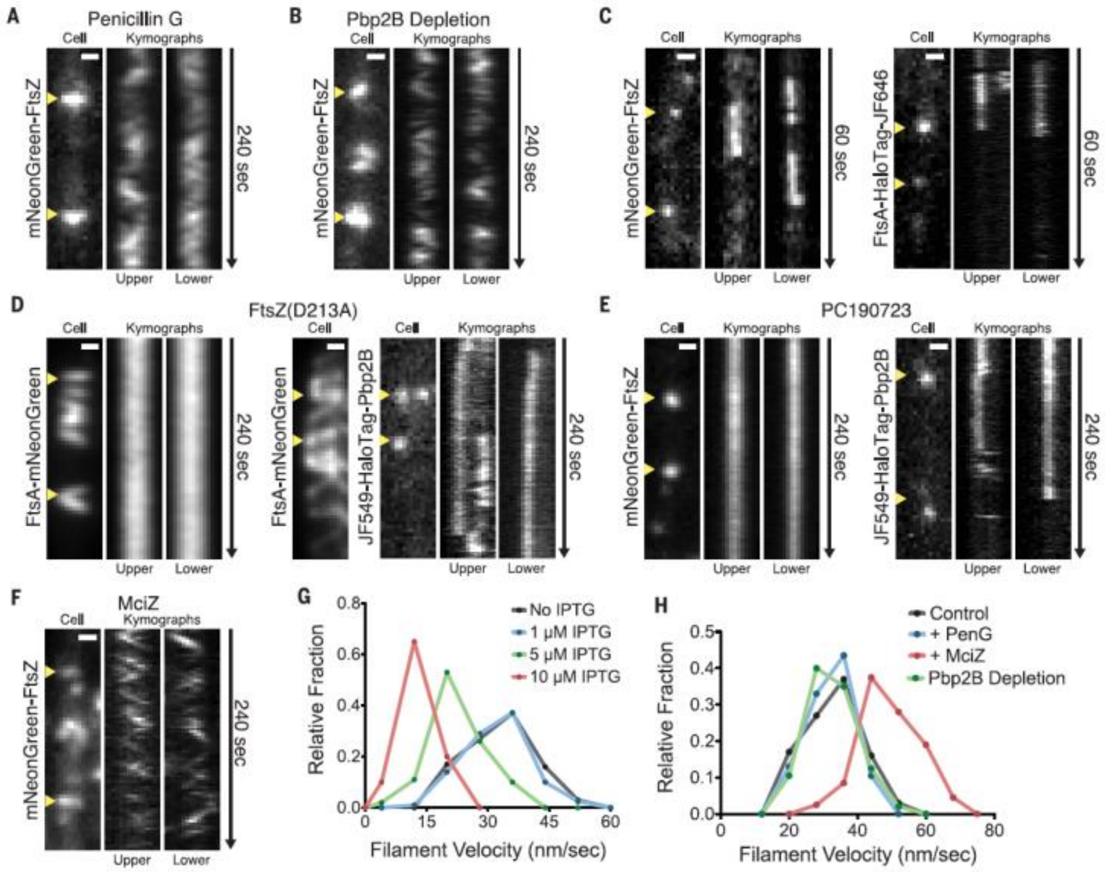

Fig. 3. Directional FtsAZ motion is driven by treadmilling, independent of cell wall synthesis, and is required for Pbp2B motion. (**A**) FtsZ continues to move directionally after treatment with penicillin G. bAB185 imaged 5 min after addition of 3 μl of 10 mg/ml penicillin G to an agarose pad. (**B**) FtsZ continues to move directionally after Pbp2B depletion. Before imaging, bGS31 was grown without IPTG until no divisions were observed (3 hours). (**C**) Single molecules of FtsZ and FtsA are immobile within the division site. Single molecules were obtained by growing bAB219 with no IPTG (left) or bAB229 with 15 min of 250 pM JF646 (right). (**D**) Overexpression of GTPase-deficient FtsZ stops FtsZ and Pbp2B motion. bAB217 (left) and bGS90 (right) were imaged after induction of FtsZ(D213A) (100 μM IPTG, 1 hour). (**E**) Directional motion of FtsZ and Pbp2B is stopped by PC190723. bAB185 (left) and bGS31 with 15-min incubation of 50 pM JF549 (right) 5 min after addition of 10 μM PC190723. (**F**) FtsZ velocity increases after exposure to MciZ. bAB185 was imaged after addition of 1 μM MciZ in a microfluidic device. Kymographs drawn at yellow arrowheads. Scale bars, 0.5 μm. (**G**) Velocity distributions of FtsZ filaments (bAB217) at different levels of FtsZ(D213A) induction. (**H**) Velocity distributions of FtsZ filaments under different perturbations.

Furthermore, in almost every cell, we observed small mNeonGreen-FtsZ filaments outside the Z ring moving directionally around the cell at the same rate as within Z rings, similar to oscillations previously observed in *Escherichia coli* (*8*). A functional FtsA-mNeonGreen fusion showed motions identical to FtsZ (Fig. 2B and movie S1), and two-color imaging confirmed that FtsA and FtsZ colocalized and moved together (Fig. 2C) (*9*). Overexpression of a second *ftsAZ* operon (FtsA, mNeonGreen-FtsZ) resulted in many more directionally moving filaments outside the Z ring that did not affect fitness (Fig. 2D and fig. S3F). To resolve FtsZ motion in dense, actively constricting Z rings, we vertically immobilized bacteria in agarose microholes, orienting the division plane parallel to the objective (fig. S4). This revealed multiple FtsZ filaments moving in both directions around the constriction site over a wide range of ring diameters (600 to 1000 nm) (Fig. 2E, fig. S4E, and movie S2). The movement of multiple FtsZ filaments around the Z ring may explain the heterogeneous structures and complex "patch" dynamics observed via superresolution microscopy (*10*–*12*), as well as the fast turnover of FtsZ subunits (*13*).

We next asked if the division-associated transpeptidase Pbp2B moves with FtsAZ. At native expression levels, mNeonGreen-Pbp2B moved directionally along the Z ring; this became more apparent with reduced expression (fig. S5, A and B). To observe the motions of single Pbp2B molecules, we labeled HaloTag-Pbp2B expressed from the native locus with low concentrations of HaloLigand-JF549 (*14*). TIRFM revealed two types of Pbp2B motion: (i) directional motion around the cell width, always localized to Z rings, and (ii) diffusion on the membrane, not localized to Z rings (Fig. 2F; fig. S5, C to E; and movie S3). We did not observe diffusive Pbp2B motion along Z rings at any acquisition rate. In some cases, we observed multiple Pbp2B molecules moving directionally within the same ring, sometimes in opposite directions, indicating that the Z ring contains multiple, independent synthetic

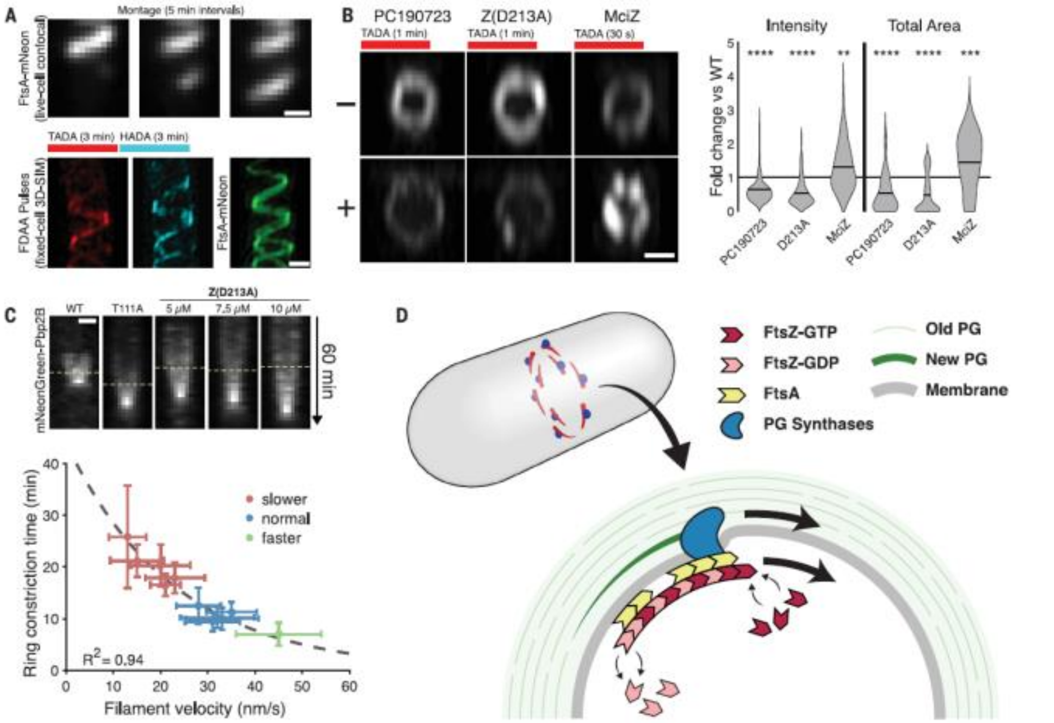

Fig. 4. Cytokinesis is controlled by directional motion of FtsAZ filaments. (**A**) FtsZ(D213A) overexpression (1 mM IPTG in bAB217) produces slowly growing FtsA spirals with spiral FDAA insertion. (Top) Montage of growing FtsA spiral acquired with spinning-disk confocal imaging. (Bottom) Sequential FDAA labeling and FtsA localization imaged with 3D-SIM in a fixed cell. (**B**) Altering FtsZ velocity changes the amount and total area of FDAA incorporation. (Left) PY79 with 1 μg/ml PC190723 for 10 min, (center) bAB217 with 20 μM IPTG for 1 hour, (right) AH93 with 50 mM xylose for 5 min. After treatment, cells were incubated with TADA for the indicated time, fixed, then imaged with 3D-SIM. (Far right) Total intensity and area of septal FDAA incorporation. Lines, mean. $^{**}P < 0.01$; $^{***}P < 0.001$; $^{****}P < 0.0001$. (**C**) Cytokinesis scales with FtsZ treadmilling velocity. For each condition, pairs of strains were used to measure (i) FtsZ velocity (using mNeonGreen-FtsZ) and (ii) septation rates (using mNeonGreen-Pbp2B). (Top) Kymographs of constricting Pbp2B rings in different FtsZ backgrounds (dashed line marks start of constriction). (Bottom) Plot of constriction time versus FtsZ velocity under different conditions. Treadmilling velocity and septation rates were acquired in identical conditions, save for measurements with MciZ (see supplementary materials). Error bars, SD of the mean. (A), (B), and (C): Scale bars, 0.5 μm. Dashed line in (C, bottom), slope. (**D**) Model for treadmilling-coupled cell division. (Top) The Z ring contains multiple FtsAZ filaments that treadmill around the division plane, pulling associated PG synthases. (Bottom) FtsZ treadmilling both regulates and distributes the activity of the PG synthases, building sequentially smaller uniform arcs of PG to divide the cell.

sites. FtsZ, FtsA, and Pbp2B all moved at similar velocities (Fig. 2G and fig. S5, D and E), suggesting that their motions are associated.

We investigated the mechanism driving FtsAZ/Pbp2B motion, first testing if, similar to MreB (*15*), Pbp2B inactivation would halt FtsAZ motion. However, FtsAZ motion was unaffected by multiple PG synthesis inhibitors (Fig. 3, A and H, and movie S4) or depletion of Pbp2B (Fig. 3, B and H, and movie S5).

We next tested if directional FtsAZ motion arose from filament treadmilling, as observed in vitro (*16*). Consistent with treadmilling, sparse labeling of FtsZ or FtsA in cells demonstrated that single molecules of both proteins were immobile within moving filaments (*17*) (Fig. 3C; fig. S5, F to J; and movie S6). Because treadmilling requires nucleotide hydrolysis, we assayed FtsA motion as we modulated the guanosine triphosphatase (GTPase) activity of FtsZ. Exogenous expression of FtsZ(D213A), a mutant shown to have greatly reduced GTPase activity in *E. coli* (*18*), gradually reduced FtsAZ velocity, stopping motion at high inductions (Fig. 3, D and G, and movie S7A). Likewise, addition of PC190723, an inhibitor of FtsZ guanosine triphosphate (GTP) hydrolysis (*19*) halted FtsZ movement (Fig. 3E and movie S8A). Conversely, addition of MciZ, a Z ring antagonist that, at low levels, increases FtsZ GTPase activity (*20*), increased FtsZ velocity (Fig. 3, F and H, and movie S7B). We next tested whether FtsZ treadmilling dynamics affected Pbp2B movement. PC190723 or overexpression of FtsZ(D213A) caused Pbp2B molecules to become immobile while the remaining colocalized with FtsZ (Fig. 3, D and E, and movie S8B). Pbp2B velocity scaled with FtsZ treadmilling velocity under various perturbations (fig. S5K). Thus, FtsZ treadmilling is required for the directional motions of both FtsAZ filaments and septal PG synthases.

Given the mobile nature of septal PG synthesis, we reasoned that the directional movements of FtsAZ and Pbp2B around the division plane could be coupled to septal PG synthesis. To test this, we labeled cells with FDAAs as we altered FtsZ dynamics. Overexpression of FtsZ(D213A) created long, slowly growing FtsA-mNeonGreen spirals, which incorporated FDAAs along their entire length (Fig. 4A and movie S9). Likewise, long PC190723 treatments resulted in fragmented patches of both FtsZ and FDAA incorporation (fig. S6A), indicating Pbp2B activity is constrained by FtsAZ location. However, these strong inhibitions of FtsZ dynamics required much longer pulses to achieve FDAA labeling, suggesting that FtsZ treadmilling limits PG synthesis. To test this, we altered FtsAZ velocity as we pulse-labeled cells with FDAAs. This revealed that both the total amount and total area of PG synthesis within the ring are modulated by FtsAZ velocity: Conditions that slowed dynamics decreased both the total amount and area of FDAA labeling (Fig. 4B and fig. S6, B and C). Conversely, increasing FtsAZ velocity (with MciZ) increased both the total amount and area of labeling. Thus, in *B. subtilis*, both the amount and spatial distribution of septal PG synthesis are directly coupled to, and limited by, the rate of FtsZ filament treadmilling.

Because FtsAZ dynamics control the rate of septal synthesis, we asked whether the rate of cytokinesis depended on FtsAZ treadmilling. We modulated treadmilling velocity by (i) introducing mutations affecting GTP hydrolysis into FtsZ at the native locus, (ii) titrating exogenous FtsZ(D213A), (iii) expressing MciZ, and (iv) other perturbations (table S4). This revealed that the cytokinesis rate scaled with FtsZ treadmilling: Division was slower when velocity was decreased and faster when velocity was increased (Fig. 4C; fig. S7, A to C; and movie S10). Even under the strongest perturbations, these decreased rates of cytokinesis did not alter the rate of cell elongation (fig. S7, D to F). Thus, in *B. subtilis*, FtsAZ treadmilling is both coupled to, and limiting for, septal PG synthesis and cell constriction.

Our results indicate that cell division occurs by the action of discrete enzyme-filament complexes that, driven by FtsZ treadmilling, move around the division plane, building new PG during their transit (Fig. 4D). FtsZ treadmilling creates long-range order from the local activity of the PG synthases, linking circumferential enzyme motion to the insertion of cell wall. This tight coupling may yield uniform insertion of new material around the division plane, building the septum inward in progressively smaller concentric rings. Cell division slightly differs in *E. coli*, where FtsZ treadmilling also distributes PG synthesis around the ring (*21*), perhaps because the rate of PG synthesis is limiting relative to FtsZ treadmilling (*10*). This difference may arise from different levels of cell wall precursors between the two organisms or because *E. coli* must also couple PG synthesis to outer membrane insertion.

The coupling between FtsZ treadmilling and PG synthesis can unify previously conflicting models of cell division. FtsZ filaments have been proposed to generate force to bend membranes (*2*, *22*) and to scaffold PG synthesis (*10*, *23*). If FtsZ filaments deform membranes, coupling their movement to PG synthesis would allow each deformation to be reinforced by synthesis of PG (*24*). Thus, multiple sites of local deformation and coupled reinforcing synthesis moving around the division site would iteratively build the invaginating septum.

REFERENCES AND NOTES

1. Y. Chen, H. P. Erickson, *J. Biol. Chem.* **280**, 22549–22554 (2005).
2. P. Szwedziak, Q. Wang, T. A. M. Bharat, M. Tsim, J. Löwe, *eLife* **3**, e04601 (2014).
3. X. Ma, D. W. Ehrhardt, W. Margolin, *Proc. Natl. Acad. Sci. U.S.A.* **93**, 12998–13003 (1996).
4. P. Gamba, J. W. Veening, N. J. Saunders, L. W. Hamoen, R. A. Daniel, *J. Bacteriol.* **191**, 4186–4194 (2009).
5. E. Kuru *et al.*, *Angew. Chem. Int. Ed. Engl.* **51**, 12519–12523 (2012).
6. T. J. Lupoli *et al.*, *J. Am. Chem. Soc.* **133**, 10748–10751 (2011).
7. C. Eberhardt, L. Kuerschner, D. S. Weiss, *J. Bacteriol.* **185**, 3726–3734 (2003).
8. S. Thanedar, W. Margolin, *Curr. Biol.* **14**, 1167–1173 (2004).
9. V. W. Rowlett, W. Margolin, *Biophys. J.* **107**, L17–L20 (2014).
10. C. Coltharp, J. Buss, T. M. Plumer, J. Xiao, *Proc. Natl. Acad. Sci. U.S.A.* **113**, E1044–E1053 (2016).
11. S. J. Holden *et al.*, *Proc. Natl. Acad. Sci. U.S.A.* **111**, 4566–4571 (2014).
12. M. P. Strauss *et al.*, *PLOS Biol.* **10**, e1001389 (2012).
13. D. E. Anderson, F. J. Gueiros-Filho, H. P. Erickson, *J. Bacteriol.* **186**, 5775–5781 (2004).
14. J. B. Grimm *et al.*, *Nat. Methods* **12**, 244–250 (2015).
15. E. C. Garner *et al.*, *Science* **333**, 222–225 (2011).
16. M. Loose, T. J. Mitchison, *Nat. Cell Biol.* **16**, 38–46 (2014).
17. L. Niu, J. Yu, *Biophys. J.* **95**, 2009–2016 (2008).
18. S. D. Redick, J. Stricker, G. Briscoe, H. P. Erickson, *J. Bacteriol.* **187**, 2727–2736 (2005).
19. D. J. Haydon *et al.*, *Science* **321**, 1673–1675 (2008).
20. A. W. Bisson-Filho *et al.*, *Proc. Natl. Acad. Sci. U.S.A.* **112**, E2130–E2138 (2015).
21. X. Yang *et al.*, *bioRxiv* 10.1101/077610 (2016).
22. M. Osawa, H. P. Erickson, *Proc. Natl. Acad. Sci. U.S.A.* **110**, 11000–11004 (2013).
23. A. J. F. Egan, W. Vollmer, *Front. Microbiol.* **6**, 455 (2015).
24. Z. Li, M. J. Trimble, Y. V. Brun, G. J. Jensen, *EMBO J.* **26**, 4694–4708 (2007).

ACKNOWLEDGMENTS

We thank F. Gueiros-Filho, R. Losick, M. Erb, and P. Levin for strains; J. Xiao for discussions; L. Lavis for Janelia Fluor dyes; B. Murphy and E. Pasciak for FDAA synthesis help; F. Gueiros-Filho, R. Daniel, and J. Errington for antibodies; R. Losick, B. LaSarre, and D. Kearns for comments. This work was supported by NIH grants GM113172 to M.S.V. and Y.V.B., GM51986 to Y.V.B., and DP2AI117923-01 to E.C.G.; a Newcastle University Research Fellowship and Royal Society Research Grant RG150475 to S.H.; a Science Without Borders Research Fellowship to A.W.B.-F.; a European Research Council Advanced Grant (SynDiv 669598) to C.D.; and an NSF Graduate Research Fellowship Program (DGE1144152) to G.R.S. SIM was performed in the Indiana University Light Microscopy Imaging Center supported by S10RR028697-01. E.K., Y.V.B., and M.S.V. are inventors on U.S. Patent Application 14/395,815 (PCT Patent Application PCT/US2013/037504), submitted by the Indiana University Research and Technology Corporation, that covers the use of FDAAs for labeling of bacterial cell walls. Data are available in the text and supplementary materials. Movies S1 to S10 are also available at http://garnerlab.fas.harvard.edu/FtsZ/. Code is available at https://bitbucket.org/garnerlab/bisson-2016.

SUPPLEMENTARY MATERIALS

www.sciencemag.org/content/355/6326/739/suppl/DC1
Materials and Methods
Figs. S1 to S7
Tables S1 to S4
Movies S1 to S10
References (25–45)

26 September 2016; accepted 20 January 2017
10.1126/science.aak9973

Erratum

In the Report "Treadmilling by FtsZ filaments drives peptidoglycan synthesis and bacterial cell division," the authors reported that a strain that expressed a sole copy of *ftsZ* fused to mNeonGreen (mNG) from the native locus [bAB185—*ftsA*-(*mNG*-*ftsZ*)]. Later, whole-genome sequencing revealed that this locus contained duplications of the *ftsAZ* operon (Fig. E1A). Likewise, the native locus fusions to *ftsA* revealed similar duplications (Fig. E1A).

To test if these duplications affected their measurements of filament dynamics or cell division rates, the authors created different merodiploid strains containing a second copy of the *ftsAZ* operon where each was labeled (Table E1). These mixed expression strains assembled competent Z-rings (Fig. E1B), as observed previously with both the duplicates and previously published merodiploid strains [AH175—*EYFP-ftsZ* in Handler *et al.* (*2*)—and SB168—(*ftsA-EGFP*)-*ftsZ* in Ben-Yehuda and Losick (*3*)]. All strains showed comparable distributions of cell lengths (Fig. E1C), a hallmark of cell division health; filament treadmilling rates (Fig. E1D); and cytokinesis periods (Fig. E1F).

To confirm the findings that (i) GTP hydrolysis drives FtsZ treadmilling and (ii) treadmilling limits cell division were not affected by these duplications, the authors measured how increasing the expression of FtsZ(D213A) altered the treadmilling rates and cytokinesis period with an independent FtsZ fusion from what was used in Bisson-Filho *et al.*, the previously published EYFP-FtsZ merodiploid (AH175). As before, increasing FtsZ(D213A) decreased treadmilling rates (Fig. E1E), while increasing the cytokinesis period (Fig. E1G). Overlaying their new measurements of treadmilling and constriction of all of these new tests onto the correlation plot in the original Fig. 4C of Bisson-Filho *et al.* indicated that all data fit into the previous trend (Fig. E1H). Thus, these additional measurements confirm that the strain duplications do not affect the Report's measurements or conclusions.

The authors additionally note that Fig. 2E from Bisson-Filho *et al.* shows FtsA-mNG dynamics rather than FtsZ-mNG as originally indicated, owing to an inadvertent error.

REFERENCES AND NOTES

1. A. W. Bisson-Filho *et al.*, Treadmilling by FtsZ filaments drives peptidoglycan synthesis and bacterial cell division. *Science*. **355**, 739–743 (2017).
2. A. A. Handler, J. E. Lim, R. Losick, Peptide inhibitor of cytokinesis during sporulation in Bacillus subtilis. *Mol. Microbiol.* **68**, 588–599 (2008).
3. S. Ben-Yehuda, R. Losick, Asymmetric cell division in B. subtilis involves a spiral-like intermediate of the cytokinetic protein FtsZ. *Cell*. **109**, 257–266 (2002).

10.1126/science.aba6311

Fig. E1. FtsZ treadmilling and cytokinesis are unperturbed despite the presence of multiple *ftsAZ* copies.

(**A**) Multiple copies of *ftsAZ* detected by Illumina and Nanopore whole-genome sequencing. Sequencing data from all strains, including the wild-type reference assembly, can be downloaded from https://garnerlab.fas.harvard.edu/BissonWGS.zip. (**B**) Comparison of Z-ring localization in different strains. Images were taken in both phase-contrast and FITC channels. (**C**) Box plots from cell length distributions from duplication and merodiploid strains. Cells were grown from single colonies to mid-exponential phase, diluted to an optical density at 600 nm (OD_{600}) of 0.05, and regrown to OD_{600} 0.5. Merodiploid strains were grown in the presence of 20 μM IPTG during the second growth cycle (~2.5 hours). Prior to imaging, cells were incubated with 1 μg/ml of FM5-95 (Invitrogen) membrane dye. (**D**) FtsAZ filament (and PBP2B single molecule) speeds present robust measurements across different strains despite the presence of the tagged divisome protein and fluorescent protein of choice. Strains used for measurements from Bisson-Filho *et al.* (2017) (left) and new data collected with different FtsAZ fusions from the literature (right). (**E**) FtsAZ treadmilling rates decrease under the expression of the FtsZ(D213A) mutant across multiple strains. (**F**) Cytokinesis periods are consistent across multiple strains using different fluorescent proteins tagging different components of the division machinery. (**G**) Cytokinesis periods consistently increase under the expression of the FtsZ(D213A) mutant across multiple strains. (**H**) Updated correlation plot as presented in Fig. 4C from Bisson-Filho *et al.* (2017) (black) with the new collected data (green) presented here. Correlation between cytokinesis and FtsZ treadmilling rates is unperturbed despite the presence of multiple *ftsAZ* copies, merodiploids, and fluorescent protein of choice

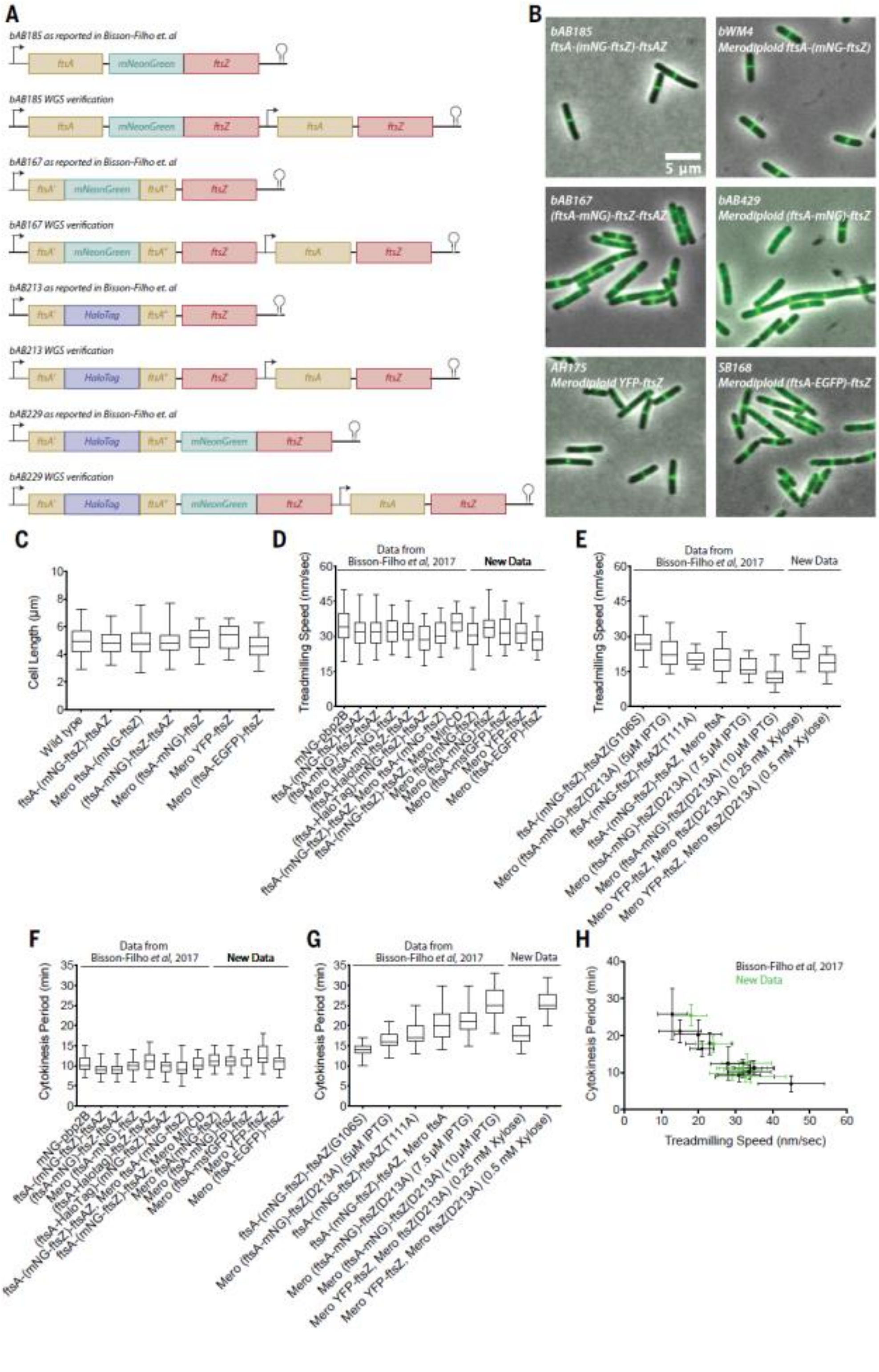

Table E1. Strains used in this study.

Strain	Description	Genotype	Reference
bWM4	mNG-FtsZ Merodiploid	*amyE::erm-Phyperspank-ftsA-mNeonGreen(M10S)-15aa(v2)-ftsZ(opt)*	This work
bAB431	FtsA-msfGFP Merodiploid	*amyE::erm-Phyperspank-ftsA-msfGFP(SW)-ftsZ*	Bisson-Filho *et al.* (2017)
bAB434	FtsA-msfGFP Complementation	*amyE::erm-Phyperspank-ftsA-msfGFP(SW)-ftsZ* *ftsAZ::cat-Pxyl-ftsAZ*	This work
bAB229	FtsA-HaloTag(SW)-mNG-ftsZ at the native site	*ftsAZ::erm-ftsA-HaloTag(SW)-mNeonGreen-15aa-ftsZ-cat*	Bisson-Filho *et al.* (2017)
bAB429	FtsA-mNG Merodiploid	*amyE::erm-Phyperspank-ftsA-Trunc_mNeonGreen(SW)-ftsZ*	This work
SB168	FtsA-GFP Merodiploid	*amyE::ftsAZ-cat::ftsA-gfp-ftsZ-kan*	Ben-Yehuda and Losick (2002)
bAB213	FtsA-HaloTag(SW) at the native site	*ftsA::erm-ftsA-HaloTag(SW)-cat*	Bisson-Filho *et al.* (2017)
AH175	YFP-FtsZ Merodiploid	*thrC::Pspac-YFP-ftsZ-erm*	Handler *et al.* (2008)
bAB185	mNG-FtsZ at the native site	*ftsZ::mNeonGreen-15aa-ftsZ*	Bisson-Filho *et al.* (2017)
bAB167	FtsA-mNeonGreen sandwich at the native site	*ftsA::ftsA-mNeonGreen(SW)*	Bisson-Filho *et al.* (2017)
bAB221	mNG-ftsZ at the native site mNG-FtsZ Merodiploid	*Native mNeonGreen-15aa-ftsZ* *amyE::erm-Physpank-ftsA-15aa-mNeonGreen-ftsZ*	Bisson-Filho *et al.* (2017)
bWM4	mNG-FtsZ Merodiploid	*amyE::erm-Phyperspank-ftsA-mNeonGreen(M10S)-15aa(v2)-ftsZ(opt)*	This work
bAB282	FtsZ-G106S (Z84) mutant at the native site FtsA-mNG-FtsZ under Physpank promoter	*amyE::erm-Physpank-ftsA-mNeonGreen-15aa-ftsZ* *ftsZ(G106S)-tetΩftsZ*	Bisson-Filho *et al.* (2017)
bAB281	FtsZ-T111A mutant at the native site FtsA-mNG-FtsZ under Physpank promoter	*amyE::erm-Physpank-ftsA-mNeonGreen-15aa-ftsZ* *ftsZ(T111A)-tetΩftsZ*	Bisson-Filho *et al.* (2017)
bAB199	mNG-ftsZ at the native site FtsA under Physpank promoter	*ftsZ::mNeonGreen-15aa-ftsZ* *amyE::erm-Physpank-ftsA*	Bisson-Filho *et al.* (2017)
bAB209	mNG-ftsZ at the native site MciZ under Pxyl promoter	*FtsZ::mNeonGreen-15aa-ftsZ* *amyE::Pxyl-mciZ-cat*	Bisson-Filho *et al.* (2017)
bAB248	mNG-ftsZ at the native site MinCD under Physpank promoter	*ftsZ::mNeonGreen-15aa-ftsZ* *amyE::Physpank-minCD-spc*	Bisson-Filho *et al.* (2017)
bAB217	FtsA-mNG and FtsZ-D213A mutant under Physpank promoter	*amyE::erm-Physpank-ftsA-mNeonGreen(SW)-ftsZ(D213A)*	Bisson-Filho *et al.* (2017)
ME7	Native mNG-Pbp2B	*pbpB::mNeonGreen-15aa-pbpB*	Bisson-Filho *et al.* (2017)
bAB156	YFP-FtsZ merodiploid FtsZ-D213A mutant under Pxyl promoter	*amyE::cat-Pxyl-ftsZ(D213A)* *thrC::Pspac-YFP-ftsZ-erm*	This work
bAB270	mNG-pbpB at the native site FtsZ-T111A mutant at the native site	*pbpB::mNeonGreen-15aa-pbpB* *ftsZ(T111A)-tetΩftsZ*	Bisson-Filho *et al.* (2017)

bAB271	mNG-pbpB at the native site ftsZ-G106S (Z84) mutant at the native site	*pbpB::mNeonGreen-15aa-pbpB* *ftsZ(G106S)-tetΩftsZ*	Bisson-Filho *et al.* (2017
bAB272	mNG-pbpB at the native site FtsAZ under Physpank promoter	*pbpB::mNeonGreen-15aa-pbpB* *amyE::erm-Physpank-ftsAZ*	Bisson-Filho *et al.* (2017)
bAB273	mNG-pbpB at the native site FtsA-mNG FtsZ-D213A mutant under Physpank promoter	*pbpB::mNeonGreen-15aa-pbpB* *amyE::erm-Physpank-ftsAZ(D213A)*	Bisson-Filho *et al.* (2017)
bAB274	mNG-pbpB at the native site MciZ under Pxyl promoter	*pbpB::mNeonGreen-15aa-pbpB* *amyE::cat-Pxyl-mciZ*	Bisson-Filho *et al.* (2017)
bAB285	mNG-pbpB at the native site MinCD under Physpabk promoter	*pbpB::mNeonGreen-15aa-pbpB* *amyE::Physpank-minCD-spc*	Bisson-Filho *et al.* (2017)
bAB153	ZapA-mNG at the native site	*zapA::zapA-40aa-mNeonGreen*	This work

Science

Treadmilling by FtsZ filaments drives peptidoglycan synthesis and bacterial cell division

Alexandre W. Bisson-Filho, Yen-Pang Hsu, Georgia R. Squyres, Erkin Kuru, Fabai Wu, Calum Jukes, Yingjie Sun, Cees Dekker, Seamus Holden, Michael S. VanNieuwenhze, Yves V. Brun and Ethan C. Garner

Science **355** (6326), 739-743.
DOI: 10.1126/science.aak9973

Coordinating cell wall synthesis and cell division

Most bacteria are protected by peptidoglycan cell walls, which must be remodeled to split the cell. Cell division requires the tubulin homolog FtsZ, a highly conserved cytoskeletal polymer that specifies the future site of division. Bisson-Filho *et al.* and Yang *et al.* found that the dynamic treadmilling of FtsZ filaments controls both the location and activity of the associated cell wall synthetic enzymes. This creates discrete sites of cell wall synthesis that circle around the division plane to divide the cell.

Science, this issue p. 739, p. 744

FtsZ treadmilling is essential for Z-ring condensation and septal constriction initiation in *Bacillus subtilis* cell division

Kevin D. Whitley[1,2+], Calum Jukes[1+], Nicholas Tregidgo[1], Eleni Karinou[1], Pedro Almada[3], Ricardo Henriques[3], Cees Dekker[2], and Séamus Holden[1*]

[1]Centre for Bacterial Cell Biology, Biosciences Institute, Faculty of Medical Sciences, Newcastle University, Newcastle upon Tyne, UK; [2]Department of Bionanoscience, Kavli Institute of Nanoscience Delft, Delft University of Technology, Delft, The Netherlands; [3]MRC-Laboratory for Molecular Cell Biology, University College London, London, UK

*Corresponding author: seamus.holden@ncl.ac.uk

+Equal author contribution

ABSTRACT

Despite the central role of division in bacterial physiology, how division proteins work together as a nanoscale machine to divide the cell remains poorly understood. Cell division by cell wall synthesis proteins is guided by the cytoskeleton protein FtsZ, which assembles at mid-cell as a dense Z-ring formed of treadmilling filaments[1,2]. However, although FtsZ treadmilling is essential for cell division, the function of FtsZ treadmilling remains unclear[2–5]. Here, we systematically resolve the function of FtsZ treadmilling across each stage of division in the Gram-positive model organism *Bacillus subtilis* using a novel combination of nanofabrication, advanced microscopy, and microfluidics to measure the division-protein dynamics in live cells with ultrahigh sensitivity. We find that FtsZ treadmilling has two essential functions: mediating condensation of diffuse FtsZ filaments into a dense Z-ring, and initiating constriction by guiding septal cell wall synthesis. After constriction initiation, FtsZ treadmilling has a dispensable function in accelerating septal constriction rate. Our results show that FtsZ treadmilling is critical for assembling and initiating the bacterial cell division machine.

INTRODUCTION

Bacterial cell division is an essential cellular process and a key target for antibiotics. Bacterial cell division is also a remarkable feat of molecular self-assembly where a nanoscale divisome machine builds a micron-scale wall (septum) at mid-cell. The core components of this machine include the septal cell-wall synthases that insert new peptidoglycan (PG) to build the septum, and the essential cytoskeletal tubulin homologue FtsZ that polymerises into a dense "Z-ring" band of short filaments at mid-cell[6–8]. These short FtsZ filaments move by treadmilling, a type of motion where an asymmetric filament undergoes plus-end polymerisation and minus-end depolymerisation, with GTP hydrolysis setting the rate of FtsZ depolymerisation and overall treadmilling speed[1,2,9]. FtsZ treadmilling dynamics are essential for cell division[2–5].

However, the role of FtsZ treadmilling in cell division remains unclear. In the Gram-positive model organism *Bacillus subtilis*, we previously observed that constriction rate and synthase speed was dependent upon FtsZ filament speed[1], leading to an initial model of a tightly coupled motile cytoskeleton-synthase complex, where FtsZ acts an obligatory guide and rate-limiting step for septal PG synthesis. In contrast, FtsZ treadmilling is dispensable after constriction initiation in *Staphylococcus aureus*[3], even though the two organisms belong to the same phylogenetic class. This could reflect genuine differences between species, or there may exist a common division mechanism where FtsZ treadmilling plays different roles at different division stages. To date, it remains unclear how the role of treadmilling FtsZ filaments varies across the full division process.

Here, we measure the dynamics and function of FtsZ treadmilling across all division stages in *B. subtilis*. To make these observations, we developed a new method combining nanofabrication, advanced microscopy, and microfluidics. This approach allowed us to measure native FtsZ dynamics at near-single-filament resolution throughout division. We found that treadmilling dynamics drive FtsZ filament interactions during Z-ring assembly and that this stabilises filaments into dense Z-rings. We determined that the FtsZ inhibitor PC190723 arrests FtsZ treadmilling within seconds, independent of division stage, allowing us to elucidate the rapid response of cells to treadmilling arrest. By systematically determining the response of single cells to FtsZ treadmilling arrest by PC190723, we found that FtsZ treadmilling has two separate essential functions: mediating Z-ring assembly during the earliest stage of cell division, and subsequently for guiding septal constriction initiation. We found that FtsZ treadmilling becomes dispensable after constriction initiation but increases septal constriction rate, reconciling the findings from previous studies[1,3]. Our results show that the key roles of FtsZ treadmilling are to drive Z-ring assembly and to initiate septal constriction.

RESULTS

FtsZ assembly at mid-cell has three distinct phases: nascent, mature, and constricting Z-rings

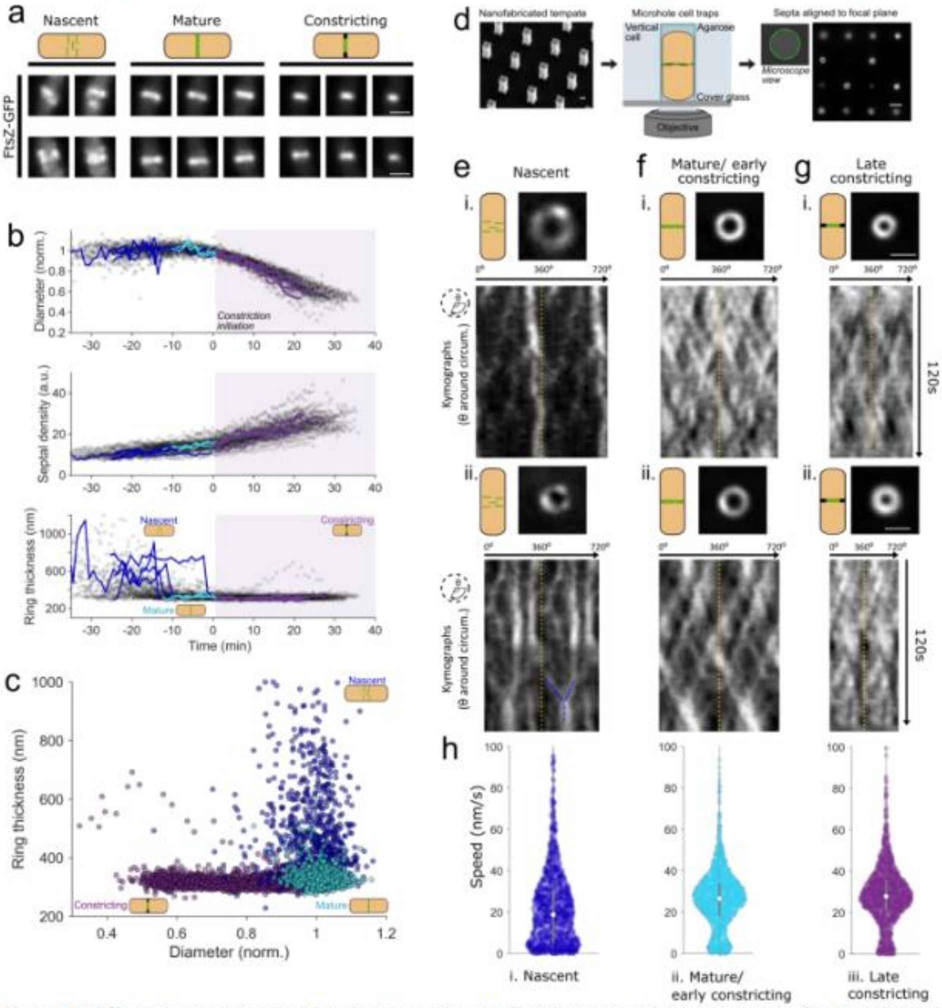

Figure 1. FtsZ filament organisation and dynamics throughout the division process. *(a) Exemplar images of FtsZ-GFP (SH130) filament organisation throughout division, classified by division phase. (b) Quantification of FtsZ-ring diameter, ring thickness and septal density (septal intensity divided by ring circumference) throughout division from time-lapse microscopy data.* Nascent Z-rings have large axial width (ring thickness) due to the diffuse distribution of filaments, which condense into a thin mature Z-ring, followed by constriction initiation. Traces are temporally aligned relative to the start time of constriction (Methods). Grey scatter points represent all data points. Lines show individual, representative traces, which are split into coloured segments indicating cell division state: nascent (blue), mature (cyan), and constricting (purple). *(c) FtsZ-ring thickness and relative septal diameter.* Colour indicates cell division state as per (b). Cell division state of FtsZ-rings in (b-c) determined by automated classification of Z-ring diameter and axial thickness time lapse data (Methods, SI Note 3). *(d) VerCINI schematic.* Rod-shaped bacteria are trapped in agarose microholes, rotating the division septum into microscope imaging plane. *(e-g) VerCINI microscopy of FtsZ filament dynamics for each Z-ring phase, two representative examples per phase (i-ii).* Nascent Z-rings are composed of sparse filaments diffusely distributed around the circumference of the cell, and a large fraction of immobile FtsZ filaments. Mature and constricting Z-rings possess a more uniform distribution of FtsZ filaments around the division site, with most filaments treadmilling. Images of septa show the first frame in kymographs (t=0 s). Kymographs were obtained by fitting septal images to circles and plotting intensity values around the circumference of

the cell for each frame of the time-lapse (1 frame/ s). Two full revolutions around the cell (0-720°) are plotted side-by-side in each kymograph to resolve filament trajectories that pass 0°/360°, separated by yellow dotted lines. Blue lines highlight example of motile FtsZ filament aggregation. *(h) Violin plots of FtsZ filament speed for each Z-ring phase.* White circles, median; thick grey lines, interquartile range; thin grey lines, 1.5x interquartile range.

We first determined FtsZ organisation during cell division in *B. subtilis* using an FtsZ-GFP fusion[10] expressed from the native locus at wild-type protein levels (SH130, Methods, Supplementary Figure 1). Cell morphology analysis showed near native morphology at 30°C and only a mild elongation phenotype at 37°C (Supplementary Figure 2), although growth in liquid culture was not impaired at either temperature (Supplementary Figure 3).

We performed time-lapse imaging of FtsZ-GFP organisation in slow growth conditions (Figure 1; Supplementary Video 1). We observed that FtsZ filaments initially formed a diffuse structure at mid-cell which rapidly condensed into a dense narrow band, followed by the onset of constriction (Figure 1a). We quantified these changes in Z-ring structure by measuring the dimensions (thicknesses and diameters) and septal density (total septal intensity divided by Z-ring circumference) of the Z-rings in each frame (Methods). The resulting traces of thicknesses and diameters over time were aligned by the start time of constriction (Methods, Figure 1b). These time traces revealed three distinct Z-ring stages that we classified as 'nascent', 'mature', and 'constricting' based on Z-ring diameter and axial thickness (Figure 1b, Methods, Supplementary Note 3). During the nascent Z-ring stage, low density FtsZ filaments transiently assemble at mid-cell over a wide region, consistent with previous reports[4,13–15]. FtsZ filaments then rapidly condense into a thin mature Z-ring structure, which remains unconstricted but increases in intensity for some time. Finally, the Z-ring begins constricting until division is finished. Step finding analysis of Z-ring axial thickness time traces showed that Z-ring condensation occurs rapidly and stochastically approximately 10 minutes before constriction initiation (Figure 1b, Methods, Supplementary Figure 4).

VerCINI microscopy reveals FtsZ filament dynamics are division stage regulated and FtsZ treadmilling drives filament encounter in nascent Z-rings

FtsZ filament dynamics are difficult to observe *in vivo*. TIRF imaging only illuminates a thin slice of the septum, limiting observation to partial snapshots of filament dynamics in nascent Z-rings[1,2]. We previously developed a prototype approach which resolves this problem by vertically immobilizing cells in nanofabricated chambers, allowing continuous imaging of the entire division septum, including dense actively constricting Z-rings[1,4]. However, the prototype method was not capable of imaging dim, nascent Z-rings due to high background, suffered from fast photobleaching and lacked the throughput required.

We created an entirely redesigned vertical cell immobilisation method which addresses all of these issues and allows ultrasensitive high-resolution imaging of FtsZ filament dynamics at all stages of division, termed VerCINI (Vertical Cell Imaging by Nanostructured Immobilisation). This new method features a high-throughput chip design, centrifugation loading, high SNR ring-HiLO illumination[16], imaging denoising[17], and custom septal localisation and background subtraction algorithms (Methods, Supplementary Figure 5-6, Supplementary Videos 2-3). We measured FtsZ filament dynamics during each division stage using VerCINI (Figure 1e-h, Supplementary Figure 7, Supplementary Videos 4-6)[1,21]. Division stage was determined based on septal intensity and diameter (Methods, Supplementary Figure 8, Supplementary Note 3).

In nascent Z-rings, we observed that FtsZ filaments are sparsely distributed, with a mixture of treadmilling and immobile filaments (Figure 1f, Supplementary Figure 9a, 35% immobile, filament speed < 10 nm/s), leading to a low average filament speed with large spread (median 19 nm/s, interquartile range, IQR, 5-31, N=526). Surprisingly, we frequently observed two or more treadmilling

FtsZ filaments colliding, leading to aggregation and temporary arrest of both filaments (Figure 1eii, Supplementary Figure 7). FtsZ filament aggregation by lateral filament interactions is required to bundle FtsZ filaments and condense the Z-ring[22–26]. These data show that FtsZ treadmilling can drive filament aggregation by promoting the filament encounters required for lateral interactions.

Z-ring condensation led to a drop in the number of immobile FtsZ filaments in mature/early constricting Z-rings, yielding a significant increase in average filament speed with narrower speed distribution (15% immobile, median 27 nm/s, IQR 19-34, N=1053; Figure 1h). Simulations showed that changes in filament density had little effect on observed filaments speeds or observed fraction of immobile FtsZ filaments (Supplementary Figure 10). Filament speeds in late constricting Z-rings were similar to those of mature/early constricting Z-rings (13% immobile, median speed 28 nm/s, IQR 21-36, N=1677; Figure 1h). Due to the decreased immobile population, filaments in mature and constricting Z-rings traversed, on average, twice the distance around the septum of those in nascent rings (Supplementary Figure 9c).

The FtsZ filament lifetime (time bound to the septum) was similar at each stage of cell division: that is, although FtsZ filaments in the nascent stage are less dense and less motile, their bound lifetime remains similar (Supplementary Figure 9b). Furthermore, we found that treadmilling and immobile filaments displayed similar lifetimes (Supplementary Figure 11), suggesting that immobile filaments are dynamic. These results show that the fraction of treadmilling FtsZ filaments and their speeds are division stage regulated.

PC190723 arrests FtsZ treadmilling within seconds throughout division

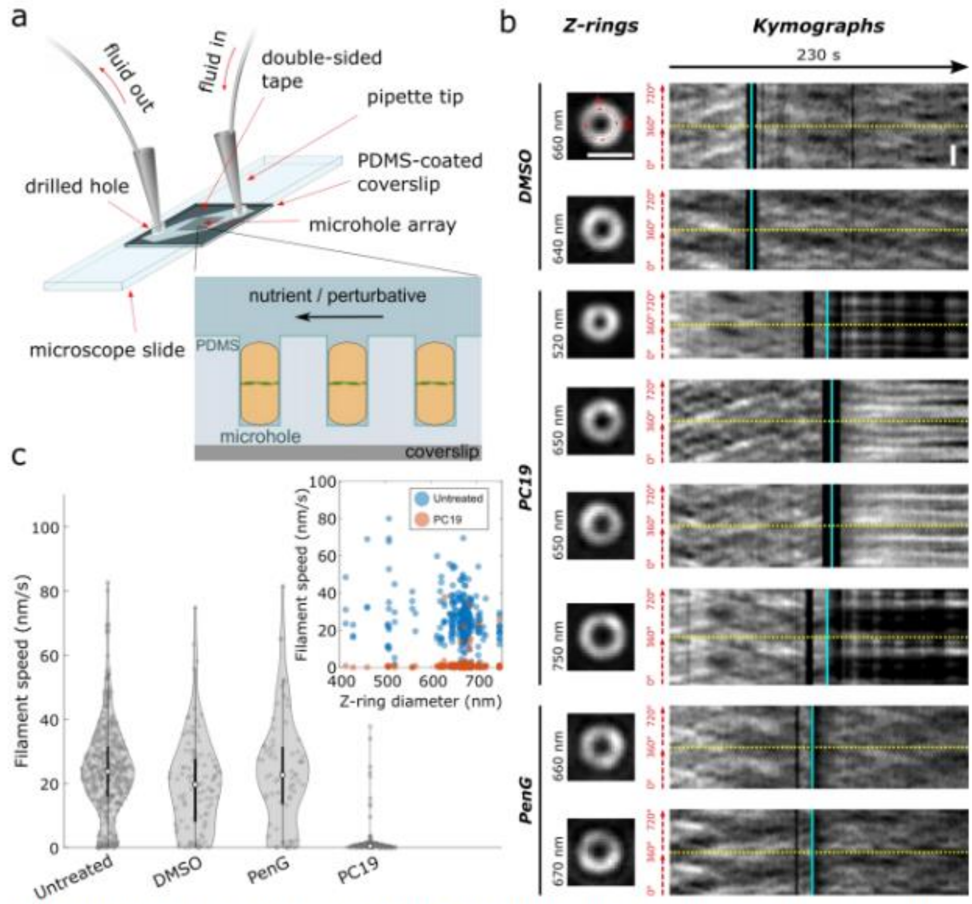

Figure 2. PC190723 arrests cellular FtsZ treadmilling within seconds across all stages of constriction. *(a) Schematic of microfluidic VerCINI.* Rod-shaped cells are confined in open-topped microholes in a thin layer of PDMS atop a microscope coverslip as solutions flow over them. The flow channel is formed from a cut piece of double-sided tape sandwiched between the PDMS layer and a microscope cover slide with drilled holes to allow inlet and outlet tubes. *(b) Representative images of septa and associated kymographs of FtsZ-GFP (SH130) dynamics in vertically-immobilised cells during rapid treatment with either DMSO (top), PC19 (middle), or PenG (bottom) at multiple septal diameters.* Images of septa show the first frame in kymographs (t=0 s). Kymographs were obtained by fitting septal images to circles and plotting intensity values around the circumference of the cell for each frame of the time-lapse (1 frame/s). Two full revolutions around the cell (0-720°) are plotted side-by-side in each kymograph to resolve filament trajectories that pass 0°/360°, separated by yellow dotted lines. Cyan lines show arrival time of media containing DMSO, PenG, or PC19. Black bands around time of treatment resulted from a loss of focus during fluid exchange. Fluctuations in intensity for two septa post-PC19 treatment (750 nm and 520 nm diameter septa) resulted from manual refocusing during imaging. Scale bars: 1000 nm. *(c) Violin plots of FtsZ treadmilling speeds pre- and post-treatment measured from kymographs.* White circles, median; thick black lines, interquartile range; thin black lines, 1.5x interquartile range. DABEST plots of effect size can be found in Supplementary Figure 12. *Inset:* FtsZ treadmilling speed distributions for untreated (white circles) and PC19-treated (red circles) cells from violin plots separated by septal diameter.

We next set out to determine the function of FtsZ treadmilling during each stage of cell division. For this we needed to observe the effect on cell division in response to rapid FtsZ treadmilling arrest. The antibiotic PC190723 (PC19) arrests FtsZ treadmilling in *B. subtilis* and related species by supporting the 'open' conformation of FtsZ and stabilizing protofilaments[1,18–21] without fully abolishing subunit turnover or GTPase activity[22]. Since the entire cell division process takes only 10-20 minutes in fast growth conditions, it was critical to determine whether PC19 acted sufficiently rapidly and robustly for use in dissecting the effect of treadmilling during each division stage. To determine how PC19 and other cell division inhibitors perturb FtsZ treadmilling, we developed microfluidic VerCINI, which combines high-resolution imaging of cell division protein dynamics *in vivo* with rapid chemical perturbation (Methods, Figure 2a). In this method, cells are confined in an array of open-topped microholes formed from PDMS atop a microscope coverslip, which is contained within a microfluidic chamber to allow continual flow of fresh media as well as chemical inhibitors. PDMS was used rather than agarose in order to produce a thin enough layer (~50 µm) to image through. Cells continued to grow and divide, consistent with previous observations that growth of *B. subtilis* cells in sufficiently wide (>0.8 µm) PDMS channels is not impaired[23], and models demonstrating that nutrient transport does not significantly limit growth in short (<20 µm) channels[24]. A real-time image-based autofocus system was used to stabilise focus during high-speed imaging[25].

We imaged FtsZ-GFP (SH130) using microfluidic VerCINI to observe the effects of division inhibitors PC19 and Penicillin G (PenG) on FtsZ treadmilling. We recorded untreated FtsZ dynamics for 90 s while blank media flowed over the cells, then continuously treated cells with an excess of division inhibitor by changing fluid flow to media laced with the compound (Figure 2b, Supplementary Video 7). FtsZ treadmilling dynamics were abolished by PC19 within a few seconds for all diameters of septa observed (Figure 2c). When we treated cells with Penicillin G (PenG), which inhibits cell wall synthesis by binding to cell wall synthase transpeptidation sites, FtsZ dynamics continued unperturbed for the duration of the experiment (several minutes). FtsZ dynamics were also unaffected by a DMSO-only control, the solvent for PC19 (Figure 2c, Supplementary Videos 8-9).

By providing high spatiotemporal resolution during rapid chemical perturbation, microfluidic VerCINI revealed the effect of division inhibitors on FtsZ treadmilling throughout division. Our results demonstrate that PC19 inhibits FtsZ treadmilling within seconds well after the start of constriction, whereas PenG treatment does not directly affect FtsZ dynamics.

FtsZ treadmilling is essential for Z-ring condensation and septal constriction initiation, but is subsequently dispensable

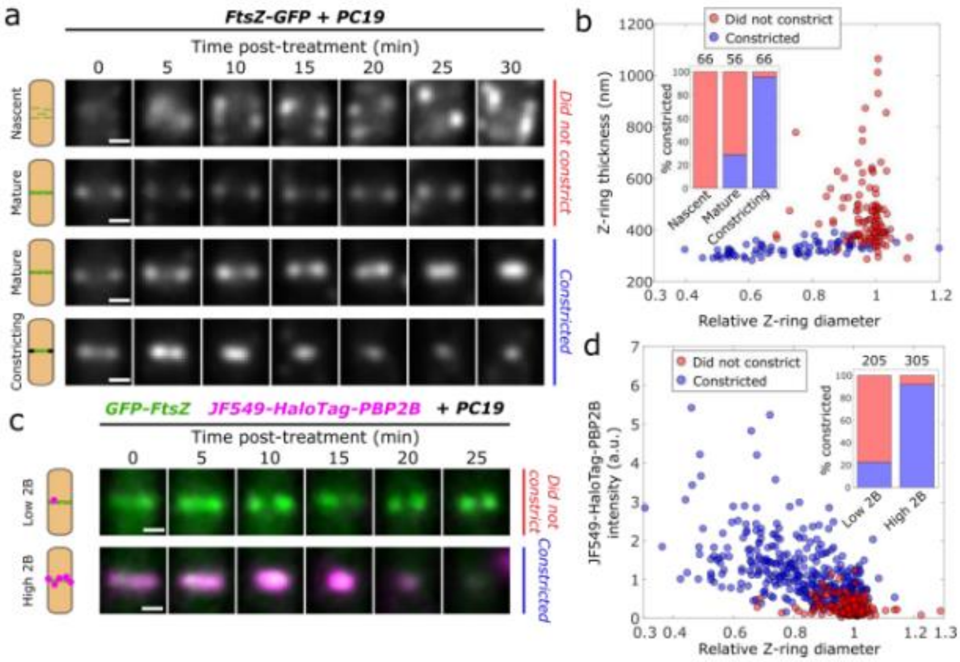

Figure 3. FtsZ treadmilling is required until the arrival of PG synthesis machinery. *(a) Representative time-lapses of Z-rings for FtsZ-GFP cells (SH130) after arrival of 10 µM PC19-laced media.* Nascent rings and many mature rings do not constrict for tens of minutes after PC19 treatment, whereas constricting rings and many mature rings continue constricting after treatment. *(b) Scatter plot of Z-ring diameters and thicknesses for all FtsZ-GFP cells at t=0 min showing whether they continued constricting (blue) or not (red). Inset*: Percentage of cells that continued constricting classified by division stage. Nascent: thickness>400 nm, mature: thickness<400 nm, relative diameter>0.9, constricting: thickness<400 nm, relative diameter<0.9. *(c) Representative time-lapses of rings from two-colour strain SH212 (Green: GFP-FtsZ, magenta: JF549-HaloTag-PBP2B) after the arrival of PC19-laced media.* Z-rings with low HT-PBP2B signal typically do not continue constricting while those with high signal typically do. *(d) Scatter plot of Z-ring diameters and normalised HT-PBP2B intensities for mature Z-rings only at t=0 min showing whether they continued constricting (blue) or not (red). Inset:* Percentage of cells that continued constricting classified by JF549-HaloTag-PBP2B signal. Low 2B: intensity<0.5, high 2B: intensity>0.5. Scale bars: 500 nm. Numbers above stacked bars indicate number of cells.

We used PC19 to investigate the role of FtsZ treadmilling throughout cell division. We imaged cells in fast growth conditions (rich media, 37°C) using a commercial microfluidic device with continual fluid flow both before and during treatment with excess PC19 (Figure 3, Methods). Treatment with PC19 prevented Z-rings in earlier stages of division from continuing to divide, but Z-rings in later stages continued dividing (Figure 3a-b, Supplementary Videos 10-13). PC19 treatment prevented 96% (N=62) of nascent Z-rings from condensing into mature Z-rings (Supplementary Figure 13) and 100% (N=66) from constricting (Figure 3b). Furthermore, we found that treatment prevented 71% (N=56) of mature Z-rings from beginning constriction, while only 5% (N=66) of initially constricting Z-rings were prevented from continuing constriction. In contrast, treatment with PenG inhibited constriction altogether (Supplementary Video 14). Similar results were observed in slow growth conditions (poor media, 30°C; Supplementary Figure 14, Supplementary Video 15). Together these data suggest that FtsZ treadmilling is required for the condensation of filaments from a nascent to a mature Z-ring, but becomes dispensable at some point during the mature Z-ring stage.

It is worth noting that PC19 also affects FtsZ GTPase activity and filament structure[18]. These are likely downstream effects of the primary mode of action, which is to stabilize the polymeric state of the protein. We note that FtsZ retains ~25% GTPase activity even with excess PC19[18]. Furthermore, in cells treated with 8j (a relative of PC19) the subunits in immobile FtsZ foci still turn over slowly[22], which suggests filaments are still dynamic despite not treadmilling. So, while we cannot strictly rule out the possibility that our observations result from a downstream effect of PC19, we believe the most parsimonious explanation for our results is that the arrest of treadmilling specifically is responsible.

We considered whether these effects were specific to PC19 by repeating the assay with the non-benzamide FtsZ inhibitor PC58538 (PC58). This compound inhibits FtsZ by a separate mode of action from PC19: Rather than stabilizing protofilaments, it prevents filament assembly[26]. As with PC19, PC58 prevented 84% (N=50) of nascent Z-rings from condensing into mature Z-rings and 90% (N=50) from constricting, but prevented 60% (N=52) of mature and only 6% (N=33) of constricting Z-rings from constricting (Supplementary Figure 15, Supplementary Video 16). Interestingly, similar results were recently demonstrated using ADEP antibiotics, which activate the protease ClpP to degrade FtsZ monomers and thereby deplete the cytoplasmic pool needed for filament assembly[27]. We conclude that arresting FtsZ treadmilling with PC19 produces an effect similar to, and as severe as, preventing FtsZ filament assembly altogether, emphasizing the critical role of FtsZ treadmilling in cell division initiation.

To further investigate the role of FtsZ treadmilling in Z-ring condensation, we examined the effect of an FtsZ mutant that is deficient in GTP hydrolysis. The mutant FtsZ(D212A) in *E. coli* was shown to have greatly reduced GTPase activity[28,29], and exogenous expression of the equivalent FtsZ(D213A) mutant in *B. subtilis* reduces FtsZ treadmilling speed[1] (Supplementary Figure 16). We constructed a merodiploid strain expressing FtsZ-GFP from the native locus and FtsZ(D213A) from a secondary locus under an IPTG-inducible promoter (SH131, Methods). For comparison to wild-type (Figure 1) we imaged this strain under slow growth conditions (poor media, 30°C) with an induction level (10 µM IPTG) that supported growth in liquid culture (Supplementary Figure 3) and cell division (Supplementary Video 17). Condensation of nascent Z-rings was significantly perturbed under these conditions: 54% (N=74) of nascent Z-rings failed to fully condense prior to constriction initiation, and even throughout constriction Z-rings remained 65 nm (95% CI [63,67]) thicker than wild-type (Supplementary Figure 17), consistent with previous measurements in *E. coli*[30]. This partially deleterious effect on Z-ring condensation is consistent with partial inhibition of FtsZ treadmilling caused by expression of the GTPase-deficient mutant. Interestingly, many incompletely-condensed Z-rings were still able to constrict, implying that cells can tolerate some degree of error in the condensation step.

We next wondered what events within the mature Z-ring stage corresponded to the change in dispensability of FtsZ treadmilling. Divisome assembly in *B. subtilis* is approximately a two-step process where FtsZ and other cytoplasmic proteins arrive first, followed by arrival of the PG synthesis machinery just before constriction initiation, including the septal transpeptidase PBP2B[31]. To determine when FtsZ treadmilling becomes dispensable within mature Z-rings, we repeated the treadmilling inhibition assay using a 2-colour strain where FtsZ and PBP2B are both labelled. Since fully-labelled FtsZ slightly perturbed cell physiology (Supplementary Figure 2) and full labelling of FtsZ was unnecessary for this assay, for the labelled FtsZ we decided to use a well-characterized merodiploid harbouring an N-terminal GFP-FtsZ fusion[22] that could be expressed at a low non-perturbative level. We therefore constructed a 2-colour strain (SH212, Methods) expressing GFP-FtsZ from an ectopic locus and HaloTag-PBP2B from its native locus. To quantify the amount of PBP2B at septa, we labelled HaloTag-PBP2B with an excess of JF549 HaloTag ligand[32] (Methods). This strain showed the same response overall to PC19 treatment as before (Supplementary Figure 18, Supplementary Videos 18-19). For mature rings we found that the amount of PBP2B present at time of FtsZ treadmilling arrest correlated strongly with whether rings would constrict or not (Figure 3c-d). Similar results were obtained for a functional mNeonGreen-PBP2B fusion expressed from the native locus[1] (ME7 Supplementary Video 20, Supplementary Figure 19). The GFP-FtsZ signal also increased during the mature ring stage, but unlike PBP2B the FtsZ signal was only weakly correlated with the percentage of cells continuing constriction (Supplementary Figure 18b). FtsZ treadmilling thus becomes dispensable for cell division just after the arrival of the PG synthesis machinery. These results are consistent with previous findings in *S. aureus* that FtsZ treadmilling is required until constriction has initiated, and thereafter becomes dispensable[3]. Since we previously observed that FtsZ treadmilling guides processive PG synthesis around the septum[1], we conclude that FtsZ treadmilling in mature Z-rings likely functions by guiding the processive motion of septal synthases during the earliest stages of septal synthesis, before a septum has been formed.

Together, our data reveal two essential functions for FtsZ treadmilling in division. The first is a novel peptidoglycan synthesis-independent function, to condense sparse FtsZ filaments into a dense Z-ring. The second function is to initiate constriction by guiding initial cell-wall synthesis.

FtsZ treadmilling accelerates constriction

We wondered how to reconcile the finding that FtsZ treadmilling is dispensable for constriction after initiation, with our previous observation that FtsZ treadmilling sets the rate of constriction[1]. To address this, we set out to determine the effect of rapid, total arrest of FtsZ treadmilling on the septal constriction rate. In order to precisely measure constriction rates immediately after PC19 treatment, we developed a physical model for Gram-positive septal constriction which could be fitted to partial septal constriction trajectories immediately after cell treatment with PC19 (Methods, Supplementary Note 2, Figure 4a). For comparison to previous observations we converted the observed constriction rates of partially constricted cells to an effective constriction time t_{eff}, the total amount of time it would take for an average septum to constrict completely (Methods).

We observed that the constriction time of untreated cells in fast growth conditions was 15.3 min, IQR 13.5-17.9 (N=765, Figure 4b). FtsZ treadmilling inhibition by PC19 treatment caused a robust 7.7 min, 95% CI [6.9,8.3] (N=419), increase in constriction time for cells grown in rich media. This is similar to the increase in constriction time caused by high expression of the GTP-hydrolysis-impaired FtsZ(D213A) mutant (Supplementary Figure 20). Fluorescent PBP2B signal continued to increase after treatment with PC19 (Supplementary Figure 21), indicating that the reduced constriction rate is unlikely to be caused by indirect reduction of synthase levels at the septum. These results show that although FtsZ treadmilling is not required for septal PG synthesis after constriction initiation, treadmilling promotes efficient constriction by increasing septal constriction rate. This reconciles apparently contradictory models previously proposed for the role of FtsZ treadmilling in septal constriction[1,3].

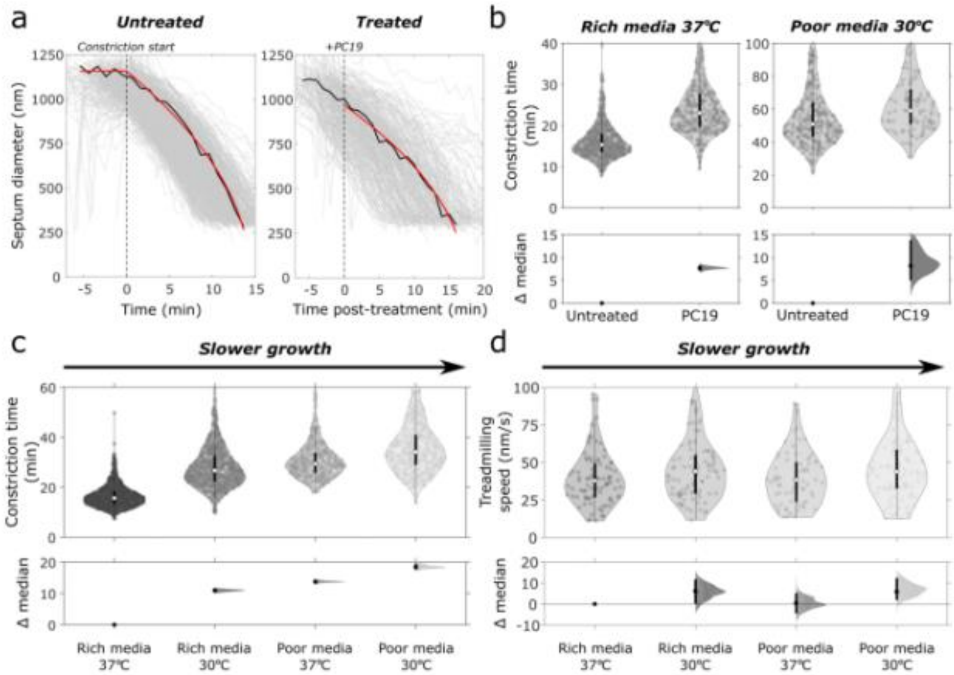

Figure 4. Constriction rate is accelerated by FtsZ treadmilling and fast cell growth rate. *(a) Time traces of ring diameters from mNeonGreen-PBP2B strain (ME7) for untreated (left) and PC19-treated (right) cells with constant PG synthesis model (red) fitted to representative traces (black).* Untreated cell trajectories are aligned relative to fitted constriction start time. PC19-treated cell trajectories are aligned relative to the arrival time of PC19-laced media. *(b) Constriction time before and after PC19 treatment for both fast growth (rich media 37°C) and slow growth (poor media, 30°C) conditions. (c) Constriction time of mNeonGreen-PBP2B cells in rich and poor media at two growth temperatures. (d) FtsZ-mNeonGreen (bWM4) treadmilling speeds in different media and temperature. Top panels, b-d:* violin plots; white circle, sample median; thick black lines, interquartile range; thin black lines, 1.5x interquartile range. *Bottom panels, b-d: Bottom panels:* DABEST plots showing effect size analysis, compared to leftmost condition; black circles, median difference; error bars, 95% confidence interval of median difference.

Cell growth rate limits septal constriction rate independently of FtsZ treadmilling

Growth rate and cell size for most bacterial species are linked to nutrient availability and culture temperature[33]. We sought to identify how growth rate affects the constriction rate of *B. subtilis* cells. We measured the constriction rate in media and temperature conditions (Supplementary Figure 3c; Supplementary Table 1) using a strain expressing PBP2B from its native promoter fused to mNeonGreen (ME7, Methods). Slower growth in either minimal media or at low temperature led to correspondingly longer constriction times (Figure 4a, Supplementary Figure 3d), with a 2.18-fold (95% CI [2.12,2.24]) difference in constriction time between fastest and slowest growth conditions. We determined FtsZ treadmilling speed for all conditions using a dilute exogenous label of FtsZ-mNeonGreen (bWM4) which shows no growth or morphology phenotype at 37°C[1]. FtsZ treadmilling speed was constant across all growth conditions tested (Figure 4b), showing that the effect of growth rate on septal constriction is independent of FtsZ treadmilling.

We next investigated whether FtsZ treadmilling also promotes constriction in slow growth conditions. As in fast growth conditions, arresting FtsZ treadmilling increased the constriction time (Figure 4b, Supplementary Video 21). However, the relative increase in constriction time was much lower in slow growth conditions (1.16-fold 95% CI [1.09,1.24] vs 1.50-fold 95% CI [1.46,1.55] change). These observations show that cell growth rate is a major regulator of active septal constriction, with treadmilling FtsZ filaments acting as a secondary promotor of septal synthesis.

DISCUSSION

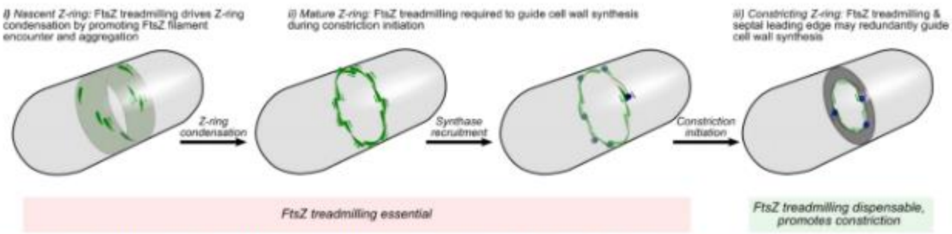

Figure 5: Model for function of FtsZ treadmilling in Z-ring assembly and septal constriction.

Using bespoke ultra-sensitive microscopy of cell division protein dynamics, we discovered that FtsZ treadmilling plays two separate essential roles in cell division: to establish the mature divisome by condensing diffuse filaments into a dense ring, and to guide septal constriction initiation (Figure 5).

We found that condensation of sparse FtsZ filaments into a dense Z-ring is required for cell division. Using VerCINI microscopy we observed that treadmilling FtsZ filaments frequently collide and aggregate in nascent Z-rings. We also found that nascent Z-rings contain a large fraction of immobile FtsZ filaments, which do not treadmill, and that Z-ring condensation promotes formation of treadmilling FtsZ filaments. While the mechanism of FtsZ filament motility regulation requires further study, *in vitro* measurements of FtsZ dynamics suggest that immobile FtsZ filaments could result from low septal FtsZ concentration or regulation by accessory/anchor proteins[9].

Chemical arrest of treadmilling completely abolished FtsZ ring condensation. Attractive lateral interactions between FtsZ filaments, via the FtsZ C-terminal-linker and cytoplasmic FtsZ-associated proteins are known to mediate FtsZ bundling and Z-ring condensation[34–38]. Our results reveal an additional key factor in assembling the Z-ring: FtsZ filament treadmilling drives filament interactions by enabling FtsZ filaments to rapidly search the mid-cell surface circumferentially and efficiently encounter one another. This finding contrasts with previous models of Z-ring condensation involving lateral sliding of filaments[13,14]. We conclude that FtsZ treadmilling—likely along with FtsZ lateral interactions—drives aggregation of FtsZ filaments into a condensed Z-ring. This is remarkably reminiscent of treadmilling-driven partitioning of FtsZ filaments into higher-order structures previously observed *in vitro*[9,39].

The second role of FtsZ treadmilling is to guide septal PG synthesis. We found that this role is essential in the constriction initiation phase of *B. subtilis* cell division, but dispensable afterwards. Together with our previous observations that FtsZ treadmilling guides individual synthase molecules during PG synthesis[1], it is likely that during constriction initiation FtsZ filament treadmilling is required to guide the synthases around the circumference of the mid-cell in the absence of an established septum. We also observed that FtsZ treadmilling dynamics are division stage regulated, with Z-ring condensation promoting efficient FtsZ treadmilling. In addition to concentrating the division machinery into a small area, Z-ring condensation may indirectly promote efficient constriction initiation by increasing the fraction of treadmilling filaments available to guide cell-wall synthesis.

Although FtsZ treadmilling is dispensable after constriction initiation, we found that treadmilling increases the rate of septal constriction by up to 1.5-fold. However, we found that overall cell growth rate has a much stronger effect on septal constriction rate than FtsZ treadmilling, increasing constriction rate up to 2.2-fold between fast and slow growth conditions. We conclude that FtsZ treadmilling plays only a secondary role in active constriction, while its critical roles occur prior to constriction initiation. This contrasts with the previous model of *B. subtilis* FtsZ as an obligatory guide and rate-determining factor for constriction[1]. After constriction initiation, the highly ordered septal leading edge[40] may be sufficient to act as a guide for processive septal PG synthesis, with FtsZ filaments acting as a mid-cell localiser and redundant guide during active constriction.

The VerCINI method presented here is a powerful tool for ultra-sensitive measurement of cell division protein dynamics and mode of action of cell division targeting antibiotics. We anticipate that many other bacterial structures, especially the bacterial cell envelope and associated proteins, could also benefit from VerCINI's high resolution top-down cell view.

A key puzzle in bacterial cell biology is how nanoscale division proteins spontaneously and accurately build a micron-size wall at mid-cell. Treadmilling gives FtsZ filaments the remarkable ability to autonomously drive their own circumferential motion around the mid-cell surface. Our results show that the self-driving capability of FtsZ filaments is crucial to solving the scale problem of cell division by directing divisome assembly and initial septal synthesis to a narrow band around the mid-cell, laying the template for septum construction. Dynamic, self-organizing FtsZ filaments thus provide long-distance order and collective motion around the bacterial mid-cell in the absence of cytoskeletal motor proteins.

ACKNOWLEDGEMENTS

We thank Henrik Strahl (Newcastle) for helpful discussions, Ling Wu and Jeff Errington (Newcastle) for strains and antibodies, Luke Lavis (HHMI) for Janelia Fluor dyes, and Ethan Garner (Harvard) for strains. SH, KW, CJ and EK acknowledge funding support by a Newcastle University Research Fellowship and a Wellcome Trust & Royal Society Sir Henry Dale Fellowship grant number 206670/Z/17/Z. NT supported by a UK Engineering and Physical Sciences Research Council doctoral studentship. RH and PA funded by grants from the UK Biotechnology and Biological Sciences Research Council (BB/M022374/1), the UK Medical Research Council (MR/K015826/1), and Wellcome Trust (203276/Z/16/Z). CD and KW acknowledge funding support by ERC grant SynDiv (669598) and the Netherlands Organisation for Scientific Research (NWO/OCW) as part of the Frontiers of Nanoscience and Basyc programs.

AUTHOR CONTRIBUTIONS

KW, CJ and NT acquired data. KW, CJ, NT and SH analysed data. KW, CJ, SH and CD developed the VerCINI method. KW performed nanofabrication, supervised by CD. SH, KW, PA and RH wrote software. CJ, EK, NT created and characterised bacterial strains. SH and CD directed the research. KW, SH and CJ wrote the manuscript with input from all authors.

MATERIALS AND METHODS

Bacterial strains and growth conditions

Strains used in this study are listed in Supplementary Table 2. Strains were streaked from -80°C freezer glycerol stocks onto Nutrient Agar (NA) plates containing the relevant antibiotics and/or inducers and grown overnight at 37°C. Single colonies were transferred to liquid starter cultures in either Time-Lapse Medium (TLM[42]) or PHMM media and grown with agitation at 200 rpm overnight at either 30°C (TLM) or 22°C (PHMM[1]). The next day, TLM starter cultures were diluted to a starting OD_{600} of 0.1 in Chemically-Defined Medium (CDM[42]), while PHMM starter cultures were diluted to a starting OD_{600} of 0.05 in PHMM, and these liquid cultures were grown at 30°C or 37°C with any required inducer until they reached the appropriate OD_{600}. When necessary, antibiotics and inducers were used at the following final concentrations: chloramphenicol 5 µg/ml, spectinomycin 60 µg/ml, erythromycin 1 µg/ml, lincomycin 10 µg/ml, kanamycin 5 µg/ml, xylose 0.08% and IPTG 20 µM.

Strain construction

SH211 (PY79 Δ*hag*) was constructed by transforming competent PY79 with genomic DNA extracted from strain PB5250, using standard protocols[43]. The antibiotic resistance cassette was removed using pDR224 as described previously[44].

SH130 (PY79 Δ*hag ftsZ::ftsZ-gfp-cam*) was constructed by transforming SH211 competent cells with genomic DNA extracted from strain PL642.

SH131 (PY79 Δ*hag ftsZ::ftsZ-gfp-cam* Ω *amyE::erm*-$P_{hyperspank}$-*ftsAZ*(D213A)) was constructed by transforming competent SH130 cells with genomic DNA extracted from strain bAB215.

SH132 (PY79 *pbp2B::mNeonGreen-15aa-pbp2B* Ω *amyE::erm*-Phyperspank-*ftsAZ*(D213A)) was constructed by transforming competent ME7 cells with genomic DNA extracted from strain bAB215.

SH212 (PY79 *pbp2B::erm*-$P_{hyperspank}$-*HaloTag-15aa-pbp2B* Ω *amyE::spc* P_{xyl} *gfp-ftsZ*) was constructed by transforming competent bGS28 cells with genomic DNA extracted from strain 2020. All published strains are available on request to the authors.

Bacterial strain characterization

Strains were characterised by growth in liquid culture (Supplementary Figure 3) and cell morphology analysis (Supplementary Figure 2). Fluorescent fusion protein levels for relevant strains were determined by Western blotting (Supplementary Figure 1).

Growth curves

B. subtilis PY79 and variant strains were grown overnight in TLM or PHMM containing the relevant inducers. Overnight cells were diluted to an OD_{600} of 0.05 in either CDM or PHMM, respectively, and 200 µL were used in a 96-well microtiter plate. Growth was monitored for 12 hours using a FluoStar plate reader (BMG Labtech).

Cell morphology analysis

PY79 and SH130 cultures were prepared for imaging in CDM or PHMM as described above. Once the cultures had reached OD_{600} 0.4-0.5, Nile Red was added to 200 µl of cells to a working concentration of 1 µg/ml, and incubated at growth temperatures for 5 mins, prepared on agarose microscope slides as described below and cell morphology images recorded. Cell length was then manually determined using ImageJ.

Western blotting

Overnight cultures of specified strains were grown overnight in LB at 30°C. The following morning, cultures were diluted to ~OD_{600} 0.05 and grown at 30°C until ~OD_{600} 0.6. Cells were harvested by centrifugation and stored at 20°C for further processing. Samples were normalised based on OD600, re-suspended in 2x SDS protein sample buffer and heated at 80°C for 10 minutes followed by centrifugation.20 µL lysates were then separated by SDS PAGE in 10% polyacrylamide gel.. FtsZ and PBP2B were detected using a FtsZ polyclonal (Sigma, 1:10000 dilution) and a PBP2B polyclonal (Merck, 1:5000 dilution) antibody, respectively, followed by a HRP-conjugated anti-rabbit IgG antibody (Sigma). Samples were developed using Pierce™ ECL Western Blotting Substrate (Thermofisher) and imaged using an ImageQuant LAS 4000 mini Biomolecular Imager (GE Healthcare).

Microscopy

Power density, exposure time and other key parameters are listed for each microscopy experiment in Supplementary Table 4. All imaging was done using either a Nikon N-SIM/N-STORM inverted fluorescence microscope (Figure 4, Supplementary Figure 22) or a custom-built inverted microscope (otherwise).

Nikon N-STORM. Cells were illuminated with a 488 nm line from an Argon Ion laser (CVI Melles-Griot). A 100x TIRF objective (Nikon CFI Apochromat TIRF 100XC Oil) was used for imaging and an Andor iXon DU897 EMCCD camera was used, with a 1.5x OptoVar (Nikon) and standard Nikon tube lens, giving an effective image pixel size of 106 nm/pixel. Cells were illuminated via HiLO[45] inclined illumination to minimise background using an objective TIRF module (Nikon N-STORM module) using 488 nm laser excitation.

Custom microscope. Cells were illuminated with a 488 nm laser (Obis) and/or a 561 nm laser (Obis) as indicated. A 100x TIRF objective (Nikon CFI Apochromat TIRF 100XC Oil) was used for all experiments except microfluidic VerCINI measurements where a 100x silicone immersion objective (CFI SR HP Plan Apochromat Lambda S 100XC Sil, Nikon) was used for deep focusing. A 200 mm tube lens (Thorlabs TTL200) and Prime BSI sCMOS camera (Teledyne Photometrics) were used for imaging, giving effective image pixel size of 65 nm/pixel. Imaging was done with a custom-built ring-TIRF module operated in ring-HiLO[45] using a pair of galvanometer mirrors (Thorlabs) spinning at 200 Hz to provide uniform, high SNR illumination.

Nanofabrication

Micropillars were patterned using electron-beam lithography and etched using reactive-ion etching. Briefly, a silicon wafer was spin coated with AR-N 7700.18 (Allresist GmbH). Features were patterned using a Leica EBPG 5000+ with 56 nm beam step size. The unexposed resist was removed with solvent Microposit MF-321 and the exposed wafer surface was etched using an AMS Bosch etcher. The remaining resist was removed using oxygen plasma. Pillars widths ranged from 1.0 to 13 µm with height 6.7 µm, spaced 5 µm apart. Final micropillar dimensions were confirmed using SEM.

Micropillar wafers were silanised to allow cured polydimethylsiloxane (PDMS) to be removed without damaging structures. To do this, wafers were coated with (tridecafluoro-1,1,2,2-tetrahydrooctyl) trichlorosilane (abcr GmbH) by vapour deposition.

VerCINI

Agarose microholes were formed by pouring molten 6% agarose onto the silicon micropillar array. Patterned agarose was transferred into a Geneframe (Thermo Scientific) mounted on a glass slide, and excess agarose was cut away to ensure sufficient oxygen. Cells at $OD_{600} \sim 0.4$ were concentrated 100x by centrifugation and added onto the agarose pad. Cells were then loaded into the microholes by centrifuging the mounted agarose pad with concentrated cell culture in an Eppendorf 5810 centrifuge with MTP/Flex buckets. Unloaded cells were rinsed off with excess media.

FtsZ treadmilling dynamics were imaged at 1 frame/s (continuous exposure) for 2 mins at 1-8 W/cm^2. After each field of view was imaged, a multi-slice Z-stack was taken at 500 nm intervals to exclude tilted or improperly trapped cells, in addition to excluding Z-rings that have an adjacent Z-ring 1 µm above or below the imaging plane. VerCINI experiments were performed on cells in a *Δhag* mutant background, preventing undesirable cell rotation within the microholes by disabling flagellar motility.

Microfluidic VerCINI

Device assembly

Open-topped microhole coverslips were formed from PDMS using the silicon micropillar array (Supplementary Figure 23). All PDMS reagents and processing equipment were from BlackHoleLab. PDMS elastomer base and curing agent were mixed in a 1:1 ratio and degassed. The degassed mixture was then poured on top of the microhole array and a microscope coverslip was pressed down to form a thin layer. PDMS was cured by baking at 80°C for 1 hr, and the coverslip with patterned PDMS layer was removed from the silicon mould.

Microfluidic chambers were prepared using readily-available components (Supplementary Figure 23). First, holes were drilled into a glass microscope cover slide using a diamond drill bit (Kingsley North). A flow channel was then made by cutting a strip of double-sided tape using either a scalpel or laser engraver. One side of the double-sided tape was then adhered to the microscope cover slide. Cut pipette tips were then inserted into the drilled holes, and polyethylene tubing (Smiths Medical) was inserted into them. Leakage was prevented by sealing pipette tips and tubing using epoxy.

To load cells into the microholes, PDMS was first rendered hydrophilic by treating with air plasma for 3 min. A 9 mm diameter silicone gasket (Grace Bio-Labs) was then placed over the PDMS microholes. Cells at $OD_{600} \sim 0.4$ were concentrated 100x by centrifugation and pipetted into the silicone gasket. Cells were then loaded into the microholes by centrifuging the microhole-containing coverslip with concentrated cell culture in an Eppendorf 5810 centrifuge with MTP/Flex buckets. The coverslip was covered during centrifugation to prevent evaporation. Unloaded cells were rinsed off with excess media. To ensure adequate loading, this loading-and-rinsing protocol was then repeated.

After cells were loaded into microholes, the silicone gasket was removed and the flow chamber was fully assembled by adhering the PDMS-covered coverslip to the exposed side of double-sided tape on the glass cover slide (Supplementary Figure 23).

Imaging

Due to the relatively thick (~50 µm) layer of PDMS between the coverslip surface and the confined cells, a Nikon silicone immersion objective (CFI SR HP Plan Apochromat Lambda S 100XC Sil, Nikon) was used for imaging due to its high working distance (0.3 mm).

Since the indices of refraction for PDMS and aqueous solution are similar, autofocusing systems relying on the reflection of an IR signal from two interfaces were not adequate due to weak signal. Instead, autofocusing was done using an image-based approach first described by McGorty and co-workers[25] using cross-correlation of brightfield images. Briefly, a separate brightfield imaging pathway was added to the microscope using a 1050 nm IR LED (Thorlabs) and IR-sensitive camera (UI-1220LE-M-GL, Imaging Development Systems GmbH), and a plugin for Micro-Manager was developed to calculate cross-correlations and move the sample stage (https://github.com/HoldenLab/DeepAutoFocus). At the start of an experiment, a z-stack of IR brightfield images was obtained as a reference. During the experiment, the cross-correlation map between every new IR brightfield image and this reference stack was calculated, and the sample stage was moved to compensate for any drift. To our knowledge this is the first application of IR cross-correlation autofocusing to live cell imaging.

Fluid control

Media was flowed through the chamber by a syringe pump (Aladdin-220, World Precision Instruments). To prevent potential leakage, media was pulled through the chamber from fluid reservoirs by operating the syringe pump in withdraw mode. Complete solution exchange occurred within 7 s of initial compound arrival time, estimated using a rhodamine tracer.

CellASIC experiments

The microfluidic CellASIC system (EMD Millipore) was used to image constricting cells during treatment with division inhibitors. Cells were loaded into B04A plates and equilibrated in blank media for ~15 min with a pressure of 2 psi (~6 µL/hr flow rate) prior to imaging.

In a typical experiment, untreated constricting cells were imaged for 30 min (1 min/frame, 1 s exposure, 1-2 W/cm^2) while blank media was flowed using 2 psi. Solution exchange was done by first flowing media with compound using 8 psi (~34 µL/hr flow rate) for 15 s, then dropping the pressure to 2 psi for the remainder of the experiment (50-90 min). DMSO treatment alone caused a small but robust increase in constriction time (Supplementary Figure 24). However, pre-adaptation of cells to blank media containing DMSO eliminated this effect, showing that observed effects of PC19 treatment resulted from the drug and not the solvent that accompanied it (Supplementary Figure 24).

The arrival time of the compound at the cells was most estimated by treating the FtsZ-GFP strain with 10 µM PC19 using our standard flow protocol. PC19 causes the diffuse cytoplasmic FtsZ-GFP to rapidly polymerise into short filaments throughout the cell (Supplementary Videos 10-13), providing a clear signal for compound arrival. From these experiments we determined that compound arrives 3-4 min after fluid exchange.

Microscopy of horizontal cells

Sample preparation

Coverslips were first cleaned by treating with air plasma for 5 min. Slides were prepared as described previously[42]: Flat 2% agarose pads of either CDM or PHMM were prepared inside Geneframes (Thermo Scientific) and cut down to strips of 5 mm width to ensure sufficient oxygen supply to cells. Cell cultures were grown to OD_{600} between 0.2 and 0.4, when 0.5 µL of cell culture was spotted on the pad. Cells were allowed to adsorb to the pad for 30 s before a plasma-cleaned coverslip was placed on them. After spotting on agarose pads, cells were allowed to equilibrate within the microscope body for 15 min before being imaged. Cells were then imaged either by TIRF microscopy for observation of FtsZ filament dynamics, or ring-HiLO for time-lapse observation, with experimental parameters defined in Supplementary Table 4.

HaloTag labelling with JF549 dye

Full labelling of HaloTag-PBP2B was done by incubating strain SH212 with 50 nM JF549 HaloTag ligand for 15 min. Cells were washed once with fresh media before imaging. JF549 HaloTag ligand was a gift from Luke Lavis[32].

Image analysis

VerCINI data analysis

Pre-processing

Videos were denoised using the ImageJ plugin PureDenoise[17], which is based on wavelet decomposition. Key assumptions of the method are (i) local spatiotemporal similarity within the image (ii) absence of sharp discontinuities, guaranteed by diffraction-limited nature of the image. The denoising algorithm makes does not make any assumptions on the type of underlying biological structure.

Denoised videos were registered using the ImageJ plugin StackReg[46]. Image stacks of vertically immobilised cells were inspected to exclude tilted cells or out of focus FtsZ-rings, or FtsZ rings where a second Z-ring was closer than 1 um to the focal plane. Cropped region of interest movies containing single in-focus cells were manually selected and exported for analysis. An ImageJ package for VerCINI data processing is available (https://github.com/HoldenLab/Ring_Analysis_IJ).

VerCINI background subtraction, kymograph extraction, quantification

Custom software for quantitative cytoplasmic background subtraction and kymograph extraction was developed for analysis of VerCINI movies (https://github.com/HoldenLab/ring-fitting2). Fluorescence images of isolated vertical cells were fitted to a joint explicit model for diffuse out-of-focus cytoplasmic background (Gaussian + Cauchy model) plus septal protein signal, modelled as a 12 sectored annulus with each sector of variable amplitude.

$$F(x,y) = Signal(x,y) + Bg(x,y)$$

Signal is calculated in polar coordinates, around the septal ring centre fit parameter (x_0, y_0), and then transformed into Cartesian coordinates. Signal is defined as

$$S(r,\theta) = A_i(\theta)\exp\left(-\frac{(r-R_0)^2}{2\sigma^2}\right),$$

where $A_i(\theta)$ defines a 12 sectored ring. Background is defined as

$$Bg(x,y) = a\exp\left(\frac{-((x-x_0)^2+(y-y_0)^2)}{2\sigma_{bg1}^2}\right) + b\frac{\sigma_{bg2}^2}{(x-x_0)^2+(y-y_0)^2+\sigma_{bg2}^2} + c.$$

This explicit model allowed accurate sub-pixel location of a circular line profile at the septal leading edge. Explicit subtraction of complex background signal also allowed septal intensity quantification. The background subtracted intensity along the circular line profile was then calculated for each frame and automatically plotted as a kymograph. Kymographs were plotted over the [0,720°] ie two complete revolutions around the line profile for ease of visualization, specifically to allow straightforward visualization of treadmilling filaments crossing the 360°,0° boundary. For each cell, the Z-ring diameter was determined from the fitted model in the kymograph extraction step. Median septal intensity was calculated as the median value of all kymograph pixels from the first 60 image frames.

FtsZ filament treadmilling analysis using VerCINI

We found that automated methods for in vitro FtsZ filament speed measurements, either after Dos Santos Caldas and coworkers[47] or using a similar in-house algorithm, are currently insufficient for FtsZ filament speed analysis in either horizontal or vertical cells compared to manual analysis, because at cellular filament density they currently perform poorly at detecting immobile filaments, break the complete trajectories of treadmilling filaments into multiple shorter trajectories, and cannot reliably process images from dense Z-rings in horizontal cells.

We therefore performed manual measurement of filament speed and processivity by kymograph analysis, annotating filaments as lines in ImageJ and then measuring the angle via ImageJ script. As the intensity range across kymographs is large, manual detection and analysis of filaments was aided by applying a ridge filter[48] to the kymograph which detects ridges in the image, independent of absolute intensity. The ridge filter consists of a Gaussian blur operation to set the feature scale and suppress noise (here 2 pixels, 130 nm), followed by calculation of the major eigenvalue of the Hessian matrix for each pixel, implemented as an ImageJ macro in the package listed above. Joint annotation of the ridge filtered and raw intensity kymograph was performed, allowing sensitive annotation of both bright and dim filaments (Supplementary Figure 25).

Horizontal cell image analysis

Pre-processing

Images were denoised and registered as described above.

Cell segmentation and tracking of division protein localization

MicrobeJ[11] was used to track individual FtsZ-/PBP2B-rings and export their centroid coordinates for analysis. To do this, image backgrounds were first subtracted using a sliding paraboloid window of 50 pixels and all frames were converted to 8-bit for easier thresholding.

Two approaches were used to identify division protein localization, depending on the experiment. For measurements of septal constriction rate only (Figure 4a), which requires only detection of bright dense FtsZ/PBP2B rings, a simple approach of intensity-based threshold detection was applied in MicrobeJ a threshold was selected manually for each field of view using MinError. Additional area and length thresholds (Area: [0.08 Inf] μm^2, Length: [0.02 1.8] µm) were established to exclude objects in fields of view that were not rings. Tracks shorter than 7 frames were excluded. Data was then exported for analysis in MATLAB.

For analysis of FtsZ ring dynamics over the entire division process, from nascent Z-ring assembly to late constriction (Figure 1), it was necessary to additionally robustly detecting diffuse patchy FtsZ-rings. We trained the machine learning segmentation tool Ilastik[12] to detect cell outlines with fluorescence images of cells labelled with FtsZ. For detection of diffuse Z-rings, we applied a large Gaussian blur filter to the images, and then multiplied this by the Ilastik-segmented binary image, which had the effect of separating any overlap of Z-rings between adjacent cells. Intensity threshold-based detection of Z-rings was then performed in MicrobeJ as above.

Quantification of division protein septal localization

Custom MATLAB software was developed to measure the diameters and intensities of Z- and 2B-rings obtained from either MicrobeJ or Ilastik. Each frame of each individual ring was first segmented using a multi-level threshold to distinguish the septum, cytoplasm, and background. The septal axis and the cell axis were identified using the segmented image, and the image was rotated such that pixels were aligned along these axes. Line profiles of Z- and 2B-rings were obtained by averaging pixel values along the septal axis ±2 pixels to reduce noise. Diameter were then obtained by fitting line profiles to a toy model that describes a circle of uniform intensity rotated to be orthogonal to the axis of the imaging plane ('Tilted Circle Model', Supplementary Note 1, Supplementary Figure 26). Septal density was calculated as the total intensity along the lateral line profile, divided by the ring circumference, as calculated from the constriction rated analysis (below) to reduce single frame noise. Septal density was used in place of total intensity, in order to compare to the septal intensity measurements obtained during the VerCINI experiments. Axial thickness was estimated by fitting an axial line profile to an analytical super-Gaussian and calculating the full-width half maximum.

Evaluation of percentage Z-rings condensed and constricted post-treatment

Since PC19 treatment causes bright fluorescent foci to appear randomly throughout the cell in strains where FtsZ is labelled, tracking software fails to consistently follow most Z-rings post-treatment in the SH130 and SH212 strains. Furthermore, measurements of Z-ring thickness and diameter were inaccurate due to the proximity of fluorescent foci. Since it was typically straightforward to observe, whether Z-rings condensed and/or constricted post-PC19 treatment was evaluated manually.

FtsZ filament treadmilling analysis from TIRF microscopy data

Images were denoised and registered as above. TrackMate[49] was used to help identifying treadmilling FtsZ filaments outside of dense Z-rings. A line region of interest (ROI) was drawn perpendicular to the cell axis where treadmilling filaments were identified. Kymographs were calculated along this line profile FtsZ filaments trajectories in the kymograph were marked with a line ROI (Supplementary Figure 22). Treadmilling speed for each filament trajectory was calculated from the angle of the line ROIs.

Constriction rate analysis

Previous models for septal constriction have either been *ad hoc*[26] or tailored to Gram-negative cell division based on remodelling of a hemispherical cap[27]. We derived a simple model for Gram-positive constriction, assuming (i) outside-in synthesis of a flat plate at mid-cell and (ii) total PG synthesis rate around the septal leading edge is constant (Supplementary note 2)

$$d(t) = \begin{cases} d_0, & t < t_0 \\ \sqrt{d_0^2 - \frac{4k}{\pi}(t - t_0)}, & t \geq t_0 \end{cases}$$

Where d_0 is the initial Z- or 2B-ring diameter, t_0 is the time constriction begins, and k is the rate at which area is added to the septal plate. This model fitted measured constriction trajectories well, and the estimated time of constriction completion corresponded closely to completion times independently estimated from PBP2B departure in wild type cells (Supplementary Figure 27).

We measured constriction rates in the mNeonGreen-PBP2B strain, since FtsZ-GFP mislocalises post-treatment with PC19 and makes it difficult to track large numbers of septa. A small amount of mNeonGreen-PBP2B signal remained at mid-cell after constriction had finished. This excess signal was excluded from the rate analysis by cutting the 2B-ring data after this drop in intensity. We obtained constriction time distributions for PC19-treated cells by fitting only to post-treatment data.

For comparison to previous observations we converted the observed constriction rates to an effective constriction time t_{eff}, the total amount of time it would take for an unconstricted septum to constrict completely (Methods) given the fitted rate k : $t_{eff} = 2\pi \cdot \frac{d_0^2}{k}$. The average diameter of the unconstricted septum d_0 was estimated as 1100 ± 100 nm (mean, SD) for the mNeonGreen-PBP2B based on the background fluorescence signal in the cell.

Statistics

Data were analysed using estimation statistics, which focusses on magnitude and robustness of effect size using DABEST[50] (Data Analysis with Bootstrap Coupled Estimation), rather than just statistical significance/ p-value. Averages reported were median values unless otherwise indicated. All effect size estimates were calculated based on difference of medians. 95% confidence interval of the median, or of the difference of medians, was estimated by bootstrapping (https://github.com/HoldenLab/violinplusDABEST-Matlab) and indicated with square brackets [].

Interquartile range was indicated by IQR. Thick error bar lines in Violin plots indicate interquartile range, thin lines indicate adjacent vales. Error bars in DABEST plots indicate 95% CI of median difference, estimated by bootstrapping. Sample size, indicating number of filaments/Z-ring, cells, microscope fields of view, technical and biological replicates, as appropriate, is presented for each dataset in Supplementary Table 3.

Simulations of FtsZ filament dynamics

Simulated time lapse movies of FtsZ filament dynamics in vertically immobilized cells were generated. Source code for simulations is available (https://github.com/HoldenLab/ring-simulator). Filament speed and lifetime were sampled from distributions obtained from experiments via bootstrap resampling. FtsZ filament distributions were taken from cells expressing FtsZ-GFP in the nascent Z-ring cell division state. Sub-diffraction-limited treadmilling filaments were simulated on a diffuse Gaussian-Cauchy cytoplasmic background described above. Filament intensity, background amplitude and shape parameters all matched average parameters experimentally observed in nascent Z-rings. Photon noise and manufacturer specified camera gain and read noise were added to the images. The number of filaments in each simulated Z-ring was drawn from a Poisson distribution with average filament density equal to observed nascent, mature, 2x mature or 12x mature Z-ring density of (1.3, 3.3, 6.5, 37.5 filaments/ Z-ring/ frame). Filament density of real nascent Z-rings was calculated directly from observed number of manually traced filaments, as the filament density there was low enough that filament detection bias was expected to be low. To minimize possible under-detection bias, filament density in mature Z-rings was estimated by multiplying the estimated nascent Z-ring density by the ratio of total Z-ring intensity for mature and nascent Z-rings (Supplementary Figure 8b). Additional simulations at 2x and 12x mature Z-ring filament densities were performed in order to investigate the extent to which large increases to filament density could perturb observed FtsZ filament speeds. Simulated FtsZ ring time lapse movies were analysed identically to the experimental data, with FtsZ filament speed estimated by kymograph analysis. Increased FtsZ filament density caused a decrease in the fraction of detected filaments but had minimal effect on observed FtsZ filament speeds, or the ratio of immobile:treadmilling FtsZ filaments, i.e. the ability to robustly detect both immobile and treadmilling FtsZ filaments (Supplementary Figure 10).

Step finding analysis of Z-ring axial thickness data

Transitions between a decondensed and condensed Z-ring for SH130 cells expressing FtsZ-GFP Z-rings was measured using a step finding algorithm to detect either one or two states in time series Z-ring axial thickness, using a global change point detection algorithm[51] implemented in the MATLAB function *findchangepts()*. State detection was performed based on changes in standard deviation of the time series, with an additional threshold that detected axial thickness states should differ by at least 50 nm.

Analysis of Z-ring axial thickness data for FtsZ(D213A) mutant

Although the step-finding method described above accurately located the decondensed-to-condensed transition in wild-type cells, we found that this method was inadequate for the FtsZ(D213A) mutant, as the condensation transition was often slower and more gradual than in wild-type. Instead, Z-rings were considered to have condensed if the thickness dropped below a threshold value for at least one frame (1 min) prior to the start of constriction. The threshold was chosen as 1σ above the mean thickness for condensed wild-type cells (356 nm; Supplementary Figure 17).

DATA AVAILABILITY

Source data for all figures presented in the paper and Supplementary Information, as well as raw movie files for all Supplementary Videos are available at

https://data.ncl.ac.uk/projects/FtsZ_treadmilling_is_essential_for_Z-ring_condensation_and_septal_constriction_initiation_in_Bacillus_subtilis_cell_division/92465

CODE AVAILABILITY

Custom software is available on the Holden lab GitHub page:

https://github.com/HoldenLab/Ring_Analysis_IJ
https://github.com/HoldenLab/ring-fitting2
https://github.com/HoldenLab/DeepAutoFocus
https://github.com/HoldenLab/ring-simulator

REFERENCES

1. Bisson-Filho, A. W. *et al.* Treadmilling by FtsZ filaments drives peptidoglycan synthesis and bacterial cell division. *Science* **355**, 739–743 (2017).
2. Yang, X. *et al.* GTPase activity–coupled treadmilling of the bacterial tubulin FtsZ organizes septal cell wall synthesis. *Science* **355**, 744–747 (2017).
3. Monteiro, J. M. *et al.* Peptidoglycan synthesis drives an FtsZ-treadmilling-independent step of cytokinesis. *Nature* (2018) doi:10.1038/nature25506.
4. Perez, A. J. *et al.* Movement dynamics of divisome proteins and PBP2x:FtsW in cells of Streptococcus pneumoniae. *Proc. Natl. Acad. Sci.* **116**, 3211–3220 (2019).
5. Baranova, N. *et al.* Diffusion and capture permits dynamic coupling between treadmilling FtsZ filaments and cell division proteins. *Nat. Microbiol.* **5**, 407–417 (2020).
6. Yao, Q. *et al.* Short FtsZ filaments can drive asymmetric cell envelope constriction at the onset of bacterial cytokinesis. *EMBO J.* e201696235 (2017) doi:10.15252/embj.201696235.
7. Strauss, M. P. *et al.* 3D-SIM Super Resolution Microscopy Reveals a Bead-Like Arrangement for FtsZ and the Division Machinery: Implications for Triggering Cytokinesis. *PLoS Biol* **10**, e1001389 (2012).
8. Holden, S. J. *et al.* High throughput 3D super-resolution microscopy reveals *Caulobacter crescentus* in vivo Z-ring organization. *Proc. Natl. Acad. Sci.* **111**, 4566–4571 (2014).
9. Loose, M. & Mitchison, T. J. The bacterial cell division proteins FtsA and FtsZ self-organize into dynamic cytoskeletal patterns. *Nat. Cell Biol.* **16**, 38–46 (2014).
10. Levin, P. A., Kurtser, I. G. & Grossman, A. D. Identification and characterization of a negative regulator of FtsZ ring formation in Bacillus subtilis. *Proc. Natl. Acad. Sci.* **96**, 9642–9647 (1999).
11. Ducret, A., Quardokus, E. M. & Brun, Y. V. MicrobeJ, a tool for high throughput bacterial cell detection and quantitative analysis. *Nat. Microbiol.* **1**, 1–7 (2016).
12. Berg, S. *et al.* ilastik: interactive machine learning for (bio)image analysis. *Nat. Methods* **16**, 1226–1232 (2019).

13. Monahan, L. G., Robinson, A. & Harry, E. J. Lateral FtsZ association and the assembly of the cytokinetic Z ring in bacteria. *Mol. Microbiol.* **74**, 1004–1017 (2009).
14. Erickson, H. P., Anderson, D. E. & Osawa, M. FtsZ in Bacterial Cytokinesis: Cytoskeleton and Force Generator All in One. *Microbiol. Mol. Biol. Rev.* **74**, 504–528 (2010).
15. Walker, B. E., Männik, J. & Männik, J. Transient Membrane-Linked FtsZ Assemblies Precede Z-Ring Formation in Escherichia coli. *Curr. Biol.* **30**, 499-508.e6 (2020).
16. Ellefsen, K. L., Dynes, J. L. & Parker, I. Spinning-Spot Shadowless TIRF Microscopy. *PLOS ONE* **10**, e0136055 (2015).
17. Luisier, F., Vonesch, C., Blu, T. & Unser, M. Fast interscale wavelet denoising of Poisson-corrupted images. *Signal Process.* **90**, 415–427 (2010).
18. Haydon, D. J. *et al.* An Inhibitor of FtsZ with Potent and Selective Anti-Staphylococcal Activity. *Science* **321**, 1673–1675 (2008).
19. Elsen, N. L. *et al.* Mechanism of action of the cell-division inhibitor PC190723: Modulation of FtsZ assembly cooperativity. *J. Am. Chem. Soc.* **134**, 12342–12345 (2012).
20. Wagstaff, J. M. *et al.* A polymerization-associated structural switch in FtsZ that enables treadmilling of model filaments. *mBio* **8**, e00254-17 (2017).
21. Artola, M. *et al.* The structural assembly switch of cell division protein FtsZ probed with fluorescent allosteric inhibitors. *Chem. Sci.* **8**, 1525–1534 (2017).
22. Adams, D. W., Wu, L. J., Czaplewski, L. G. & Errington, J. Multiple effects of benzamide antibiotics on FtsZ function. *Mol. Microbiol.* **80**, 68–84 (2011).
23. Männik, J., Driessen, R., Galajda, P., Keymer, J. E. & Dekker, C. Bacterial growth and motility in sub-micron constrictions. *Proc. Natl. Acad. Sci. U. S. A.* **106**, 14861–14866 (2009).
24. Yang, D., Jennings, A. D., Borrego, E., Retterer, S. T. & Männik, J. Analysis of factors limiting bacterial growth in PDMS mother machine devices. *Front. Microbiol.* **9**, (2018).
25. McGorty, R., Kamiyama, D. & Huang, B. Active microscope stabilization in three dimensions using image correlation. *Opt. Nanoscopy* **2**, 3 (2013).

798 26. Stokes, N. R. *et al.* Novel inhibitors of bacterial cytokinesis identified by a cell-based antibiotic screening assay. *J. Biol. Chem.* **280**, 39709–39715 (2005).

800 27. Silber, N., Mayer, C., Matos de Opitz, C. L. & Sass, P. Antibiotic-induced degradation of FtsZ reveals distinct stages of Bacillus subtilis FtsZ ring assembly and constriction. *bioRxiv* (2020).

802 28. Lu, C., Stricker, J. & Erickson, H. P. Site-specific mutations of FtsZ - Effects on GTPase and in vitro assembly. *BMC Microbiol.* **1**, (2001).

804 29. Redick, S. D., Stricker, J., Briscoe, G. & Erickson, H. P. Mutants of FtsZ targeting the protofilament interface: Effects on cell division and GTPase activity. *J. Bacteriol.* **187**, 2727–2736 (2005).

806 30. Lyu, Z., Coltharp, C., Yang, X. & Xiao, J. Influence of FtsZ GTPase activity and concentration on nanoscale Z-ring structure in vivo revealed by three-dimensional Superresolution imaging. *Biopolymers* **105**, 725–734 (2016).

809 31. Gamba, P., Veening, J.-W., Saunders, N. J., Hamoen, L. W. & Daniel, R. A. Two-Step Assembly Dynamics of the Bacillus subtilis Divisome. *J. Bacteriol.* **191**, 4186–4194 (2009).

811 32. Grimm, J. B. *et al.* A general method to improve fluorophores for live-cell and single-molecule microscopy. *Nat. Methods* **12**, 244–250 (2015).

813 33. Westfall, C. S. & Levin, P. A. Bacterial Cell Size: Multifactorial and Multifaceted. *Annu. Rev. Microbiol.* **71**, 499–517 (2017).

815 34. Dajkovic, A., Pichoff, S., Lutkenhaus, J. & Wirtz, D. Cross-linking FtsZ polymers into coherent Z rings. *Mol. Microbiol.* **78**, 651–668 (2010).

817 35. Caldas, P. *et al.* Cooperative ordering of treadmilling filaments in cytoskeletal networks of FtsZ and its crosslinker ZapA. *Nat. Commun.* **10**, 5744 (2019).

819 36. Huecas, S. *et al.* Self-Organization of FtsZ Polymers in Solution Reveals Spacer Role of the Disordered C-Terminal Tail. *Biophys. J.* **113**, 1831–1844 (2017).

821 37. Sundararajan, K. & Goley, E. D. The intrinsically disordered C-terminal linker of FtsZ regulates protofilament dynamics and superstructure in vitro. *J. Biol. Chem.* **292**, 20509–20527 (2017).

38. Buske, P. J. & Levin, P. A. A flexible C-terminal linker is required for proper FtsZ assembly in vitro and cytokinetic ring formation in vivo. *Mol. Microbiol.* **89**, 249–263 (2013).

39. Denk, J., Huber, L., Reithmann, E. & Frey, E. Active Curved Polymers Form Vortex Patterns on Membranes. *Phys. Rev. Lett.* **116**, 178301 (2016).

40. Pasquina-Lemonche, L. *et al.* The architecture of the Gram-positive bacterial cell wall. *Nature* **582**, 294–297 (2020).

41. Coltharp, C., Buss, J., Plumer, T. M. & Xiao, J. Defining the rate-limiting processes of bacterial cytokinesis. *Proc. Natl. Acad. Sci.* 201514296 (2016) doi:10.1073/pnas.1514296113.

42. de Jong, I. G., Beilharz, K., Kuipers, O. P. & Veening, J.-W. Live Cell Imaging of Bacillus subtilis and Streptococcus pneumoniae using Automated Time-lapse Microscopy. *J. Vis. Exp.* (2011) doi:10.3791/3145.

43. Harwood, C. R. & Cutting, S. M. *Molecular biological methods for Bacillus*. (Wiley, 1990).

44. Koo, B.-M. *et al.* Construction and Analysis of Two Genome-Scale Deletion Libraries for Bacillus subtilis. *Cell Syst.* **4**, 291-305.e7 (2017).

45. Ellefsen, K. L., Dynes, J. L. & Parker, I. Spinning-Spot Shadowless TIRF Microscopy. *PLOS ONE* **10**, e0136055 (2015).

46. Thevenaz, P., Ruttimann, U. E. & Unser, M. A pyramid approach to subpixel registration based on intensity. *IEEE Trans. Image Process.* **7**, 27–41 (1998).

47. Dos Santos Caldas, P. R., Radler, P., Sommer, C. M. & Loose, M. Computational analysis of filament polymerization dynamics in cytoskeletal networks. *Methods Cell Biol.* (2020).

48. Eberly, D., Gardner, R., Morse, B., Pizer, S. & Scharlach, C. Ridges for image analysis. *J. Math. Imaging Vis.* **4**, 353–373 (1994).

49. Tinevez, J.-Y. *et al.* TrackMate: An open and extensible platform for single-particle tracking. *Methods* **115**, 80–90 (2017).

50. Ho, J., Tumkaya, T., Aryal, S., Choi, H. & Claridge-Chang, A. Moving beyond P values: data analysis with estimation graphics. *Nat. Methods* **16**, 565–566 (2019).

51. Killick, R., Fearnhead, P. & Eckley, I. A. Optimal Detection of Changepoints With a Linear Computational Cost. *J. Am. Stat. Assoc.* **107**, 1590–1598 (2012).